Photoproduction of the $f_1(1285)/\eta(1295)$ Mesons using CLAS at Jefferson Lab

by

Ryan Dickson

A dissertation submitted in partial fulfillment of the requirements
for the degree of

Doctor of Philosophy

in the Department of Physics

Carnegie Mellon University

July 18, 2011

Abstract

This work presents the results of analysis of a meson of mass $m_x = 1281.0 \pm 0.8$ MeV/c^2 and a FWHM of $\Gamma_x = 18.4 \pm 1.4$ MeV/c^2 seen in CLAS at Jefferson Lab in photoproduction off the proton, $\gamma p \to xp$. The $f_1(1285)$, $\eta(1295)$ or both are candidates for this observed state. Neither of these states has previously been observed in photoproduction. The meson was measured in the decay modes $x \to \eta\pi^+\pi^-$, $K^+\bar{K^0}\pi^-$, $K^-K^0\pi^+$, and $\rho^0\gamma$ through detection of its charged decay products and the recoil proton.

Differential cross sections were obtained via the $x \to \eta\pi^+\pi^-$, $K^+\bar{K^0}\pi^-$, and $K^-K^0\pi^+$ decay channels from threshold up to a center-of-mass energy of 2.8 GeV, and compared to recent Regge model predictions. Dalitz analysis showed strong evidence for the $f_1(1285)$ identity, with the dominance of $\eta\pi^+\pi^-$ decays via $a_0^{\pm}(980)\pi^{\mp}$ intermediate state and with interference consistent with a spin one particle. The relative branching fractions $\Gamma(K\bar{K}\pi)/\Gamma(\eta\pi\pi)$ and $\Gamma(\rho^0\gamma)/\Gamma(\eta\pi\pi)$ were measured, with agreement to world data for the $f_1(1285)$ in the former and lower than the world average for the latter.

Contents

List of Figures

List of Tables

Acknowledgments

First I must thank my family and friends for their tremendous support during my long academic journey. This document would not have been possible with the love and patience of my wife Kimberly. She bravely joined me in Pittsburgh after my first year of study and has been keeping me on task ever since. Thanks also to my parents for their support of my interest in science since my early years (as my bookshelf will attest).

I came to Carnegie Mellon not quite sure which area of physics I would pursue. It is serendipitous that I found myself working with the Medium Energy Experiment Group as part of introductory research seminar, not only for their knowledge of physics and experimental methods, but for camaraderie and encouragement. Professor Reinhard Schumacher has given me excellent guidance and instruction as my adviser, always with understanding and tremendous patience. I thank Professors Curtis Meyer, Brian Quinn, Gregg Franklin, and Dennis Weygand for serving on my thesis committee. Their critique and recommendations have greatly strengthened this document.

I must also thank the post-docs and students of the Medium Energy Group whose work has provided the scaffold that from which this and many other analyses have been built. Mike Williams provided software frameworks that made accessing and analyzing CLAS data as painless as possible, and so thoroughly documented that it shames other CLAS software packages. Mike also provided clear explanations regarding all things programming-related and excellent musical recommendations. The systematic studies of g11 by Mike, Matt Bellis and the rest of the PWA group were invaluable. Matt will disappointed that I have kicked the fantasy football addiction, but his sense of humor has possibly infected me forever.

I am thankful for the friendship of a large number of other people at CMU: Kevin Bandura, Jules Gardener, Seamus Riordan, Zeb Krahn, Diana Parno, Mike McCracken, Kei Moriya, Biplab Dey, Megan Friend, Brian Vernarsky, among many others. I would also like to thank the friends I have in met outside of physics in Pittsburgh: Jen Martin, Lyn Cote, Caleb Wattley, Neil Uranic, Danielle Goudeau and Lindsay and Joe Pulman. You have all helped make da'Burgh feel like home and have made it a tough place to leave.

I also must offer thanks to my high school physics and chemistry teacher Stephen Dixon, whose enthusiasm led me to purse science in college and beyond.

Finally, and definitely not least, I would like to thank my son Wyatt. While a recent addition to the team, his smiles and giggles have been just what I needed to finish this work with my sanity intact.

Chapter 1

Introduction

The aim of the analysis is to study of the *photoproduction* reaction

$$\gamma p \to xp, \tag{1.1}$$

in data obtained by the CLAS detector at Jefferson Lab, where γ is a high energy photon incident on the a proton p. The x is one or both of two nearly mass-degenerate mesons near 1280 MeV/c^2, the $f_1(1285)$ and the $\eta(1295)$. Table 1.1 lists the basic properties of these states compiled from world data by the Particle Data Group (PDG) [1]. This chapter will detail the motivation for studying $f_1(1285)/\eta(1295)$, from both experimental and theoretical standpoints. As the identity of the observed experimental state is the ultimate result of this thesis, we will refer to the state as the "x" or $x(1280)$ until Chapter 6.

Meson	$I^G(J^{PC})$	Mass MeV/c^2	Full Width Γ MeV/c^2
$f_1(1285)$	$0^+(1^{++})$	1281.8 ± 0.6	24.3 ± 1.1
$\eta(1295)$	$0^+(0^{-+})$	1294 ± 4	55 ± 5

Table 1.1: Properties of $f_1(1285)/\eta(1295)$ mesons as compiled by the Particle Data Group[1].

1.1 Quantum Chromodynamics

The goal of particle physics is to determine the fundamental building blocks of the universe and the rules that govern their interactions. The *Standard Model* of particle physics is the current theory encompassing the electromagnetic, weak, and strong nuclear interactions, which mediate the dynamics of the known subatomic particles. The *strong* force is responsible for binding protons and neutrons together in the nucleus of atoms. These *nucleons* are not the fundamental particles of the interaction. The strong force is mediated by massless spin one bosons called *gluons*, acting upon massive spin 1/2 fermions known as *quarks* and upon the *gluons* themselves. This is detailed in the theory of Quantum Chromodynamics (QCD), so called for the three *color* charges, labeled red, green, and blue carried by both quarks and gluons.

In contrast to the theory for the electromagnetic interaction, Quantum Electrodynamics(QED), where the force-carrying photons do not directly self-interact, the gluons of QCD carry color-charge themselves. As a result, analytic or perturbative solutions in low-energy QCD are impossible due to the highly nonlinear nature of the strong force.

It was found that that the coupling constant of QCD would asymptotically reach small values at sufficiently high energies (discovered by David Gross and Frank Wilczek [2], and H. David

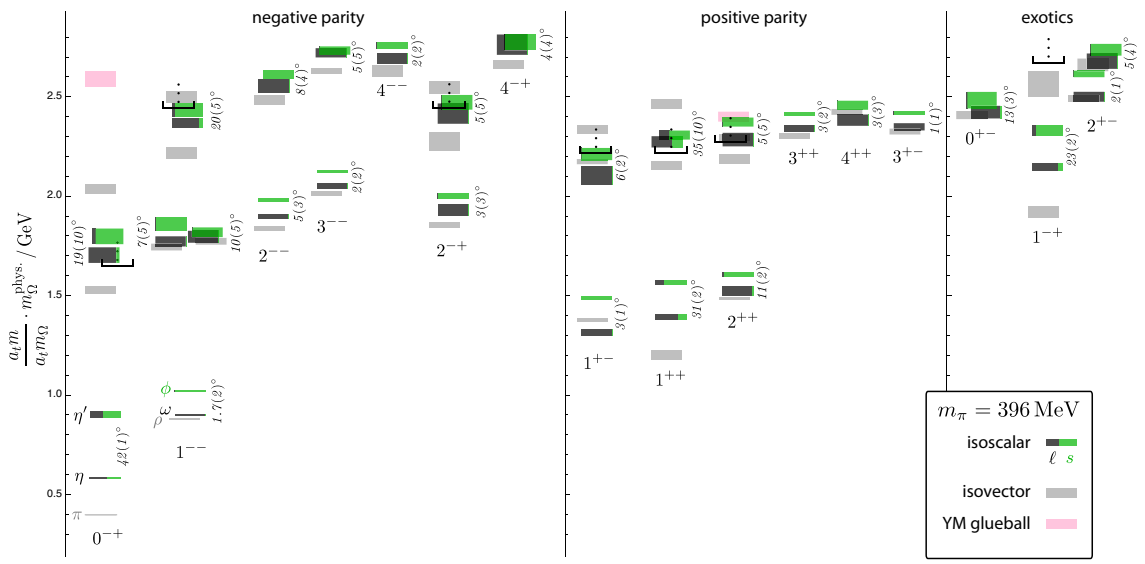

Figure 1.1: Isoscalar meson spectrum labeled by J^{PC} calculated in lattice QCD at pion mass of 400 MeV. The box height indicates the one sigma statistical uncertainty above and below the central value. The light-strange content of each state $(\cos^2\alpha, \sin^2\alpha)$ is given by the fraction of (black, green) and the mixing angle for identified pairs is also shown. Grey boxes indicate the positions of isovector meson states extracted on the same lattice. Pink boxes indicate the position of glueballs in the quark-less Yang-Mills theory. Calculations and Image from Ref [4].

Politzer [3]). This weakening of the interaction between quarks and gluons known as *asymptotic freedom* allows perturbation theory to be applied to QCD calculations at high energy.

In the regime of the nucleons, however, the coupling strength is of order unity and no perturbative cutoff can be applied. Together with *confinement*, the property that the strength of the strong force does not fall off as the quarks are separated, this means we can not directly measure the behavior of quarks. Instead we must observe them bound into states called *hadrons*.

Hadrons comprise two observed categories, *baryons* made of three valence quarks (qqq), and *mesons* made of a valence quark and antiquark ($q\bar{q}$). There is no intrinsic prohibition of states of more than three quarks. Though experimental searches have sparked controversy, there are no confirmed candidates at present.

Despite the lack of analytic solution to QCD, there are many predictions for the spectrum of hadrons at low-energies. Various phenomenological quark models exist which simplify QCD, usually by ignoring gluon degrees of freedom, in such a manner as to allow for analytical calculations to be made. Additionally, great strides have been made in numerical calculations known as *lattice QCD*. This approach evaluates QCD in discrete rather than continuous spacetime, which regularizes the theory by introducing a momentum cut off at the order $1/a$, where a is the lattice spacing. In this framework, Monte Carlo methods are used to estimate the two-point function or *correlator* to generate the spectrum of excited states. Figure 1.1 shows the isoscalar meson spectrum recently calculated by J. Dudek *et al.* [4], with $m_\pi = 396$ MeV$/c^2$. The lowest lying 1^{++} isoscalar is predicted with a mass near 1400 MeV and the lowest lying 0^{-+} isoscalar state above the η' has a mass around 1700 MeV.

Study of the spectrum of mesons, including the $f_1(1285)/\eta(1295)$, gives access to many properties of that describe the phenomena of strong interaction. The goal of this analysis is to expand the body

of experimental knowledge of these states and compare our results to available theoretical models, leading towards a better understanding of the non-perturbative realm of QCD.

1.2 Meson Spectroscopy

The study of the spectra of masses and widths of quantum-mechanical states is known as spectroscopy. Hadron spectroscopy studies the measured masses and decay widths of states of bound quarks in comparison with predictions from phenomenological models and lattice QCD. In the case of baryons, the number of expected states of the constituent quark model is much greater than the number of experimentally observed states; this is known as "missing baryons problem". In this model, the relevant degrees of freedom are in the valence quarks. The gluonic degrees of freedom are not excited. The standard spectrum of baryons generated from CQM calculations of Capstick and Roberts [5] has nearly four times as many predicted states as experimentally confirmed. Determining whether these states exist or not is motivation for many medium energy analyses.

In contrast, for mesons such as the $x(1280)$ studied in this analysis there exist more experimentally observed states than expected for the just $q\bar{q}$ states. QCD also has the potential for bound states of just gluons called glueballs, as well as hybrid mesons($q\bar{q}+glue$), tetraquarks, and molecules of hadrons. One of the goals of the field of hadronic spectroscopy is to find experimental evidence for such states. Many experimentally observed mesons have been and continue to be candidates for these possibilities.

Through studying the spectrum of mesons observed experimentally and their properties we can gain insight into the role of *gluons*, "molecular" states, and dynamically generated structures in non-perturbative QCD. Determining the nature of $f_1(1285)/\eta(1295)$ and describing their interactions imposes constraints on models of the strong force in this sector.

Table 1.2 lists the properties of light spin zero and spin one $q\bar{q}$ mesons. These states are considered well-established by the PDG. Not included in the table are the scalar resonances which have the same quantum numbers as the vacuum ($J^{PC} = 0^{++}$). Such states are difficult to measure because of their large decay widths which cause a strong overlap between resonances and background, and also because several decay channels open up within a short range in mass. Additionally, the thresholds for KK and $\eta\eta$ production produce sharp cusps in the energy dependence of the resonant amplitude. These states are often seen as candidates for non-$q\bar{q}$ scalar objects, like glueballs and multiquark states.

$n^{2s+1}L_J$	J^{PC}	$I=1$ $u\bar{d}, \bar{u}d, \frac{1}{\sqrt{2}}(d\bar{d}-u\bar{u})$	$I=1/2$ $u\bar{s}, d\bar{s}; \bar{d}s, -\bar{u}s$	$I=0$ f'	$I=0$ f	Θ_{quad} [°]	Θ_{lin} [°]
1^1S_0	0^{-+}	π	K	η	η'	-11.5	-24.6
1^3S_1	1^{--}	$\rho(770)$	$K^*(892)$	$\phi(1020)$	$\omega(782)$	38.7	36.0
1^1P_1	1^{+-}	$b_1(1235)$	$K^\dagger_{1B}$	$h_1(1380)$	$h_1(1170)$		
1^3P_1	1^{++}	$a_1(1260)$	$K^\dagger_{1A}$	$f_1(1420)$	$\mathbf{f_1(1285)}$		
1^3P_2	2^{++}	$a_2(1320)$	$K^*_2(1430)$	$f'_2(1525)$	$f_2(1270)$	29.6	28.0
2^1S_0	0^{-+}	$\pi(1300)$	$K(1460)$	$\eta(1475)$	$\eta(\mathbf{1295})$		
2^3S_1	1^{--}	$\rho(1450)$	$K^*(1410)$	$\phi(1680)$	$\omega(1420)$		

Table 1.2: Properties of S-wave and P-wave mesons (scalar mesons omitted) as tabulated by the Particle Data Group[1]. The Θ_{quad} and Θ_{lin} mixing angles of the octet and singlet states come from the quadratic and linear dependence upon the mesons masses formulation of the relevant sum rules as described in PDG review. Note: the $1^{+\pm}$ $K^\dagger_{1A}$, $K^\dagger_{1A}$ states mix with the $2^{-\pm}$ isospin 1/2 states (not listed).

Also left out are four poorly experimentally-established mesons the 1^{+-} $h_1(1380)$, 0^{-+} $\eta(1405)$,

2^{++} $f_2(1430)$ and 1^{++} $f_1(1510)$. Of these, the $\eta(1405)$ and $f_1(1510)$ are of interest in understanding the nature of $f_1(1285)$ and $\eta(1295)$ states.

The first pseudoscalar discovered in this region was the $\eta(1440)$ in $p\bar{p}$ annihilation at rest into $\eta(1440)\pi^+\pi^-$, $\eta(1440) \to K\bar{K}\pi$ [6], observed decaying through $a_0(980)\pi$ and $K^*(892)\bar{K}$ with roughly equal contributions. Later evidence replaced the $\eta(1440)$ with two separate pseudoscalars in this mass region, the $\eta(1405)$ and $\eta(1475)$. The former decaying mainly through $a_0(980)\pi$ (or direct $K\bar{K}\pi$) and the latter mainly to $K^*(892)\bar{K}$. Together with the $\eta(1295)$ we have three pseudoscalar mesons in a region where only the two radial-excitations are expected. The current interpretation favored by the Particle Data Group in their review [1] is that the $\eta(1475)$ is the more likely partner of the $\eta(1295)$ as radial excitations, with the $\eta(1405)$ being a good glueball candidate in the flux-tube model. However, as we will discuss further in §1.3.3, the existence of the $\eta(1295)$ is controversial.

The $f_1(1510)$ faces a similar status in relation to the $f_1(1285)$ and $f_1(1420)$. Again the simple mixing model would produce two mass states for the axial-vector nonet with the higher mass state having the larger $s\bar{s}$ contribution. The $f_1(1510)$ competes with the $f_1(1420)$ for this identity but its existence has not been as clearly confirmed experimentally. Review of the experimental evidence by the PDG for both states concluded the $f_1(1510)$ was poorly established [1]. Three mass states can be produced by including a gluonic degree of freedom to the mass mixing matrix [7], reproducing the observed masses. In any case, there is evidence that non-$q\bar{q}$ states contribute to the spectrum of mesons in the 1200-1500 MeV region.

1.3 Theoretical Status of $f_1(1285)/\eta(1295)$

The $f_1(1285)$ fits well into the Quark Model and its predictions with regard to the spectrum of light mesons. The conventional view is the $f_1(1285)$ is a member of the axial-vector nonet (see Figure 1.2c), being the lower mass partner of the $f_1(1420)$. The experimentally observed masses are mixed states of the octet and singlet states, analogous to the η and η' in the pseudoscalar case, Figure 1.2a.

$$|f_1(1285)\rangle = |f_1\rangle \cos\Theta + |f_8\rangle \sin\Theta, \qquad |f(1420)\rangle = |f_1\rangle \cos\Theta + |f_8\rangle \sin\Theta. \tag{1.2}$$

$$\tag{1.3}$$

where

$$f_1 = \frac{1}{\sqrt{3}}(\bar{u}u + \bar{d}d + \bar{s}s), \tag{1.4}$$

$$f_8 = \frac{1}{\sqrt{6}}(\bar{u}u + \bar{d}d - 2\bar{s}s), \tag{1.5}$$

showing the conventional choice of relative sign between the $\bar{s}s$ terms. It has also been proposed that $f_1(1285)$ may have a significant gluonic component to its wave-function [7], 14% of the total amplitude. This model has the isoscalar triplet of axial vector mesons mix with a gluonic state to reproduce the masses of the $f_1(1285)$ $f_1(1420)$ and the poorly-established $f_1(1510)$. However, such simplistic models of gluonic mixing such models yielded branching ratios and electromagnetic decay widths for the $f_1(1285)$ and $f_1(1420)$ that are strongly contradicted by experimental evidence.

The $\eta(1295)$ along with the η's above 1400 MeV, have a more complicated status with regard to the predicted spectrum, and theoretical interpretation of the $\eta(1295)$ is more controversial. Concurrent to its discovery were predictions by Cohen and Lipkin[8] that the first radial excitations of the η and η' mesons should lie the 1200-1500 MeV mass region. Figure 1.2b depicts such an assignment as members of the radially excited nonet. Complicating the picture is the separation of the original $\eta(1440)$ into the $\eta(1405)$ and $\eta(1475)$ in later experiments. The possible situation is that two of these states are radial excitations of the η and η' ground state, while the third would

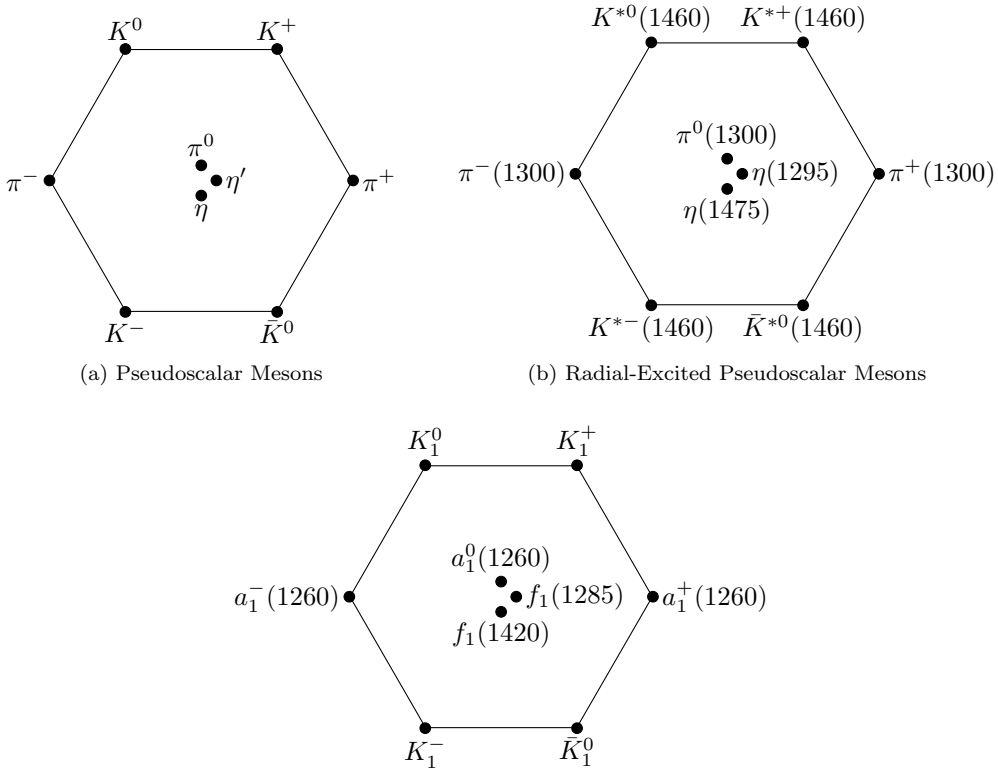

(a) Pseudoscalar Mesons

(b) Radial-Excited Pseudoscalar Mesons

(c) Axial Vector Mesons

Figure 1.2: Nonets of the pseudoscalar (a), radially-excited pseudoscalar (b) and axial-vector mesons (c).

be a glueball or hybrid meson candidate. Though glueballs are not expected below 2 GeV in lattice gauge theories, fluxtube models [9] have predicted the lowest gluonic states to be around 1.5 GeV/c, with the $\eta(1405)$ being an excellent experimental candidate [10]. It would then follow to assign the $\eta(1295)$ and $\eta(1475)$ as the radially-excited pseudoscalars, with the $\eta(1475)$ having the larger $s\bar{s}$ state consistent with the mass hierarchy and observed decay modes. Another possibility is that the $\eta(1295)$ and $\eta(1405)$ are the first radial excitations and the $\eta(1475)$ is the 2nd radial excitation of the η.

There is still a fair amount of disagreement over such an assignment with some authors suggesting a single $\eta(1440)$ in this mass region as the radial excitation [11] or the splitting of $\eta(1440)$ into the $\eta(1405)$ and $\eta(1475)$ as a decay-mode dependent rescattering effect [12]. In any case, three 0^{-+} states are too many for the simple radial excitation picture. More experimental data is necessary to clear up the situation. Several recent theoretical predictions have been made which are relevant to this analysis. The radiative decay width of these states have been calculated according to constituent quark model approach. And more recently, two independent models have produced predictions for the photoproduction cross section of the 1.28 GeV states in the Regge-model framework.

1.3.1 Regge Model Photoproduction Predictions

Two separate groups have calculated exclusive $f_1(1285)$ meson photoproduction cross section on the proton in the medium energy regime within the Regge approach. The Regge model is an effective

Coupling	value	source
$g_{\omega NN}$	10.6	AIP Conf.Proc 2004 [14]
$g_{\rho NN}$	3.9	"
g_{ω}^{T}	0	"
g_{ρ}^{T}/g_{ρ}	6.1	"
$g^2_{f_1\rho\gamma}$	0.94 GeV^{-2}	$\Gamma(f_1 \to \rho^0\gamma)$ [1]
$g_{f_1\omega\gamma}$	$\approx \frac{e_u+e_d}{e_u-e_d} g_{f_1\rho\gamma} = \frac{1}{3} g_{f_1\rho\gamma}$	$SU(2)_f$ limit
$g^2_{\eta(1295)_{\rho\gamma}}$	0.0032 GeV^{-2}	$\Gamma(\eta(1295) \to \gamma\gamma)$ [1]
$g_{\eta(1295)_{\omega\gamma}}$	$\approx \frac{e_u+e_d}{e_u-e_d} g_{f_1\rho\gamma} = \frac{1}{3} g_{f_1\rho\gamma}$	$SU(2)_f$ limit

Table 1.3: Couplings used in Kochelev Regge model [13] of $f_1(1285)/\eta(1295)$ photoproduction.

Lagrangian $t-$channel exchange featuring Regge propagators in lieu of the standard propagators of Feynman diagrams. Regge propagators incorporate trajectories such that the scattering amplitude

$$A \propto s^{2(\alpha(t)-1)} \tag{1.6}$$

where $\alpha(t)$ is the Regge parametrization of families of exchanged particles. The usual form of the Regge trajectory is a linear function, $\alpha(t) = a + bt$.

Kochelev

N. Kochelev's calculations[13] utilized exchange of ρ and ω trajectories in the Regge framework for small momentum transfer ($|t| \leq 1\,GeV^2$). The model uses phenomenological input from available experimental data to constrain the relevant couplings and vector-meson-dominance inspired form factors. Table 1.3 lists the couplings used. The Regge trajectories used were $\alpha_\rho = 0.55 + 0.8t$ and $\alpha_\omega = 0.44 + 0.9t$. The model produces differential cross sections for the η,$f_1(1285)$, and $\eta(1295)$. The model describes experimental data for $\gamma p \to \eta(548)p$ from SAPHIR reasonably well. Figure 1.3 shows the calculated differential cross sections at $E_\gamma = 3.1\,GeV$. The calculated $f_1(1285)$ total cross section is about four times that of the $\eta(1295)$, integration over t yields the values

$$\sigma_{f_1(1285)} = 68\,nb, \tag{1.7}$$

$$\sigma_{\eta(1295)} = 18\,nb, \tag{1.8}$$

predicting that photoproduction in the energy range studied in this analysis is dominated by the $f_1(1285)$. This calculation was made with the kinematics of Jefferson Lab in mind, and predicts photoproduction of $f_1(1285)/\eta(1295)$ mesons to be of sufficient strength for detailed analysis. A comparison of our differential cross section results to these calculations recomputed [15] as $d\sigma/d\Omega$ for our choice of energy and $\cos\Theta$ bins will be given Chapter 5.

Domokos

Recent calculations motivated by a dual description of QCD in terms of string theory have also produced differential cross sections for $f_1(1285)$ in the Regge framework. A model of photoproduction motivated from Chern-Simons-term-induced interactions in holographic QCD by S. Domokos [16] calculated the anomalous couplings and vertex functions derived from the general principles of AdS/QCD (anti-de Sitter) correspondence. The resultant couplings, given in Table 1.4, are similar to the those of phenomenological models.

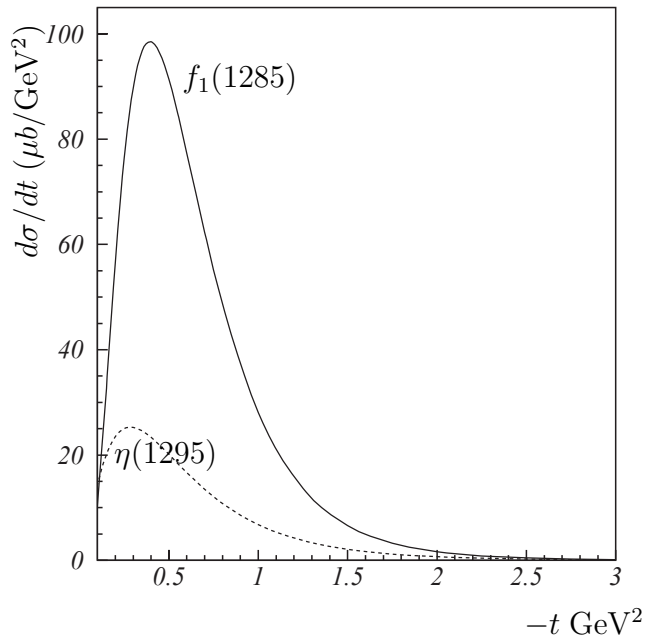

Figure 1.3: Regge Model estimations of $d\sigma/dt$ for the $f_1(1285)$(solid line) and $\eta(1295)$(dashed line) in photoproduction at $E_\gamma = 3.1\,GeV$ by N. Kochelev. Image Source [13]

Coupling	value
$g_{\omega NN}$	9
$g_{\rho NN}$	2.4
$g_{f_1 NN}$	2.5
$g_{\gamma\omega f_1}$	-0.33
$g_{\gamma\rho f_1}$	-0.99

Table 1.4: Couplings used in Domokos Regge model [16] of $f_1(1285)$ photoproduction.

A comparison to experiment for this model is the decay-rate,

$$\Gamma(f_1(1285) \to \rho^0\gamma) = \frac{\alpha_{em} g^2_{\gamma\rho f}}{3} \frac{E^3_\gamma}{m^2_\rho} \left(1 + \frac{m^2_\rho}{m^2_f}\right) \tag{1.9}$$

dependent upon two-body phase-space where $E_\gamma = (m_f^2 - m_\rho^2)/2m_f$ in the CM-frame, α_{em} is the fine structure constant and their coupling $g_{\gamma\rho f} \simeq -1$. Calculating this coupling from the experimental width $\Gamma_{exp} = 1.33 \pm 0.37\,MeV$ [1] yields a slightly incompatible $|g_{\gamma\rho f}| = 1.7 \pm 0.4$. However, they conclude this disagreement can be negated by adjusting the method of calculation of another parameter in their model. Figure 1.4 shows the calculated differential cross sections at $E_\gamma = 4.6\,GeV$. Though computed at a higher energy, the predicted $f_1(1285)$ cross section is quite different in shape from that of the Kochelev model. The Domokos calculation has its maximum value at $t = 0$ and features an interference minimum around $-t = 0.55$ GeV^2. In Chapter 5 we will compare our results to curves calculated from the Domokos model for our kinematics. A detailed summary of the calculations appear in Appendix A.

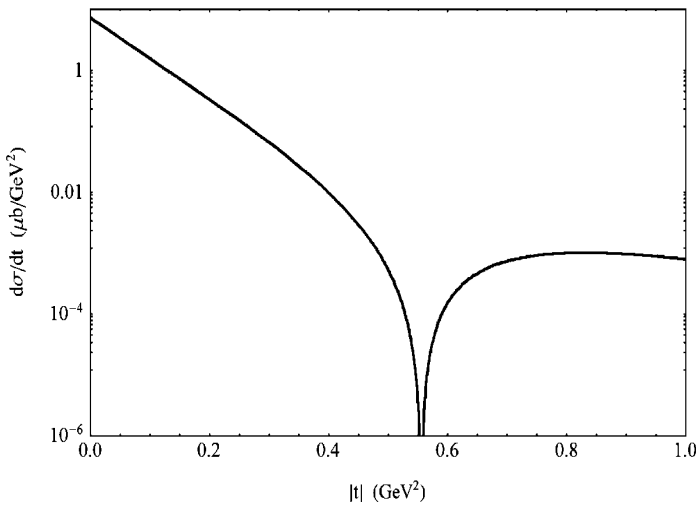

Figure 1.4: The differential cross section $d\sigma_R/dt$ for $f_1(1285)$ photoproduction calculated with ρ and ω-meson Regge trajectories for $|t| \leq 1\ GeV^2$ at $s = 10\ GeV^2$ ($E_\gamma \sim 4.6\ GeV$ in lab frame) in the Domokos Model. Image Source [16]

1.3.2 Radiative Decays

In addition to the recent calculations of differential cross sections some predictions of radiative decay rates of the $f_1(1285)/\eta(1295)$ mesons have been made. At present there are no reported branching ratios for the $\eta(1295)$, though quark model radiative decay calculations performed by Lakhina and Swanson [17][18] predict a radial excitation $\eta(1295)$ to have a $\rho^0\gamma$ coupling strength between a third and a half of that for the $f_1(1285)$. Table 1.5 lists the calculated widths for the radiative decays of the $f_1(1285)/\eta(1295)$ mesons. The predictions were calculated using both relativistic and non-relativistic models in the Coulomb gauge [17].

Meson	Radiative Transition	non-relativistic	relativistic
$f_1(1285)$	$(1\ ^3P_1) \rightarrow \rho^0\gamma(E1)$	1200 keV	480 keV
$\eta(1295)$	$(2\ ^1S_0) \rightarrow \rho^0\gamma(M1)$	400 keV	240 keV

Table 1.5: Quark Model Radiative Transitions for $f_1(1285)/\eta(1295)$ by E. Swanson[17][18]. $f_1(1285) \rightarrow \rho^0\gamma$ has been seen experimentally with branching fraction in good agreement with the non-relativistic model.

Similar predictions were made using a covariant oscillator quark model by Ishida *et al.* [16]. The predicted $f_1(1285)$ partial width was found to be 509-565 keV depending upon the chosen mixing angle $\Theta s\bar{s}$ between the octet and singlet 1^{++} states. Table 1.6 shows the predictions of the Ishida model.

Meson	Radiative Transition	width	$\Theta_{s\bar{s}}$
$f_1(1285)$	$(1\ ^3P_1) \rightarrow \rho^0\gamma(E1)$	509 keV	21°
$f_1(1285)$	$(1\ ^3P_1) \rightarrow \rho^0\gamma(E1)$	565 keV	10°

Table 1.6: Quark Model predictions for radiative transitions for $f_1(1285)/\eta(1295)$ by Ishida[16]. $f_1(1285) \rightarrow \rho^0\gamma$ has been seen experimentally with a branching fraction in good agreement with the non-relativistic model.

As with the Kochelev differential cross section predictions, the $f_1(1285)$ is predicted to have a stronger $g_{\gamma Nx}$ coupling than the $\eta(1295)$. We will revisit these predictions as they relate to our analysis in Chapter 5.

1.3.3 Is $\eta(1295)$ a Phantom State?

An opposing view of $f_1(1285)/\eta(1295)$ world data was brought forth by E. Klempt and A. Zaitsev in a review of the experimental status of glueballs and hybrids in meson spectroscopy[11] They proposed that the $\eta(1295)$ is not the radial excitation of the η meson, but rather is "faked" by feed-through from the nearly mass-degenerate $f_1(1285)$ and the Deck effect[19] in $\eta\sigma$ $\hat{\text{S}}$-wave interactions. This effect was seen in early analyses of the $a_1(1260)$, the properties of which were obscured by the $\rho - \pi$ re-scattering in the final state. For the $\eta(1295)$, it is possible that $a_0(980)\pi$ re-scattering fakes a resonant-like behavior, though less likely due to the narrow width.

Furthering the argument against the existence of the $\eta(1295)$ is that, although it has been seen in $\pi^- p \to n(\eta\pi\pi)$, it is not seen in $p\bar{p}$ annihilation, nor in radiative J/Ψ decay, nor in $\gamma\gamma$ fusion. If it is a $q\bar{q}$ state it should have been observed in such reactions. Also, most theories do not expect glueballs, hybrids or multiquark states at such a low mass.

The other explanation suggested is the possibility that the $\eta(1295)$ signal is mimicked by feed-through from the $f_1(1285)$ in the PWA-analyses. That is, the strength in the 0^{-+} waves comes not from the presence of the $\eta(1295)$, but from leakage of other waves due to either experimental losses in angular coverage and/or as a result of the set of partial-waves used in fitting. The "art" of PWA is choosing the reasonable set of partial-waves for both the physics and statistics of the available data.

1.4 Experimental History

The meson now identified as the $f_1(1285)$ was first observed in 1965, and it has since been observed in various production modes, both directly and through partial wave analyses.

A pseudoscalar meson of near-degenerate mass, the $\eta(1295)$ was first identified in the late 1970's, also in partial wave analyses of hadronic data [20]. Some controversy exists around both these states, since at least one paper [21] argues that many of the earlier observations of the $f_1(1285)$ were actually a mix of both of these mesons. Some authors [11] go as far to suggest the $\eta(1295)$ is a phantom observation as discussed above.

1.4.1 $f_1(1285)$

The $f_1(1285)$, named the D meson at the time, was discovered independently at BNL[22] and at CERN[23]. Both experiments used $p\bar{p}$ annihilation and observed a 1^+ resonance decaying to $K\bar{K}\pi$. The letter D is now used to denote mesons with open charm and f_1 denotes axial-vector mesons with isospin and strangeness of zero. Early experiments that did not perform a spin-parity analysis or were limited statistically might have contained some $0^{-+}(\eta(1295))$ component, as suggested in criticism of earlier world data brought up by the E852 collaboration [21]. Two, more recent, experiments that made very clean measurements of the $f_1(1285)$ in central production and $\gamma\gamma$ collisions will be discussed next.

CERN WA102

Experiment WA102, which ran at CERN in 1995-96, searched for non-$q\bar{q}$ mesons produced in the central region in the reaction

$$pp \to p_f(X^0)p_s \tag{1.10}$$

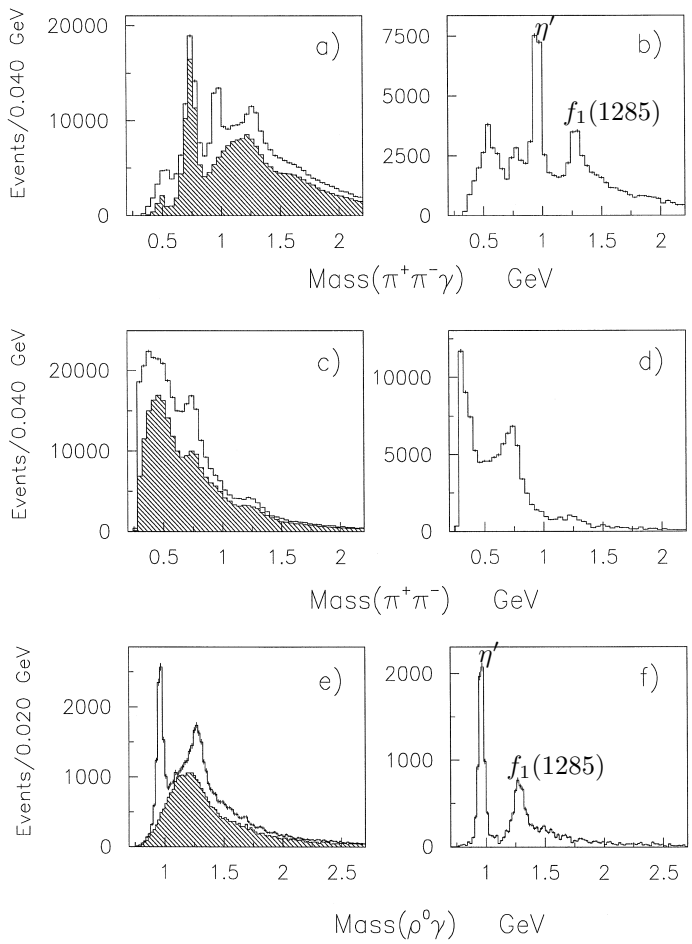

Figure 1.5: WA102 results (a) The $\pi^+\pi^-\gamma$ spectrum with shaded the background from the $\pi^+\pi^-\pi^0$ channel (b) the background-subtracted $\pi^+\pi^-\gamma$ mass spectrum. (c) The $\pi^+\pi^-$ mass spectrum with shaded the background from the $\pi^+\pi^-\pi^0$ channel (d) the background-subtracted $\pi^+\pi^-$ mass spectrum. (e) The $\rho^0\gamma$ mass spectrum with shaded the background from the $\pi^+\pi^-\pi^0$ channel (f) the background-subtracted $\rho^0\gamma$ mass spectrum. Image Source [24].

at 450 GeV/c using the Omega Spectrometer for charged particle reconstruction and GAMS-4000 for multiphoton detection. X^0 represents the central system presumed to have been produced by double-exchange processes and $p_f(p_s)$ are the fast(slow) protons in the laboratory frame. The goal of experiment WA102 was to make a more complete study of the mass region from 1.2 to 2.5 GeV, continuing the work of the WA76, WA91 and NA122 experiments. Central production was important for the goal of finding non-$q\bar{q}$ mesons through the "gluon-rich" production mechanism of double pomeron exchange (DPE).

The experiment made clean measurements of the $f_1(1285)$ and $f_1(1420)$ mesons decaying to $\eta\pi\pi$ [24],$\rho^0\gamma$ [24], four pion [25][26], and $K\bar{K}\pi$ [27] final states. Figure 1.5 shows the $f_1(1285)$ signal and associated background spectra observed for the $\rho^0\gamma$ decay mode. As discussed earlier in §1.3.2, the $f_1(1285)$ couples more strongly to $\rho^0\gamma$ than does $\eta(1295)$. The WA102 result for the branching ratio $f_1(1285) \to \rho^0\gamma/f_1(1285) \to \eta\pi^+\pi^-$ of $0.10\pm0.01\pm0.02$ is in fair agreement with the non-relativistic prediction of Swanson and Lakhina mentioned earlier (1.2Mev/(24.3MeV $\times\ \mathcal{B}_{\eta\pi\pi}$).

Figure 1.6 shows the result of their spin-parity analysis of the $\eta\pi^+\pi^-$ channel with clear identi-

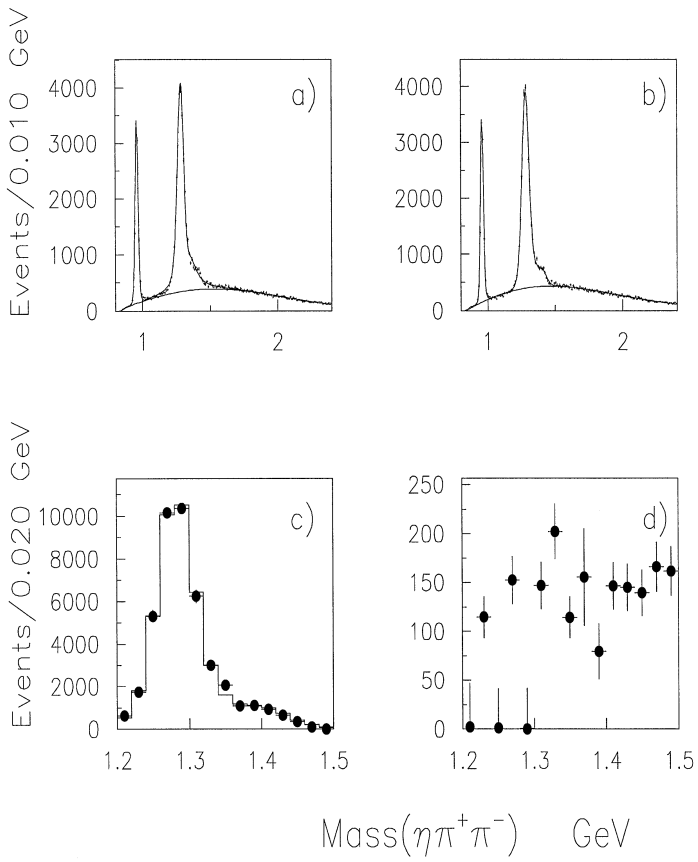

Figure 1.6: WA102 Spin-Parity results for the $p\bar{p}$ central production of the $f_1(1285)$ decaying to $\eta\pi^+\pi^-$. The $\eta\pi^+\pi^-$ mass spectrum was fit (a) without and (b) with interference between the $f_1(1285)$ and $f_1(1420)$ Breit-Wigners. The (c) $J^{PC} = 1^{++}$ $a_0(980)\pi$ wave and the (d) $J^{PC} = 0^{-+}$ $a_0(980)\pi$ wave. Image Source [24].

fication of the 1^{++} as the spin-parity state. The WA102 experiment found no evidence for presence of 0^{-+} states in this mass region, in agreement with earlier central production experiments WA76 at CERN and E690 at Fermilab. The suppression of 0^{-+} production in central production allowed the WA102 collaborators to measure $f_1(1285)$ branching fractions in the major decay channels with good accuracy without worry of $\eta(1295)$ contamination.

LEP

The L3 collaboration at CERN observed the $f_1(1285)$ in the reaction

$$e^+e^- \to e^+e^-\gamma_v\gamma_v \to e^+e^-\eta\pi^+\pi^- \tag{1.11}$$

at the Large Electron Positron collider (LEP). L3 experiment measured the $f_1(1285)$ in "untagged" events those consistent with a virtual photon(s) γ_v. "Untagged" two-photon collisions meaning events where the outgoing electron and positron carry almost the full beam energy and were not detected. According to the Landau-Yang theorem[28], the production of a spin-one resonance is suppressed for nearly real photons $Q^2 \simeq 0$. For increasing virtuality of the photons ($Q^2 > 0$), the relative production of a spin-0 state to a spin-1 state diminishes. The experimenters used this to disentangle the pseudoscalar and axial-vector contributions to data through binning their spectra in

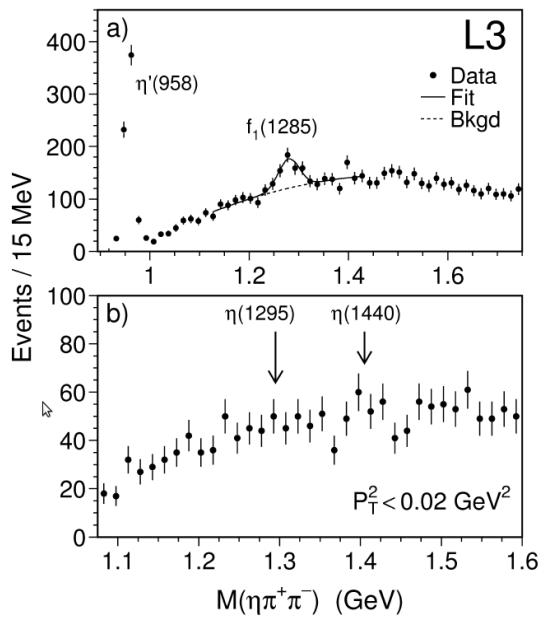

Figure 1.7: L3 Results. For low $P_T \simeq Q^2$, axial-vector production is highly suppressed relative to pseudoscalars. Image Source [29].

total transverse momentum P_T which equals Q^2 to good approximation and fitting the yields with the calculated effective form factors.

The L3 collaborators observed the $f_1(1285)$ decaying to both $\eta\pi\pi$ and $K_S^{\pm}K^0\pi^{\mp}$, and set an upper-limit on two-photon production limit of $\eta(1295)$, $\Gamma_{\gamma\gamma}(\eta(1295)) \times BR(\eta(1295) \to \eta\pi\pi) <$ 66 eV [29]. They also observed both the $\eta(1440)$ and the $f_1(1420)$ decaying to $K_S^{\pm}K^0\pi^{\mp}$ at low- and high-Q^2 respectively. They determined that the two-photon width of the $\eta(1440)$ was consistent with it being the first radial-excitation of the pseudoscalar nonet, a hypothesis usually assigned to the $\eta(1295)$. Figure 1.7 shows the signal extracted for $f_1(1285)$ and the absence of the $\eta(1295)$ and higher mass 0^{-+} states in the $\eta\pi^+\pi^-$ mass spectrum.

Furthermore, their analysis of $\eta\pi^+\pi^-$ data found $\Gamma(f_1(1285) \to a_0\pi)/\Gamma(f_1(1285) \to \eta\pi\pi)$ consistent with 100% $a_o\pi$ with a lower limit of 0.69 at 95% confidence level [30].

1.4.2 $\eta(1295)$

The $\eta(1295)$ was first observed in partial-wave analysis of $\pi^-p \to \eta\pi^+\pi^-n$ data obtained at the Argonne National Laboratory zero-gradient synchrotron[20]. It was later confirmed in partial-wave analyses of data from other π^-p experiments at the KEK and Brookhaven. We will summarize the results of the discovery experiment and the higher statistics work done at Brookhaven. As noted earlier, the $\eta(1295)$ has also been absent in several analyses of data from other production mechanisms, both expected and unexpected.

Argonne National Laboratory 1979

The $\eta(1295)$ was observed along with the $f_1(1285)$ in the reaction $\pi^-p \to \eta\pi^+\pi^-n$ at 8.45 GeV/c. The results were extracted from an isobar-model phase-shift analysis of the $\eta\pi^+\pi^-$ system. They found the broader 0^{-+}-resonance ($\eta(1295)$) to have a width of around 70 MeV/c and a mass of about

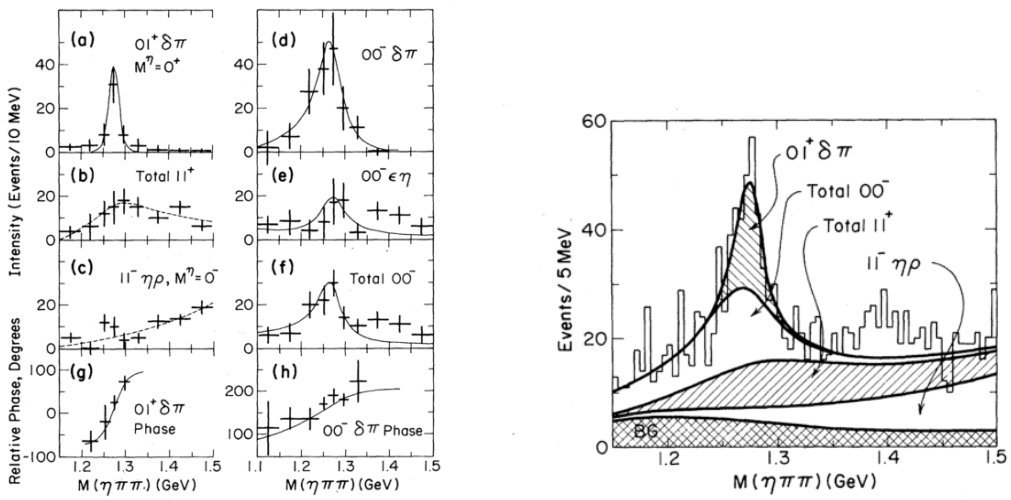

Figure 1.8: Partial-wave analysis results from $\pi^-p \to \eta\pi^+\pi^-n$ data obtained at Argonne National Laboratory. Left Figure (a) shows the strength of 1^{++} $f_1(1285)$ $a_0(980)\pi$ wave, the a_0 denoted as δ. Left Figure (d) shows the corresponding 0^{-+} $\eta(1295)$ $a_0(980)\pi$ wave. Right Figure shows these and other intensities used overlaying their data spectrum. Image Source[20].

1275 MeV/c with an integrated production cross section two to three times that of the $f_1(1285)$. Figure 1.8 shows the results of their partial-wave analysis.

Brookhaven E852

The E852 experiment at Brookhaven National Laboratory collected 9082 $\pi^-p \to \eta\pi^+\pi^-n$ events at 18.3 GeV/c using the Multi-Particle Spectrometer (MPS) at the Alternating Gradient Synchrotron (AGS). Figure 1.9 shows the $\eta\pi^+\pi^-$ mass spectrum obtained. Figure 1.10 shows the results of their partial-wave analysis [21]. The isobar model employed in the final fit used a set of six partial-waves with $J < 2$ in the reflectivity basis, $0^{-+}a_0\pi$, $0^{-+}\sigma\eta$, $1^{+-}\rho\eta$, $1^{++}a_0\pi$, $1^{++}\sigma\eta$ and $1^{--}\rho\eta$. Fits were carried out independently in 30 MeV/c wide mass bins in $M(\eta\pi^+\pi^-)$. The results of the fits showed production of the $\eta(1295)$ dominates the peak at 1.28 GeV, accounting for 80% of the signal in their estimate. Note, however the low statistical strength of the data. They found the $\eta(1295)$ to have a mass $M = 1282 \pm 5$ and width $\Gamma = 66 \pm 13$. The mass and width of the $f_1(1285)$ from their partial wave analysis was not reported in the paper.

Analysis of the $\pi^-p \to K^+K^-\pi^0n$ data was also performed [31]. The analysis found strength in both 1^{++}- and 0^{-+}-waves at the $f_1(1285)/\eta(1295)$ mass range. No quantitative value is reported for the relative production strengths, compared to the 80% $\eta(1295)$ claim made in $\eta\pi^+\pi^-$ analysis. Figure 1.11 shows the intensity plots which are of similar scale for both spin-parity states. The masses of the $f_1(1285)$ and $\eta(1295)$ were found to be $1288 \pm 4 \pm 5$ and width $M = 1302 \pm 9 \pm 8$ respectively and the width of the $\eta(1295)$was found to be $57 \pm 23 \pm 21$. However, the extracted width obtained for the 1^{++} ($f_1(1285)$) wave was $\Gamma = 45 \pm 9 \pm 7$ MeV/c, but a fit to only the intensity function for the $f_1(1285)$ 1^{++}-wave yielded a much smaller width, $\Gamma = 23 \pm 5$. They concluded that interference between the $f_1(1285)$ and $\eta(1295)$ was important in their determination of widths.

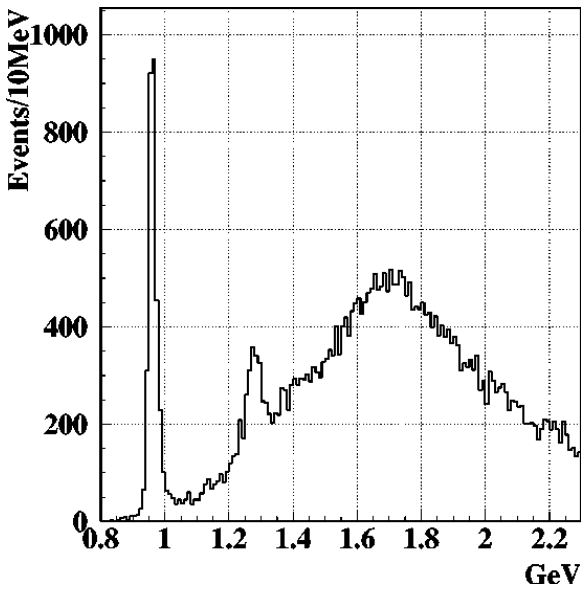

Figure 1.9: Brookhaven E852 $\eta\pi^+\pi^-$ three-body mass spectrum showing η' and $f_1(1285)/\eta(1295)$ peaks. Image Source [21]

1.5 Summary

In summary we examined the motivation for exploring photoproduction of light mesons from both theoretical and experimental viewpoint. We have discussed the current status of phenomemological models for photoproduction and radiative decay of the $f_1(1285)$ and $\eta(1295)$ mesons. We have summarized important prior experimental results and world data that will be points of comparison for this analysis. In the next chapter we will describe our experimental setup and operation of the CLAS detector.

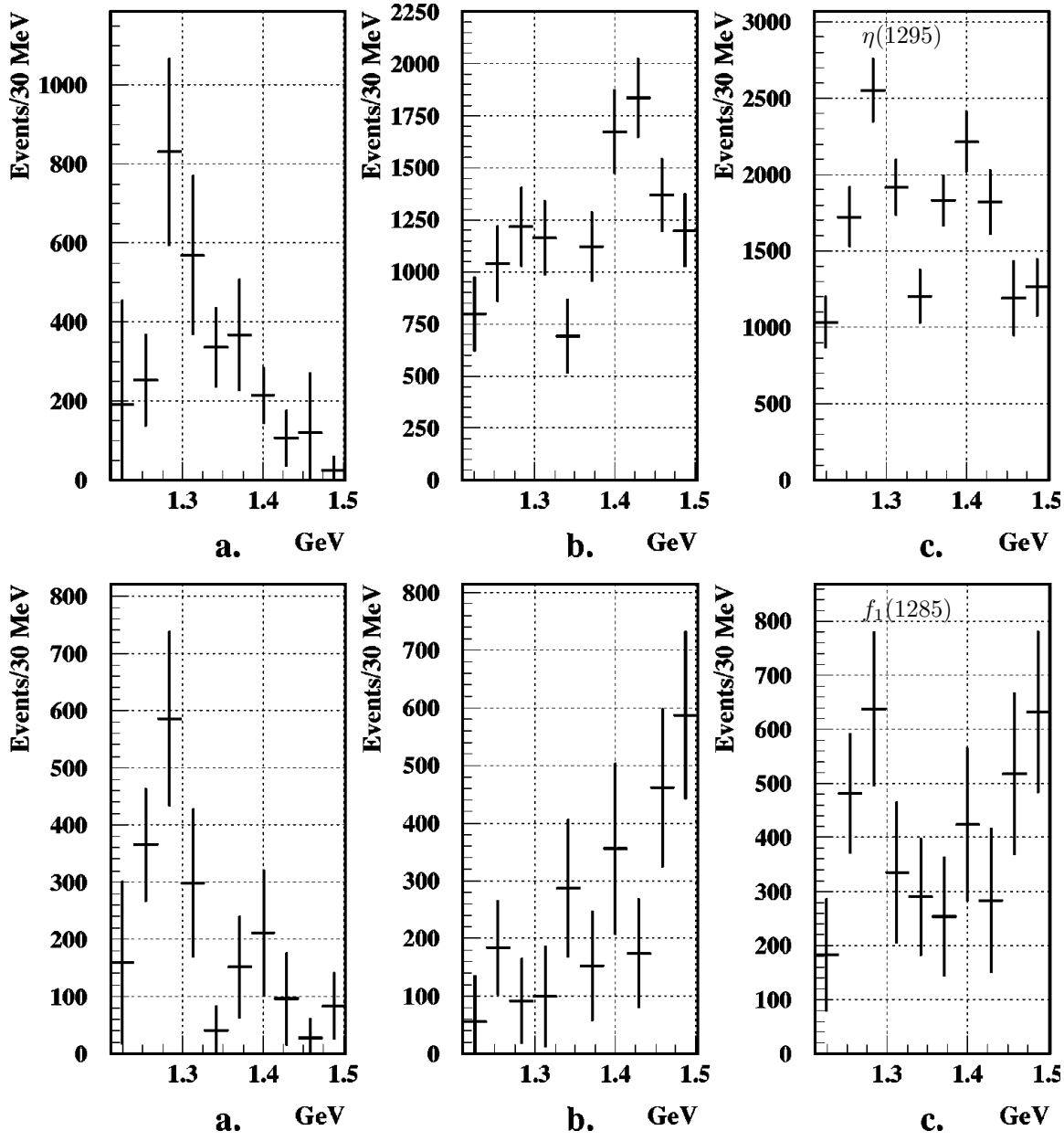

Figure 1.10: Brookhaven E852 PWA for $\pi^- p \rightarrow \eta\pi^+\pi^- n$. Top Row: (a) $0^{-+}a_0\pi$ intensity; (b) $0^{-+}\sigma\eta$ intensity; (c) total 0^{-+} intensity. Bottom Row: (a) $1^{++}a_0\pi$ intensity; (b) $1^{++}\sigma\eta$ intensity; (c) total 1^{++} intensity. This analysis determined $\sim 80\%$ of the observed signal at 1280 MeV to be $0^{-+}\eta(1295)$. Image Source [21]

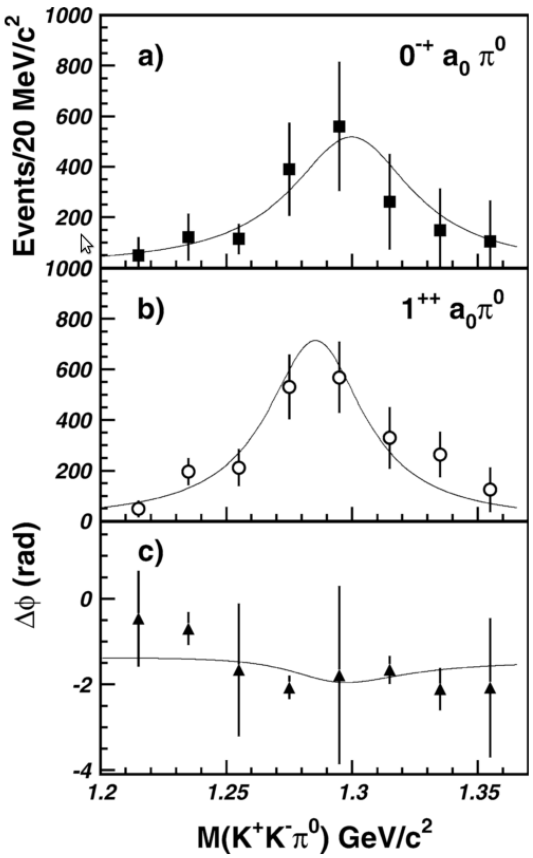

Figure 1.11: Brookhaven E852 PWA of $\pi^- p \to K^+K^-\pi^0 n$ mass-independent (points) and mass-dependent (lines) fit results for (a) $0^{-+}a_0\pi$- and (b) $1^{++}a_0\pi$-waves with (c) phase difference. Image Source [31]

Chapter 2

Experimental Apparatus and Procedure

Our analysis of the $\gamma p \to x(1280)p$ reaction makes use of the *g11* dataset collected in Experimental Hall B at Thomas Jefferson National Laboratory (TJNAF, JLAB) in Newport News, Virginia. The *g11* dataset was collected in 2004 for the E04-021 experiment [32], the primary goal of which was a high-statistics search for the purported Θ^+ pentaquark state. The high-luminosity continuous-wave electron beam provided by CEBAF along with the capabilities of the CLAS detector, trigger and data acquisition systems produced the world's largest dataset of photoproduction data in the energy range 1.55 GeV $< W <$ 2.84 GeV. The inclusive trigger allowed for the acquisition of many different final states, several of which were studied in this analysis.

The run conditions for *g11* included a tagged photon beam incident on a proton target, in the form of liquid Hydrogen, and the CEBAF Large Acceptance Spectrometer (CLAS) recording multiple-track events over a wide angular coverage. This chapter will describe the experimental setup of the CEBAF accelerator, Hall B photon tagger, the CLAS detector, and its data acquisition system.

2.1 CEBAF at Jefferson Laboratory

The Continuous Electron Beam Accelerator Facility (CEBAF) at the Thomas Jefferson National Accelerator Facility (Jefferson Lab) is an electron accelerator producing an electron beam with a maximum energy of 6 GeV. The CEBAF accelerator is laid out similar to an oval race track, about 1.4 km in total length. An aerial photograph of the accelerator site is shown in Figure 2.1. The electron beam is delivered to three experimental halls, with an upgrade to 12 GeV and addition of a fourth experimental hall, Hall D, currently underway. The locations of the injector, linear accelerators, recirculating arcs, and experimental halls are shown in Figure 2.2.

The CEBAF electron beam is produced at the *injector*, by one of several available electron guns. Three diode lasers, one for each experimental hall, produce pulses which illuminate a GaAs photocathode. The pulses are timed such that each experimental hall receives electron bunches every 2 ns. The electrons are accelerated to 100 keV by an electrostatic accelerator and then an optical chopper improves the separation of the bunches before they are accelerated further by two superconducting RF cavities to 45 MeV [34]. Finally, the electrons are sent into CEBAFs recirculating linear accelerators (LINACs).

The recirculating LINACs which make up the North and South straights of the race track each contain 168 superconducting RF Niobium cavities. Figure 2.3a shows a picture of a pair of RF cavities with associated hardware. Each cavity is immersed in liquid helium within a cryogenic

Figure 2.1: Aerial view of the Thomas Jefferson National Accelerator Facility in Newport News, VA. Image Source [33]

module and cooled to $-271°$C. At this temperature the cavity becomes superconducting, allowing for high-efficiency operation and continuous-wave operation due to the lack of resistive heating. The electron beam is accelerated through the application of radio frequency standing waves in the cavities. Tuning the standing waves to be in phase with the electron bunches results in a continuous positive electric force on each bunch as it passes the cavity. Figure 2.3b shows a diagram of the RF wave acting on an electron.

Each LINAC is currently capable of providing 600 MeV of acceleration, although this will be nearly doubled through upgrades in a few years. The LINACs are connected by nine recirculating arcs which allow the beam to make up to five passes through each LINAC, for a maximum energy of ~ 6 GeV. At this point the beam is tightly focused, at about 0.1 mm wide and can be extracted to the three experimental halls using RF separator cavities located in the "switch-yard". Each hall may extract the beam after any number of passes up to the maximum of five, yielding a set of operational energies available to each hall. However, while any number of halls can operate at the maximum energy, no two halls can run with the same lower energy [34]. After extraction, each beam pulse is then directed into either Hall A, B or C.

2.2 Photon Tagger

As CEBAF is an electron beam accelerator, the first step for any photon beam experiment is conversion of the electron beam into a photon beam. The photon tagging system of Hall B produces photons via *bremmstrahlung*, or "braking" radiation. The electron beam enters the experimental hall from the switchyard, strikes a radiator and the energy and timing of the recoiling electron are measured in the tagger spectrometer. Figure 2.5 shows a schematic layout of the system.

2.2.1 Radiator

The Hall-B tagger system has an array of radiators available for use. Diamond radiators are used for polarized photon beam and gold foil radiators are used for unpolarized photon beam production. The high atomic number of gold reduces the contamination of electron-electron scattering events.

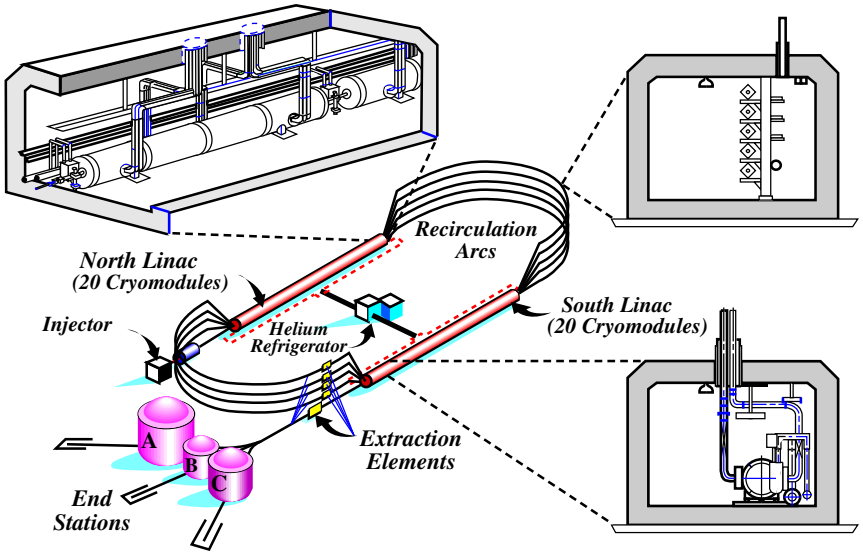

Figure 2.2: Diagram of Continuous Electron Beam Accelerator Facility (CEBAF). The electron beam, produced at the injector, is accelerated by the two LINACs to a maximum energy of 6 GeV. Maximum energy is achieved at five complete orbits. The beam is split for delivery into the three experimental halls (A,B, and C). Image Source [33]

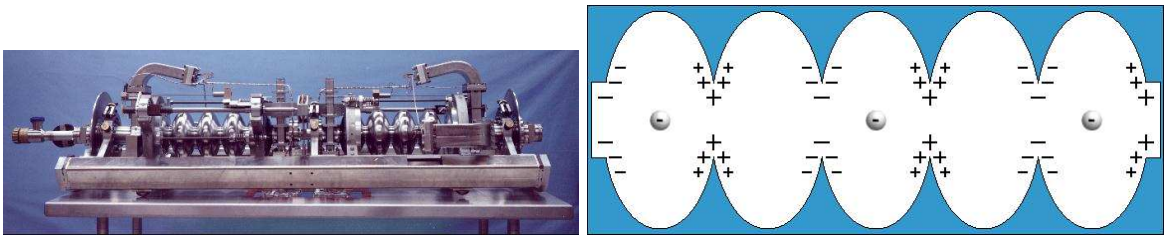

(a) (b)

Figure 2.3: A pair of CEBAF superconducting RF cavities (a). A diagram of the standing wave acting on electrons passing through a cavity (b). Each cavity is tuned to be in phase with the electron bunch so as to produce acceleration.

Production data during the *g11a* dataset was taken entirely using a gold radiator of thickness 10^{-4} radiation lengths, though thinner foils were used during *normalization* runs.

The beam, now a blend of non-interacting electrons, recoil electrons and photons, passes through a dipole magnetic field. The field bends the electrons away from CLAS, allowing a pure photon beam to proceed towards the target. Full energy electrons are directed towards the tagger beam dump, while the recoil electrons are detected by the tagger spectrometer.

2.2.2 Tagger Spectrometer

The Hall-B tagger spectrometer consists of two hodoscope planes, called the E- and T-planes. Figure 2.5 shows where in the spectrometer recoil electrons are deflected by the tagger magnet for the corresponding fractional energy given to the photon. Full energy electrons are bent towards the tagger beam dump. Electrons corresponding to photon energy from 20 to 95% of the electron beam

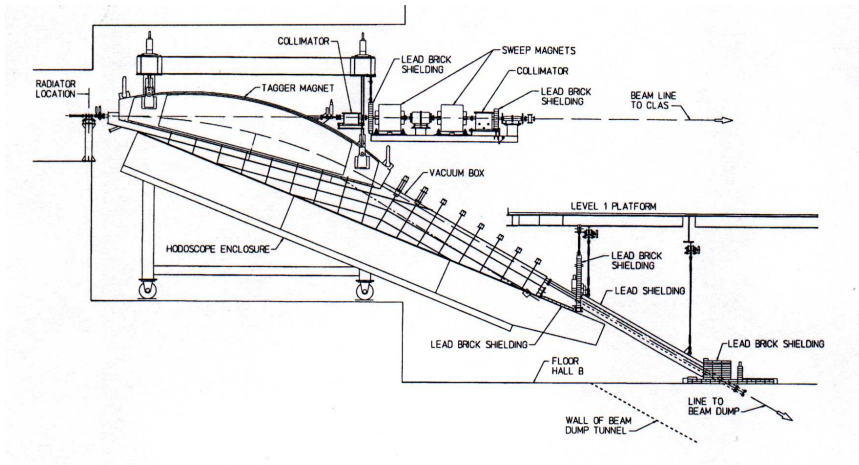

Figure 2.4: The layout of CLAS Photon Tagger Assembly including the magnet, ribbed vacuum box, radiator, hodoscope enclosure, collimators, shielding, and beam dump entrance. For scale reference, the overall length of the tagger magnet is 6 m. Figure Source [35]

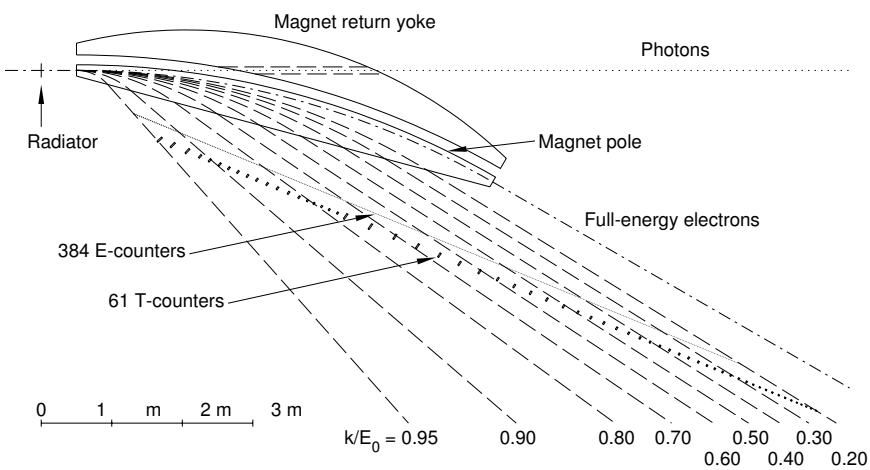

Figure 2.5: CLAS Photon Tagger Spectrometer Diagram. The dashed lines show the trajectories followed by recoil electrons given the fractional energies of the tagged photon. The location of both hodoscope scintillator planes, the E- and T-planes, is shown with the actual geometry and segmentation. Image Source [36].

energy are focused into the counters of the tagger spectrometer.

The first hodoscope plane, referred to as the E-plane, is used to determine the momentum of the recoiling electrons. It consists of 384 scintillator paddles that are 20 cm long, 4 mm thick and from 6 to 18 mm wide. The paddles overlap to create 767 logical channels for detection. Since the trajectory of an electron in the magnetic field is governed by its momentum, determining which paddle an electron passed through, allows us to determine its momentum. From the momentum of the recoil electron, we can then determine the energy of the photon through conservation of energy and momentum. The energy resolution of the E-plane is 0.1% of the incident electron beam energy.

The second hodoscope plane, referred to as the T-plane, is used to make accurate timing measurements of the recoiling electrons. This plane comprises 61 scintillator paddles that are each 2 cm thick. The greater thickness of these paddles yields a timing resolution of 110 ps. The spectrometer

is able to tag photons ranging from $20 - 95\%$ of the incident electron beam energy.

The signals from the scintillator paddles are amplified and read out using photomultiplier tubes (PMTs). The T-counter PMT signals which satisfy a discriminator threshold are then sent to the Master OR (MOR), an important part of the g11a trigger. The detection efficiency of the tagger is not 100%, but as the tagger is always included in the g11a event trigger, this efficiency cancels in the ratio of detected to tagger events, and therefore is not needed to be known.

The timing signals from both the E- and T-counters are used during offline analysis to establish coincidence between paddles. The timing resolution of the Hall B tagging system is good enough to identify which RF beam bucket each photon is associated with. The RF signal obtained from the accelerator is the most accurate timing information available in the entire experimental setup. This accuracy is used to calculate the event vertex time, the time at which all the final state particles were produced. This time is calculated by propagating (temporally) the RF time from the radiator to the event vertex, or point in space where the interaction occurred.

There are several more beamline devices downstream of the tagger before and after the target cell. The beam is cleaned up with collimators and sweeping magnets. Two collimators trim the beam halos while the magnets remove any charged particles created by interactions of photons with the first collimator. More detailed information on the Hall B tagging system can be found in [35]. The Total Absorption Shower Counter (TASC) located after the target in the downstream alcove is used to monitor the flux of the photon beam. The use of the TASC requires a much lower electron current from the accelerator, than for production data, and a thinner bremsstrahlung radiator is used, so that the TASC is not overloaded. The TASC is important for calculating the photon flux in g11a, by the method of *gflux*, explained later in §3.3.2.

2.3 CLAS

The CEBAF Large Acceptance Spectrometer, CLAS, is a large acceptance detector installed in Experimental Hall-B, at Jefferson Laboratory. In contrast to the detector systems used in Halls A and C, the CLAS detector is unique in that it can measure the momentum and angles of the charged particles produced in the electron-proton and photon-proton collisions over a large angular range.

Figure 2.6: The CEBAF Large Acceptance Spectrometer with forward carriage and TOF panels pulled away. Region 3 drift chambers are visible. Photo Source [33]

The CLAS detector apparatus measures approximately 30 feet across and is composed of several

types of particle detectors. CLAS is arranged like an onion, with successive layers of different particle detectors surrounding the target. From innermost, outwards, the detector systems are: the start counter, three regions of drift chambers, Cerenkov counters, time-of-flight scintillators and electromagnetic shower calorimeters. Data from the Cerenkov counters and electromagnetic shower calorimeters were not utilized in this analysis and we therefore omit discussion of the operation of these detector systems from this chapter.

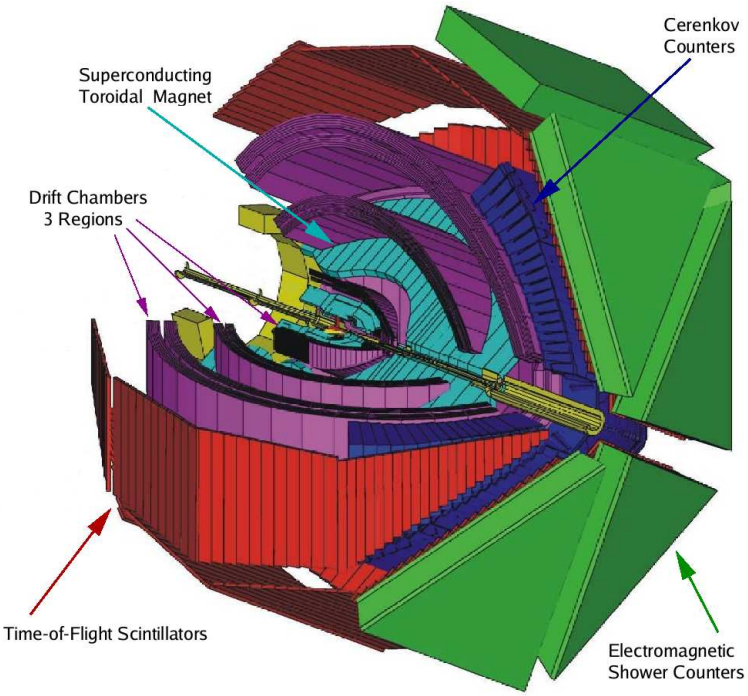

Figure 2.7: The detector systems that make up the CEBAF Large Acceptance Spectrometer are shown. Figure Source [33].

The spectrometer is built around a six-lobed superconducting magnet. Charged particles leaving the target cell have their paths bent by the toroidal field of the magnet. The curvature of the paths measured in the spectrometer is used to determine the particles' momenta. Additionally, the components of CLAS are divided azimuthally into six *sectors* between the lobes of the magnet. This division allows for independent measurements and systematic checks. Figure 2.7 shows the layout of CLAS.

2.3.1 Target

The target for the g11 running period was a 40 cm tapered tube containing liquid hydrogen. The upstream end was 51 mm in diameter tapering to 40 mm at the downstream end. The target wall is 0.005 in thick Kapton with Al beam windows. Figure 2.8 is a computer rendering of the target cell and assembly. For the g11 run period the target center was placed 10 cm upstream of the center of CLAS. Section 3.3.1 will describe the periodic measurements of pressure and temperature and resultant calculation of the density of the liquid hydrogen.

Figure 2.8: Computer rendering of the g11 target cell. Image Source [37].

2.3.2 Start Counter

The first detector component the charged tracks encounter in CLAS is the multi-segmented *start counter* surrounding the target cell. The start counter was upgraded [38] from the original model prior to the start of *g11* run period. The "new" start counter retains the hexagonal cross section of the original, but each side is made up of four 2.2 mm thick scintillator paddles for a total of 24 channels. The new counter can handle the higher rate of events needed for g11a. Figure 2.9 shows a computer rendering of the start counter. The start counter is an important component of the event trigger and photon timing measurement, achieving an excellent timing resolution of 350 ps. Though, this timing information was ultimately not used in this analysis for the event start time as the timing resolution of the tagged photon, discussed in §2.2, was superior at 110 ps[36].

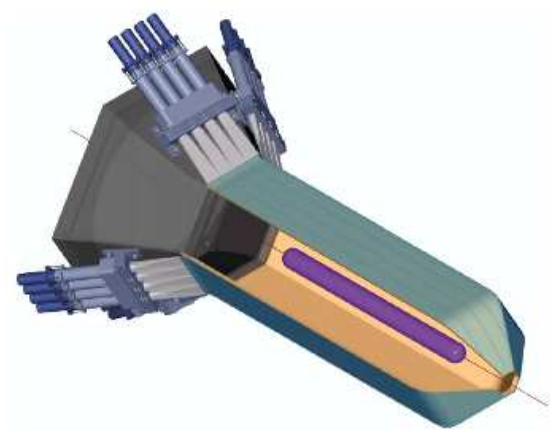

Figure 2.9: Rendering of the Start Counter. Image Source [38].

2.3.3 Main Torus and Drift Chambers

The heart of the CLAS detector is the superconducting toroidal magnet, which generates the magnetic field that bends the trajectories of charged particles on their way through the detectors. The magnet is made of six kidney-shaped superconducting coils, arranged symmetrically around the inner region containing the target. Figure 2.10 shows a map of the magnetic field strength. In its usual configuration, as was used for g11a, the toroidal magnetic field will cause positively charged

particles to bend outwards (away from the beam) and negatively charged particles to bend inwards (towards the beam). This results in a higher detection efficiency for positively-charged forward-going particles than for negative, as the inward bending particles have a greater chance of being lost into the beamline and forward hole of CLAS. To lessen this effect for g11a, the current inside the magnet was limited to about 1920 A, about half of the maximum, to enhance the acceptance for negative particles.

The trajectories of charged particles through CLAS are measured by the drift chambers. By combining the trajectory of a particle with our knowledge of the magnetic field, one can determine its momentum. Figure 2.11 shows a schematic of the magnet and drift chambers.

Charged particles in CLAS are tracked by drift chambers which are arranged in three regions. The innermost region, Region 1 is located closest to the target, inside the nearly field-free area within the main torus bore, and is used to determine the initial direction of charged tracks. Region 2 is located between the torus coils, in the region of strong magnetic field, and detects the particle track at the point of maximum curvature to achieve good energy resolution. Region 3 is located outside the coils, a region with low magnetic field, and measures the final direction of charged tracks before the time-of-flight counters, Cerenkov counters and the electromagnetic calorimeters. More information regarding the construction and operation of toroidal magnet and drift chambers can be found in Ref.[36][39].

Each region has six separate chambers corresponding to the six sectors of the CLAS. Each chamber contains one axial superlayer with up to 1200 sense wires in six layers (4 layers in the case of Region 1) and one stereo superlayer with sense wires in six layers at an angle of 6 degrees with respect to the axial wires. The wires are arranged into a hexagonal pattern, with up to 192 sense wires per layer. Each superlayer is surrounded with a row of guard wires to minimize edge effects. As the charged particles pass through a chamber, they ionize the gas within the drift chambers, and the freed electrons drift toward the sense wires. The gas within the drift chambers was chosen to satisfy the conditions of reasonably low multiple scattering, allow for reasonable gas gains, give short collection times and ensure safety. A mixture of 90% Argon and 10% CO_2 was chosen. The single-wire efficiency is greater than 98% and the average single-wire resolution is 330 μm overall. The design goal for track resolution was $\delta p/p \leq 0.5\%$ for 1 GeV/c charged particles, which has been met. The resolution is better at forward angles where the magnetic field is stronger, depicted in Figure 2.10, and falls off with increasing polar angle.

2.3.4 Time of Flight Counters

The outer layer of detectors are six segmented scintillator walls, one for each sector, located about four meters from the center of CLAS. Each scintillator wall has four panels and a total of 57 scintillator paddles of varying lengths and widths. Their primary purpose is to measure the arrival time charged tracks. Each bar is two inches thick to have ∼100% detection efficiency for minimum-ionizing particles. PMTs mounted at each end of the bars collect the signals to yield a time of arrival. The timing resolution was 80 to 160 ps, from shortest to longest paddles respectively.

In conjunction with the event vertex time measured from photon tagger, the arrival time gives the time of flight of the particle through CLAS. Dividing the path length of a particle by the time of flight, we get its speed. Knowing the speed and momentum of the particle allows us to compute its mass and its identity. The time-of-flight (TOF) scintillator system is also part of the Level 1 trigger, as described in §2.3.5 A more detailed description of the TOF system, construction and performance, is given in [39].

2.3.5 Event Triggering and Data Acquisition

Each afore-mentioned subsystem of CLAS has its own electronics package to monitor its operation and collect signals. The presence of a signal in a single detector element does not necessarily indicate

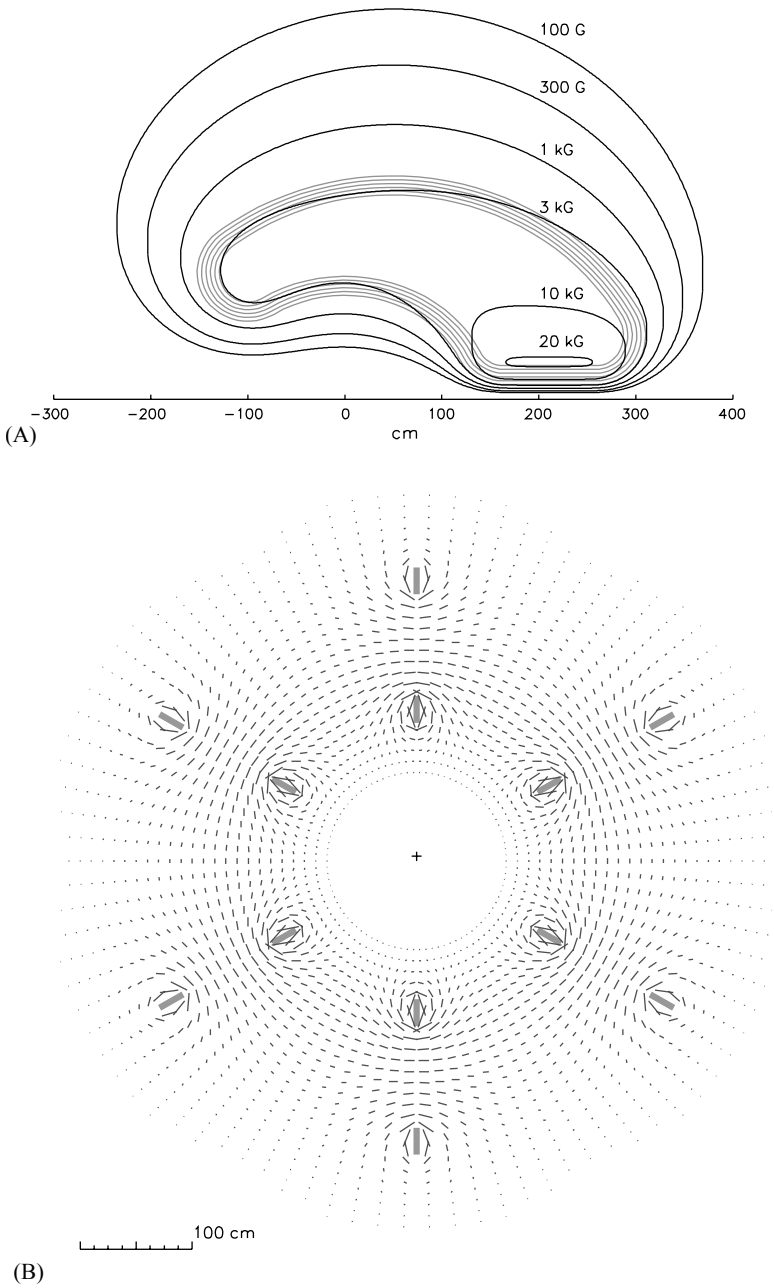

Figure 2.10: The magnetic field map of the CLAS toroidal magnet at full current. (A) shows the contours of constant magnetic field strength. The magnetic field is strongest in the forward region. (B) shows lines representing the magnetic field strength and direction in the plane transverse to the beam direction, centered at the target. The length of each line is proportional to the field strength. Image from [36].

that a physics event has occurred. Several unwanted sources of background, such as cosmic radiation passing through a detector element, electronic noise, etc., can produce signals in any given detector component. The *trigger* determines which sets of signals constitute a physics event to be recorded

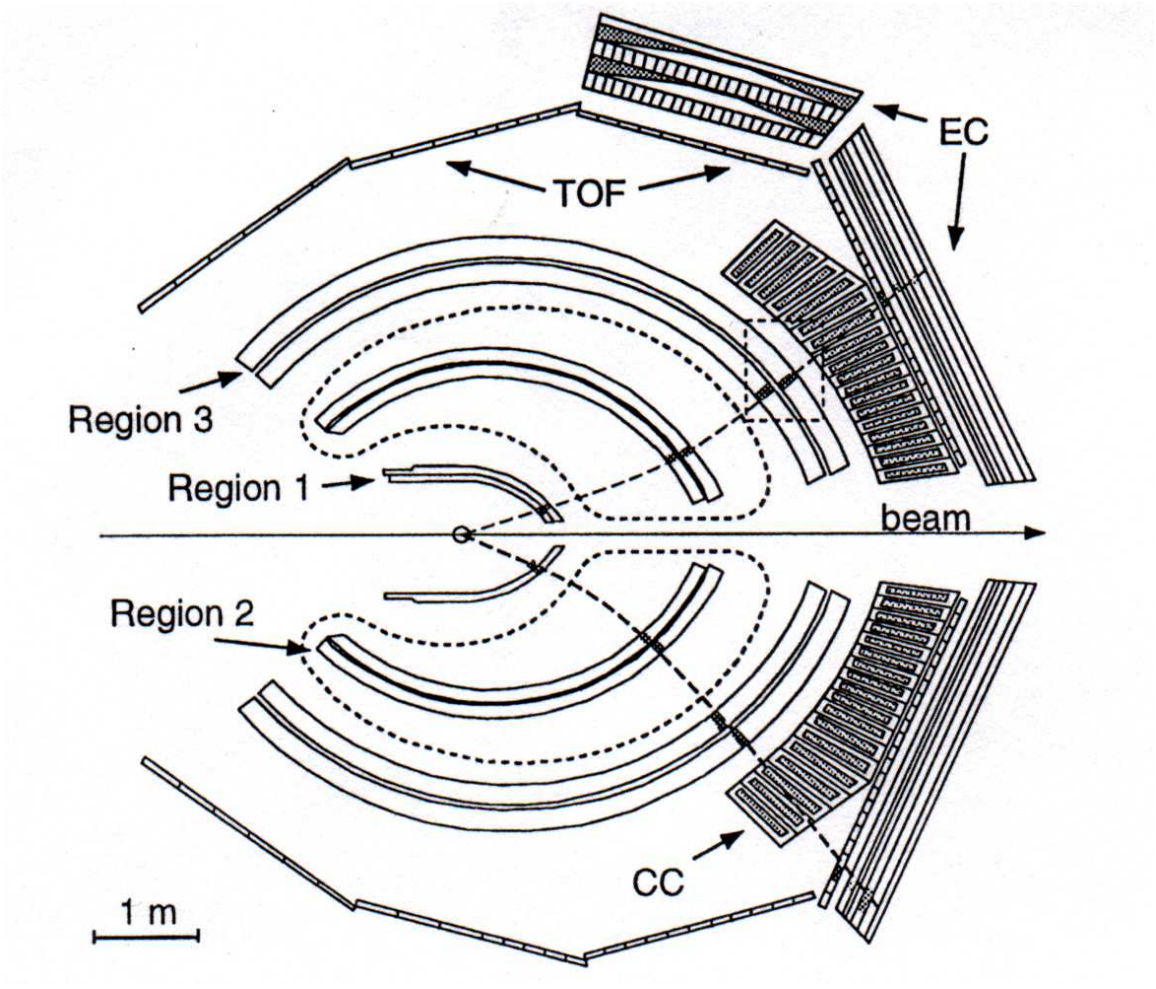

Figure 2.11: Cross section of the CLAS drift chambers in relation to other components. The dashed lines around Region 2 show the location of the toroidal magnet and its field. Also depicted are the trajectories of two charged tracks from the target through the various detector systems. Image Source [36].

for further analysis.

The g11a trigger requirement was a coincidence between the tagger Master OR (MOR) and the CLAS Level 1 trigger. While the entire tagger focal plane recorded data, only the first 40 (highest energy) tagger T-counters were enabled in the MOR trigger. The high luminosity of the g11 run period, however, made it quite likely for more than one photon in the tagger for a triggered event, so low energy photon events were recorded if there was a high energy photon in the tagger in the same event window.

For an individual CLAS sector to satisfy the Level 1 trigger, a signal was required from any of the four start counter channels int that sector and any of the 48 TOF paddles in the sector within a coincidence window of 150 ns. The complete Level 1 trigger requirement was met if at least two CLAS sectors satisfied the above conditions. The final requirement for the g11a trigger was a coincidence between the tagger MOR and the start counter OR within a timing window of 15 ns [40].

Once an event was triggered, the data acquisition system (DAQ) collected the signals from all detector components and cached them to disk. The recorded events were then copied to the JLAB robotic tape library for storage and further offline processing. For the g11a run period, the DAQ was capable of running up to ∼5 kHz. The typical electron beam current for g11a run periods was 65 nA, corresponding to a event rate of ∼3 kHz, with a deadtime of 20% [41].

2.4 Summary

To analyze the reaction $\gamma p \to x(1280)p$, we needed a large dataset of experimental photoproduction events. Production of the such events was accomplished using the photon beam generated by the Hall B photon tagging system using the electron beam provided by the CEBAF accelerator. The tagged photons were incident on the CLAS cryogenic liquid Hydrogen target. The events were observed by the various subsystems of the CLAS detector and recorded by the data acquisition system. The g11a experiment produced ∼21 TB of digitized signals stored on magnetic tape. The next chapter will describe our analysis of this data, and the physics events and measurements obtained.

Chapter 3

Data Analysis

The reaction chain that we study in this analysis is

$$\gamma p \rightarrow xp \tag{3.1}$$

where the detected particles are the proton and the charged decay products of the $x(1280)$ meson. We reconstruct the $x(1280)$ from the missing mass $p(\gamma, p)x$ off the target proton and the measured (tagged) photon. The $x(1280)$ meson decays strongly and its charged decay products further constrain the kinematics to identify events containing this reaction. The decay modes

$$\gamma p \rightarrow p\pi^+\pi^-\eta \tag{3.2}$$

$$\gamma p \rightarrow p\pi^+\pi^-\gamma \tag{3.3}$$

$$\gamma p \rightarrow pK^+\pi^-K^0 \tag{3.4}$$

$$\gamma p \rightarrow pK^-\pi^+K^0, \tag{3.5}$$

are detectable in CLAS and studied in this analysis. As discussed in §2.3.5 the *g11* trigger required at least two charged tracks in different sectors, thus we can not detect events in which the $x(1280)$ decays into final states composed entirely of neutral particles.

This chapter will discuss the methodology of event selection and all cuts and corrections that were made to the data. Then in turn the technique of each of the measurements will be detailed. Specifically these are: the yield of η' and $x(1280)$ mesons in the observed decay modes, the mass and width of the mesons, differential cross sections, relative branching fractions and Dalitz plot analysis. We also present our calculations of the photon normalization, the acceptance of the CLAS detector and the effects of the cuts imposed in this analysis.

3.1 Event Selection

The *g11* dataset was obtained from May 17th to July 29th in 2004 by the CLAS Collaboration. In this period 20 billion events were recorded resulting in 21 TB of data. The process of calibrating the subsystems of CLAS and converting "raw" information into events containing tracks with momentum and timing information is called "cooking". The "chef" for *g11* run period was Maurizo Ungaro and the cooking process is detailed in [42].

The *g11* dataset comprises many *runs*, periods during which experimental conditions were ideally kept near the nominal values. Each complete run consists of approximately 50 million triggered events. This subdivision allowed for time-dependent detector and data acquisition problems to be identified and corrected for during the cooking process.

The *g11* dataset contains CLAS runs numbered 43490 to 44133. We exclude some of these runs from our analysis. The initial runs taken during the *commissioning* period of the experiment were made under varying conditions to calibrate detector components and study the effects of different configurations. The data obtained were useful to the *cooking* team and for certain systematic studies but are excluded from the physics results. The last runs taken in *g11* experiment were taken with a higher energy electron beam of 5.021GeV. These few runs do not represent a large enough increase in statistics for our analysis to merit reconciling any systematic effects of the higher beam energy. Finally, within the *production* data, several runs were noted by the operators to have problems or undesirable conditions. Table 3.1 details the runs omitted from this analysis. The list is the same as used in previous g11a analysis of $\gamma p \to K^+\Lambda$ by M. McCracken [43], though he also cut run 43871 due to a data processing error. Recent analysis of g11a data by K. Moriya [44] found evidence that the TOF issues identified by M. McCracken were not sufficient to require removal.

Excluded Run	Description
43490-43525	commissioning runs
44108-44133	5.021 GeV e^- beam
43675-43676, 43777-43778,44103	alternate trigger
43989,43990-43991, 44000-44002, 44007-44008,44010-44102	TOF problem in sector 2
43586-43589,43590-43596	TOF problem in sector 3

Table 3.1: Runs excluded from analysis and justification.

The calibrated events were reduced to a "$++-$" charged track skim by the CMU group for local storage in a compressed file format. That is a set of events containing a minimum of two positively charged tracks and at least one negatively charged track per event. Our analysis starts from this reduced dataset with identifying our *signal* events, i.e. those consistent with the reactions (3.2)–(3.5) and separating them from both physical and non-physical *background* events.

3.1.1 Kinematic Fitting

Our particle identification method and several corrections employed in the analysis make prominent use of *kinematic fitting*, specifically in the form of software routines developed at Carnegie Mellon[45][46]. The goal of kinematic fitting is to use the physical constraints of energy and momentum conservation in conjunction with our knowledge of detector uncertainties to improve precision of measured quantities. Generically this can be written as

$$\vec{\eta} = \vec{y} + \vec{\epsilon}, \tag{3.6}$$

where $\vec{\eta}$ is our set of measured observables and $\vec{y}$ is the set of *actual* values. $\vec{\epsilon}$ is the set of deviations needed to shift the observed values to satisfy the constraints. The kinematic fitter we employ uses the method of Lagrange multipliers to perform a least-squares fit of a physics hypothesis, dictated by the physical constraints of energy and momentum conservation, to the measured quantities.

The shifts $\vec{\epsilon}$ are in the ideal case are normally distributed, but in practice these must checked by examining the *pulls*

$$z = \frac{\eta - \hat{y}}{\sigma_\eta^2 - \sigma_{\hat{y}}^2}, \tag{3.7}$$

for each measured quantity. The pull measures the difference between the measured quantity and the estimator given by the fit, relative to their errors. The covariance matrix employed in our

kinematic fitting routines has been empirically parametrized for the *g11* dataset, to ensure that pulls are reasonably close to the ideal Gaussian distribution, centered at zero with unit mean. This tuning of the covariance matrix reconciles σ_η^2 to agree with the measured experimental resolutions of the measurable tracking quantities.

The outputs of this fit are estimators, $\hat{y}$, of the true values along their errors, $\sigma_{\hat{y}}$, and the measure of the "goodness of fit" of the constraint hypothesis in the form:

$$CL = \int_{\chi^2}^{\infty} f(z;n)\, dz \tag{3.8}$$

where the *confidence level* of a fit is the integral of the χ^2 probability density function $f(z;n)$ for n degrees of freedom. The confidence level is the probability that a statistically chosen event would have a χ^2 greater than the result of our fit. Events from a process properly described by the given hypothesis will yield a uniform distribution in confidence level in the range $[0,1]$. Events poorly described by the hypothesis will have small confidence level values. To select events for a given reaction we fit each event to a physics hypothesis and cut events below a minimum confidence level.

Kinematic fitting with an empirically determined covariance matrix and equations of constraint based on physical conservation laws allows us to correct measurable quantities for known detectors errors in a comprehensive manner. In addition to improving data quality, we later utilize kinematic fitting to a particle identity hypothesis as an event selection criterion.

3.1.2 Energy and Momentum Corrections

Before we can apply our event identification kinematic fit we need to be certain the energies and momenta of our tracks are as accurate as possible. The large statistical power of the *g11* dataset has allowed CLAS collaborators to perform detailed systematic studies of its component detectors. Three corrections to the measured momenta which are important for event identification are the those in the *eloss* package, and the CMU-developed tagger and momentum corrections. These corrections are applied before event selection in our analysis to improve our data quality in order to recover as many signal events as possible.

Energy-Loss Corrections

The first component of the CLAS tracking system, the Region 1 drift chamber is about $0.75\,m$ from the center of the *g11* target cell. The energy and momentum of each particle measured in CLAS are therefore reduced from its initial values by interactions with the materials that make up the target cell, beam-pipe, start counter, and the air volume before the Region 1 drift chamber. The *eloss* package[47], developed by Eugene Pasyuk for use in CLAS analyses, corrects for this effect. This package corrects each measured track momentum according to its assigned particle type and the materials present along its path from the drift chamber back to the interaction vertex.

Tagger and Momentum Corrections

The detector components that make up CLAS can also be misaligned from their nominal locations. While calibration during the "cooking" process accounts for most of these effects, two additional corrections to the data were found and implemented at CMU by Mike Williams[40]. The first is a correction to the tagged photon energy due to the photon tagger physically sagging in areas between its support points. The second correction accounts for drift chamber spatial misalignment and differences between the ideal and actual toroidal magnetic field. Both corrections were implemented by using the exclusive reaction

$$\gamma p \to p\pi^+\pi^-, \tag{3.9}$$

as an empirical test channel.

Tagger corrections were calculated by determining the difference between the measured photon energy and the best energy from a four constraint (4-C) kinematic fit to the above reaction. Figure 3.1 shows the difference between the measured and fitted values. The shape of the correction plot was found to be consistent with a small deflection in the tagger spectrometer's focal plane. The three curved segments seen in the plot were found to correspond the physical sagging of the aluminum frame of the tagger focal plane between its support points on the scale of 2–5 mm [48].

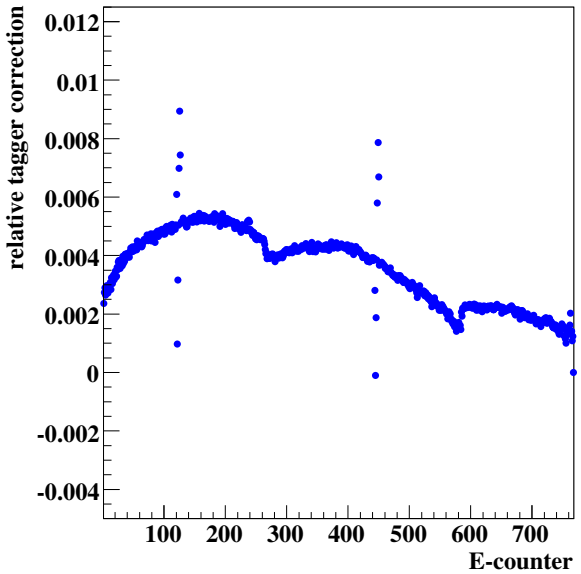

Figure 3.1: Relative Tagger energy correction $\Delta E_\gamma / E_{beam}$ as a function of E-counter. The general shape is due to physical sagging in the tagger spectrometer's support structure. The other points that are inconsistent with the curve are the result of cabling swaps. Figure Source [40]

The drift chamber momentum corrections were also calculated from $\gamma p \rightarrow p\pi^+\pi^-$. First the afore-mentioned *eloss* and tagger corrections were applied to each event, then a set of 1-C kinematic fits to $\gamma p \rightarrow (p)\pi^+\pi^-$,$\gamma p \rightarrow p(\pi^+)\pi^-$ and $\gamma p \rightarrow p\pi^+(\pi^-)$ were performed in turn, treating one of the detected particles as "missing". The measured momentum of the "missing" particle was compared to the missing momentum from the kinematic fit. Corrections were calculated as a function of the charge, sector, azimuthal angle ϕ, and polar angle θ. The ϕ binning was twelve 5° bins per sector. The polar binning was in the form: nine 5° bins from 5° to 50°, four 10° bins from 50° to 90°, and two 25° bins from 90° to 140°. Corrections were typically less than 10 MeV/c.

3.1.3 Particle Identification

After application of the energy and momentum corrections to our tracks we return our attention to selecting events in our decay channels of interest:(3.2)-(3.5).

Traditionally experimentalists in particle physics have performed particle identification on a track-by-track basis. Early in our work we determined it to be beneficial to perform an event-based particle identification scheme. This is desirable because it takes advantage of the constraints of momentum and energy conservation, a track whose individual momentum and/or timing resolution(s) may be inadequate to identify it in isolation can be still be kept when combined into an event candidate. Events are selected by assigning tracks identities according to a reaction hypothesis and then testing the quality of the assignment using the method of kinematic fitting.

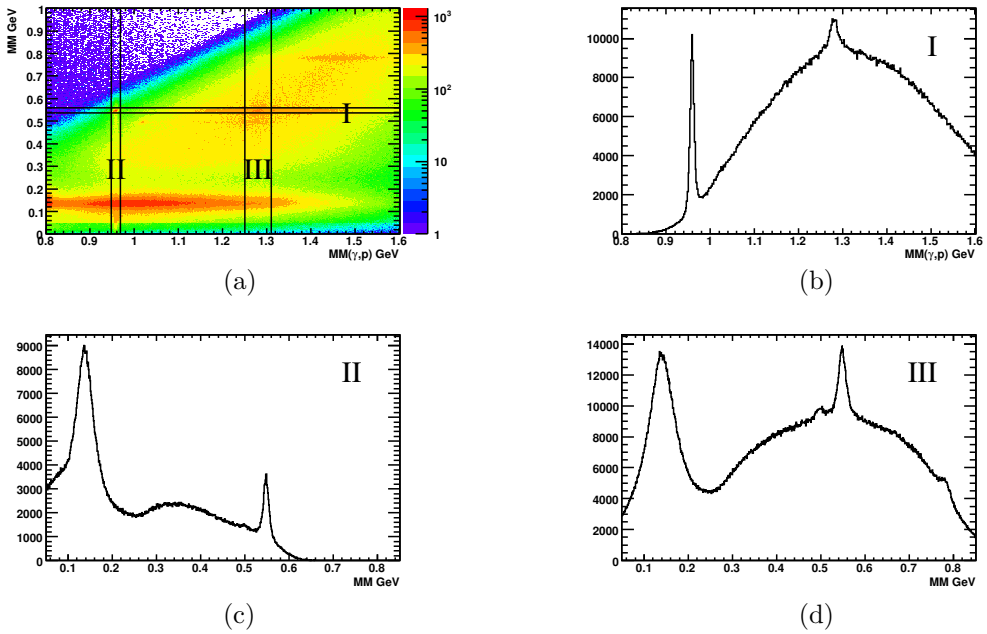

Figure 3.2: (a) Missing mass versus missing mass off the proton for $p\pi^+\pi^-$ events before kinematic fitting. (b) missing mass off the proton for η events in region I. (c) missing mass for η' events from region II. (d) missing mass for $x(1280)$ events from region III.

Each track in the event is assigned a particle identity and corresponding mass according to the selected event hypothesis. As evident in the simplest case where we wish to select events with a proton, π^+ and π^- from events having exactly three tracks with charges of +,+, and −, we must iterate over all assignment orders with regard to charge. We consider the event both with the first track being the proton and the second track being the π^+ and then repeat our analysis for the reverse order. The *g11* dataset was run under high luminosity for statistical power to achieve its aim of measuring pentaquark production. Thus, most events in the data set have multiple photons in the tagger to consider and additional charged tracks. All combinations with reasonable timing are iterated through and considered in this study.

The missing mass versus the missing mass off the proton for events assigned to the $p\pi^+\pi^-(\eta)$ hypothesis are shown in Figure 3.2 before applying the kinematic fit. The projections clearly show the number of non-η background events are much greater under the $x(1280)$ signal than for the η' case.

Each candidate event is kinematically fit to energy-momentum conservation constraints. Since all the decay modes considered in this analysis have an undetected neutral particle, there is left just one constraint, as the three freely adjustable components of its momentum use up three constraints. We select events by placing a cut on the *confidence level* of the particle mass hypothesis. Figure 3.3 shows the confidence level of events from run 43582 from fits to our four final states of interest compared to that of our $x(1280)$ Monte Carlo events. A large number of background events remain in the data as evident in the excess of events at lower confidence levels. We keep events with confidence level greater than 0.1 for a given hypothesis, based on the Monte Carlo. The non-flat confidence level of data events shows the necessity for additional cuts to remove background events. At this stage it also possible for events to pass more than one hypothesis/combination. The next step in our event selection resolves these ambiguities using timing information for the charged tracks passage through CLAS.

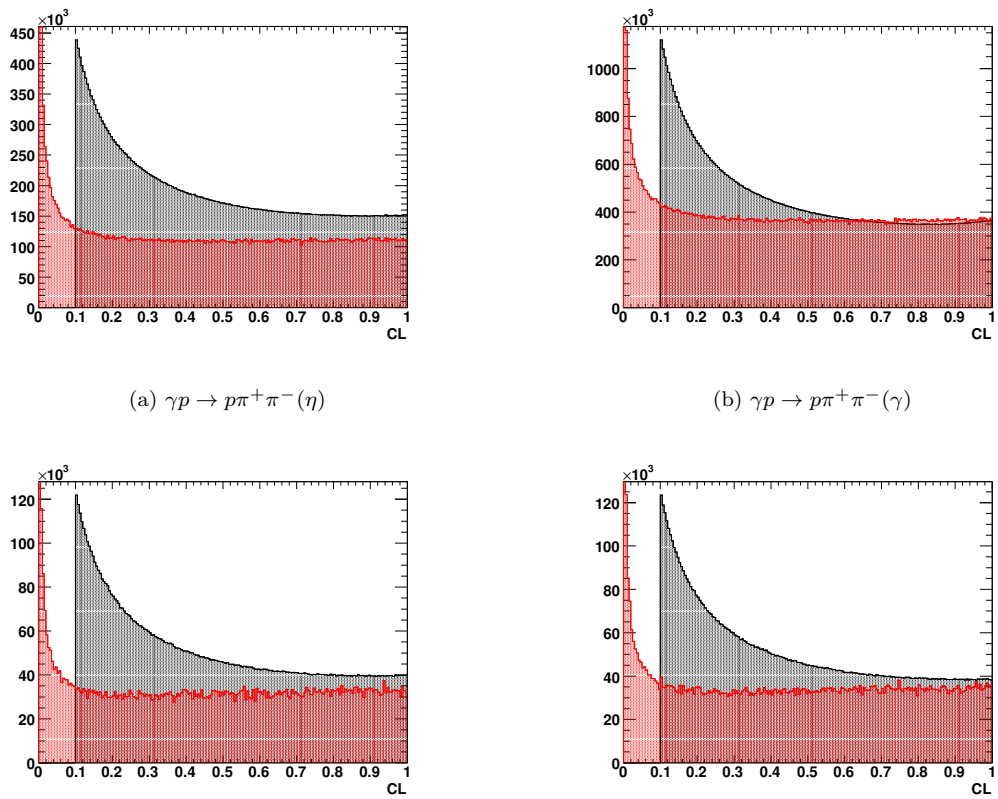

(a) $\gamma p \to p\pi^+\pi^-(\eta)$

(b) $\gamma p \to p\pi^+\pi^-(\gamma)$

(c) $\gamma p \to pK^+\pi^-(\bar{K}^0)$

(d) $\gamma p \to pK^-\pi^+(\bar{K}^0)$

Figure 3.3: Confidence level of 1-C kinematic fits to: (a) $\gamma p \to p\pi^+\pi^-(\eta)$; (b) $\gamma p \to p\pi^+\pi^-(\gamma)$; (c) $\gamma p \to pK^+\pi^-(\bar{K}^0)$; and, (d) $\gamma p \to p\pi^+K^-(K^0)$ events compared to that $x(1280)$ signal Monte Carlo events (red). The non-flat distribution is indicative of background events which poorly fit the physics hypothesis. Note our cut at 0.1 has already been applied to data events in this figure.

3.1.4 Time of Flight Cuts

Kinematic fitting alone is insufficient to narrow our event sample down to our desired reaction modes. Due to the high luminosity of the *g11* run period we expect multiple photons in the tagger for most events. The only cut on photon timing made at this point was imposed at the skimming/compression stage to select photons within 10 ns of the nominal event time (five beam buckets). The multiplicity of photons present at this stage in the analysis is shown in Figure 3.4. The accelerator RF time is the most precise "clock" in Hall B with a resolution on the order of a few picoseconds compared to the $\sim$ 110 ps resolution of the tagger spectrometer, and the photon we choose for the event will give us our best measurement of the event start time by propagating the RF time to event vertex.

It is also possible for tracks to be assigned the wrong mass identity and still pass the kinematic fit. The next step in our particle identification is to make use of timing information to further separate our reactions of interest from background events. To reject these undesired events we make a cut on

$$\Delta TOF = TOF_{calc} - TOF_{meas}, \tag{3.10}$$

which is the difference between the expected time-of-flight for a given particle hypothesis, TOF_{calc},

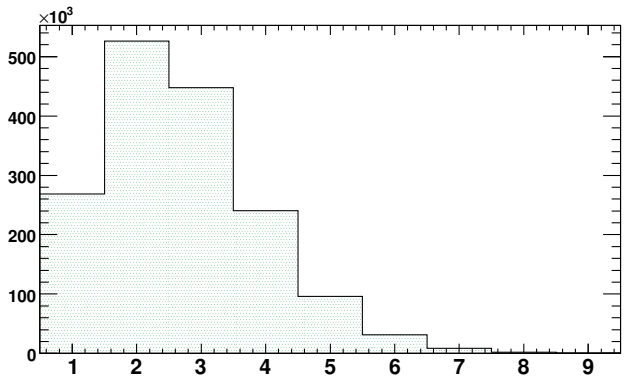

Figure 3.4: Photon multiplicity in the photon tagger for run 43582 of the CLAS *g11* run period. The high luminosity of the experiment resulted in most events having several possible candidate photons.

and the reconstructed time-of-flight, TOF_{meas}, for the track. TOF_{calc} is calculated for a given particle hypothesis according to

$$TOF_{calc} = \frac{L}{c}\sqrt{1+\left(\frac{m}{p}\right)^2}, \tag{3.11}$$

where L is the measured path length of the particle from target to the TOF scintillator, c is the speed of light, m is the mass according to the PID hypothesis and p is the magnitude of the momentum. TOF_{meas} is simply

$$TOF_{meas} = t_{SC} - t_{\gamma}, \tag{3.12}$$

where t_{SC} is the time when the particle was detected in CLAS TOF scintillators and t_{γ} is the the time when the incident photon was at the reaction vertex. The difference ΔTOF should be close to zero for events for which the PID hypothesis is correct.

$p\pi^+\pi^-$ detected

The detected charged particles are the same for both $\gamma p \to p\pi^+\pi^-(\eta)$ and $\gamma p \to p\pi^+\pi^-(\gamma)$. Background in the form of out-of-time shadow bands from other beam buckets are clearly visible in Figure 3.5 in the form of horizontal bands. Besides these accidental tracks, positive track misidentification is also visible in the proton and π^+ ΔTOF plots in the form of additional curved bands. Thus, it is possible to also have duplicate copies of good events for which the two positive particles have similar enough momentum to pass both hypotheses. Good events lie along the band near zero ΔTOF.

In choosing a selection criteria our aim was to eliminate the out-of-time bands and misidentified tracks without significantly impinging on the central band of good events. The chosen boundaries of ΔTOF cuts for $p\pi^+\pi^-$ detected were

$$\pi^{\pm} : \Delta TOF = \pm 1.0 ns \tag{3.13}$$

$$proton : -4.4e^{-2.67P} - 0.55 < \Delta TOF(ns) < 10e^{-10P} - 0.7P + 2.2 \qquad \text{where } P \text{ is in GeV}/c \tag{3.14}$$

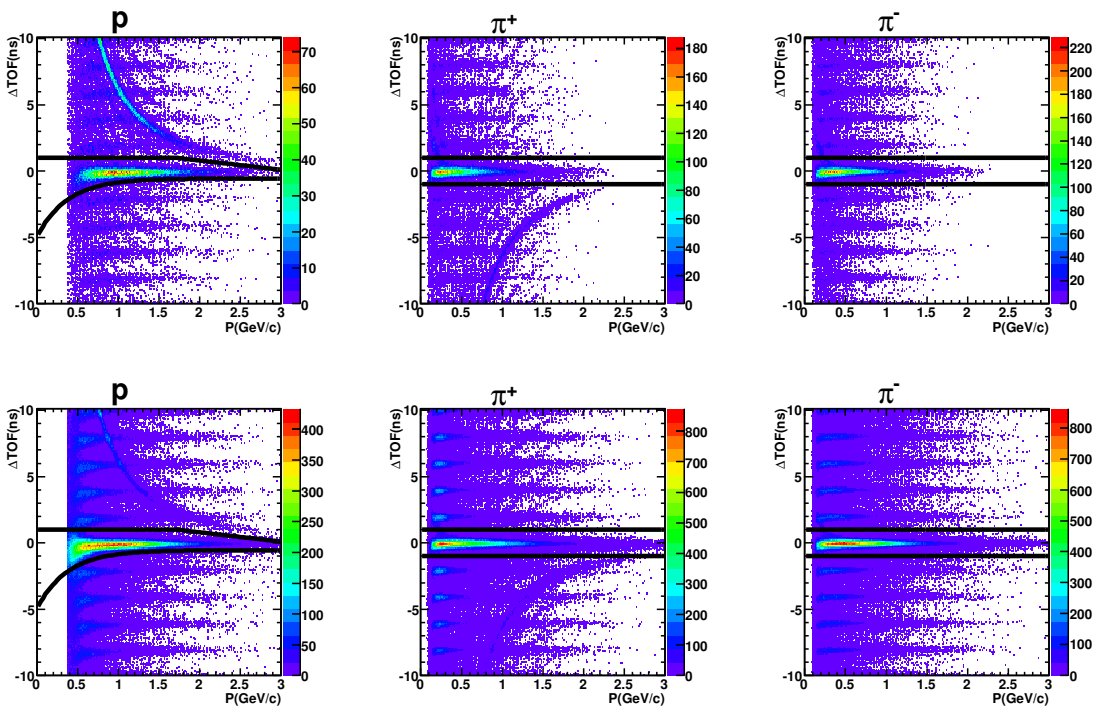

Figure 3.5: ΔTOF vs P_p, P_{π^+} and P_{π^-}. The top row is for events which pass the kinematic fit to a missing η; the bottom row events fit to a missing γ. Note the visible bands of events from other beam buckets and events with mis-identified particle assignments. Black lines are timing boundaries described in the text.

We kept events in which two of the three tracks fall within these defined boundaries. This criteria sufficiently reduces the backgrounds while allowing for cases in which timing information is poor for one track to minimize signal loss. The proton boundary is broader at low momentum to allow for poorer timing resolution of these slow protons.

$pK^{\pm}\pi^{\mp}$ detected

For kaon-containing channels we needed to strengthen our selection criteria as our kaons are dwarfed by the number of mis-assigned protons and pions before any timing cuts are made, as seen in Figure 3.6. Our boundary for kaons

$$K^{\pm} : -0.5 < \Delta TOF(ns) < 10e^{-10P} - 0.5P + 1.25 \qquad \text{where } P \text{ is in GeV}/c \tag{3.15}$$

like the proton curve is wider at low momentum, while narrowing at high momentum to cut false "kaons". We required all three tracks to pass the appropriate ΔTOF cuts for the kaon-containing decay modes, $\gamma p \to pK^+\pi^-(\bar{K}^0)$ and $\gamma p \to p\pi^+K^-(K^0)$.

3.1.5 Fiducial Cuts

Finally, even with the corrections made so far, there are regions of CLAS that yield poor data or cannot be reliably modeled in simulations. Measurements such as differential cross sections and branching fractions require correction for the detector acceptance. For our analysis we calculate

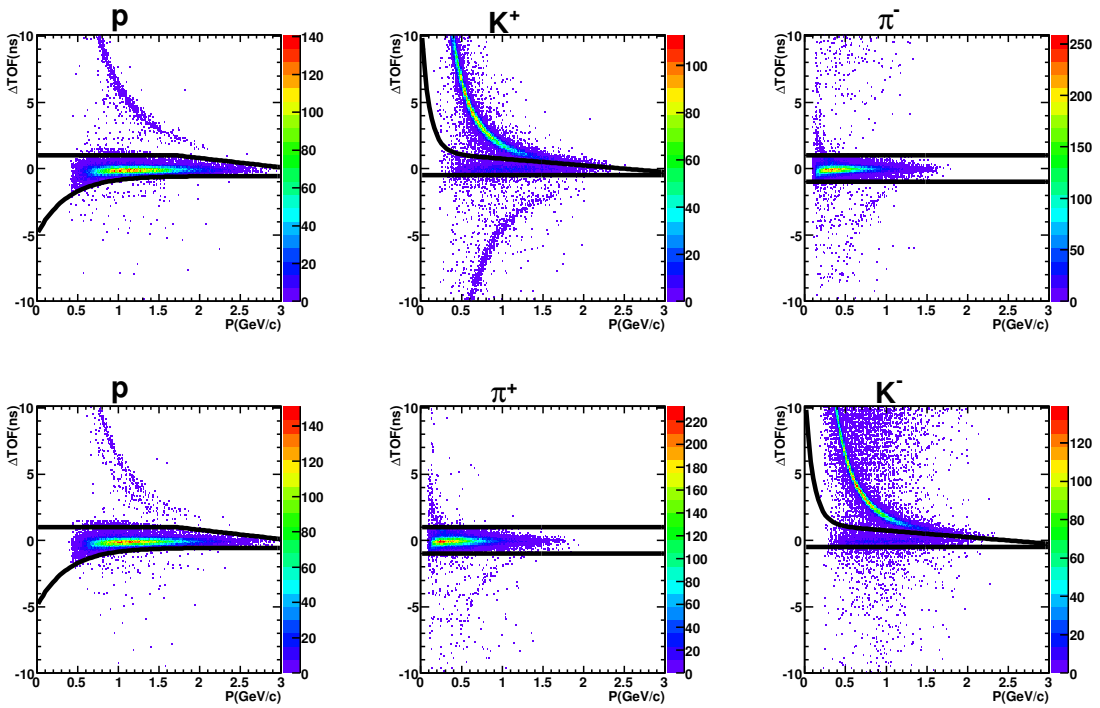

Figure 3.6: Events passing kinematic fit to missing K^0. Top row: ΔTOF vs P_p, P_{K^+} and P_{π^-}. Bottom row: ΔTOF vs P_p, P_{π^+} and P_{K^-}. Both kaon plots show large contamination of misidentified protons and pions.

channel-specific acceptances using GSIM, a GEANT-based computer simulation of the CLAS detector. The simulation is described in greater detail in §3.4.1. The overall agreement is excellent between the experimental apparatus and simulation. Empirical testing by CMU researchers [49] mapped regions of disagreement between the CLAS and GSIM. These regions of the detector where the simulation does not correctly match experiment must be cut from our analysis. The cuts are categorized according to the detector system and/or measurement variable selected. The categories are bad time-of-flight paddles, drift chamber minimum track momentum, and drift chamber fiducial volume as a function of tracking angles.

TOF Paddle Cuts

Certain time-of-flight scintillator channels or *paddles* were found to have inconsistent occupancy rates between data and Monte Carlo simulation. Events having any of the final-state particles striking these "bad" paddles were removed from our analysis. Table 3.2 lists these TOF paddles by sector and identification number. The afore-mentioned empirical studies at CMU [49] compared $\gamma p \to p\pi^+\pi^-$ data to Monte Carlo events to determine TOF channels that had occupancies lower than detector model in GSIM.

Sector	Bad TOF Paddles
1	18,26,27,33
2	none
3	11,24,25
4	26
5	20,23
6	25,30,34

Table 3.2: Time-of-Flight paddles removed from this analysis.

Minimum Particle Momentum Cuts

The momentum of charged particles has been corrected for energy loss and alignment issues. As low-momentum tracks lose more energy and track reconstruction becomes more difficult, our acceptance can be affected for these tracks. Protons with their higher mass are the most likely source of discrepancy. Again we refer to empirical testing done at CMU using the $\gamma p \to p\pi^+\pi-$ channel[49]. Events having the charged pions were selected and then kinematically fit to the test channel. By checking the data for a proton in the correct sector of CLAS, a "data" acceptance $\mathcal{A}_{data}$ can be computed. The test value was the absolute fractional difference

$$A = \frac{|\mathcal{A}_{data} - \mathcal{A}_{mc}|}{\mathcal{A}_{data} + \mathcal{A}_{mc}}, \tag{3.16}$$

where $\mathcal{A}_{data}$ is the aforementioned data acceptance for protons and $\mathcal{A}_{mc}$ is the acceptance for Monte Carlo events. This value should ideally be zero for regions where GSIM accurately describes CLAS. The study examined the fractional difference as a function of proton momentum and angle in the center-of-mass frame and found overall good agreement, that is A near zero, in most regions. The areas of significant discrepancy correspond to the previously mentioned bad TOF paddles, the forward hole of CLAS, and the lowest-momentum tracks.

We found it sufficient to cut protons of less than 375 MeV/c in magnitude of momentum. The study was also performed for pions and found good agreement between data and simulation down to the lowest momenta detected. Pions and kaons down to their lowest detected momenta of $\sim$100MeV/c and $\sim$200MeV/c were kept for analysis. The forward hole is discussed along with other geometric cuts below.

Fiducial Volume Cuts

The final category of fiducial cuts we employ are fiducial volume cuts. These are geometric areas of CLAS where the agreement between data and simulation is poor. They are primarily along the geometric limits of the detector components i.e., the forward and backward holes, and the edges of the drift chambers near the the toroidal magnet's coils.

The forward and backward holes of CLAS were removed from analysis according to cuts on the lab polar angle Θ of each track. The cut in the forward direction is at $\cos\Theta = 0.985$ and the

backward cut is sector-dependent. The magnetic field of the main torus magnet varies rapidly close to the torus coils, as a result the field map used for simulation is poorly known close to the edges of drift chamber segments. This leads to poor track reconstruction agreement between data and simulation. These regions cut were defined in terms of the DC tracking angles and the effect upon the data is shown in Figure 3.7.

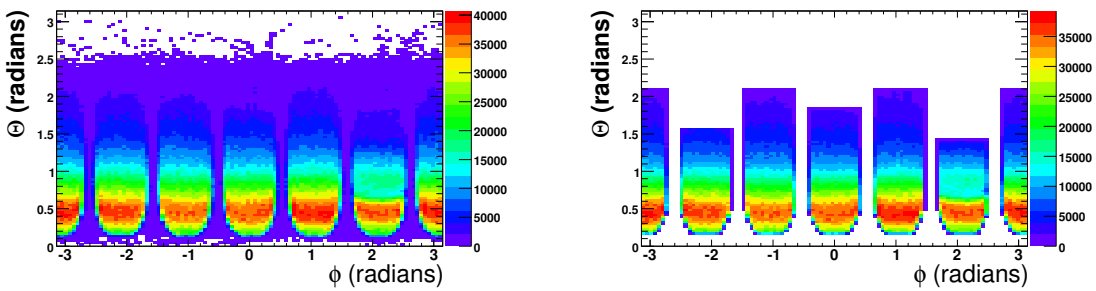

(a) (b)

Figure 3.7: Θ(radians) vs ϕ(radians): (a) All tracks from run 43582. (b) Tracks from 43582 passing our fiducial volume cuts as described in the text.

3.2 Yield Extraction

Due to the large multi-pion background present in our data, we used two different methods to extract the yield of the $x(1280)$ meson. As Figure 3.8 shows, the background is peaked at roughly the same location as our signal of interest for the $\eta\pi^+\pi^-$ decay mode.

The situation is somewhat more favorable in the $\gamma p \to pK^\pm K^0\pi^\mp$ data. The total mass of the decay products is about 300 MeV higher than for $\gamma p \to p\pi^+\pi^-\eta$. This effectively translates into a higher "threshold" for possible background reactions and as is seen Figure 3.9, the background peaks higher in missing mass off the proton than in the $\pi^+\pi^-\eta$ case.

The first method we use is a traditional fit to a Voigtian signal lineshape plus polynomial background function. The second method we use employs our $x(1280)$ signal Monte Carlo along with a set of simulated multi-pion backgrounds to approximate the spectrum seen in the $\eta\pi^+\pi^-$ channel. We use only the Voigtian method in the $K^\pm K^0\pi^\mp$ and $\rho^0\gamma$ decay modes.

3.2.1 Voigtian Fit Method

For mesons states having moderately narrow width, as is the case for our $x(1280)$, the standard expected signal lineshape is in the form of a non-relativistic Breit-Wigner or Lorentzian distribution. The resolution of CLAS, however, is large enough to broaden the observed peak in the missing mass off the proton spectrum. The η' for comparison is a narrow state with an intrinsic width of $\Gamma = 0.194 \pm 0.009\text{MeV}/c^2$. The η' seen in Figure 3.8 is broadened by our experimental resolution. From fitting this peak with a Gaussian distribution we find the experimental resolution to be between 3 to 6 MeV) over the full energy and production angle range.

To account for this broadening effect in fitting the $x(1280)$ peak we utilize a Voigtian profile as our signal function. The Voigtian distribution is a convolution

$$V(E; M, \sigma, \Gamma) = \int_{-\infty}^{\infty} G(x'; \sigma) L(E - x'; M, \Gamma)\, dx' \tag{3.17}$$

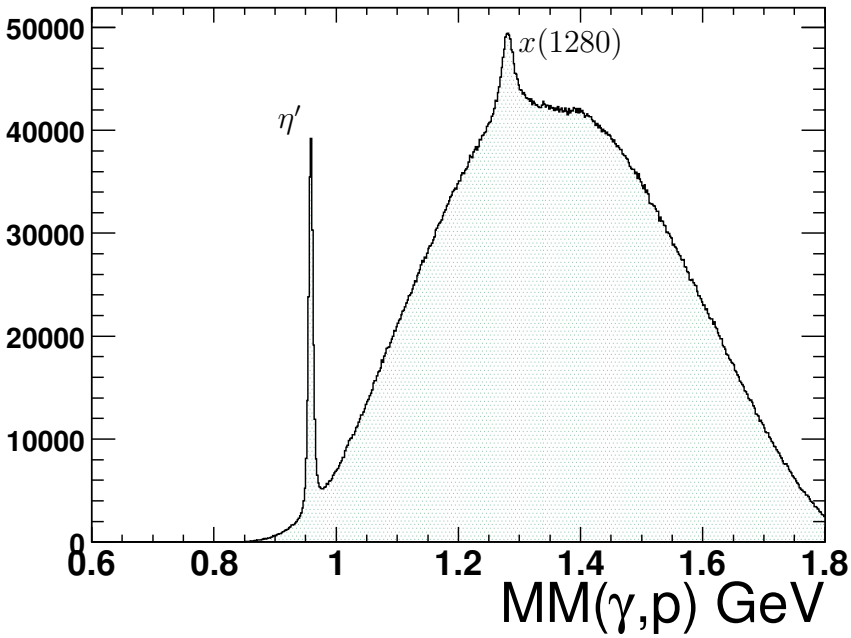

Figure 3.8: Missing mass off the proton for $\eta\pi^+\pi^-$ decay mode. The η' and $x(1280)$ mesons are visible. The $x(1280)$ lies atop a substantial background.

of the Lorentzian profile

$$L(E; M, \Gamma) = \frac{1}{\pi} \frac{\Gamma/2}{(E-M)^2 + (\Gamma/2)^2}, \tag{3.18}$$

$$\tag{3.19}$$

with a Gaussian

$$G(E; \sigma) = \frac{1}{\sqrt{2\pi\sigma^2}} e^{-(E)^2/(2\sigma^2)}. \tag{3.20}$$

$$\tag{3.21}$$

For our fits the Lorentzian width Γ is the intrinsic width of the meson state and the Gaussian σ represents the detector resolution. M is the mass of the meson, and the energy E is equivalent to the missing mass off the proton.

To measure the photoproduction differential cross section of the η' and $x(1280)$ we binned the data in center-of-mass energy W and cosine of the meson production angle $\cos\Theta_{CM}$. We binned our data in ten 100 MeV bins in W, from 1.8 to 2.8 GeV. We binned the data into nine bins in $\cos\Theta_{CM}$, eight of width 0.2 from -0.8 to 0.8, and one 0.1 wide bin from 0.8 to 0.9. The forward and backward holes of the CLAS detector were the limiting factor in angular coverage.

Two difficulties presented themselves when fitting yields in the binned data. As shown earlier, our $x(1280)$ signal in $\gamma p \to \eta\pi\pi$ is atop a considerable background. In binning our data in W and $\cos\Theta_{CM}$ we find it necessary to fix the mass and width of the $x(1280)$ in many bins where fitting would otherwise fail. Our method was to fix Γ_x and M_x to our overall "best" values in these bins,

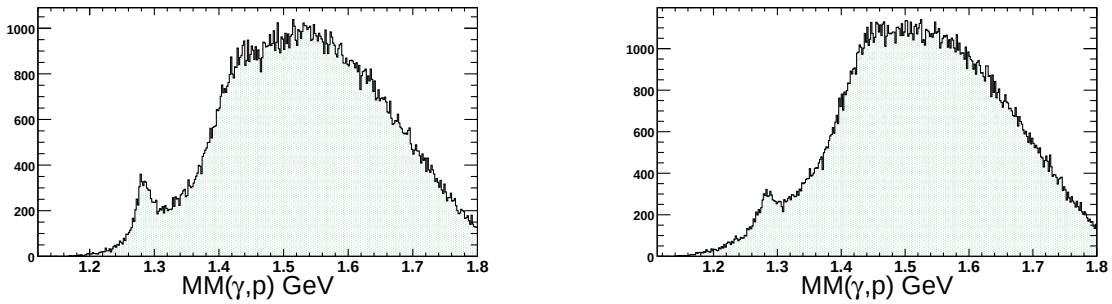

(a) (b)

Figure 3.9: Missing mass off the proton for (a) $\gamma p \to pK^+\pi^-(K^0)$ and (b) $\gamma p \to p\pi^+K^-(K^0)$. Background in these channels is more favorable for fitting with a Voigtian plus polynomial function.

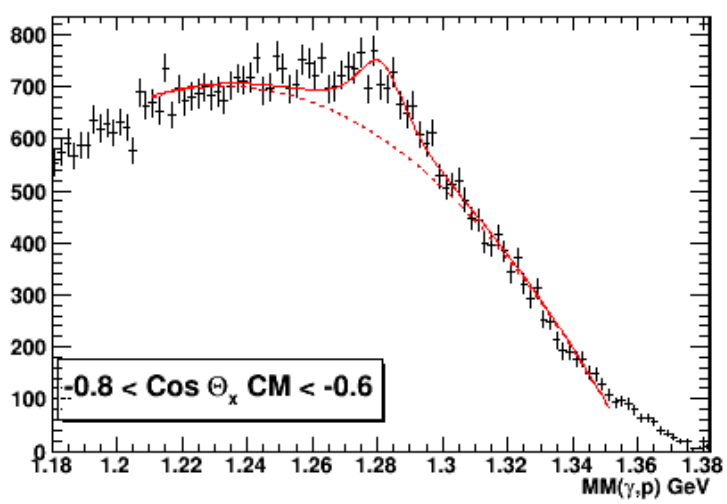

Figure 3.10: Example fit of missing mass off the proton for $\gamma p \to p\pi^+\pi^-\eta$. The W of this bin is 2.35 GeVwith $\cos\Theta^x_{CM} = -0.7$.

while leaving them free in the more stable bins. In addition we fixed σ on a bin-by-bin basis to the values obtained from our Monte Carlo simulation in § 3.4.1. Figure 3.10 shows an example fit of the $x(1280)$ signal in one of the more challenging bins for $\gamma p \to p\pi^+\pi^-\eta$. The fit range for most bins was 140 MeV/c^2 in missing mass off the proton, centered at 1281 MeV/c^2.

The mass and width values extracted from bins with sufficient statistics and background quality are shown in Figure 3.11 along with the overall weighted mean, error and χ^2/ndf for both quantities. The scatter of the width values is slightly larger than expected for the reported errors from the fitting routine as indicated by the normalized χ^2 statistic of about 1.7. The complete set of fits for all energy and angle bins is available in Appendix B.

For the $K^\pm K^0\pi^\mp$ decay mode, despite the smaller statistics the signal-to-background and shape of the background was more favorable to Voigtian fits. This lead to quite simple yield extrac-

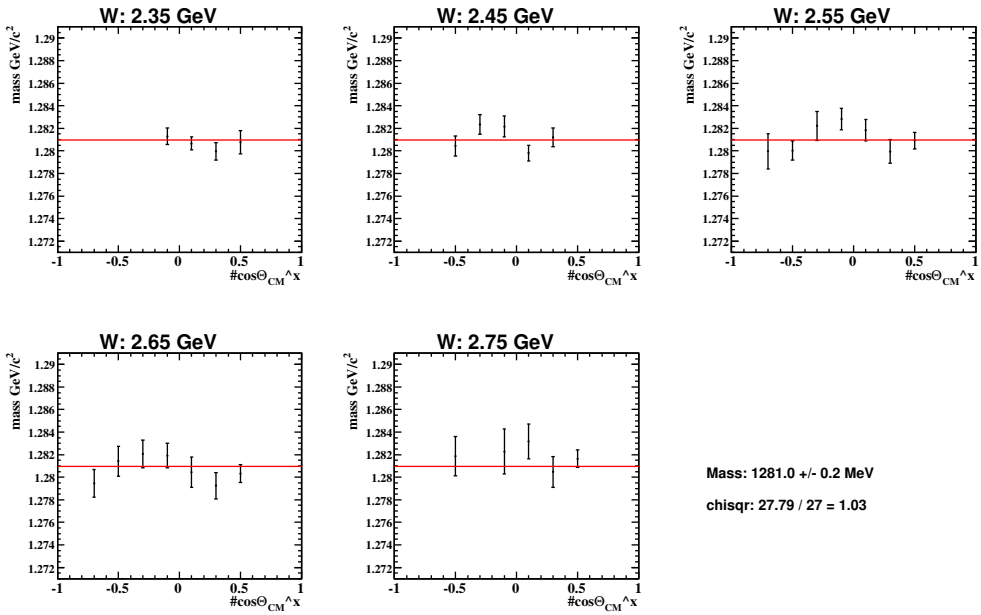

(a) Mass

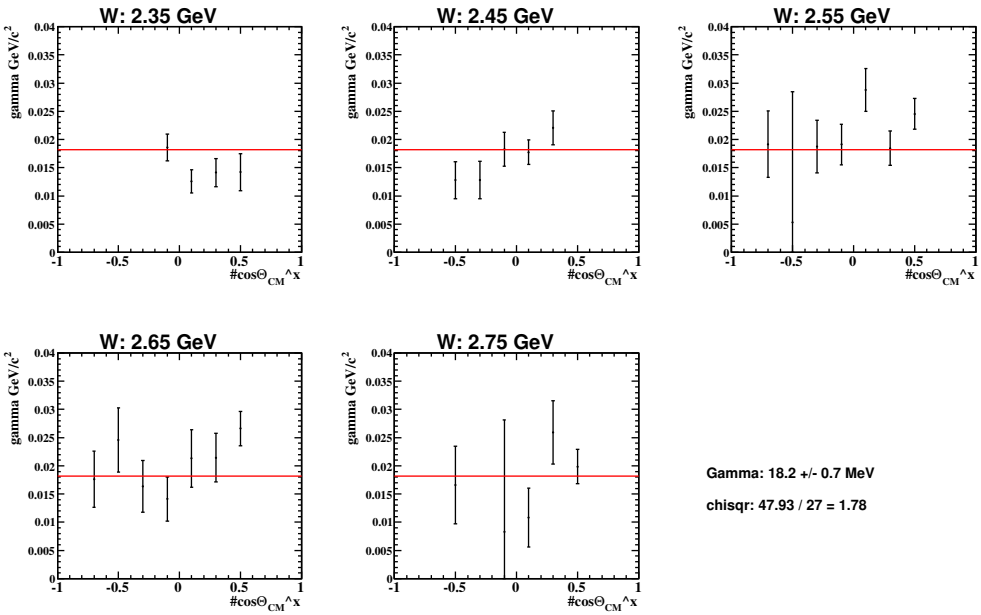

(b) Width Γ

Figure 3.11: Mass and Width Γ of the $x(1280)$ from Voigtian fits binned in W and $\cos\Theta^x_{CM}$. The weighted mean of each quantity is shown by the corresponding red line.

tion in almost all kinematic bins. However, the fit range was expanded in the $K^{\pm}K^{0}\pi^{\mp}$ mode to 160 MeV/c^2. An example is shown in Figure 3.12. Again, we fixed the σ to the value obtained from Monte Carlo. The mass and width of the $x(1280)$ were fixed in all bins to values obtained from a fit of the unbinned spectrum (full energy and $\cos\Theta$ range).

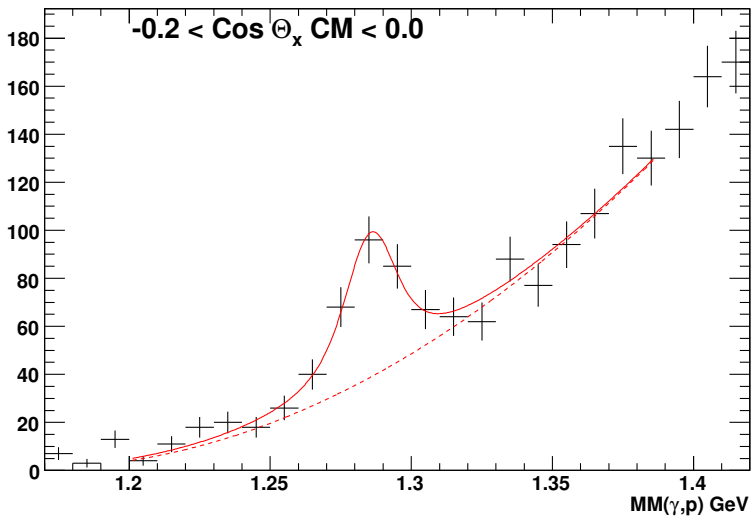

Figure 3.12: Example fit of $x(1280)$ yield in $K^{\pm}K^{0}\pi^{\mp}$ at W = 2.45 GeV and moderately forward angle. Combined missing mass off the proton spectra for $\gamma p \to pK^{+}\pi^{-}(K^{0})$ plus $\gamma p \to p\pi^{+}K^{-}(K^{0})$ has been fitted to a Voigtian lineshape plus polynomial function with the mass and width fixed to the best values obtained from the integrated spectrum.

3.2.2 Simulated Background Method

The second method employed utilized a set of simulated reactions to approximate the background shape seen in $MM(\gamma, p)$ spectrum. A likely type of reactions not rejected by our event selection criteria are events with a proton plus four pion events, in which the "extra" pions are either neutral or undetected charged pions. Both of these types of final state pass our kinematic fit to $p\pi^{+}\pi^{-}$ if the invariant mass of the "missing" pions is near the mass of the η. Several reactions,

$$\gamma p \to p\pi\pi\pi\pi, \tag{3.22}$$
$$\gamma p \to p\rho\pi\pi, \tag{3.23}$$
$$\gamma p \to \Delta\pi\pi\pi, \tag{3.24}$$
$$\gamma p \to pf_0(1370), \tag{3.25}$$

all of which have a final state of a proton and four pions were generated according to phase space, passed though our detector simulation, event building software and analysis cuts. The Monte Carlo simulation of the detector is the subject of §3.4.1. The presence of the Δ and ρ modes is motivated by the presence of these states in the invariant mass spectra $IM(p, \pi)$ and $IM(\pi, \pi)$ as seen in Figures 3.13 and 3.14. Other reactions with higher multiplicity of particles were not investigated as this set adequately approximated the shape of the background in the missing mass off the proton spectrum. However, we make no claim that above reactions represent the entirety of the actual background physics. Rather, these four pion final states were chosen to populate the kinematic space of our data.

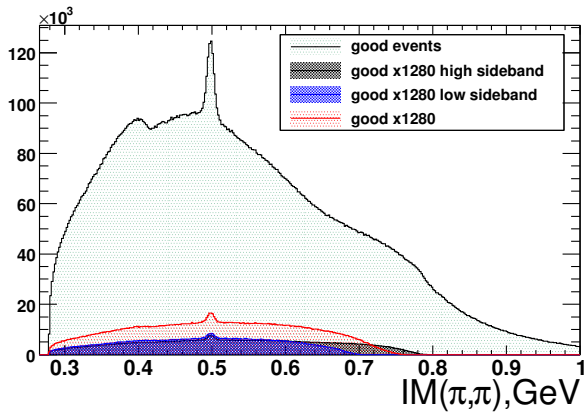

Figure 3.13: Invariant mass spectrum $IM(\pi,\pi)$ in the reaction $\gamma p \to p\eta\pi^+\pi^-$ for all good events, and selected mass bands in missing mass off the proton. The ρ^0 visible in the complete sample does not significantly impact the $x(1280)$ or its sidebands.

The acceptance for these background reactions is much lower than for the signal reaction. Even with between 100 and 200 million events generated for each reaction, we still have poor statistics in the highest W bins. As sharp structures are not expected in the missing mass off the proton for any of these reactions we implemented a smoothing algorithm.

First, histograms were rebinned into 4 MeV-wide bins in the missing mass off the proton. Then distributions were smoothed using a quadratic polynomial over a 100 MeV range. This was done by iterating over the bins in each histogram and fitting with the range centered on the chosen bin to the quadratic polynomial. Finally, each bin's content is replaced with the evaluated value of the polynomial at that point. The error on each bin remains its original counting uncertainty. Figure 3.15 shows a comparison of a smoothed background compared to the original for an example kinematic bin.

The data histograms were fit with the set of smoothed backgrounds were fit in addition to the $x(1280) \to \eta\pi\pi$ MC spectra. The yield from this method is simply the integrated signal Monte Carlo scaled by its fit coefficient. Figure 3.16 shows a fit to our $x(1280)$ signal in an example bin for $\gamma p \to p\pi^+\pi^-\eta$, the same bin as seen in Figure 3.10.

A complete set of histograms with fits for each channel and method is available in Appendix B.

3.2.3 $\rho^0\gamma$ Decay mode

The remaining yield to extract is the channel $x(1280) \to \rho^0\gamma$, where the ρ^0 decays $\sim 100\%$ of the time to $\pi^+\pi^-$. As the ρ^0 is quite wide with $\Gamma \approx 150\ MeV/c^2$ we do not impose any cuts on the invariant mass of the two pion system. We found it necessary to impose two additional cuts to reject background events that leak into our missing photon kinematic fit. The first cut is on the missing transverse momentum to reject $\gamma p \to p\pi^+\pi^-$ exclusive events; the second cut is a rejection of $\gamma p \to p\pi^+\pi^-\pi^0$ events using a kinematic fit to the missing π^0 mass. The necessity of these cuts is obvious from the presence of ω,ρ^0 and $a_2(1320)$ mesons in addition to the expected η' in the missing mass off the proton spectrum as seen in Figure 3.17.

Missing $P_\perp$ Cut

Our kinematic fit to $\gamma p \to p\pi^+\pi^-(\gamma)$ selects events with zero missing mass and appropriate missing momentum consistent with the covariance matrix of our momentum measurements. The confidence

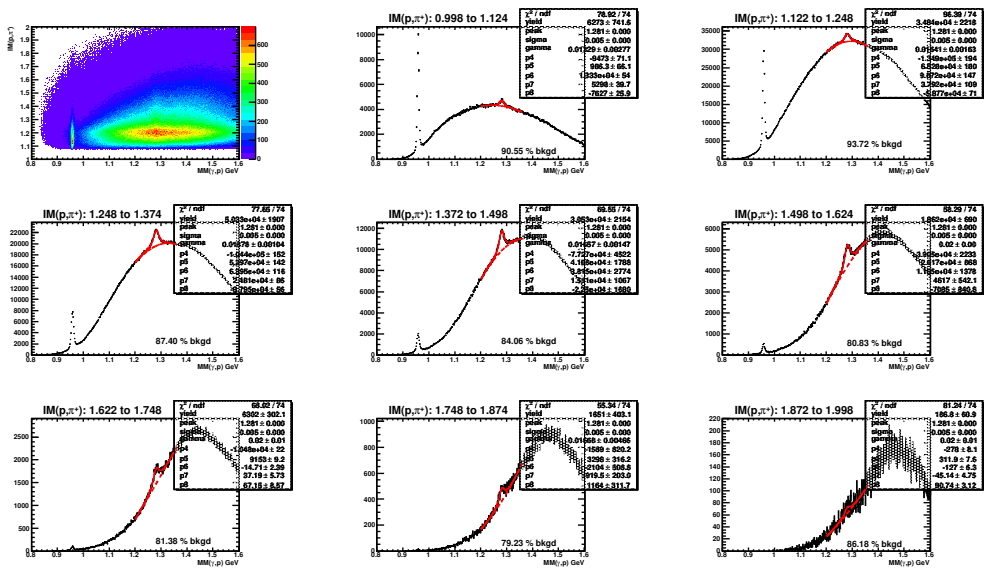

Figure 3.14: Invariant mass $IM(p, \pi^+)$ versus missing mass off the proton $MM(\gamma, p)$ in the reaction $\gamma p \to p\eta\pi^+\pi^-$ clearly shows the Δ^{++} background respectively. Slices in $IM(p, \pi^+)$ show the $x(1280)$ signal to background improves only slightly at higher values of $IM(p, \pi^+)$ such that no clean removal of Δ^{++} background can be made.

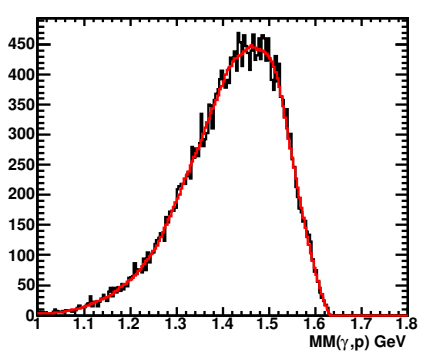

Figure 3.15: Smoothing of simulated background events using a local polynomial technique. The black histogram shows the missing mass off the proton for Monte Carlo $\gamma p \to p\rho\pi^+\pi^-$ events that pass our $\pi^+\pi^-\eta$ analysis cuts. The red histogram shows the effect of our smoothing algorithm applied over 25 bins (50 MeV).

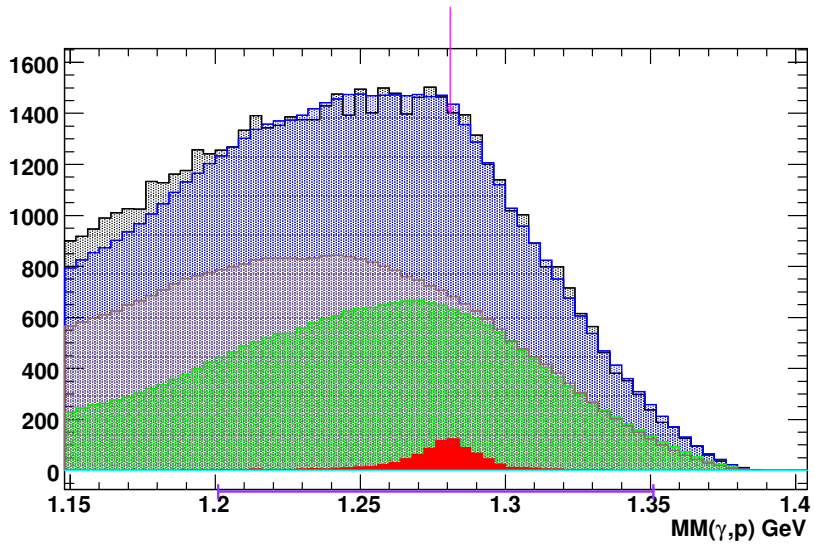

Figure 3.16: Example fit of missing mass off the proton for $\gamma p \to p\pi^+\pi^-\eta$. W bin is 2.35 GeVwith $\cos\Theta^x_{CM} = -0.7$. This is the same bin as used in the Voigtian Figure 3.10, but with 4 MeV wide bins. The $x(1280)$ signal is shown in red, with the $p\rho\pi\pi$ background in green, the $f(1370)p$ background in brown and the sum of the three Monte Carlo spectra in blue.

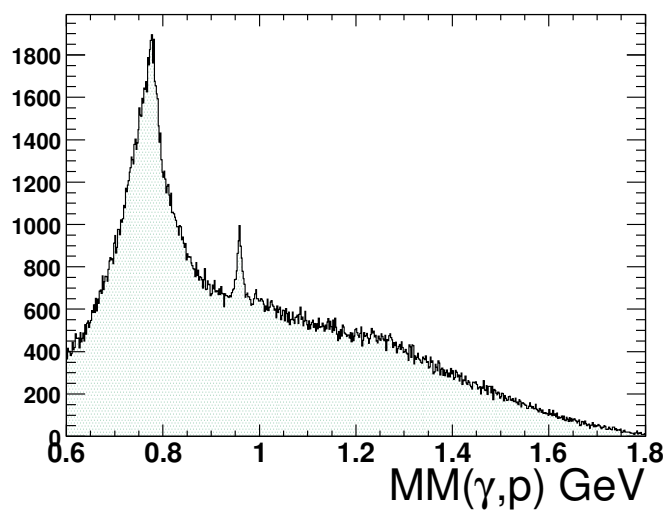

Figure 3.17: Missing mass off the proton for $\gamma p \to p\pi^+\pi^-(\gamma)$ after kinematic fitting and confidence level cut for run 43582. Strong signal for ω/ρ^0 around $800\,\mathrm{MeV}/c^2$ remains, as well as the $\eta'(958)$ and slight hint of the broad $a_2(1320)$.

level cut on this fit does not distinguish between signal events with the photon and those with no missing particle. The η', $f_1(1285)$, or $\eta(1295)$ mesons cannot decay to $\pi^+\pi^-$ (parity violating), so it is desirable to remove these events to improve our signal to background for fitting considerations. To separate events with a missing photon from $\gamma p \to p\pi^+\pi^-$ exclusive events we impose a minimum missing momentum cut. The kinematic fit has more freedom to adjust momentum along the beam direction than perpendicular to it. This is due to the uncertainty on the incident photon energy along with the possibility of having chosen the wrong photon from the multiplicity of photons in a given event, as per Figure 3.4. A $p\pi^+\pi^-$ event with no missing particle cannot have any appreciable transverse momentum $P_\perp$. To determine a reasonable minimum transverse momentum cut we examine the spectrum for η' events as it has a smaller breakup momentum and sufficient statistics to fit the signal in the low-$P_\perp$ region.

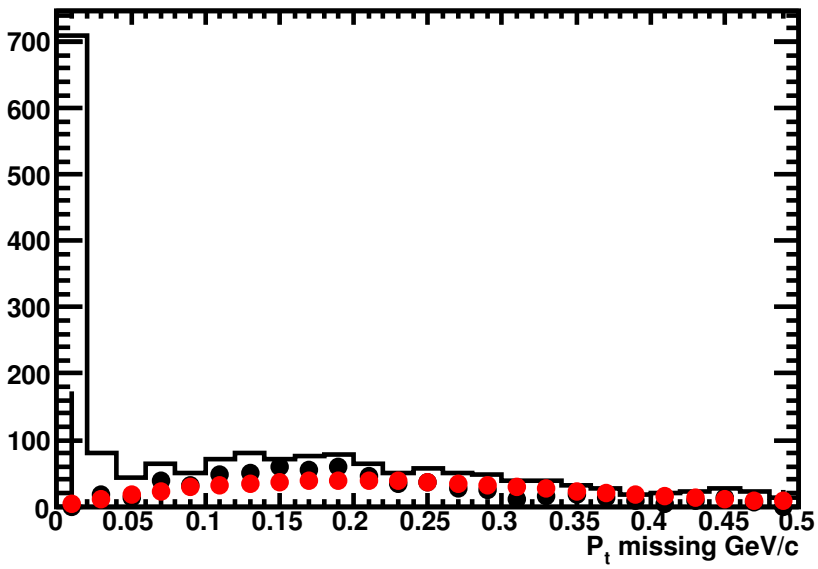

Figure 3.18: Missing transverse momentum for events kinematically fit to $\gamma p \to p\rho^0\gamma$ with CL > 0.1. Histogram is projection of events with missing mass off the proton at the mass of the η', 0.958 MeV/c^2. Black circles denote η' strength from fit with a Gaussian signal function, and red circles the spectrum for our $\eta' \to \rho^0\gamma$ Monte Carlo.

As seen in Figure 3.18, the missing transverse momentum falls off rapidly for events of a given range in missing mass off the proton. However, the distribution for actual η' events rises from zero to maximum between 100 to 200 MeV/c. We require the event to have $> 40 MeV/c$ missing transverse momentum. Fitting the missing mass off the proton spectrum for run 43582 before and after this selection shows the amount of η' signal lost to be 6.2%. The fraction of η' cut from our Monte Carlo sample was found to be only 2.8%. This discrepancy between data and Monte Carlo and the resultant systematic uncertainty will be discussed further in the next chapter.

Missing π^0 event rejection

The exclusion of events with negligible missing transverse momentum removed our most dominant background. As shown in the missing mass off the proton spectrum in Figure 3.19, there was still

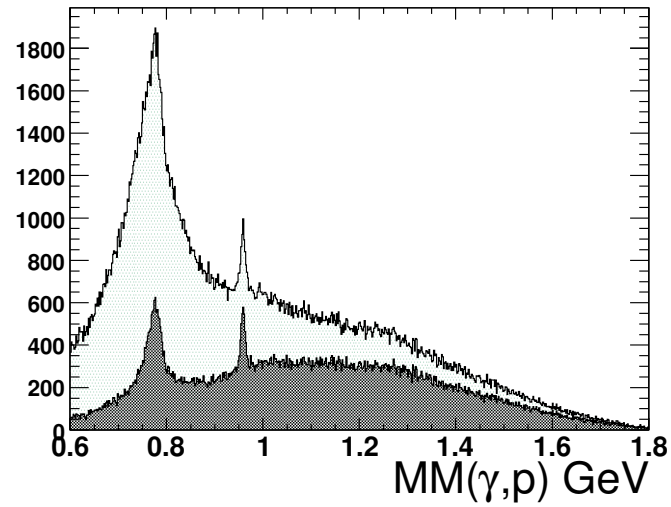

Figure 3.19: Missing mass off the proton for $\gamma p \to p\pi^+\pi^-(\gamma)$ before and after cutting on missing transverse momentum for run 43582. The signal for ω/ρ^0 around $800\,\mathrm{MeV}/c^2$ is drastically reduced by the cut.

a large amount of background beneath the η' peak. There is also a sizable ω signal present in this spectrum. The dominant decay mode of the ω is into $\pi^+\pi^-\pi^0$. The strong peak suggests that events with a missing π^0 are being pulled into our missing γ kinematic fit. Figure 3.20 shows the missing mass squared constructed from the measured four-vectors for events that pass our 10% confidence level to the $\gamma p \to p\pi^+\pi^-(\gamma)$ hypothesis. The missing mass after the fit is constrained to be zero. To remove the $\gamma p \to p\pi^+\pi^-\pi^0$ events from our $\gamma p \to p\rho^0\gamma$ events we performed a second kinematic fit to the missing π^0 hypothesis. Events which pass this fit with a confidence level of more than 0.01 were cut from our $\rho^0\gamma$ data. Figure 3.21 shows the effect of this cut. The systematic uncertainty on our yields from this cut will be discussed in the next chapter.

Yield of $x(1280)$ in $\rho^0\gamma$ Decay Mode

After our efforts to reduce background from other final states from $\gamma p \to p\pi^+\pi^-(\gamma)$ events, we find the spectrum to have a small but discernible signal at $1280\mathrm{MeV}/c^2$. The signal-to-noise ratio after the $\rho^0\gamma$-specific cuts remains too poor to bin the data for differential cross sections. We instead fit the integrated missing mass off the proton spectrum to determine the total yield of $x(1280)$ in the $\rho^0\gamma$ final state. Figure 3.22 shows the result of fitting this spectrum with a Voigtian signal function and third order polynomial background. The mass and width are fixed to the values obtained earlier in our fitting of the $\eta\pi^+\pi^-$ yields. The yield of $x(1280)$ from this fit is 3800 ± 800 events, where the error quoted is solely the statistical error from MINUIT on the Voigtian yield parameter. Section 4.2 of the next chapter will detail the systematic studies we performed to test the robustness of this signal and the estimate of systematic error on this yield.

3.2.4 Accounting for missing decay modes

In presenting branching fraction results for the $x(1280)$ it is desirable to compare to world data for the $f_1(1285)$ and $\eta(1295)$. Since CLAS is primarily optimized for charged track detection and the *g11* trigger requires at least two charged tracks, we cannot measure decays into $\eta\pi^0\pi^0$ and $K^0\bar{K}^0\pi^0$

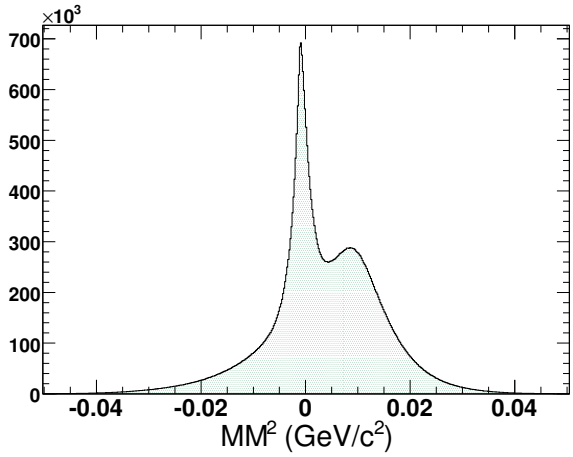

Figure 3.20: Measured missing mass squared (without kinematic fit) for events passing our confidence level cut for $\gamma p \to p\pi^+\pi^-(\gamma)$ hypothesis. The "hump" on the right side of the γ peak shows an obvious contamination of π^0 events.

modes. Also, we did not measure the $K^+K^-\pi^0$ decay mode for it was found to have a very small acceptance. To correct for this we have scaled our results by the appropriate factors to account for the omitted neutral and charged states.

The $x(1280)$ decays strongly so the relative fraction of decay modes depends on the isospin of the final state. Both candidate mesons, $f_1(1285)/\eta(1295)$ are isospin zero, so the total isospin I and its projection I_3 must also be zero in the final state. For the $\eta\pi\pi$ modes the isospin states are

$$\eta\pi^+\pi^- = |0,0\rangle|1,1\rangle|1,\,-1\rangle, \tag{3.26}$$

$$\eta\pi^-\pi^+ = |0,0\rangle|1,\,-1\rangle|1,1\rangle \text{ and} \tag{3.27}$$

$$\eta\pi^0\pi^0 = |0,0\rangle|1,0\rangle|1,0\rangle. \tag{3.28}$$

Then the expected branching fraction weights are computed with the appropriate Clebsch-Gordan coefficients to be

$$x \to \eta\pi^+\pi^- = |\langle 0,0||0,0\rangle|1,1\rangle|1,\,-1\rangle|^2 \qquad = \frac{1}{3}, \tag{3.29}$$

$$x \to \eta\pi^-\pi^+ = |\langle 0,0||0,0\rangle|1,\,-1\rangle|1,1\rangle|^2 \qquad = \frac{1}{3} \text{ and} \tag{3.30}$$

$$x \to \eta\pi^0\pi^0 = |\langle 0,0||0,0\rangle|1,0\rangle|1,0\rangle|^2 \qquad = \frac{1}{3}. \tag{3.31}$$

For the kaon-containing modes the isospin states are

$$K^+K^-\pi^0 = |\frac{1}{2},\frac{1}{2}\rangle|\frac{1}{2},-\frac{1}{2}\rangle|1,0\rangle, \tag{3.32}$$

$$K^0\bar{K}^0\pi^0 = |\frac{1}{2},-\frac{1}{2}\rangle|\frac{1}{2},\frac{1}{2}\rangle|1,0\rangle, \tag{3.33}$$

$$K^+\bar{K}^0\pi^- = |\frac{1}{2},\frac{1}{2}\rangle|\frac{1}{2},\frac{1}{2}\rangle|1,\,-1\rangle \text{ and} \tag{3.34}$$

$$K^-K^0\pi^+ = |\frac{1}{2},-\frac{1}{2}\rangle|\frac{1}{2},-\frac{1}{2}\rangle|1,1\rangle. \tag{3.35}$$

with the fractions

$$x \to K^+K^-\pi^0 = \frac{1}{6}, \tag{3.36}$$

$$x \to K^0\bar{K}^0\pi^0 = \frac{1}{6}, \tag{3.37}$$

$$x \to K^+\bar{K}^0\pi^- = \frac{1}{3} \text{ and} \tag{3.38}$$

$$x \to K^-K^0\pi^+ = \frac{1}{3}. \tag{3.39}$$

For both $K^\pm K^0\pi^\mp$ and $\eta\pi^+\pi^-$ the weight of the analyzed modes is two-thirds of the respective complete $K\bar{K}\pi$ and $\eta\pi\pi$ modes. Thus, when computing the $x(1280) \to \eta\pi\pi$ process we must scale the measured $\eta\pi^+\pi^-$ yield by a factor of 3/2 and likewise for $x(1280) \to K\bar{K}\pi$. Since the weight happens to be the same it will cancel out when calculating the relative branching ratio between these two modes, but must not be omitted in calculating branching ratios between these decay modes and the $\rho^0\gamma$ decay mode.

3.3 Normalization

Calculation of differential cross sections for the η' and $x(1280)$ mesons requires several *normalization* factors. To construct our desired differential rate we need to account for the thickness of target material present in the beam path, measure the number of tagged photons and account for the *live time* of the detector. The live time represents the fraction of running time when the data acquisition system of CLAS was ready to record data. This section describes these calculations.

3.3.1 Target

The reaction rate depends upon the length of the target cell and the density of protons contained within. As discussed in detail in §2.3.1, the target for the *g11* run period was a 40 cm vial of liquid hydrogen. The density of the liquid hydrogen varies according to temperature and pressure fluctuations in the target cryogenic system. These values were monitored on a run-by-run basis. The average density for *g11* was calculated[40] according to the method of ref.[50] to be

$$\bar{\rho} = 0.07177 \text{ g/cm}^3 \tag{3.40}$$

with a variance of

$$\sigma_\rho^2 = 6.776 \times 10^{-9} \text{ g}^2/\text{cm}^6, \tag{3.41}$$

which is an uncertainty of about 0.1%. The stability of the density allows us to use the average rather than calculating the normalization on a run-by-run basis.

3.3.2 Photon Flux

The calculation of incident photon flux as measured by the CLAS Tagger has been performed according to the standard *gflux* package[51], developed by James Ball and Eugene Pasyuk. We briefly describe the method employed by the software package. The gflux method reconstructs the number electrons that strike a given T-counter from the rate of electrons in a given time window. This number is adjusted for the live-time. To convert the number of electrons into the number of photons incident on the target, the number of photons lost between the tagger radiator foil and the target must be taken into account. This factor varies with T-counter but in general is about a 10% loss. As discussed in §2.3.5, only the first 40 (highest energy) tagger T-counters were part of the

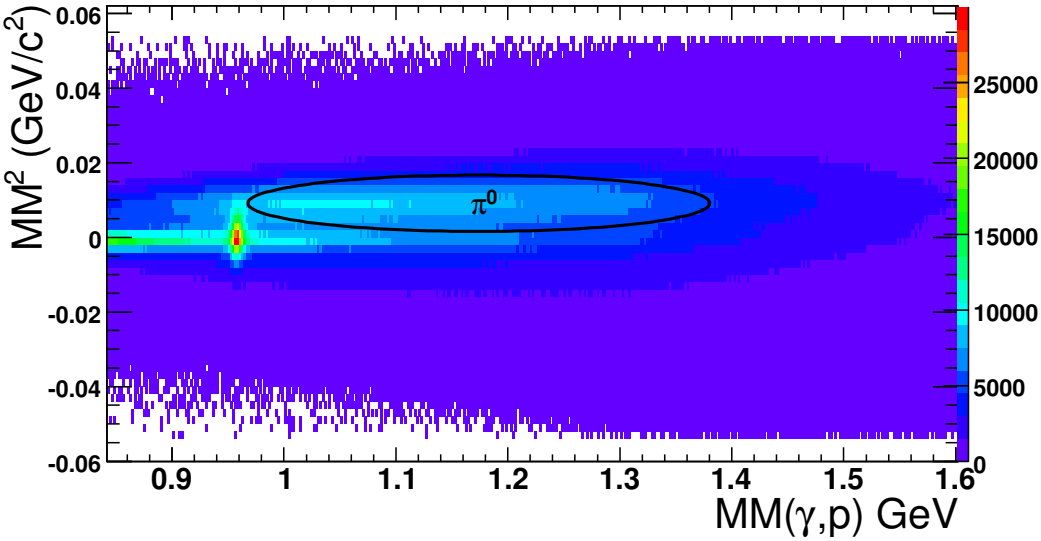

(a)

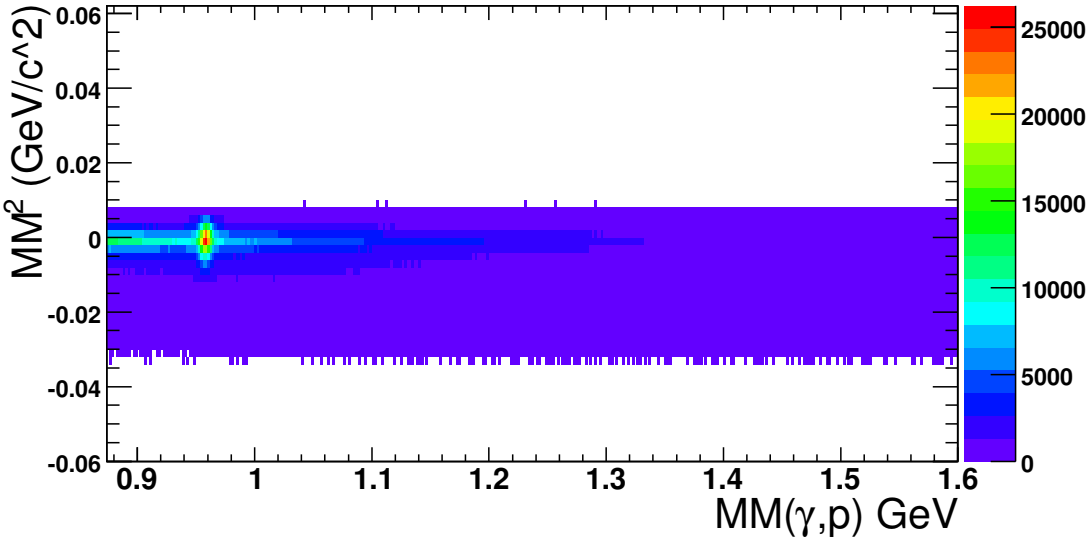

(b)

Figure 3.21: Measured missing mass squared (without kinematic fit) versus missing mass off the proton for $\gamma p \to p\pi^+\pi^-(\gamma)$. before and after cutting events that have a confidence level greater the 1% to a kinematic fit to a missing π^0. The π^0 band highlighted by the ellipse in figure (a) is cleanly removed in figure (b).

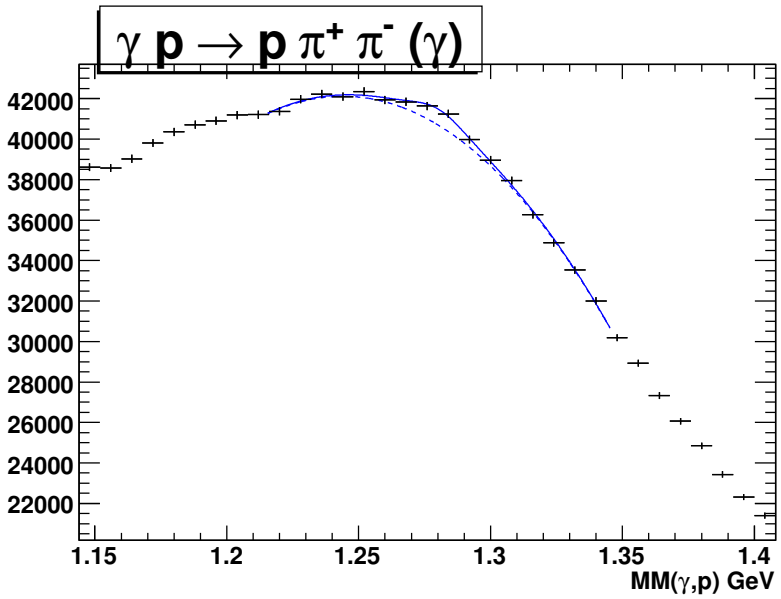

(a)

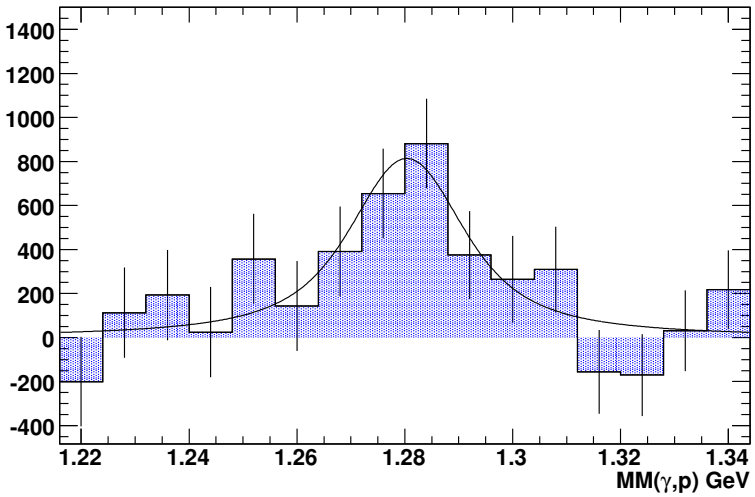

(b)

Figure 3.22: (a) Missing mass off the proton for $\gamma p \to p\pi^+\pi^-(\gamma)$ fitted with a Voigtian plus polynomial background. (b) Spectrum after background subtraction using the polynomial parameters our fit.

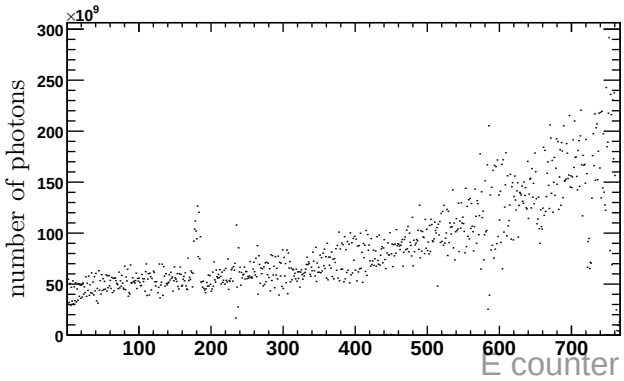

Figure 3.23: Photon Flux as measured by the CLAS Tagger. High E-counter id number corresponds to low energy photons.

event trigger, low energy photons were recorded only if there was a high energy photon in the tagger in the same event window.

The integrated number of photons for the dataset used in this analysis is shown in Figure 3.23, rebinned into E-counter bins. We then must rebin once more into our 100 MeV wide W bins to use to calculate differential cross sections. The rate varies dramatically from bin to bin as each physical paddle comprises three logical channel due to the overlapping layout as described in §2.2. As the tagger is part of the DAQ trigger such bin-to-bin "jumps" divide out and do not represent a systematic error.

3.3.3 Live-time Correction

Early analyses of the *g11* dataset observed a beam-current dependence in normalized yields of the ω and ρ. Further study of this effect found the dependence to be correlated with method of live-time calculation [40]. Through comparison of the normalization effect of using the DAQ scalar clock-based live-time, used by gflux, with the live-time calculated from the Faraday Cup, which is simply noise for photon beam operation, the current dependence was found to vanish when the Faraday Cup live-time was used. It was empirically found that the two could be brought into agreement by squaring the scalar-based live-time in the calculation. We apply the scalar clock correction to our photon flux for this analysis in the form of single multiplicative factor of 0.796 for the entire g11a dataset. The square of this value is not used as the scalar clock is already present in the gflux calculation. Details of the study and calculation of the correction factor are available in M. Williams thesis [40]. As the hardware involved was removed after the *g11* run period, the exact cause of this discrepancy was never determined.

3.4 Acceptance

Physical detectors are never ideal, and an experimental apparatus as complex as CLAS has many subsystems with individual efficiencies and resolutions to consider as part of any analysis. Also, in the course of this analysis we have made several cuts to select and enhance our signal. We need to correct our measured yields from our observed events for both of these efficiencies. We compute the fraction of events lost as a function of their kinematics, or *acceptance*, through a computer simulation of CLAS called GSIM. Then the simulated events are processed through the same event reconstruction and analysis software as used for the *g11* data. We have cut from our analysis regions where the simulation does not accurately reproduce the detector as described earlier in §3.1.5. Through studying the simulated events we obtain our acceptance as a function of the kinematic binning of our differential cross sections, as well as a measure of the expected experimental resolution in mass spectra.

3.4.1 Monte Carlo Event Generation

We begin our acceptance calculation by generating photoproduction events of the η' and $x(1280)$. Our event generator does not simulate the dynamics of photoproduction of the mesons. It does include the Bremmstrahlung photon energy distribution and an approximation of t-slope in production angle as is known to apply for the η' and likely for the $x(1280)$. We also put in a small flat baseline to ensure an adequate number of events are produced in the backward angle bins at high energy where the combination of the t-slope and Bremmstrahlung distributions leads to a very small number of events generated. Without such a requirement, we would have insufficient statistics to compute our acceptance in these bins. Figure 3.24 shows the distribution of generated events as a function of our W in our cross section binning.

We generated 20 million events for both of our studied η' decay channels. For the $x(1280)$ we generated 10 million events per decay mode. All decays were calculated according to 3-body

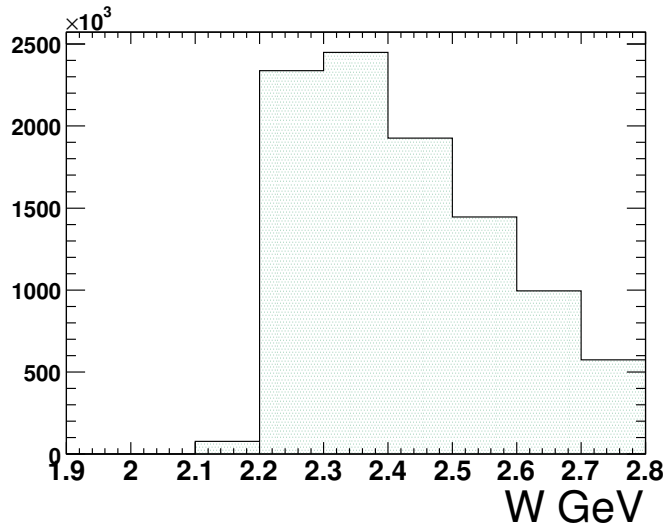

Figure 3.24: Center-of-mass energy distribution of generated Monte Carlo $x(1280)$. The shape is chosen to mimic Bremmstrahlung photon energy distribution in combination with a slight t-slope production mechanism.

phase space, except for the $\rho^0\gamma$ final state, where we simulated first the two body decay into ρ^0 and γ and then the subsequent decay of the ρ^0 into $\pi^+\pi^-$ according to the lineshape of the ρ^0, taking into account the "box-anomaly", a channel-specific shift in the centroid of $d\sigma/dm_{\pi\pi}$ from its nominal mass of $775.49 \pm 0.34\text{MeV}/c^2$[1]. The lineshape of the ρ strongly influences the momentum distribution of the missing photon, the transverse component of which we use for a background reduction cut as mentioned earlier.

We now process our "raw" physics events through GSIM[52], a GEANT-based simulation of the CLAS detector. GSIM simulates the passage of the particles of the input events through the components of CLAS accounting for material composition of the detector components and for simulated detector response. Particles decay, rescatter, and lose energy in the simulation.

The timing and momentum resolution of our simulated events have been found to be better than for the actual CLAS detector and the output of GSIM is processed further through GPP, a CLAS software package that can "smear" the timing and momentum resolution of simulated tracks to better match a dataset and remove dead TOF paddles and DC wires.

For this analysis GPP was primarily used to smear the timing for each TOF paddle according to its length and a Gaussian smearing factor chosen to best reproduce the timing resolution in the data (seen primarily in ΔTOF). Smearing of drift-chamber timing information was not used in favor a different software method developed by M. Williams detailed in [40]. This empirical algorithm smears the tracking angle and momentum of the Monte Carlo events in accordance to kinematic fit results in $\gamma p \to p\pi^+\pi^-$, similar to the momentum corrections detailed earlier. The tracking angles were smeared by $1.85\sigma_{track}$, where σ_{track} is the resolution obtained from the tracking software. The average value of the magnitude of momentum smearing was $\sim 2\text{MeV}/c$. This smearing was found to bring the confidence level distributions obtained from the Monte Carlo and experiment into good agreement in all regions of CLAS.

GSIM does not simulate the hardware trigger used in CLAS operation. To account for inefficiencies in the the trigger and empirical study was performed, using $\gamma p \to p\pi\pi$ events, by the CMU group [49]. The study measured the frequency that a particular track set the *trigger-bit* for the

CLAS trigger. The bit could not be set for a good track if the track did not meet the trigger discriminator threshold for the TOF PMTs or if the timing windows between detector component did not match. Figure 3.25 shows an example of the maps obtained by the study for Sector 1 of CLAS. We simulate the trigger for our Monte Carlo events by generating random numbers from zero to one for each track and comparing them to the efficiency values from the appropriate empirical map. If two or more tracks in different sectors pass the test, then the event is kept. We used the pion trigger maps for kaons as no empirical test case was feasible, a choice used in prior analyses [43][44].

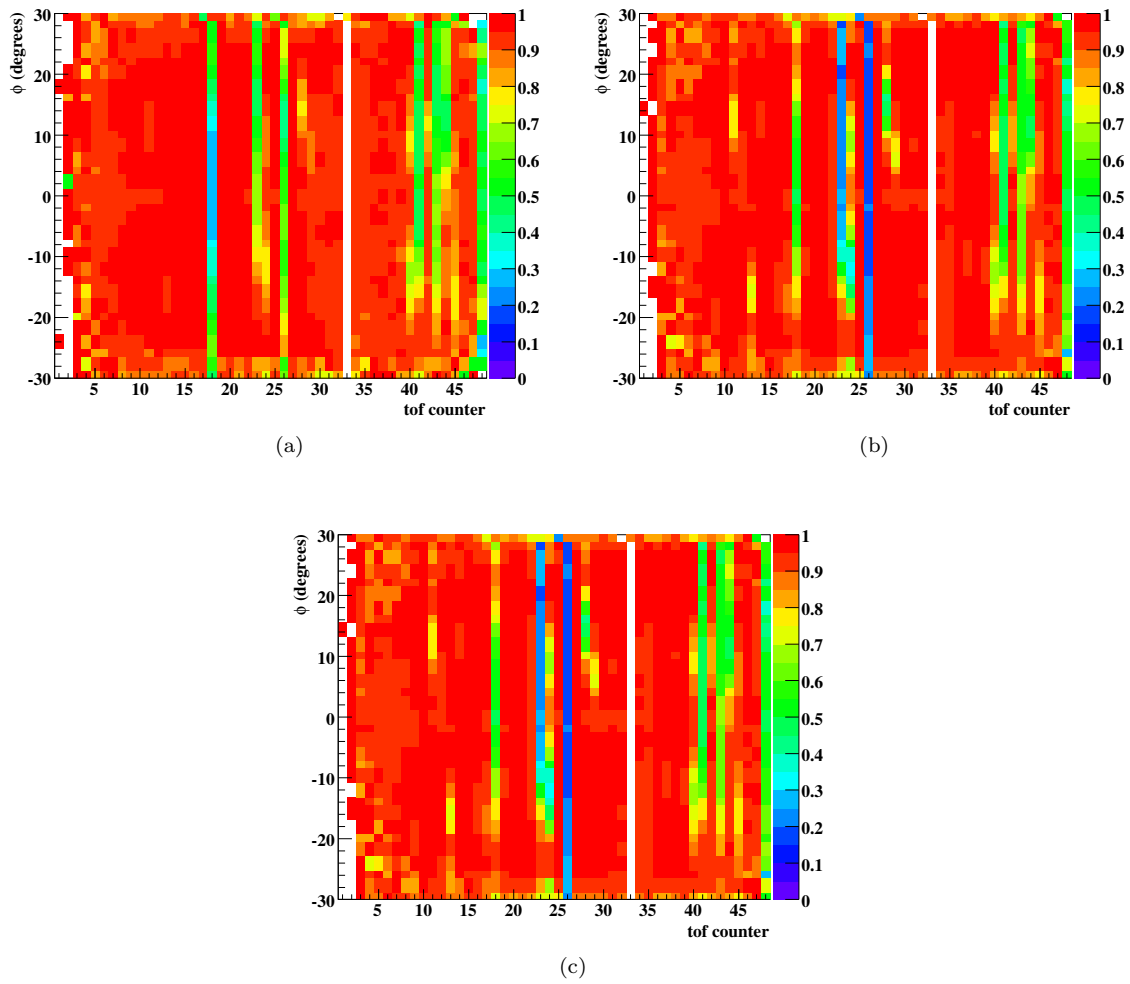

Figure 3.25: Trigger efficiency vs ϕ(degrees) and TOF-counter for Sector 1:(a) protons, (b)π^+ and (c)π^-. Image Source [40]

We found the centroid of the ΔTOF for Monte Carlo events to be about 0.5 ns away from zero, which was not seen in the data. We increased the path length of the particle 3 cm to bring our Monte Carlo simulation and data into agreement, so the same cuts could be performed on both sets of events. The size of this disagreement is consistent with difference between measuring the path from the front face versus the center of the TOF scintillators.

The simulated events were then processed through the *user_ana* routine, an implementation of the RECSIS (REConstruction and analySIS) framework. This is the same event reconstruction

framework as used to "cook" the raw *g11* data. The data files were then compressed and the events processed with the same analysis software used for the real events.

3.4.2 Acceptance Calculation

We processed our Monte Carlo events through a simulation of the the CLAS detector (GSIM), smeared the timing and momentum to match data resolutions, simulated the g11a trigger, reconstructed tracks and selected physics events with the same analysis code used for data events. We now calculate the acceptance of η' and $x(1280)$ events, including both the detector efficiency and the signal loss from our event selection criteria. For each final state the acceptance for a given energy and production angle is

$$\mathcal{A}_{\text{CLAS}}(W, \cos\Theta_{CM}) = \frac{\mathcal{N}_{acc}}{\mathcal{N}_{raw}}, \tag{3.42}$$

where $\mathcal{N}_{acc}$ is the number of *accepted* events and $\mathcal{N}_{raw}$ is the number of generated events in that kinematic bin.

The calculation of $\mathcal{N}_{acc}$ is performed according to the method of yield extraction for the meson and decay mode. For the η' we fit the missing mass off the proton in each bin with a Gaussian with no background polynomial. Figures 3.26a and 3.26b show the acceptance for the $\eta\pi^+\pi^-$ and $\rho^0\gamma$ decay modes. The two decay modes have very different acceptances as a function of center-of-mass energy. The acceptance of the $\eta\pi^+\pi^-$ decay mode increases, especially at mid to backward angles, with increasing energy. For the $\rho^0\gamma$ mode the situation is reversed, it has the highest acceptance at the lowest energy bin and decreases with increasing W.

Likewise for the $x(1280)$, we perform a Voigtian fit with the width Γ_x fixed to 18 MeV, the value used in our Monte Carlo event generator. We take the resulting σ from these Voigtian fits to be our experimental resolution and used these values as input for the yield extraction fits to the data. Figures 3.26c and 3.26d show the acceptance of $x(1280)$ events in the $\eta\pi^+\pi^-$ and $K^\pm K^0\pi^\mp$ decay modes. The acceptance for $x(1280) \to \eta\pi^+\pi^-$ is somewhat similar to that seen for $\eta' \to \eta\pi^+\pi^-$, increasing with energy with the highest values at central polar angles. The decline in acceptance from the forward hole of CLAS is not as severe as for the η' case. For $K^\pm K^0\pi^\mp$, the acceptance is smaller due to the more stringent PID cuts required for kaons, with the acceptance topping out at a maximum of four percent in the highest W bins.

To compute the acceptance for our Monte Carlo background method of §3.2.2, we integrate the Monte Carlo missing mass off the proton spectrum in each kinematic bin over the same range in missing mass off the proton used for the yield fit of the data. Figure 3.26e shows the resulting acceptance. The acceptance is slightly lower than the Voigtian case as we are not taking the full yield of $x(1280)$ per bin, but only integrating the missing mass off the proton range used in fitting each bin.

Finally, for $x(1280) \to \rho^0\gamma$ we calculate a single acceptance value for the mode for all events with W between 2.3 to 2.8 GeV and $\cos\Theta^x_{CM}$ from -0.8 to 0.9. This selection was made on both the data and Monte Carlo and brings the kinematic range used into agreement with the $\eta\pi^+\pi^-$ and $K^\pm K^0\pi^\mp$ decay modes. This acceptance was found to be $2.480 \pm 0.006\%$ (statistical error).

3.5 Differential Cross Sections

In nuclear and particle physics, a *cross section*, σ is the effective area describing the likelihood of an interaction between particles. In the classical picture it represents the interaction of point-like projectiles directed to an area that includes a solid target, the likelihood of reaction being the ratio of the cross section of the target to the total targeted region. For a scattering process such as our photoproduction reactions of interest, $\gamma p \to \eta' p$ and $\gamma p \to x(1280)p$, we measure the likelihood of

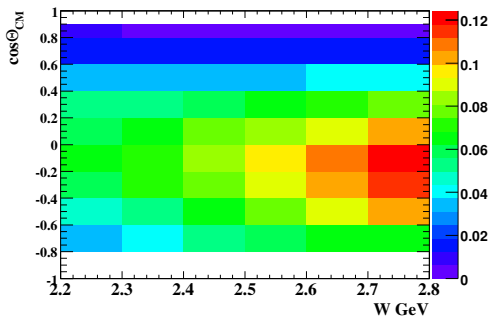

(a) $\eta' \to \eta\pi^+\pi^-$

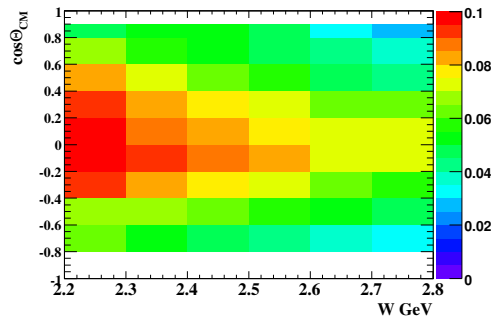

(b) $\eta' \to \rho^0\gamma$

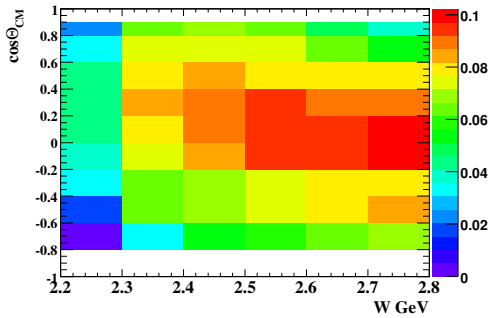

(c) $x(1280) \to \eta\pi^+\pi^-$ (Voigtian)

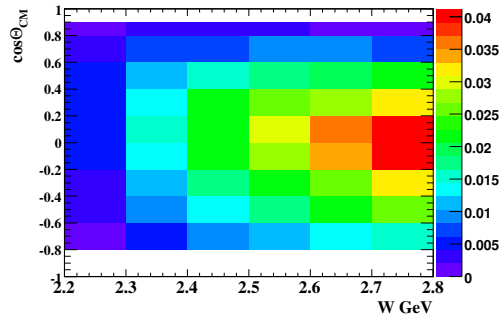

(d) $x(1280) \to K^\pm K^0\pi^\mp$ (Voigtian)

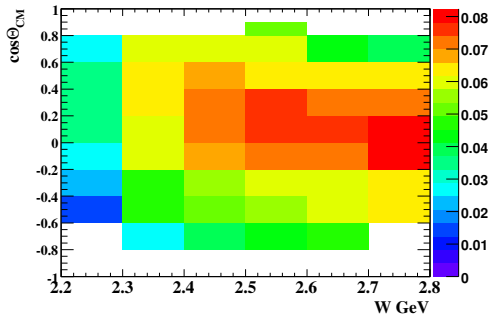

(e) $x(1280) \to \eta\pi^+\pi^-$ (MC Bkgd.)

Figure 3.26: Acceptance vs $\cos\Theta_{CM}$ and W for our reactions of interest used in computing differential cross sections.

a observing the meson, η' or $x(1280)$, per unit of solid angle, per incident photon. We assemble our measurements of yield, photon flux, target normalization, detector live-time and acceptance to calculate the differential cross section

$$\frac{d\sigma}{d\Omega} = \frac{\mathcal{Y}_{meson}}{2\pi\mathcal{N}_\gamma \rho_{target} l_{target} \mathcal{A}_{\mathrm{CLAS}} \Delta_{\cos\Theta_{CM}}}, \tag{3.43}$$

where $\mathcal{Y}_{meson}$ is the yield of the η' or $x(1280)$, $\mathcal{N}_\gamma$ is the number of photons incident on the CLAS *g11* liquid H_2 target of length l_{target} and density ρ_{target}. $\mathcal{A}_{\mathrm{CLAS}}$ is the acceptance of the CLAS detector (including deadtime and trigger inefficiencies) and $\Delta_{\cos\Theta}$ is the width of the given bin in cosine of production angle in the center-of-mass frame. Normally, one would correct the yield $\mathcal{Y}_{meson}$ by the appropriate branching fraction(s) of subsequent decay(s). We do this for η' but chose not to for the $x(1280)$ as we cannot measure the branching fractions directly and the mild controversy surrounding the $f_1(1285)/\eta(1295)$ world data. We present our differential cross sections as $\frac{d\sigma}{d\Omega} \times \mathcal{B}(\eta\pi^+\pi^-)$.

We chose to bin our yields in 100 MeV wide bins in center-of-mass energy W, from 1.8 to 2.8 GeV. We binned the data into nine bins in cosine of the meson production angle in the center-of-mass frame cos Θ_{CM}, eight of width 0.2 from -0.8 to 0.8, and one 0.1 wide bin from 0.8 to 0.9.

Figure 3.27 shows the differential cross sections for the η' meson. The cross sections show good agreement throughout the range of W and $\cos\Theta$ studied, however the $\rho^0\gamma$ results are systematically high. The study of the level of disagreement and a comparison to published CLAS data are the topic of §4.5 of the next chapter.

Figures 3.28a to 3.28e show the differential cross sections for $\gamma p \to x(1280)\, p \to \eta\pi^+\pi^-$ calculated using yields from both extraction methods with statistical errors. The agreement between methods is good, though the Monte Carlo background method is systematically low with larger errors. In the next chapter we will detail the method of combining these results and the resulting estimate of systematic errors.

Figures 3.29a to 3.29e show the differential cross sections for $\gamma p \to x(1280)\ p \to K^\pm K^0 \pi^\mp$ calculated using the Voigtian yields with statistical errors. The shape of the cross section is quite similar to that measured in $\eta\pi^+\pi^-$, but the scale is lower by about a factor of five. Since we have not corrected for branching ratios this is expected. Multiplying the $K^\pm K^0\pi^\mp$ differential cross sections by a single scale parameter and fitting them to the $\eta\pi^+\pi^-$ values yields a good fit with a χ^2 near one and a scale factor of 0.216. After scaling, the agreement between decay modes is excellent, and again in the next chapter we will detail the method of combining these results and the resulting estimate of systematic errors.

3.6 Dalitz Analysis

The Dalitz plot[53] is a well-established method for investigating the dynamics of a three-body decay. The partial decay rate for a three-body process averaged over its spin states can be expressed in terms of the energies or invariant masses as

$$d\Gamma = \frac{1}{(2\pi)^3}\frac{1}{8M}\overline{|\mathcal{M}|^2} dE_1 dE_2 \tag{3.44}$$

$$= \frac{1}{(2\pi)^3}\frac{1}{32M}\overline{|\mathcal{M}|^2} dm_{12}^2 dm_{23}^2. \tag{3.45}$$

In the standard Dalitz plot, the axes are the squares of the invariant masses m_{12}^2, m_{23}^2 of pairs of the decay products, where the mass

$$m_{12}^2 = (P_1 + P_2)^2, \tag{3.46}$$

is the square of the sum of the relevant four-vectors. For our case of $x \to \eta\pi^+\pi^-$ the chosen axes are $m_{\eta\pi^+}^2$ and $m_{\eta\pi^-}^2$. If the $x(1280)$ decays directly into the three decay products, with $|\mathcal{M}|^2$ constant,

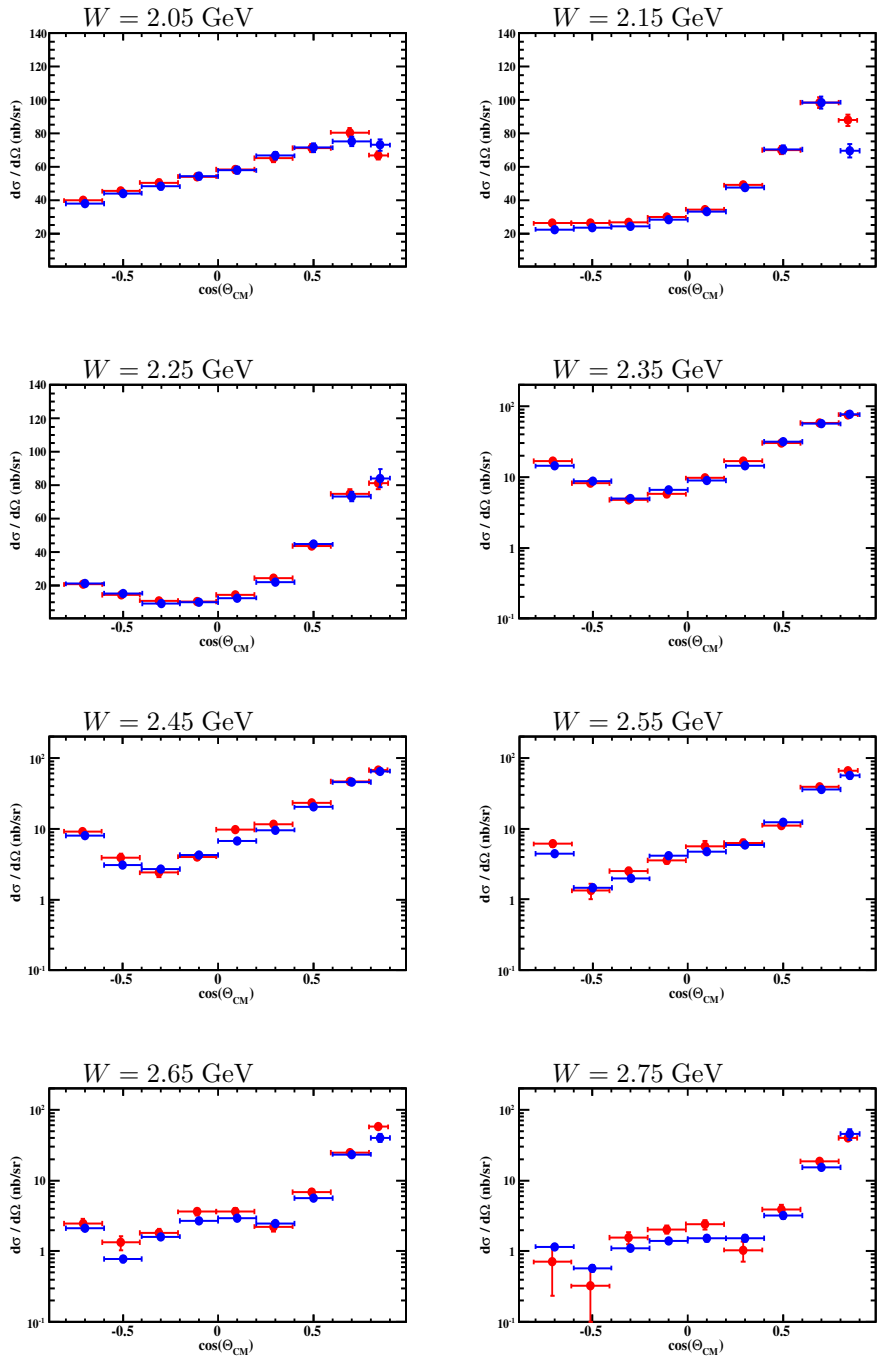

Figure 3.27: $d\sigma/d\Omega$ for η' measured in $\gamma p \to \eta' p \to p\eta\pi^+\pi^-$ (blue) and $\gamma p \to \eta' p \to p\pi^+\pi^-\gamma$ (red). Note bins from $W = 2.35$ GeV and up are on a logarithmic scale.

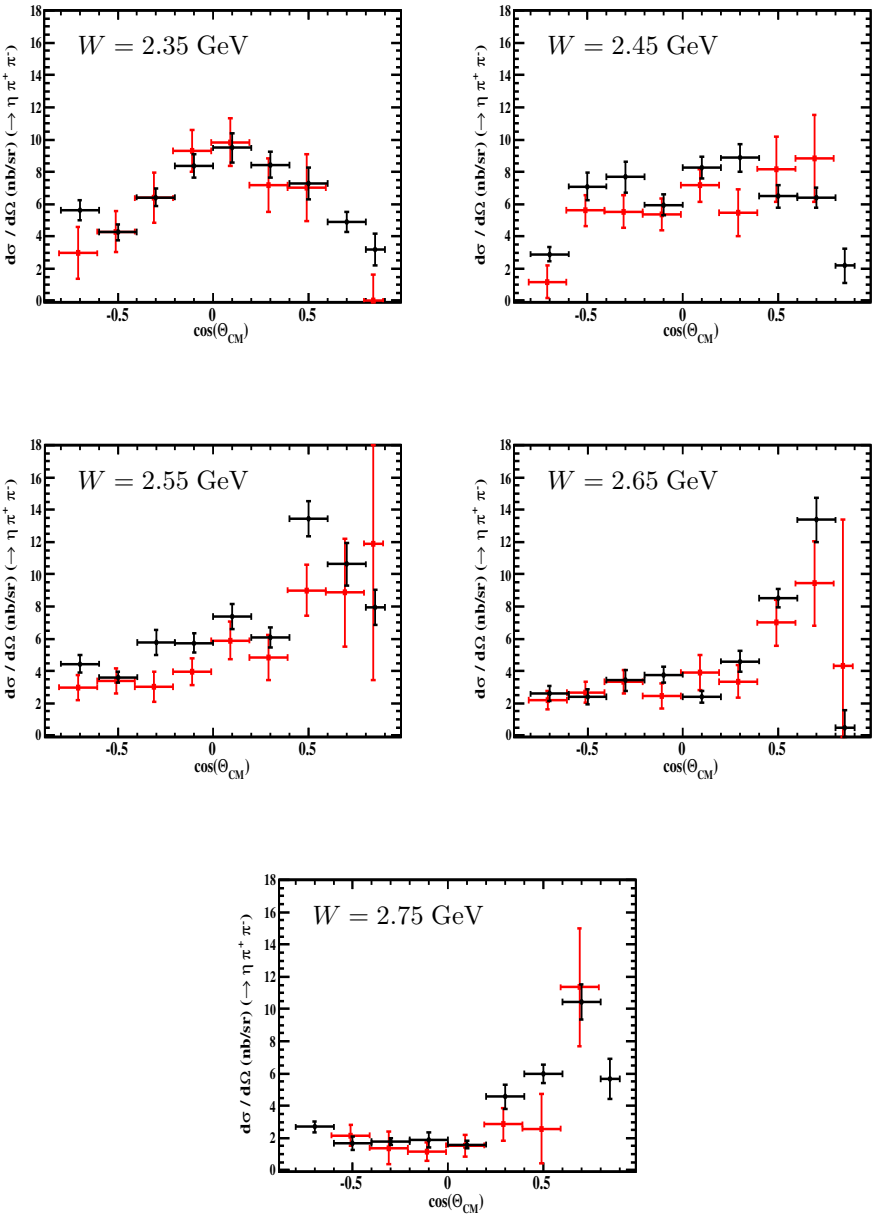

Figure 3.28: $d\sigma/d\Omega$ for $\gamma p \to x(1280)p \to p\eta\pi^+\pi^-$ by two yield extraction methods. Black data points were obtained via fit to Voigtian signal with polynomial background. Red points were obtained through fitting the missing mass off the proton spectrum with several Monte Carlo reactions representing the signal and several background channels. Some angles have missing points where one or the other yield extraction method fails.

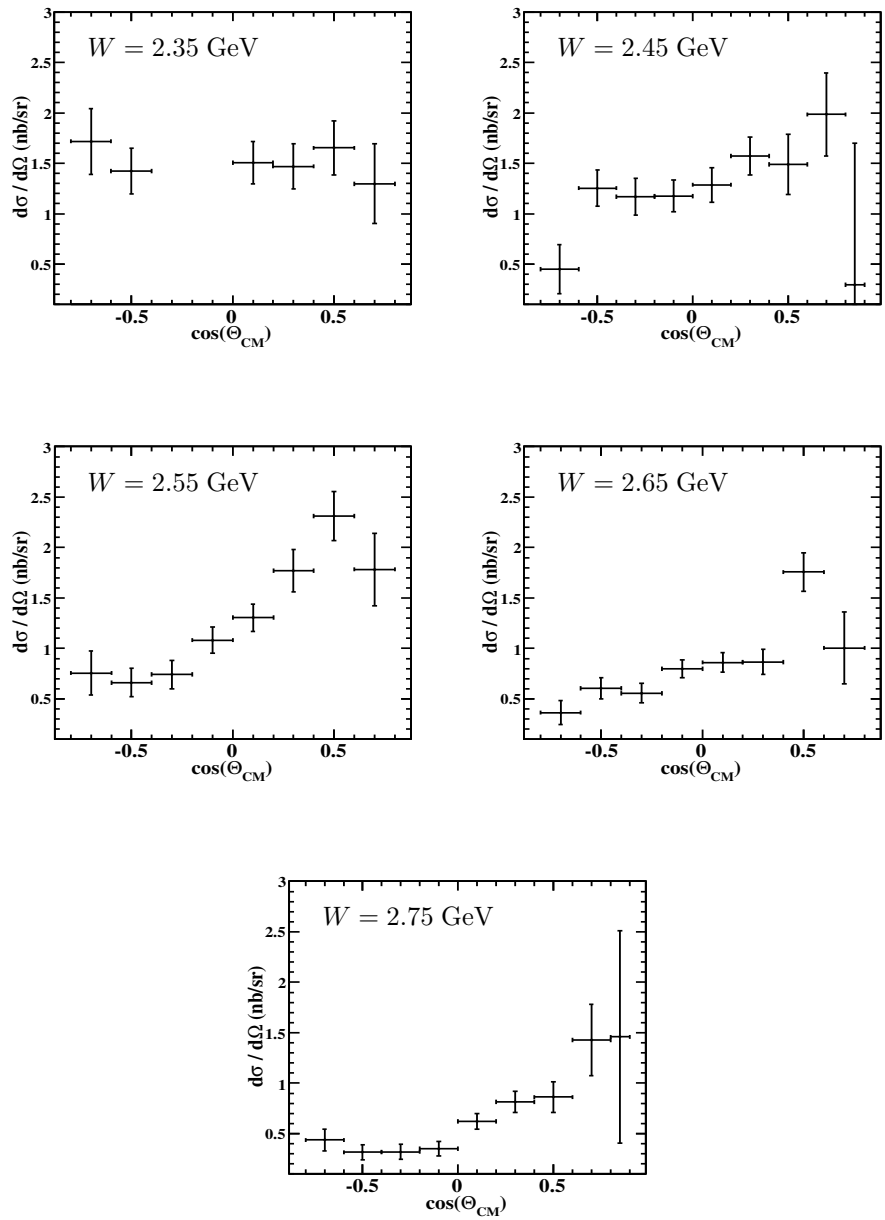

Figure 3.29: $d\sigma/d\Omega$ for $\gamma p \to x(1280)p \to pK^{\pm}K^{0}\pi^{\mp}$. Data yields were obtained via fit to Voigtian signal with polynomial background. Some angles are missing points where our yield extraction fails.

then the distribution on the Dalitz plot will be uniform. However, there may be an intermediate resonant process, in which the $x(1280)$ decays first via a two body decay, with one of those decay products immediately decaying into two additional decay products. In this case, the Dalitz plot will show a non-uniform distribution, with band(s) at the mass of any intermediate resonance(s).

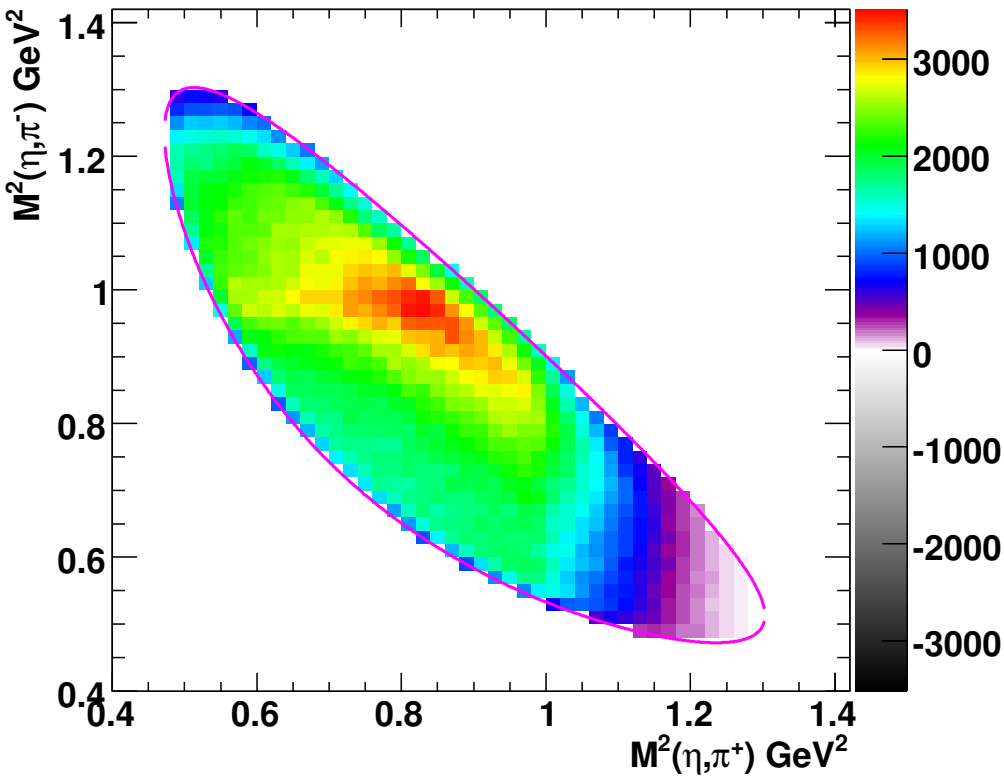

Figure 3.30: "Raw" Dalitz plot for $x(1280) \to \eta\pi^+\pi^-$ events with missing mass off the proton between 1251 and 1311 MeV/c^2. No $x(1280)$ signal enhancement or acceptance correction has been performed yet.

Events with missing mass off the proton between 1251 and 1311 MeV/c^2 are selected as the $x \to \eta\pi^+\pi^-$ sample. Figure 3.30 shows the Dalitz plot for these events. At this stage it is not possible to separate resonant structure from the dominate multi-pion background. The signal to noise is estimated at $\sim 5\%$ from fits to the MM(γ, p) spectrum.

3.6.1 Sideband Subtraction

In studying the Dalitz plot of $x(1280) \to \eta\pi^+\pi^-$ we first attempted to model the background using the same Monte Carlo technique as we used in our yield extractions. However, there were several difficulties in combining the weights from the binned fits into an integrated model that reproduced the distribution in $m^2_{\eta\pi^+}$ and $m^2_{\eta\pi^-}$ observed in the $x(1280)$ region and its sidebands. We found sideband subtraction to give superior results. The usual difficulty in applying sideband-subtraction

is assuring the background has the same coverage in the sidebands as in the central region for the variables of interest.

The kinematic coverage of a Dalitz distribution is determined by the masses of the particles involved. As the sidebands of the $x(1280)$ come from a different mass range than the signal region, they cover a different area of the Dalitz plot. Figure 3.31 shows these kinematic boundaries for the η', $x(1280)$ and the central mass values of the sidel
proton.

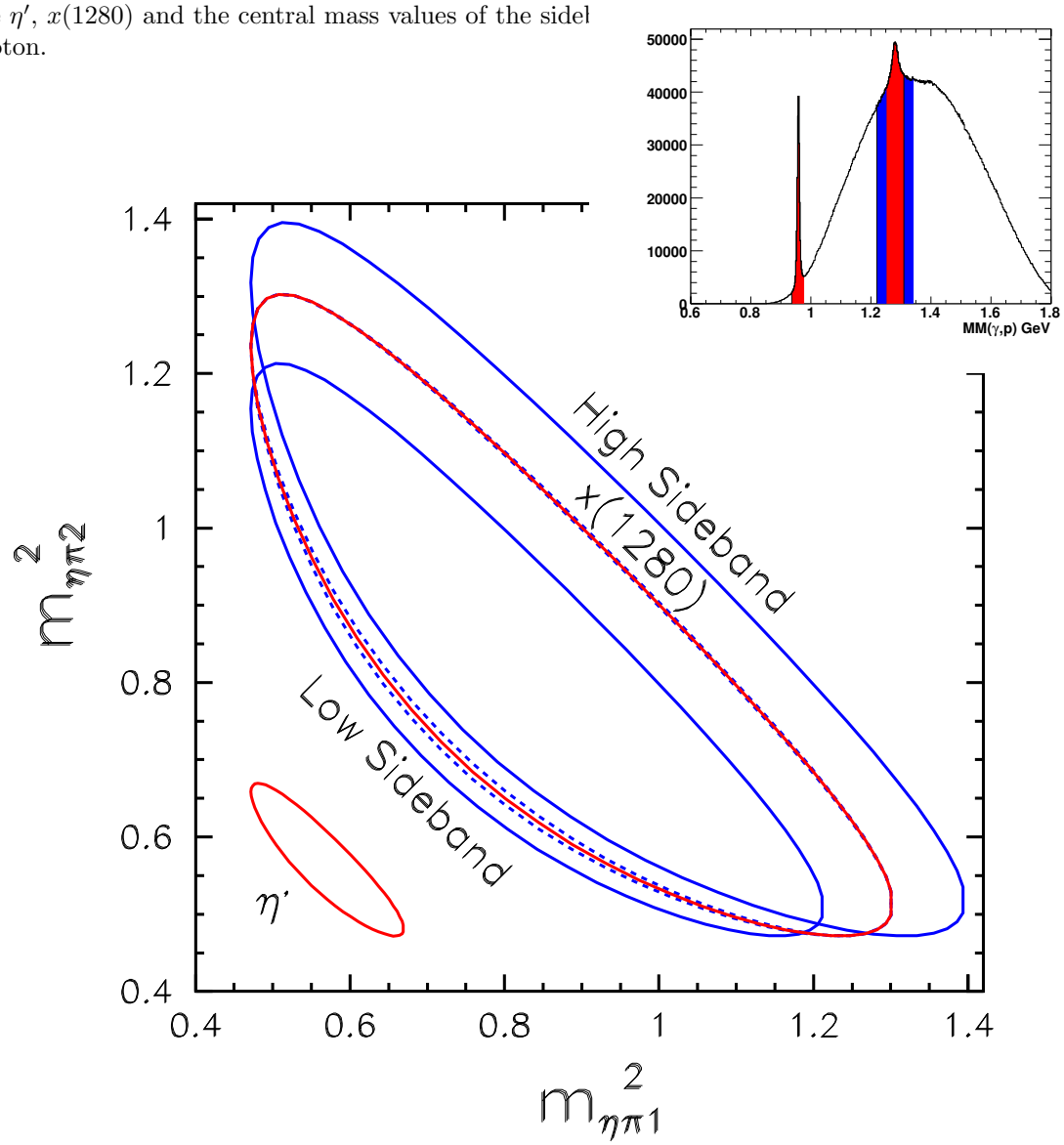

Figure 3.31: Kinematic phase space of several decays to $\eta\pi^+\pi^-$. Solid red curves show the phase space available from decaying η' and $x(1280)$ mesons. The solid blue curves outline the phase space region of events with missing mass off the proton in the 30 MeV/c^2 wide sidebands of the $x(1280)$. The dashed blue curves show the boundary of the sideband events after being transformed by our scaling method.

A particle decaying according to three-body phase space, where $\overline{|\mathcal{M}|^2}$ constant, uniformly populates the Dalitz plot, and this property permits the following method of sideband subtraction. The invariant mass combinations for a three body decay:

$$m_x \to m_i, m_j, m_k \tag{3.47}$$

are

$$m_{ij}^2 = (P_i + P_j)^2 = (P_x - P_k)^2 \tag{3.48}$$

$$(m_{ij}^2)_{\max} = (E_i^* + E_j^*)^2 - (\sqrt{E_i^{*2} - m_i^2} - \sqrt{E_j^{*2} - m_j^2})^2 \tag{3.49}$$

$$(m_{ij}^2)_{\min} = (E_i^* + E_j^*)^2 - (\sqrt{E_i^{*2} - m_i^2} + \sqrt{E_j^{*2} - m_j^2})^2 \tag{3.50}$$

$$\tag{3.51}$$

where E_i^* and E_j^* are the energies of the ith and jth particles in m_{jk} rest frame, given by equations,

$$E_i^* = \frac{m_{ij}^2 - m_i^2 + m_j^2}{2m_{jk}} \tag{3.52}$$

$$E_j^* = \frac{m_x^2 - m_{jk}^2 - m_j^2}{2m_{jk}} \tag{3.53}$$

with the maximum and minimum m_{ij}^2 values corresponding to the ith and jth particles being anti-parallel and parallel in the center-of-mass frame respectively. The local extrema of m_{ij}^2 as a function of m_{jk} simplify to the global extrema

$$(m_{ij}^2)_{\mathbf{max}} = (m_x - m_k)^2 \tag{3.54}$$

$$(m_{ij}^2)_{\mathbf{min}} = (m_i + m_j)^2 \tag{3.55}$$

The allowed boundary of $(m_{ij}^2)_{\min}$ and $(m_{ij}^2)_{\max}$ for $M_x = 1281$ MeV/c^2 appear as a guide on the Dalitz plots shown. Events outside this boundary must come from the high mass tail of the $x(1280)$and/or have incorrect momentum between the pion(s) and η.

Assuming our background is dominated by multi-pion events with no resonant structure in our chosen Dalitz axis variables, we can apply a linear transformation to each invariant mass combination to scale it to the values within the signal region.

Since a phase space decay results in a flat distribution, we performed a linear transformation on the m_{12}^2 and m_{23}^2 values of the sidebands while preserving the background shape.

To transform

$$m_{ij}^2 \Rightarrow m_{ij}'^2 \tag{3.56}$$

we utilize the range allowed as a function of the parent mass

$$\Delta m_{ij}^2 = (m_{ij}^2)_{\mathbf{max}} - (m_{ij}^2)_{\mathbf{min}} \tag{3.57}$$

$$\tag{3.58}$$

using a linear transformation of the form

$$m_{ij}'^2 = s(m_{ij}^2 - b) + b \tag{3.59}$$

where the slope s is given by

$$s = \frac{\Delta m_{ij}'^2}{\Delta m_{ij}^2} \tag{3.60}$$

$$s = \frac{(m_x' - m_k)^2 - (m_i + m_j)^2}{(m_x - m_k)^2 - (m_i + m_j)^2} \tag{3.61}$$

and b is simply the minimum value

$$b = (m_{ij}^2)_{\min} = (m_i + m_j)^2. \tag{3.62}$$

The transformation is applied event-by-event separately in $m^2_{\eta\pi^+}$ and $m^2_{\eta\pi^-}$ with the target mass

$$m'_x = m_x + d \tag{3.63}$$

where d is the difference in mass between center of the central region and the center of the relevant sideband. The dotted lines in Figure 3.31 show that the transformed sideband regions overlay the $x(1280)$ mass kinematic region quite well.

Finally, before combining the sidebands for subtraction they were weighted according to the background in missing mass off the proton. The integrated missing mass off the proton spectra was fit with the Voigtian signal for the $x(1280)$ and a 5th order polynomial for the background. The sideband Dalitz plots were filled according to the weight

$$w = \frac{B(m_x)}{B(m'_x)} \tag{3.64}$$

where $B(m)$ is the background polynomial evaluated at a given missing mass off the proton. This compensates for the slope of the background and slightly weights the high sideband more heavily as it has more background events (see inset of Figure 3.31). The effect of the weights is small and not terribly different than giving all sideband events equal weight but was seen to lessen "edge-effects" in the subtraction.

Figure 3.32 shows the Dalitz plot of the combined scaled sidebands. The kinematic coverage and gross features are quite similar to the central region shown earlier. Figure 3.33 shows the result of subtracting the scaled and weighted sideband events from those in the $x(1280)$ signal region. The $a_0(980)$ can been seen quite clearly now as bands in the resultant $x(1280) \to \eta\pi^+\pi^-$ Dalitz plot. The negative bins present are consistent with the counting statistics of the subtraction.

3.6.2 Acceptance in Dalitz Variables

Before measuring the $a_0(980)$ bands in the $x(1280) \to \eta\pi^+\pi^-$ Dalitz plot, we must correct for acceptance. As the axes, $m^2_{\eta\pi^+}$ and $m^2_{\eta\pi^-}$, are dependent upon differently charged pions, it is unlikely the acceptance will be flat over the entire plot. Our generated $x(1280)$ events yield a completely flat Dalitz plot, since we used phase-space decays as previously discussed in §3.4.1. Dividing the Dalitz plot of accepted Monte Carlo events by the raw generated distribution gives us our acceptance shown in Figure 3.34.

There are three notable features of the acceptance as a function of the Dalitz mass variables. Most obvious is the edge effect, the acceptance is highest at the very edge of the filled region. This effect is a consequence of our experimental mass resolution.

The raw Monte Carlo events were generated with $\Gamma_{x(1280)}$ of exactly 18 MeV/c^2, but the FWHM seen in the accepted events after detector simulation and analysis is of course broader, around 25 MeV/c^2 in the full spectrum. The effect in the Dalitz plot of the acceptance is an increase in the number of events in the low and high mass tails of the $x(1280)$ leading to higher acceptance in the fringe regions of the Dalitz plot which correspond to highest and lowest parent particle mass, as shown in the scaling equations earlier. We choose to suppress events from outside the kinematic boundary of the $x(1280)$ from further quantitative analysis.

Second, the acceptance of events falls off above $m^2_{\eta\pi^+}$ of 1.1 GeV^2. Above 1.2 GeV^2 the acceptance is less than one percent. This kinematic range would correspond with events with low momentum π^-'s, which bend towards the beamline in the magnetic field of the CLAS main torus and have lower acceptance than their positively charged counterparts. Finally, we note that the acceptance is higher along the lower boundary.

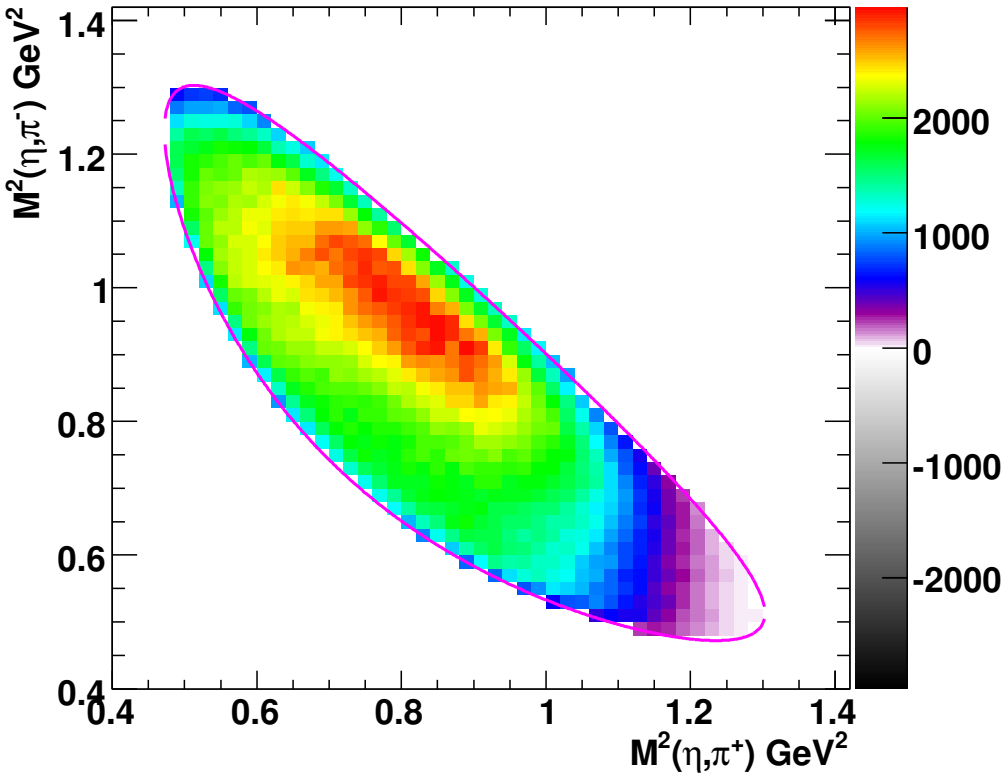

Figure 3.32: Dalitz plot for $\gamma p \to p\pi^+\pi^-\eta$ events with missing mass off the proton from 1221 to 1251 MeV/c^2 and from 1311 to 1341 MeV/c^2. Events have been weighted according to polynomial background fit and scaled according to linear transformation method according to equation 3.59.

The Dalitz plot for the $x(1280)$ after background subtraction and corrected for acceptance is shown in Figure 3.35. The $a_0^{\pm}(980)$ bands are similar in intensity. The lower right portion of the distribution has large bin-to-bin fluctuations as expected in light of the low acceptance for the kinematics of this region. There is a slight "edge-effect", an excess events along the edge of the allowed phase-space, that is especially noticeable along the low mass edge between the a_0 bands. A discussion of the systematics in light of these issues appears in the next chapter in §4.6.

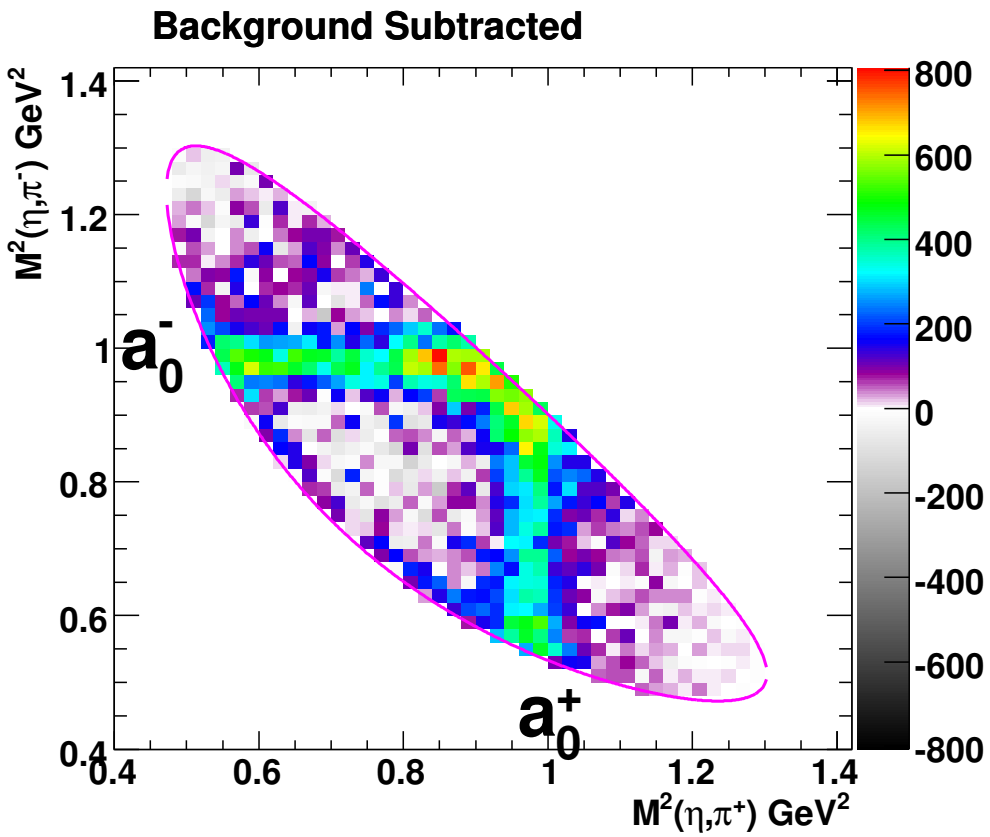

Figure 3.33: Dalitz plot for $x(1280) \to \eta\pi^+\pi^-$ events with missing mass off the proton between 1251 and 1311 MeV/c^2 after subtracting weighted and scaled sidebands. Data has not been corrected for acceptance in this plot.

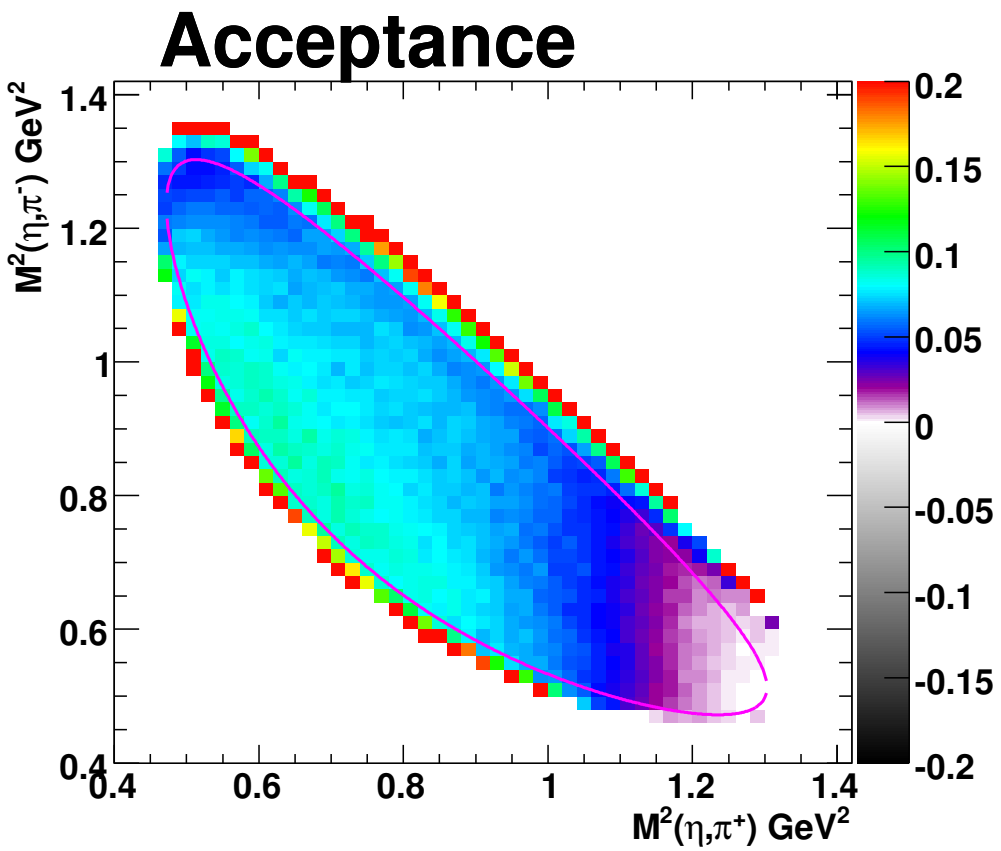

Figure 3.34: Acceptance of phase space Monte Carlo $x(1280)p \to p\pi^+\pi^-\eta$ events as a function of Dalitz variables $m^2_{\eta\pi^+}$ and $m^2_{\eta\pi^-}$. The magenta line is the kinematic boundary corresponding to 1280 MeV/c^2 parent particle. The z-axis color scale has been cutoff at 0.2 to suppress the unphysical high acceptance outside this boundary is an artifact of broadening of the $x(1280)$ due to experimental resolution of the CLAS detector.

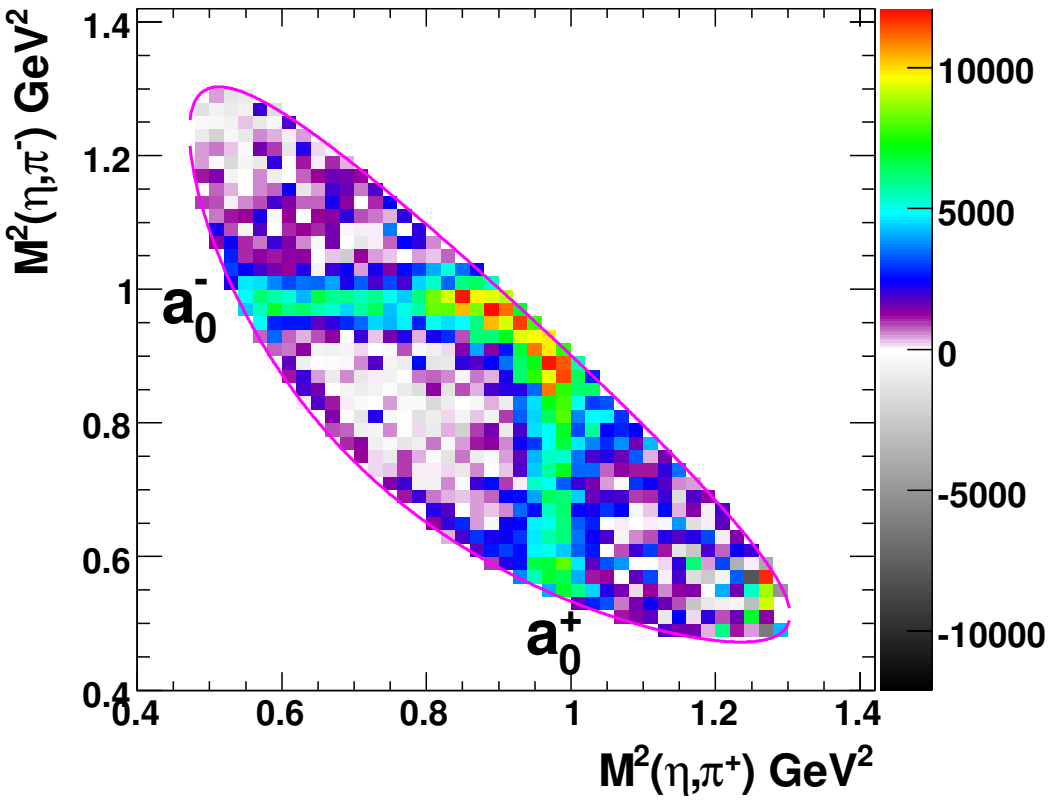

Figure 3.35: Background-subtracted and acceptance corrected Dalitz plot for $x(1280) \to \eta\pi^+\pi^-$. $a_0^-(980)$ and $a_0^+(980)$ are easily seen as horizontal and vertical bands, respectively. High counts in lower right of the plot are an artifact of low acceptance in that region.

Chapter 4

Systematics Studies

Though the *g11* dataset has been well-calibrated and corrections for known discrepancies have been implemented, there remains the possibility of effects of our measurement and analysis methods introducing bias into our results. This chapter will describe studies performed to estimate the systematic errors on the properties of the $x(1280)$ meson measured in this analysis.

We compare the signal loss for the η' and $x(1280)$ mesons through our analysis cuts between the experimental data and Monte Carlo events. The stability of yield fits with regard to the fit conditions were studied. The precision of our acceptance calculation was tested as well. The possible biases introduced in our Dalitz background scaling and subtraction methodology was also studied.

We will present a summary of discrepancies between our measurements of the preceding chapter. We will describe studies performed to investigate additional sources of bias and estimations of overall systematic uncertainties seen in combining the results of different methods and decay channels.

4.1 Event Selection in Data vs. Monte Carlo

To determine if there are any systematic biases and/or uncertainties arising from our event selection methodology we compare between data and Monte Carlo the fraction of signal lost at each cut. The signal for the $x(1280)$ meson is comparatively weak, so we chose to use the η' signal for these tests. Using events for run 43582, we fit the η' signal in the missing mass off the proton at each selection step to a Gaussian plus fourth-order polynomial background function. The events at this stage have already been loosely skimmed to have a missing mass near that of the neutral decay product for the decay mode being studied so there should be little contamination from other decay modes of the η' meson. This was confirmed through a Monte Carlo test that showed a negligible number events being skimmed into the wrong mode.

4.1.1 Confidence Level Cuts

The covariance matrix used in kinematically fitting both the data and Monte Carlo assumes Gaussian errors. Energy loss and multiple scattering include a small number of hard scatters off the nucleus rather than the electrons, giving events which do not follow a Gaussian distribution. Our cut on the probability of an event kinematically fitting our chosen particle hypothesis has the possibility of introducing significant systematic bias if our Monte Carlo does not adequately describe the detectors' response to these events.

Figure 4.1 shows the η' mass peak obtained from events from the "++-" skim in run 43582 in the $\eta\pi^+\pi^-$ and $\rho^0\gamma$ decay modes. The unshaded histogram contains "all" the events (after the loose cuts used detailed in §3.1.3), while the shaded histogram contains only the events which pass a 10% confidence level cut when kinematically fit to $\gamma p \to p\pi^+\pi^-(missing)$, where *missing* is either

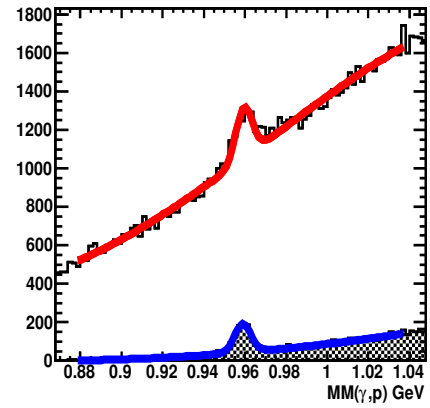

(a) CL cut $\eta\pi^+\pi^-$

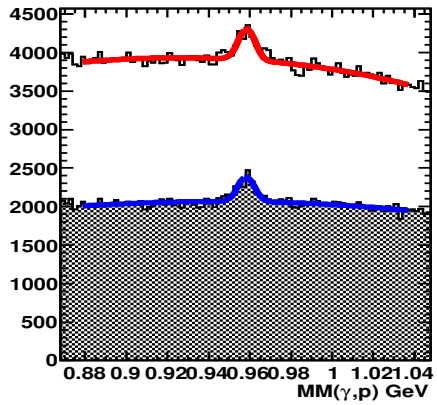

(b) CL cut $\rho^0\gamma$

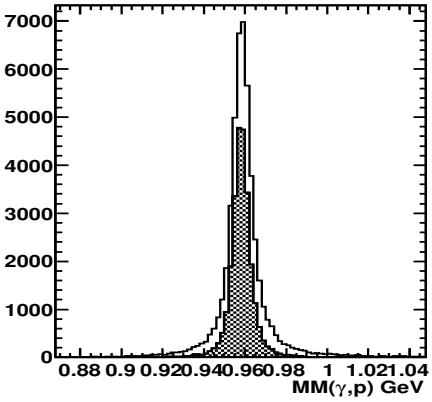

(c) CL cut MC $\eta\pi^+\pi^-$

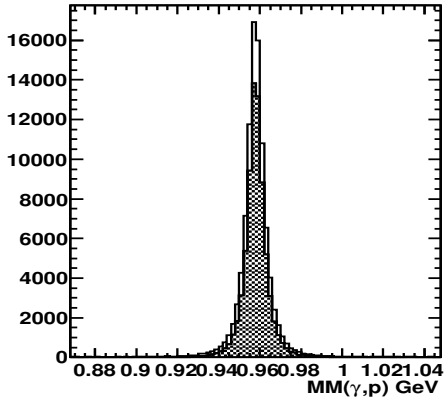

(d) CL cut MC $\rho^0\gamma$

Figure 4.1: Missing mass off the proton for $\eta' \to \eta\pi^+\pi^-$ and $\rho^0\gamma$ showing events cut by CL cut for run 43582 in (a) and (b) and Monte Carlo in (c) and (d). The red and blue curves are the fits used to extract the signal before and after the cut respectively.

the undetected η or γ. In each case, the number of signal events can be extracted by fitting both distributions to a Gaussian plus a fourth degree polynomial. The 10% confidence level cut keeps 56.4% of the $\eta\pi^+\pi^-$ signal events. For the Monte Carlo, we can simply count the number of events kept when applying the confidence level cut, giving a fraction kept of 53.2%. The cut does not simply remove 10% of the events because we have iterated over the two possible particle assignments for the positively charged tracks, so the total number of events has been doubled.

The agreement for events with a missing γ is not as good. The 10% confidence level cut keeps 79.3% of the $\rho^0\gamma$ signal events. For the Monte Carlo, this fraction is lower at 76.6%. It is plausible that despite only keeping the event combination with the best photon, that events with out-of-time tracks are still passing the 1-C fit. The correction and assignment of systematic uncertainty from these fractions will be discussed in §4.1.4.

In both cases there are roughly three percent more signal events kept in the data after the confidence level cut than in the Monte Carlo. The large amount of signal lost at this stage is expected as we have simply chosen events by charge and have not yet applied any further particle identification criteria to our initial sample to reject duplicate events created by looping over all combinations of photons and mass assignment.

4.1.2 Time of Flight Cuts

As shown in Chapter 3, many background events still remain after the confidence level cut was applied. To reject mis-identified particles and event combinations we considered ΔTOF, the difference between the measured time-of-flight of the particle through CLAS and the ideal time for its measured momentum, trajectory, and the mass assigned by its identity.

$p\pi^+\pi^-$ detected

Figure 4.2 shows the signal loss of η' events due to our ΔTOF cuts for $\eta\pi^+\pi^-$ and $\rho^0\gamma$ decay modes. These timing cuts were chosen to cut as few signal events as possible, as evident in the Monte Carlo, in which 99.1% of the $\eta\pi^+\pi^-$ and 98.3% of the $\rho^0\gamma$ events pass the selection criteria. For the data, some signal events are lost, with 93.2% of the $\eta\pi^+\pi^-$ and 95.4% of the $\rho^0\gamma$ signals remaining after the cuts. Some of the signal events which are cut are genuine η' events with poor timing information that is not adequately reproduced in the Monte Carlo. Other events which are cut are events where the positively-charged tracks have been mis-identified. These "combinatoric" background events would have ideally all been cut by requiring only the PID combination with the best probability as evident in the Monte Carlo case. However, in the data the correct PID combination does not always yield a better kinematic fit, as there are multiple candidate photons and out-of-time tracks which are not simulated in GSIM. As with the CL cuts we will use these numbers later in calculating an overall systematic uncertainty for event selection.

4.1.3 Missing $P_\perp$ Cut and Missing π^0 event rejection

For $\rho^0\gamma$ events we required two more selection criteria. First, to reject $p\pi^+\pi^-$ events with no photon we required at least 40 MeV/c in missing transverse momentum, as detailed in §3.2.3. Second, to reject $p\pi^+\pi^-$ events with a missing π^0 we ran an additional kinematic fit and cut those events which passed the π^0 hypothesis at $CL > 0.01$. Figures 4.3a and 4.3b show the effect of these cuts on the η' signal in run 43582 and Monte Carlo events.

The cut on missing transverse momentum keeps 97.8% of the data signal and 97.1% for the Monte Carlo, an excellent level of agreement. The π^0 cut keeps 85.4% of the η' signal while only keeping 78.7% of the simulated events. It is possible that this disagreement is a sign the physics of the $x(1280) \to \rho^0\gamma$ decay is quite different than the simple phase-space calculation employed by our Monte Carlo event generator.

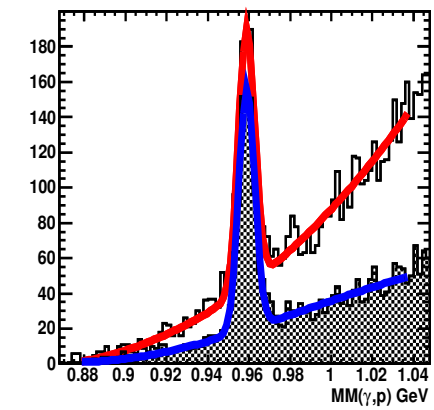

(a) ΔTOF cut $\eta\pi^+\pi^-$

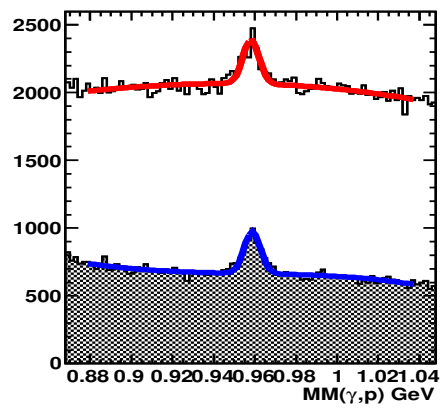

(b) ΔTOF cut $\rho^0\gamma$

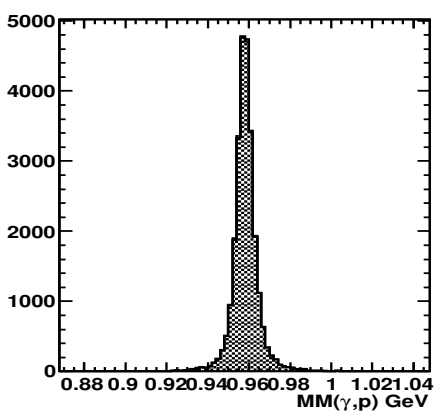

(c) ΔTOF cut MC $\rho^0\gamma$

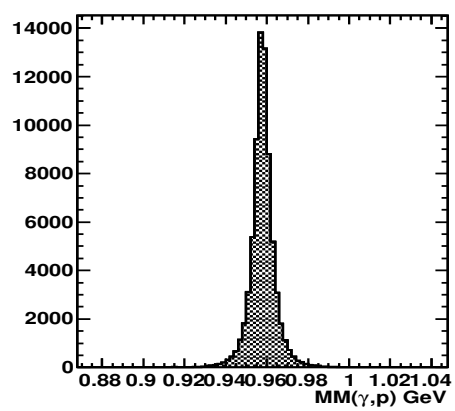

(d) ΔTOF cut MC $\eta\pi^+\pi^-$

Figure 4.2: Missing mass off the proton for $\eta' \to \eta\pi^+\pi^-$ and $\rho^0\gamma$ showing events cut by ΔTOF cut for run 43582 in (a) and (b) and MC in (c) and (d). The timing cuts were chosen to cut few signal events. The red and blue curves are the fits used to extract the signal before and after the cut respectively.

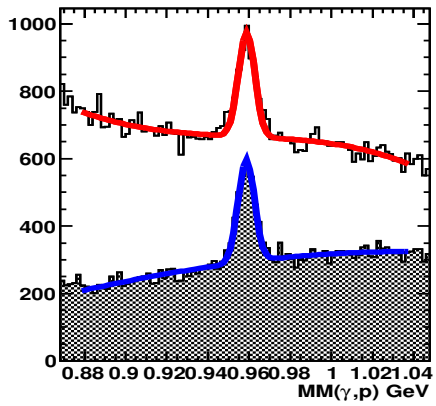

(a) Missing $P_\perp$ cut $\rho^0\gamma$

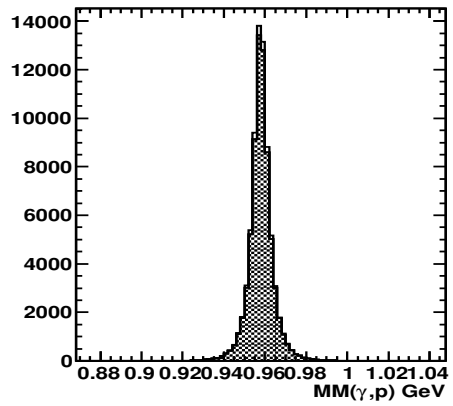

(b) Missing $P_\perp$ cut MC $\rho^0\gamma$

Figure 4.3: Missing mass off the proton for $\eta' \to \rho^0\gamma$ showing events cut by transverse momentum cut for run 43582 (a) and MC (b).The red and blue curves are the fits used to extract the signal before and after the cut respectively.

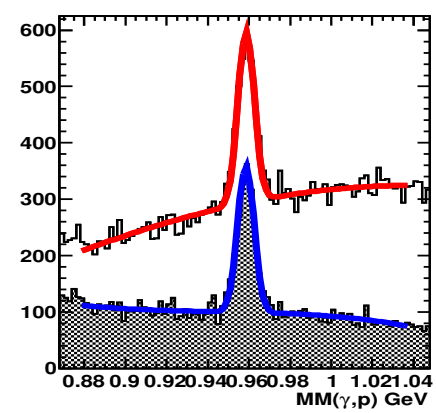

(a) Missing π^0 CL cut $\rho^0\gamma$

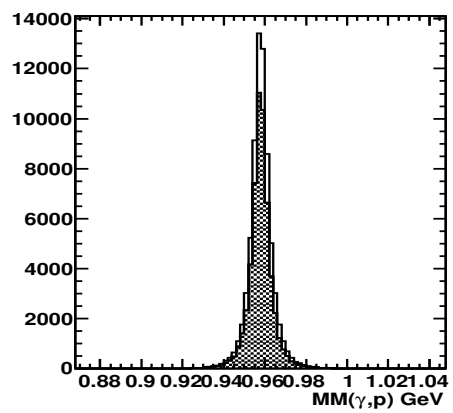

(b) Missing π^0 CL cut MC $\rho^0\gamma$

Figure 4.4: Missing mass off the proton for $\eta' \to \rho^0\gamma$ showing events cut by Missing π^0 CL cut for run 43582 (a) and MC (b).The red and blue curves are the fits used to extract the signal before and after the cut respectively.

Cut	$\eta\pi^+\pi^-$	$\rho^0\gamma$
Confidence Level	1.061	1.036
ΔTOF	0.941	0.966
Missing $P_\perp$	NA	1.006
Missing π^0 rejection	NA	1.086
Cumulative Agreement	0.998	1.093

Table 4.1: Summary of systematic effects found in events selection in $\gamma p \to p\eta\pi^+\pi^-$ and $\gamma p \to \rho^0\gamma$. These values are the ratio of η' signal kept by each of our analysis cuts to that expected from Monte Carlo. The final row is overall ratio in signal loss between data and expected.

$pK^\pm\pi^\mp$ detected

There is no comparison in the η' case for the $K^\pm K^0\pi^\mp$ decay mode. We will therefore use the same value as that obtained for the $\eta\pi^+\pi^-$ case for our systematic uncertainty due to cuts in this channel.

4.1.4 Summary of Analysis Cuts

We have calculated the discrepancy in signal-loss from our analysis cuts between the data and our Monte Carlo simulation. The overall agreement is quite good in the $\eta\pi^+\pi^-$ decay mode of the η' with the cumulative agreement of 0.2% as listed in Table 4.1. Our selection of events for the $\rho^0\gamma$ decay mode requires additional cuts to further remove background reactions from the data. The data and Monte Carlo agree well in response to the Missing $P_\perp$ cut. The rejection of missing π^0 events through kinematic fitting greatly improves our signal-to-background fraction enough to make $x(1280)$ yield measurement possible. However, the comparison of the η' signal-loss shows that the Monte Carlo does not reproduce the data well in this case. The simulated $\eta' \to \rho^0\gamma$ events lose 9.3% more events than seen in data, as shown in Table 4.1. This loss will be included in our calculation of the branching ratio $\Gamma(\rho^0\gamma)/\Gamma(\eta\pi\pi)$ as both a scale factor in the numerator and in the systematic uncertainity. We can get a better measure of this effect, however, by comparing the η' differential cross section obtained independently for the two decay modes, using the entire dataset.

4.2 Yield Extraction for the $x(1280)$

Due to the large multi-pion background present in our data, we used two different methods to extract the yield of the $x(1280)$ meson in the $\eta\pi^+\pi^-$ decay mode. As Figure 3.8 in the previous chapter showed, the background is peaked at roughly the same location as the signal being fit. The first method used is a fit to a Voigtian signal lineshape plus polynomial background function, while the second method employs $x(1280)$ signal Monte Carlo along with a set of simulated multi-pion backgrounds.

The second method resulted in systematically lower yields leading to lower differential cross sections with larger uncertainties on the yield parameter as seen in earlier in Figures 3.28a-3.28e. Before considering how to best combine these results, we survey the individual systematic studies performed.

4.2.1 Voigtian Fit Method

To test the stability and robustness of the yields obtained via our first method, Voigtian Fitting, we varied the fit conditions imposed. Through varying the order of the polynomial background and the range of missing mass off the proton bins included in the fit we obtain an estimate of the systematic uncertainty of this method.

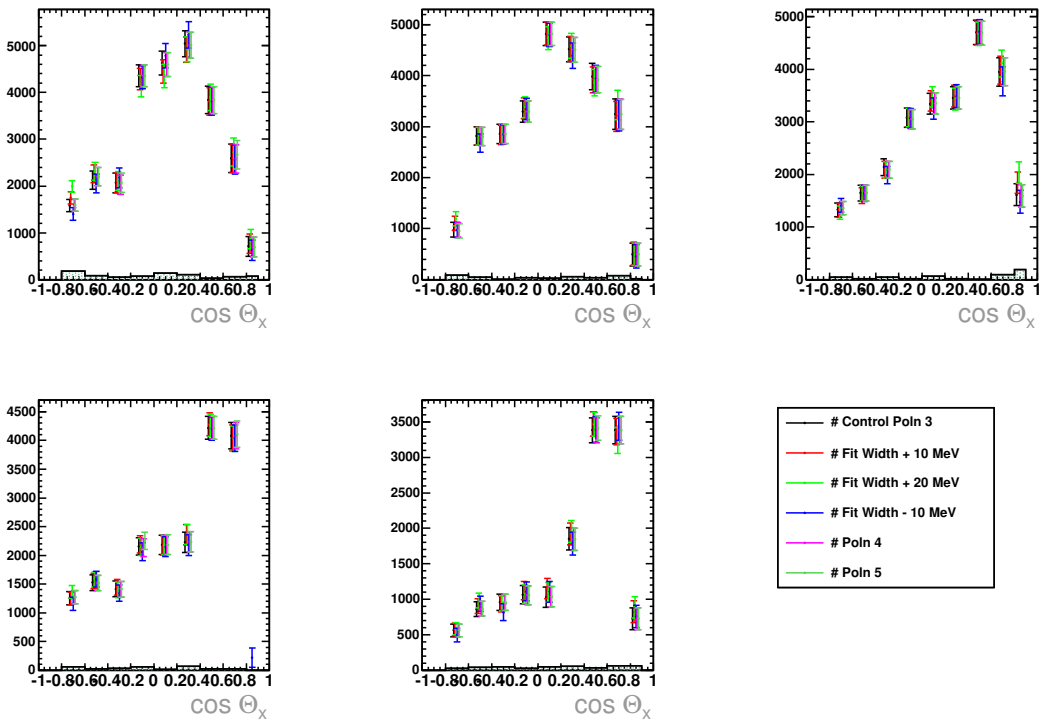

Figure 4.5: Variation of $x(1280) \to \eta\pi^+\pi^-$ yield for a range of missing mass off the proton used and order of background polynomial. Shaded histogram along bottom edge is the standard deviation between the fit versions described in the text.

$\eta\pi^+\pi^-$

We tested five variations on our fitting conditions for $x(1280) \to \eta\pi^+\pi^-$, originally described in §3.2.1. We varied the range of missing mass off the proton bins included in the fit by -10 MeV, $+10$ MeV and $+20$ MeV. We also increased the background polynomial to 4th and 5th order. Figure 4.5 shows the variation of $x(1280)$-yield obtained from these versions along with the original. The figure also indicates standard deviation between the fits. Figure 4.6 shows the fractional systematic error along with the mean value for each W bin, computed excluding the forward-most angle bin. The low statistics of forward-most and backward-most angles leads to larger variation in yields that is also seen in their statistical errors, rather than an effect f our choice in fit conditions. This estimate gives an average uncertainty from 1.9 to 4.1% of the yield of $x(1280)$ in $\eta\pi^+\pi^-$.

We also obtained estimates of the systematic uncertainty on the mass and width via this technique. The standard deviation of mass values was 0.2 MeV/c^2, the same size as the statistical error reported by the MINUIT fitter. The width Γ had a standard deviation of 0.8 MeV/c^2. As the width values were also over-dispersed for the reported error bars we apply the normalized chi-square statistic as a conservative scale factor. This gives us a systematic error of 1.4 MeV/c^2 on the width of the $x(1280)$.

$K^\pm K^0\pi^\mp$

For the $x(1280) \to K^\pm K^0\pi^\mp$ case, we again varied the fit range and polynomial background from our original conditions in the same manner as above. Figure 4.7 shows the resulting variation in

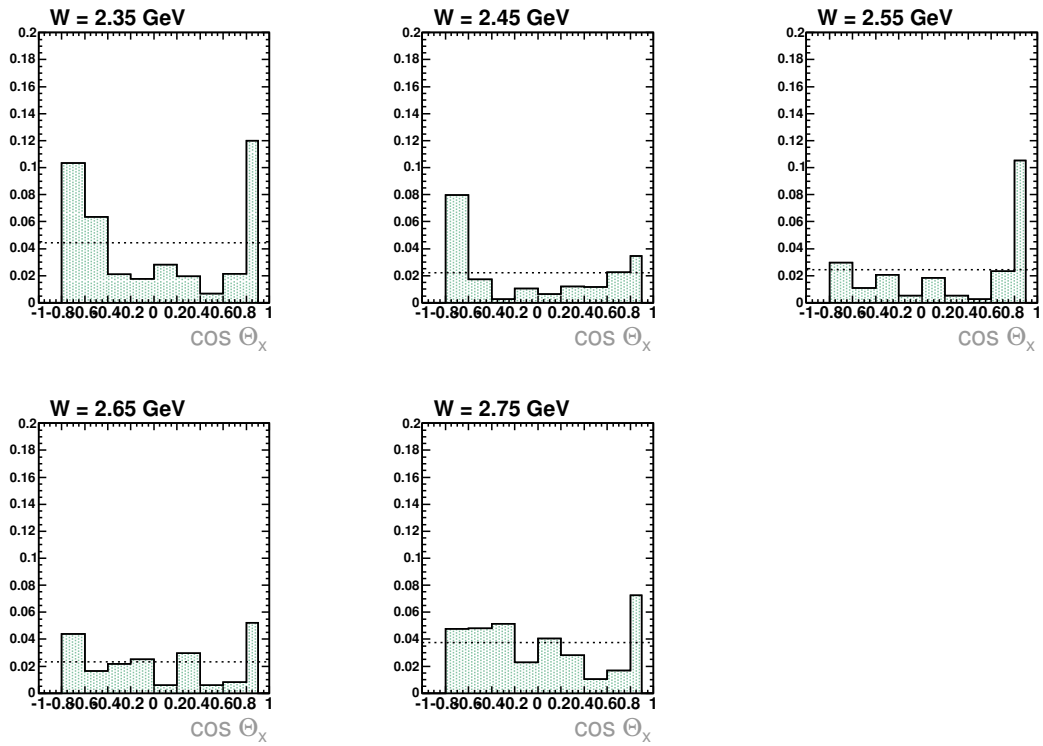

Figure 4.6: Fractional systematic uncertainty of $x(1280) \to \eta\pi^+\pi^-$ Voigtian yields. Dashed line shows the average value for the given bin.

Systematic Uncertainty (fractional)		
W (GeV)	$x(1280) \to \eta\pi^+\pi^-$	$x(1280) \to K^\pm K^0\pi^\mp$
2.35	0.041	0.032
2.45	0.022	0.030
2.55	0.026	0.022
2.65	0.018	0.022
2.75	0.040	0.057

Table 4.2: Summary of systematic uncertainties for the yield of $x(1280)$ to the given final states.

yield obtained from these version along with the original, again the standard deviation is indicated. The fractional uncertainty for $K^\pm K^0\pi^\mp$ channel was found to be higher than for $\eta\pi^+\pi^-$ as seen in Figure 4.8. Our estimate gave an average uncertainty from 2.2 to 5.7% of the yield of $x(1280)$ in $K^\pm K^0\pi^\mp$. Table 4.2 lists the values of these yield systematic error estimates for the $\eta\pi^+\pi^-$ and $K^\pm K^0\pi^\mp$ channels.

$\rho^0\gamma$

For $x \to \rho^0\gamma$, the signal to background was too small to allow binning in center-of-mass energy and production angle so only a total yield was extracted. The width and mass were fixed to the best values found from the $\eta\pi^+\pi^-$ fits while the Gaussian width σ, in the Voigtian function was fixed to the experimental resolution of 4.2 MeV, determined from analysis of $x(1280)$ Monte Carlo events.

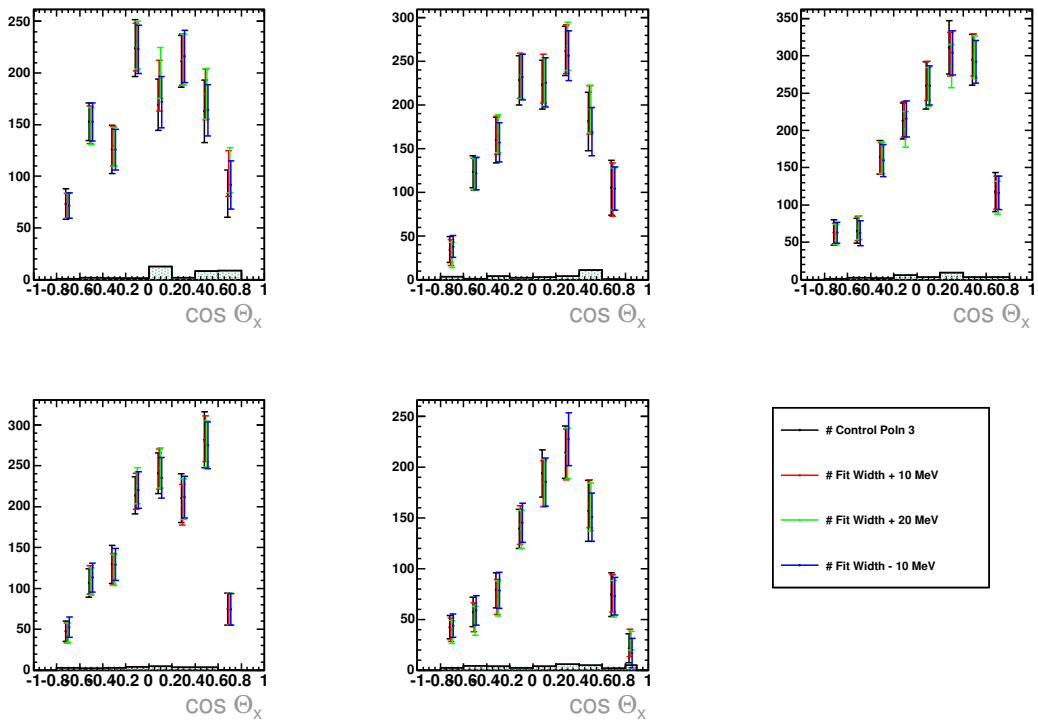

Figure 4.7: Variation of $x(1280) \to K^{\pm}K^{0}\pi^{\mp}$ yield for a range of missing mass off the proton used and order of background polynomial. Shaded histogram along bottom edge is the standard deviation between the fit versions described in the text.

To test the robustness of the small signal to changes, we varied the fitting range and the order of the polynomial background used in the fit. Figure 4.9 shows the result of these studies.

The standard deviation of the yield values was found to be 849 or 22.4% of the $x(1280) \to \rho^{0}\gamma$ yield.

4.2.2 Simulated Background Method

The simulated-background method detailed in §3.2.2 of the previous chapter gave lower yields with larger errors for almost all energy and angle bins. As seen earlier in Figures 3.28a to 3.28e, the differential cross sections calculated from this method agree with to the values obtained via the Voigtian yield fits within the given error bars of the two methods. Therefore, we did not perform a separate systematic uncertainty estimate for this method as we will be combining the results and including the half the difference between them as a systematic error included in the final uncertainties for the differential cross sections for $x(1280) \to \eta\pi^{+}\pi^{-}$.

4.3 Normalization

Several prior analyses of ω [54] and η' [55] photoproduction from the g11a dataset have studied, in detail, systematic errors affecting the normalization of yields for cross section calculation. We performed a similar study to see if our results were comparable.

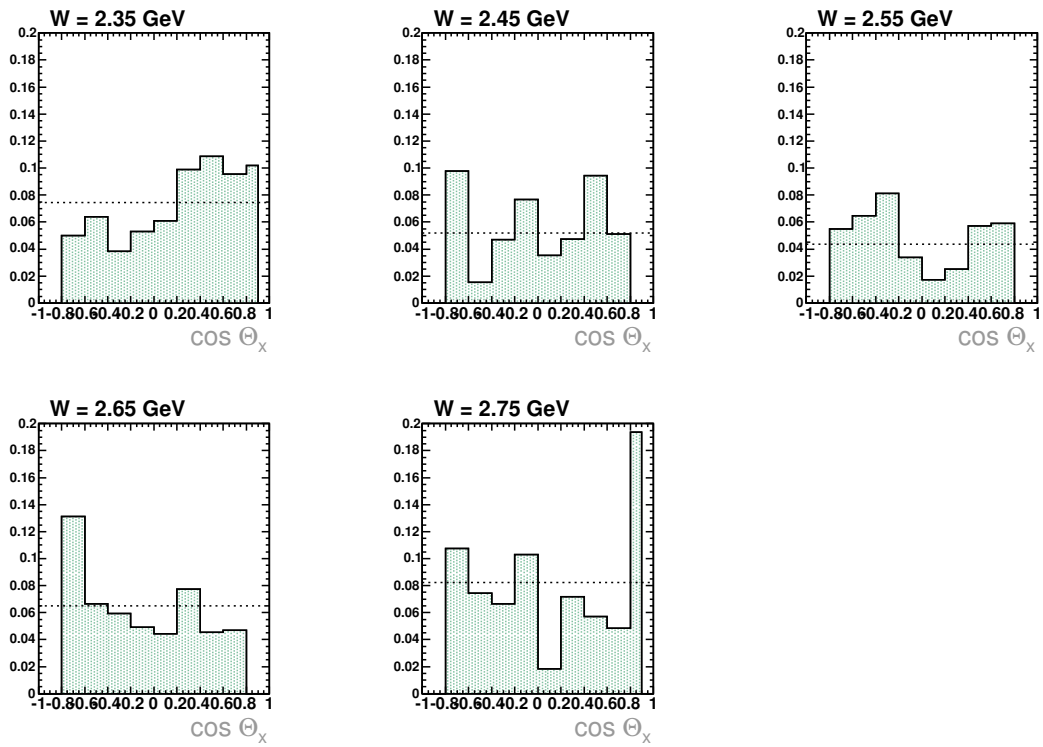

Figure 4.8: Fractional systematic uncertainty of $x(1280) \to K^{\pm}K^{0}\pi^{\mp}$ Voigtian yields. Dashed line shows the average value for the given bin.

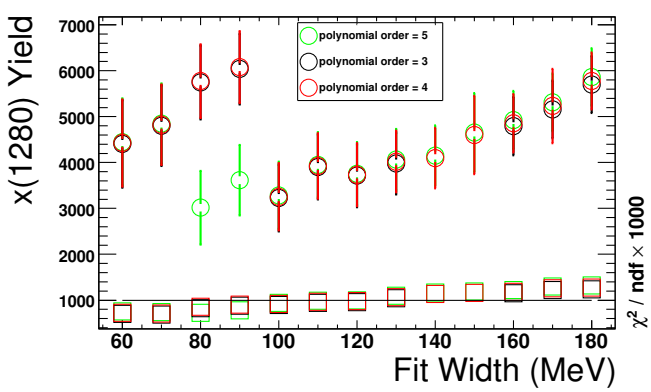

Figure 4.9: Variation of $x(1280) \to \rho^{0}\gamma$ yield (circles) as a function of the range of the fit in missing mass off the proton for three different polynomial backgrounds. The normalized χ^2 (squares) is shown multiplied by one thousand for plotting.

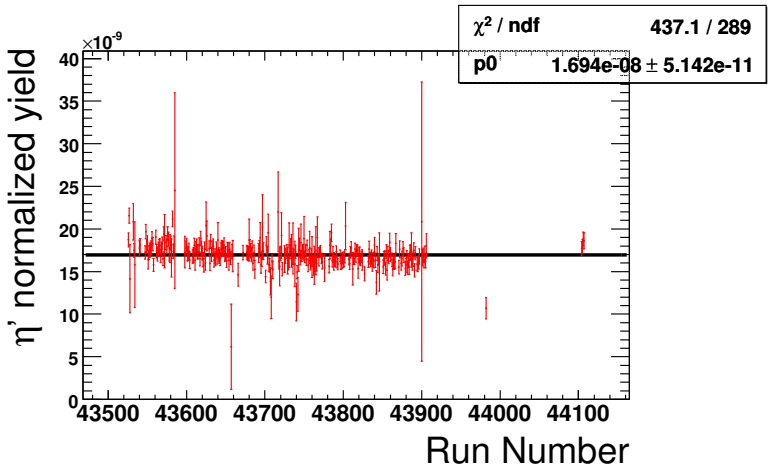

Figure 4.10: Integrated η' yield measured run-by-run as normalized by the photon flux calculated via the gflux routine. The normalization is quite stable over the course of runs used in this analysis. The standard deviation is 0.55%.

4.3.1 Photon Flux

To estimate the systematic uncertainty due to the calculation of photon flux, we studied the variation of η' yield in the $\eta\pi^+\pi^-$ channel normalized by the photon flux for each production run in the g11 dataset. The η' was chosen since the $x(1280)$ signal was too small to split into many individual runs. Figure 4.10 shows the resultant normalized yields.

The mean normalized yield was found to be 1.694x10^{-8} with standard deviation of 0.551%. This is smaller than the value of ∼1.8% found for the ω by M. Williams [40]. In our version we calculated a single yield per run integrated over a the entire energy range, and we also have not applied any correction for the un-triggered photons below $W \sim 1.956$ GeV. However, comparison of cross sections in $p\omega$, $K\Lambda$, and $p\eta$ final states extracted from g11a to previous world data including the earlier CLAS g1c dataset led the authors in Refs. [54] and [55] to assign a more conservative value for the flux normalization uncertainty. The g1c dataset used a single track trigger, and had both a lower end point energy and beam current. This comparison assigned a systematic uncertainty of 7.3% on the photon flux normalization and we adopt this value for this analysis.

4.3.2 Live-time Correction

We must also consider the effect of the live-time correction on our normalization. As discussed in §3.3.3, we apply a correction to the scalar clock live-time portion of photon flux calculation for this analysis. Through study of the dependence of flux-normalized yields versus beam current, M. Williams [40] found the uncertainty due to this correction to be ∼ 3%. Combining in quadrature the photon normalization uncertainty of 7.3% quoted earlier with an uncertainty of 0.2 to 0.5% due to photon attenuation [56] and the 3% uncertainty on the live-time gives us an overall systematic uncertainty for normalization of 7.9%.

4.4 Acceptance

The acceptance of the CLAS detector calculated using GSIM can be a source of significant systemetic error should the simulation not accurately reproduce the efficiency. As noted in §3.1.5, an extensive

empirical study of the reaction $\gamma p \to p\pi^+\pi^-$ was performed at CMU [49]. The study showed that for many kinematic regions of the detector, the efficiency of simulated events was higher than for the real data.

4.4.1 $\eta\pi^+\pi^-$ and $K^\pm K^0\pi^\mp$ Channels

To set a lower bound on the additional systematic uncertainty we utilize the symmetry of the CLAS detector. The systematic uncertainty from our acceptance calculation can be determined through the independence of the six sectors of the CLAS detector. The physics of the reaction studied in this analysis is azimuthally symmetric, allowing us to calculate differential cross-sections independently for each sector, according to the detected proton. The momentum of proton maps directly to the η' and $x(1280)$ values W and $\cos\Theta_{CM}$. To have sufficient statistics to utilize this method we use the decay modes of the η', which will further be compared with published data in the following chapter.

We calculate our estimate of systematic uncertainty such that the distribution of the deviation

$$\Delta(W, \cos\Theta_{CM}) = \frac{y - \bar{y}}{\sqrt{(\sigma_{sys}^2 + \sigma_y^2)}} \tag{4.1}$$

appoaches a normal distribution with a width

$$\sigma_\Delta \simeq \frac{n-1}{n}, \tag{4.2}$$

where $(n-1)/n$ is the number of degrees of freedom divided by the number of points included in the weighted mean (5/6 for most bins). This modification takes into the account of the loss of a degree of freedom in calculating the mean. If the statistical errors on the points are sufficient then no additional error is required.

Figure 4.11 shows $d\sigma/d\Omega$ for $\eta' \to \eta\pi^+\pi^-$ calculated for each sector of the CLAS detector. The level of agreement is quite reasonable given the lower statistics of the divided event sample. The standard deviation of points follow the distribution well, as will be seen more easily in the normalized versions.

Figure 4.12 shows $d\sigma/d\Omega$ for $\eta' \to \eta\pi^+\pi^-$ normalized to the average value. There is no strong angular dependence seen in the level of agreement. While normalization exposes some extreme values due to holes in CLAS acceptance, the mean value of the deviation is still reasonably small in each bin.

Figure 4.13 shows the deviation of the normalized cross sections from the weighted mean before and after addition the listed systematic uncertainties.

Table 4.3 lists the fractional systematic uncertainty obtained from the method for each W bin. We will also use these values as our systematic uncertainty for the $K^\pm K^0\pi^\mp$ channel as it contains no reference signal to use like the η'.

4.4.2 $\rho^0\gamma$

The acceptance value we use to correct our yield of $x(1280) \to \rho^0\gamma$ events is not binned in energy and angle. Due to the integration of events over a very wide kinematic space, this value is quite senstive to any discrepency in the between the physics of the reaction and the distribution of generated Monte Carlo events. As discussed in § 3.4.1, our $x(1280)$ Monte Carlo event generator did not simulate the dynamics of photoproduction of the mesons. It did include the Bremmstrahlung photon energy distribution and an adhoc t-slope. We generated a new sample of Monte Carlo events distributed according to the measured differential cross section to test for any systematic error in our $x(1280) \to \rho^0\gamma$ acceptance. The original Monte Carlo acceptance of $x(1280) \to \rho^0\gamma$ was 2.98% and the value for the new empirical version is 2.48%. We adopt the new value for our branching ratio results in the next chapter and use the difference between the versions as an estimate of the systematic uncertainty on this acceptance.

W GeV	Fractional Uncertainty
2.35	0.11
2.45	0.08
2.55	0.08
2.65	0.11
2.75	0.09

Table 4.3: Systematic uncertainty for $\eta\pi^+\pi^-$ acceptance estimated from sector dependent η' cross sections.

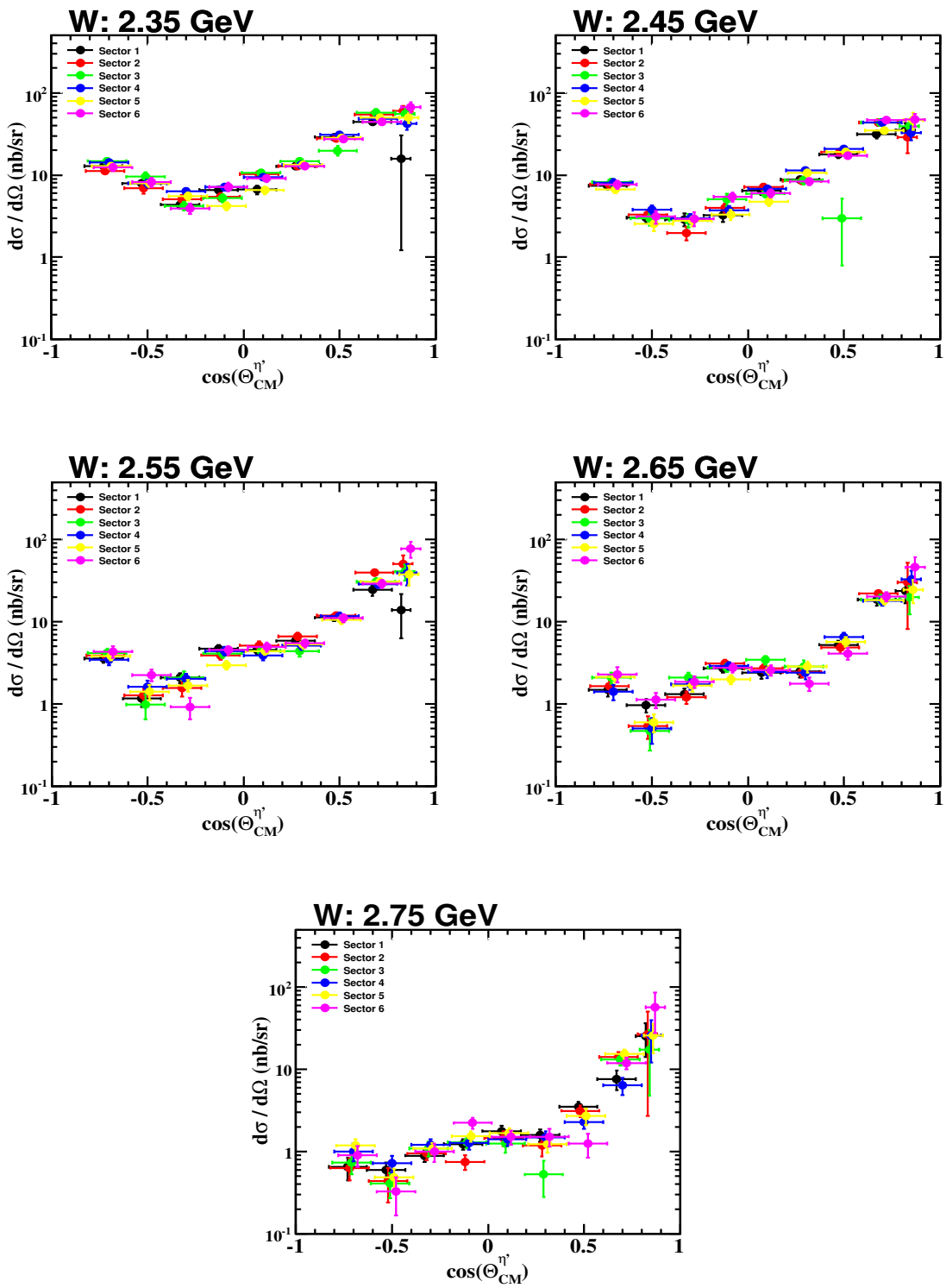

Figure 4.11: $d\sigma/d\Omega$ for η' in $\eta\pi^+\pi^-$ decay mode calculated independently for each sector of CLAS. Shaded histogram represents standard deviation between the six sectors per $\cos\Theta^{\eta'}_{CM}$ bin.

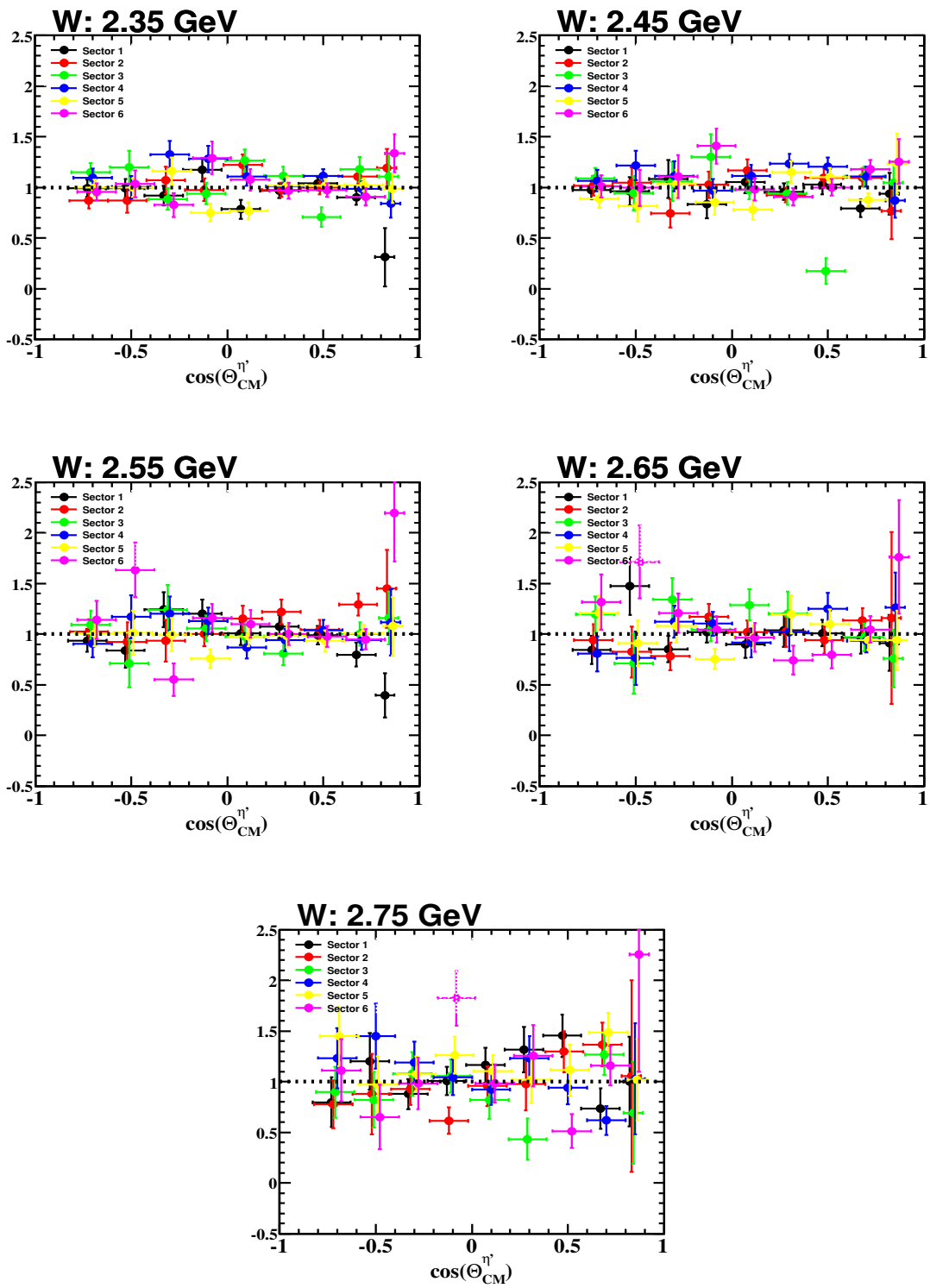

Figure 4.12: $d\sigma/d\Omega$ for η' in $\eta\pi^+\pi^-$ decay mode for each sector of CLAS normalized to the mean value. Shaded histogram represents our estimate of the systematic uncertainty between the six sectors per $\cos\Theta^{\eta'}_{CM}$ bin. Dashed lines at unity and the mean uncertainty for the given W bin.

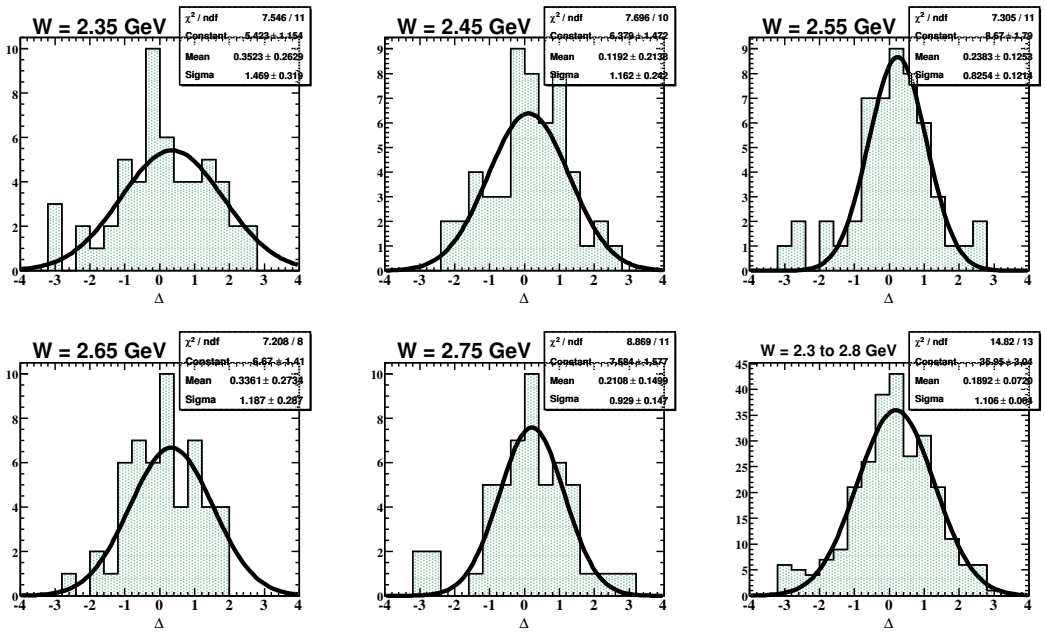

(a) Before added systematic uncertainty

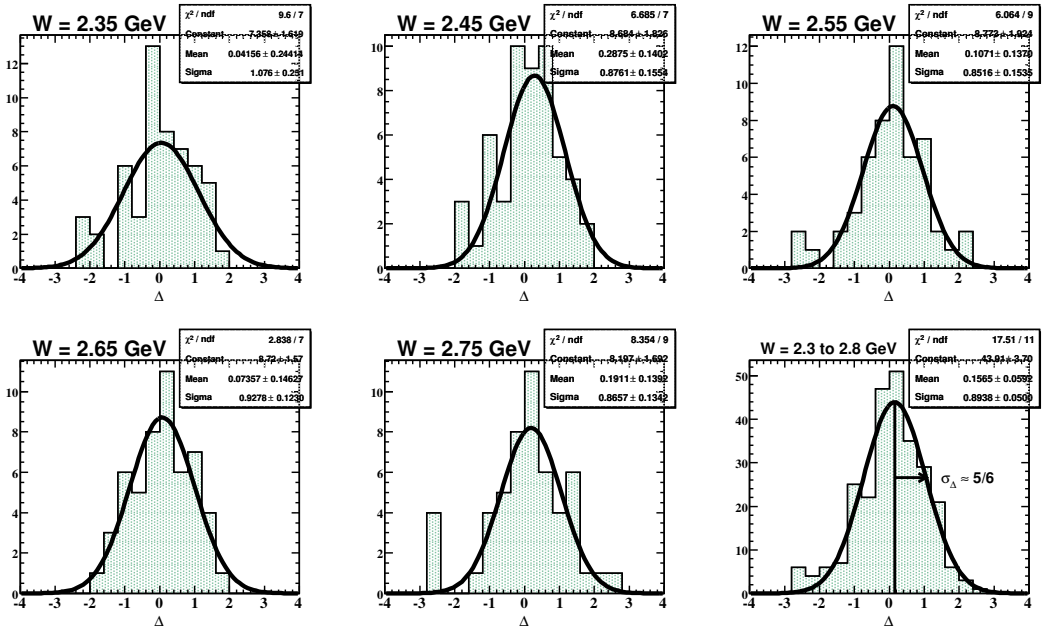

(b) After added systematic uncertainty

Figure 4.13: Deviation of the normalized differential cross sections for η' from the weighted mean (a) before and (b) after additional systematic error in Eq. 4.1. The assigned systematic uncertainties are listed in Table 4.3.

4.5 Differential Cross Sections

Our final method of estimation of systematic uncertainty is obtained by comparing the results from the different decay modes. Through comparing these independent measurements we can look for any additional systematic effects not accounted for in the previous tests.

Though we do not have sufficient statistics to measure differential cross sections for $x(1280) \rightarrow \rho^0\gamma$, the comparison of our measurements of $d\sigma/d\Omega$ for η' in the $\eta\pi^+\pi^-$ and $\rho^0\gamma$ decay modes is still useful as an estimate of systematic bias in the acceptances of these final states. Such a bias must be accounted for in calculating the branching fraction $\frac{\Gamma_x(\rho^0\gamma)}{\Gamma_x(\eta\pi^+\pi^-)}$. Figure 3.27 in the previous chapter shows our measured cross sections. We find the $d\sigma/d\Omega$ for η' calculated from $\rho^0\gamma$ measurements to be 5% higher than the results of our $\eta\pi^+\pi^-$ measurements. This effect is smaller than the 9.3% systematic uncertainty due to the missing π^0 rejection cut discussed earlier. That study only utilized data from one run and was integrated over all W and $\cos\Theta_{CM}$. We apply the value from comparing cross sections as the better estitmate of of systematic uncertainty in our branching fraction ratio calculations for the $x(1280)$.

To extract yields for $x(1280) \rightarrow \eta\pi^+\pi^-$ we utilized two fitting procedures as detailed in §3.2, a Voigtian profile with polynomial background and a combination of Monte Carlo simulation of the $x(1280)$ signal and with several different simulated background templates. As Figures 3.28a-3.28e showed the second method produced systematically lower and less precise yields on the whole. To calculate our final results for $x(1280) \rightarrow \eta\pi^+\pi^-$ differential cross sections, we take the weighted mean of these methods at each point. Figures 4.14a-4.14e present the combined $\eta\pi^+\pi^-$ values along with half the difference between the methods.

We were also able to extract $x(1280)$ yields from the combined missing mass off the proton spectra of the $K^+\pi^-(K^0)$ and $K^-\pi^+(K^0)$ decay modes solely through fits with the Voigtian signal plus polynomial background method. Figure 4.15 shows the differential cross sections for $\gamma p \rightarrow x(1280)\, p \rightarrow K^\pm K^0 \pi^\mp$ scaled by the relative branching fraction obtained through a single parameter fit to the $\eta\pi^+\pi^-$results.

4.6 Dalitz Analysis

Our Dalitz Analysis of the $x(1280) \rightarrow \eta\pi^+\pi^-$ decay has several steps that may introduce sizable systematic effects in the final result. The sidebands have been scaled in the Dalitz variables to account for the shift in kinematic coverage as a function of the mass of the parent particle. The choice of missing-mass-off-the-proton ranges selected for the $x(1280)$ and its sidebands can lead to some amount of signal over-subtraction, as portions of the tails of the peak are subtracted from the the central region. Finally, the choice of how to weight the sidebands in relation to central region will have an effect as the kinematics may differ between the low and high sidebands even after corrected for mass scaling.

4.6.1 Sideband Scaling

We first tested our technique of sideband scaling using a "toy" Monte Carlo test, without CLAS acceptance . Three million events were generated with a signal-to-background ratio approximating that seen in the $\gamma p \rightarrow p\pi^+\pi^-(\eta)$ data. Both the $x(1280)$ signal and background $\eta\pi^+\pi^-$ events were generated according to 3-body phase space. The sidebands of the $x(1280)$ were scaled in the Dalitz mass variables, $m^2_{\eta\pi^+}$ and $m^2_{\eta\pi^-}$, according to Equation (3.59) detailed in the previous chapter. The sideband events are then subtracted from the central band of events having missing mass off the proton between 1251 and 1311 MeV/c^2. This mass range is wide enough to produce a noticeable edge effect on the Dalitz plot, events lying outside the kinematic limit for a missing mass off the proton of 1281 MeV/$c^2$are cut like those in the full analysis.

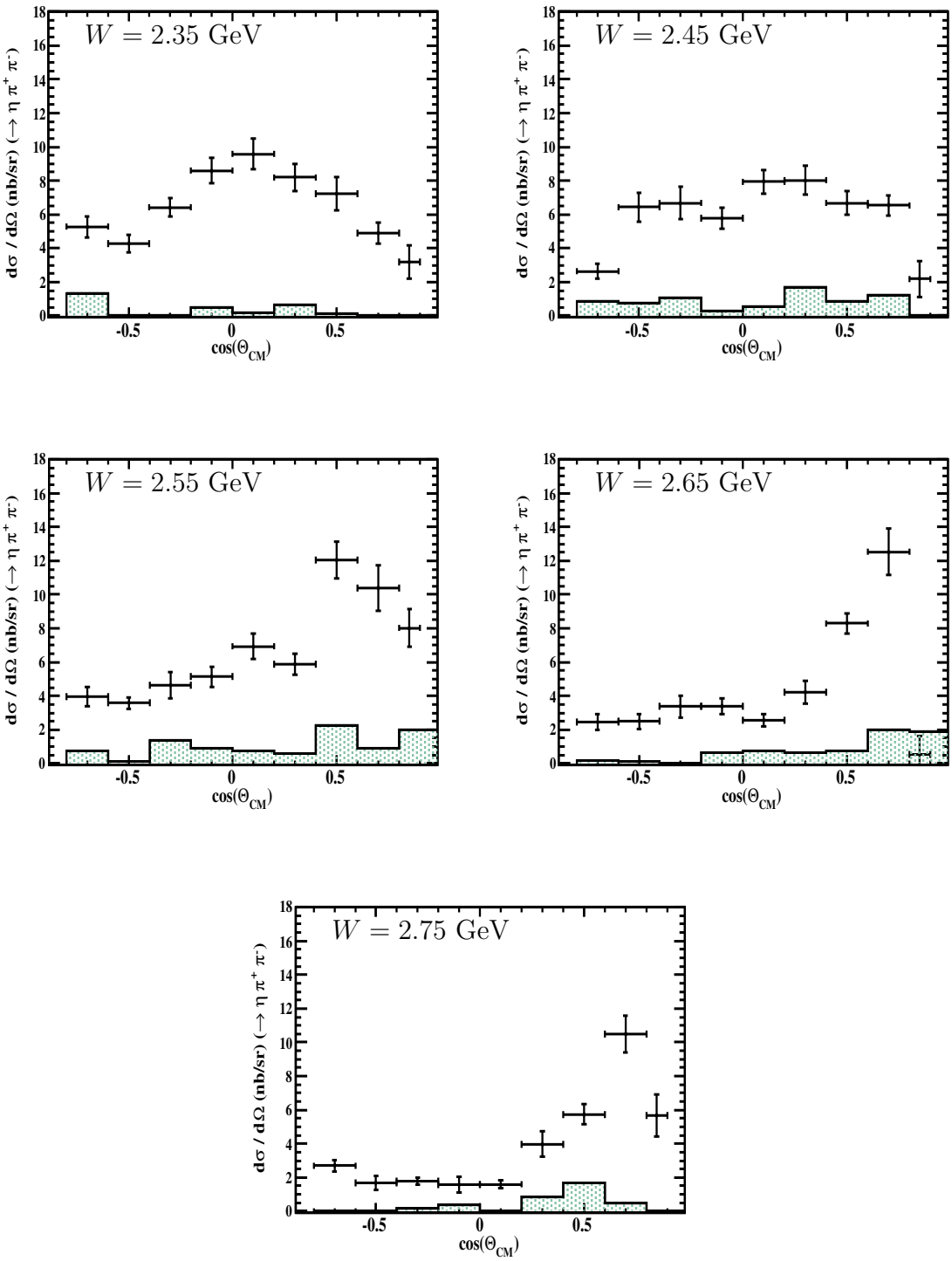

Figure 4.14: $d\sigma/d\Omega$ for $\gamma p \to x(1280)p \to p\eta\pi^+\pi^-$. Black data points are weighted mean of two yield extraction methods: a fit to Voigtian signal with polynomial background and fitting the missing mass off the proton spectrum with several Monte Carlo reactions representing the signal and several background channels. Shaded histogram is half the difference between the two methods. Points without an entry in the histogram were obtained through only one of the two methods.

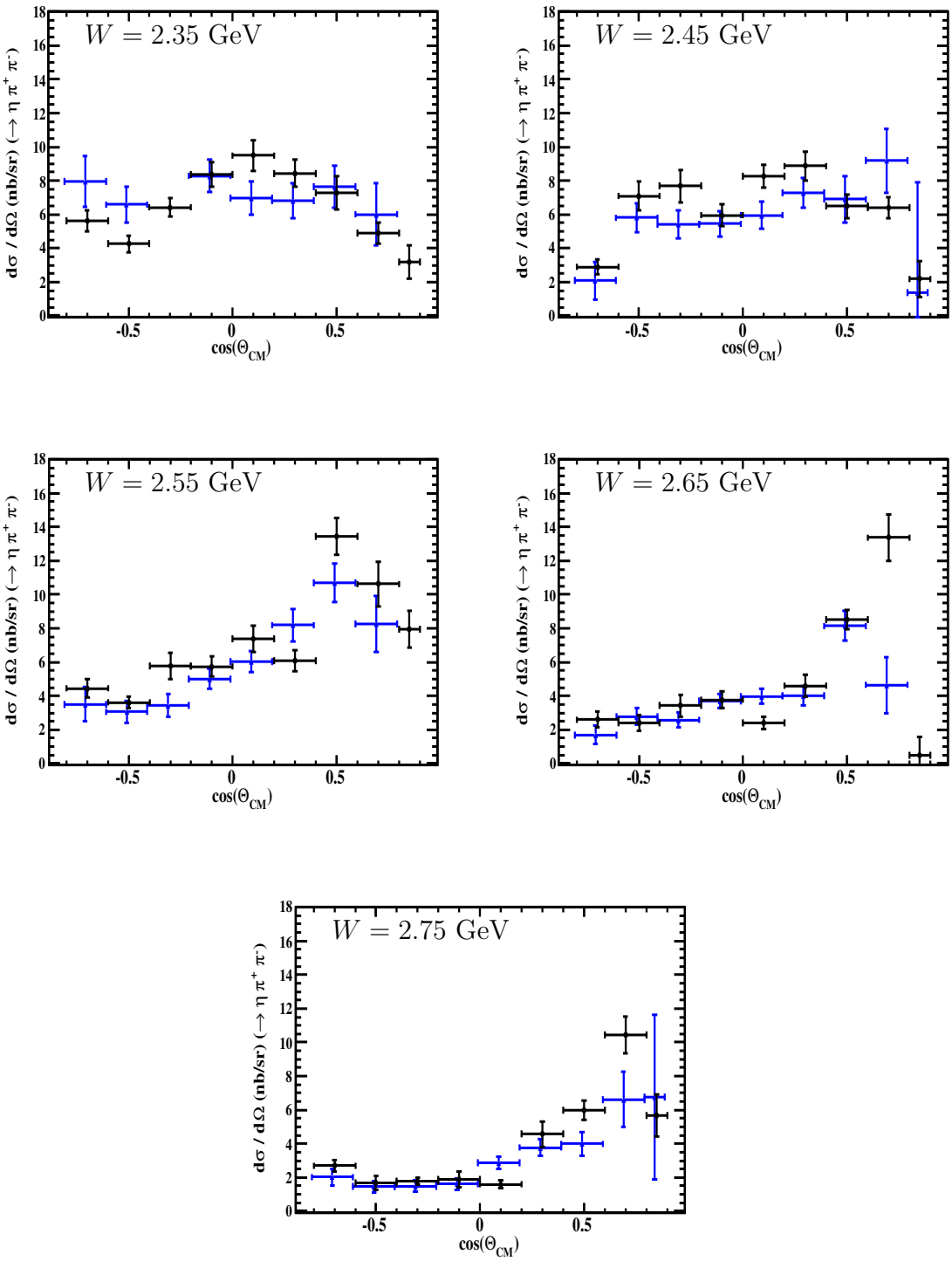

Figure 4.15: $d\sigma/d\Omega$ for $\gamma p \to x(1280)p \to p\eta\pi^+\pi^-$(black) and $\to K^\pm K^0\pi^\mp$(blue). $K^\pm K^0\pi^\mp$ results have been scaled by our measured relative branching fraction $\frac{\Gamma(K^\pm K^0\pi^\mp)}{\Gamma(\eta\pi^+\pi^-)}$.

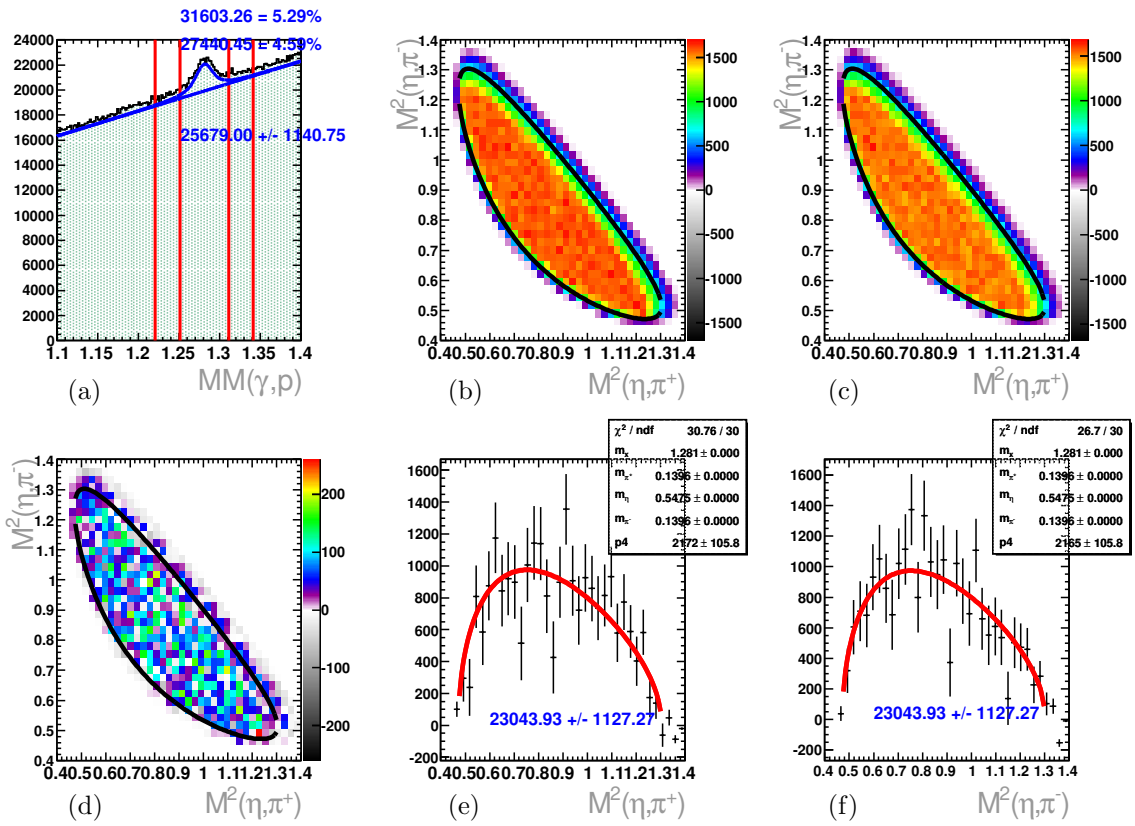

Figure 4.16: Toy Monte Carlo $x(1280) \rightarrow \eta\pi^+\pi^-$ showing the effects of our background scaling and subtraction technique. The generated missing mass off the proton spectrum (a) using $\sim 5\%$ s/b. Low (b) and high (c) sideband Dalitz plots show the flatness of the scaling technique, seen further in the background-subtracted signal (d). After the scaling and subtraction we recover the flat phase space decay used for our toy model signal as seen in comparison of the 1-D projections (e,f) of the background-subtracted Dalitz plot shown fit to phase space shape.

The resulting Dalitz plot, seen in Figure 4.16 along with the projections along both axes, does not significantly distort the phase-space events. The projections have good χ^2 when fitted with a function representing the allowed "width" of the Dalitz region. The integral of the subtracted plot yields 11.4% fewer events as a result of events outside the kinematic boundary being trimmed, 23044 events compared to 25679 events from background subtraction in the missing mass off the proton spectrum.

4.6.2 Sideband Selection

Finally, we examine the choice of mass ranges in missing mass off the proton used for the $x(1280)$ and its sidebands and the exact method of subtraction. As seen in the discussion of the toy model, there is some signal present in the sideband regions from the tails of the $x(1280)$. This leads to a calculable over-subtraction of events. While it is desirable to reduce this amount by widening the central region this has the trade-off of reducing the signal-to-background ratio and increasing the total range of background kinematics, thus reducing somewhat the applicability of our assumption that the kinematics of background events in the sideband regions is similar to that in the $x(1280)$ peak region. The dependence of our results on these choices was tested by varying the range of

the mass bands as well as introducing an offset between the $x(1280)$ band and sidebands. We also tested the weighting of the sidebands, starting with a simple equal weighting, variable weighting, and finally a point-by-point weighting based on a functional representation of the background.

Choosing the width of the $x(1280)$ region and its sidebands in missing mass off the proton for Dalitz analysis required balancing two competing effects. A larger central band of signal kept improves the statistics for measuring $a_0^{\pm}\pi^{\mp}$ signal. The further away from the centroid of the $x(1280)$ one goes, any distortion from the scaling procedure and/or changing kinematics of the background events becomes more evident. Table 4.4 lists the signal kept after subtracting the sidebands of the

Central Band	Sideband	Offset	Signal Fraction	Note
60MeV/c^2	60MeV/c^2	none	66.7%	noticable edge effect
80MeV/c^2	40MeV/c^2	none	77.4%	noticable edge effect
60MeV/c^2	30MeV/c^2	none	70.0%	best version, used for final results
60MeV/c^2	30MeV/c^2	15MeV/c^2	74.6%	good, but with larger edge effect

Table 4.4: Widths of missing mass off the proton bands used in background subtraction of Dalitz plots of the $x(1280)$. The first two columns are the widths of the signal region and sidebands. The third column is a separation region between the sidebands and the central band. The signal fraction is calculated through integration of a Voigtian profile of the $x(1280)$ and subtracting the tail regions in the sidebands. Introducing an offset to our best result improves the statistics slightly but has a larger edge effect.

mass regions tested and the quality of the the resulting Dalitz plots, which are shown in Figure 4.17. We looked to improve signal kept while reducing distortion in the form of under- or over-subtraction along the edge of the plot. A larger mass has more phase space available, so a wide range of mass results in a "fuzzy" rather than sharp cutoff at the edge. This "edge effect" is true for the sidebands as well, leading to under-subtraction along the edge for wider sidebands. We tested several configurations of widths of the mass bands and found the best result choosing 60 MeV/c^2 wide central region for the $x(1280)$, with 30 MeV/c^2 wide lower and upper sidebands.

Finally to look for any additional biases in our Dalitz procedure we ran our analysis on 10 million $\gamma p \to p\rho^0\pi\pi$ Monte Carlo events. This was one of the generated backgrounds used in our $x(1280)$ yield measurements in $\eta\pi^+\pi^-$. As Figure 4.18 shows, the raw Dalitz distribution is not flat, but after scaling, weighting, and subtracting the sidebands and then correcting for acceptance we are left with a flat Dalitz plot consistent with zero signal events as better seen in slices of the distribution in Figures 4.19 and 4.20. These figures show the $\gamma p \to p\rho^0\pi\pi$ Monte Carlo events in slices of $M^2(\eta, \pi^{\pm})$ along with the χ^2 per degree of freedom for each slice with the line at zero. The consistency of both the toy model and this Monte Carlo simulation leads us to conclude the values for the $a_0(980)\pi$ versus non-resonant $\eta\pi\pi$ are not significantly biased by our background-subtraction method.

4.7 Summary

We have performed a number of studies to estimate the systematic uncertainties on our measurements. The application of these values to our measurements will be shown in the next chapter in our final results.

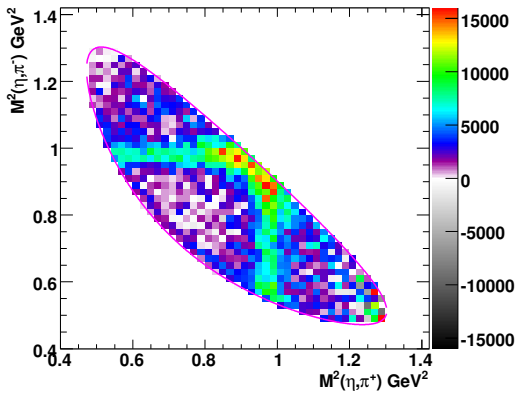

(a) 60MeV/c^2 : 60MeV/c^2

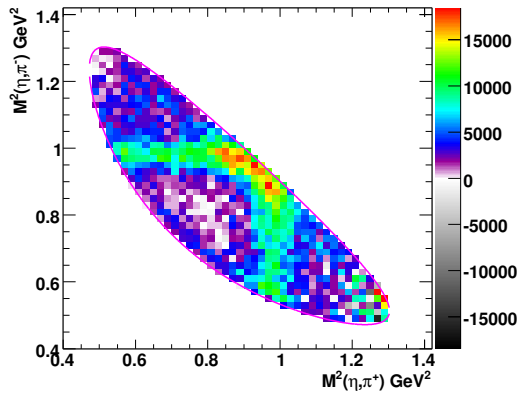

(b) 80MeV/c^2 : 40MeV/c^2

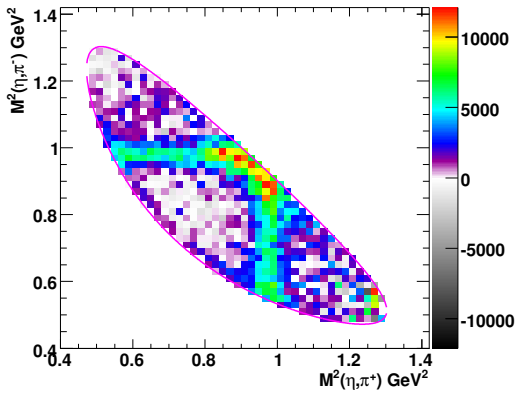

(c) 60MeV/c^2 : 30MeV/c^2

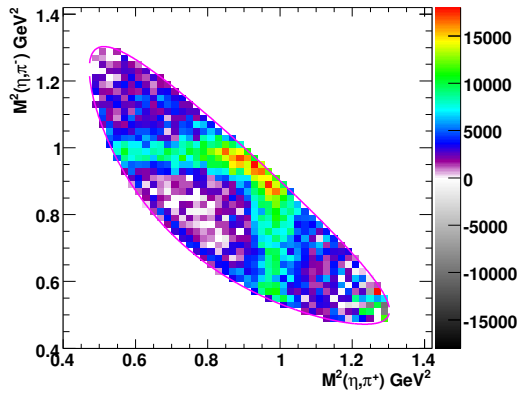

(d) 60MeV/c^2 : 30MeV/c^2 offset by 15MeV/c^2

Figure 4.17: Dalitz plot for $x(1280) \to \eta\pi^+\pi^-$ events with missing mass off the proton for various choices of signal- and sideband. The band widths are denoted as **central** : **side**. Note that version (c) was chosen for our final results as it had the minimal distortion along the edges of the plot.

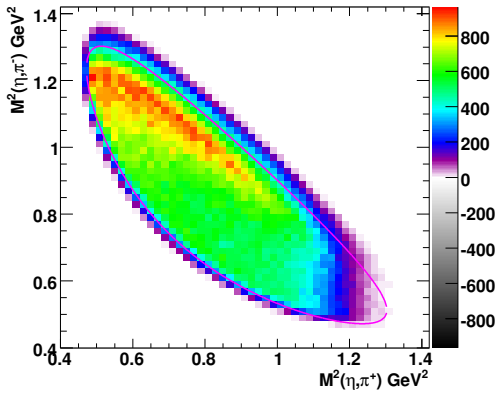

(a) $\gamma p \to p\rho^0\pi\pi$

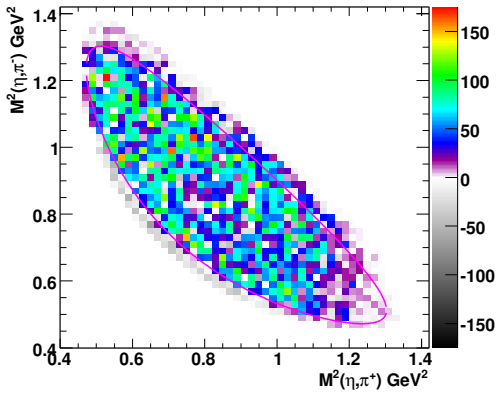

(b) background subtracted

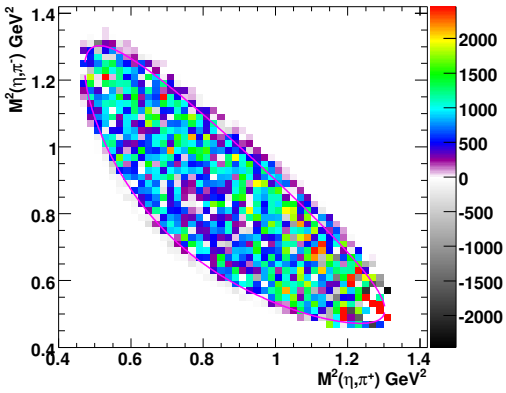

(c) acceptance corrected

Figure 4.18: Dalitz plot for Monte Carlo simulated background $\gamma p \to p\rho^0\pi\pi$ events with missing mass off the proton between 1251 and 1321 MeV/c^2. Events that have passed all of our analysis cuts for selecting $x(1280) \to \eta\pi^+\pi^-$ reaction(a), after applying our background scaling and subtraction technique(b), acceptance correction(c).

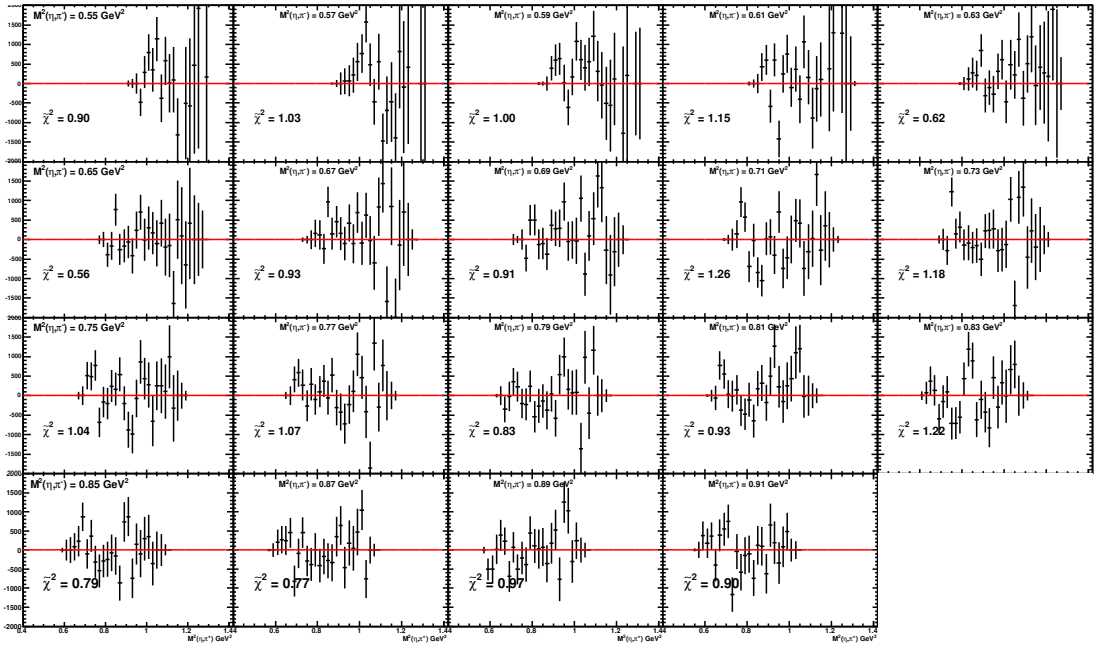

Figure 4.19: Monte Carlo $\gamma p \rightarrow p\rho^0\pi\pi$ in $M^2(\eta,\pi^+)$ for various slices of Dalitz distribution in $M^2(\eta,\pi^-)$. The slices are consistent with zero as indicated by the errors and given χ^2/ndf values.

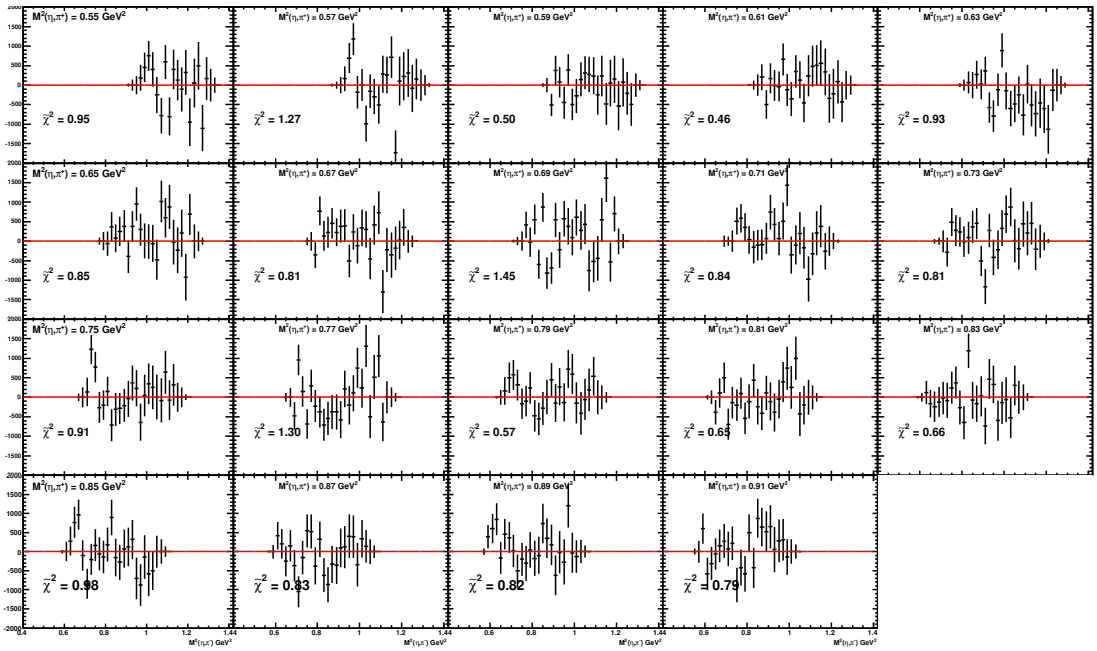

Figure 4.20: Monte Carlo $\gamma p \rightarrow p\rho^0\pi\pi$ in $M^2(\eta,\pi^-)$ for various slices of Dalitz distribution in $M^2(\eta,\pi^+)$.The slices are consistent with zero as indicated by the errors and given χ^2/ndf values.

Chapter 5

Results and Discussion

In the preceding chapters we have described our methods for measuring several properties of the reaction $\gamma p \to x(1280)p$ in the *g11* dataset in several final states, where the $x(1280)$ is shorthand for the candidate meson states, $f_1(1285)/\eta(1295)$. We have extracted yields in $\eta\pi^+\pi^-$, $K^+K^0\pi^-$, $K^-K^0\pi^+$ and $\rho^0\gamma$ decay modes. We have performed an analysis of the $\eta\pi^+\pi^-$ decay in terms of the Dalitz variables $m^2_{\eta\pi^+}$ and $m^2_{\eta\pi^-}$. We have measured the mass and intrinsic width of the meson. We have also presented our calculations of the photon normalization, the acceptance of the CLAS detector and the effects of the cuts imposed in this analysis. In this chapter we present our final results for the mass, width, differential cross sections, relative branching fractions, and Dalitz plot analysis. Where appropriate, comparisons are made to prior experiments and theoretical predictions for both the $f_1(1285)$ and $\eta(1295)$. When possible we made similar measurements for the well known η' meson as a reference state.

5.1 Mass and Width

From our fits to the missing-mass-off-the-proton spectrum, MM(γ, p), discussed in detail in §3.2, we determined the mass and width of the $x(1280)$ meson state. We obtained estimated systematic errors by varying ranges, background polynomial order, and parameter limits used in the fits as described in §4.2. The results of the fits are shown in Table 5.1, along with the PDG values for the two mesons at 1280 MeV/c^2.

Channel	Mass (MeV/c^2)	Width (MeV/c^2)
$\eta' \to \eta\pi^+\pi^-$	958.48 ± 0.04	$\Gamma \ll \sigma_{exp}$
$x(1280)$ CLAS	1281.0 ± 0.8	18.4 ± 1.4
PDG η'	957.78 ± 0.06	0.204 ± 0.018
PDG $f_1(1285)$	1281.8 ± 0.6	24.3 ± 1.1
PDG $\eta(1295)$	1294 ± 4	55 ± 5

Table 5.1: η' and $x(1280)$ mass and width measurements. The width of the η' was not measured as it is much smaller than our experimental mass resolution of 3-6MeV/c^2.

The mass we measured in this analysis are both in excellent agreement with the world average computed by the Particle Data Group for the $f_1(1285)$[1]. The best value we obtain for the intrinsic width for the $x(1280)$ in CLAS comes in narrower than both the current world average for the $f_1(1285)$ and $\eta(1295)$. The disagreement with the $f_1(1285)$ value is about "3σ" but our is nonetheless consistent with several individual measurements from a variety of experimental setups, production

methods, and final states[57][58][27][59]. While the width from the Our measurement of the mass of η' is about one MeV/c^2 larger than world data, and has been added to our estimate of our systematic error on the mass of the $x(1280)$ from the previous chapter.

5.2 Differential Cross Sections

In nuclear and particle physics, a *differential cross section*, $d\sigma$ is a effective are that relates of the likelihood of a scattering process, as a function of some chosen variable(s). For our photoproduction reactions of interest, $\gamma p \to \eta' p$ and $\gamma p \to x(1280)p$, we measure the cross section of producing the meson, η' or $x(1280)$, per unit of solid angle, per incident photon. The differential cross section is solely a function of the production process and as such is independent of the final state into which the meson decays. The full discussion of the analysis techniques and component measurements involved is available is §3.5.

We measured differential cross sections, $d\sigma/d\Omega$ for both the η' and $x(1280)$ mesons. We binned our data in ten 100 MeV bins in center of mass energy W, from 1.8 to 2.8 GeV. We binned the data into nine bins in cosine of the meson production angle in the center of mass frame $\cos\Theta_{CM}$, eight of width 0.2 from -0.8 to 0.8, and one 0.1 wide bin from 0.8 to 0.9. The forward and backward holes of the CLAS detector were the limiting factor in angular coverage. We obtained yields in several separate decay channels for each meson, $\eta' \to \eta\pi^+\pi^-$ and $\eta' \to \pi^+\pi^-\gamma$, and $x(1280) \to \eta\pi^+\pi^-$, $x(1280) \to K^+\bar{K}^0{+}\pi^-$ and $x(1280) \to K^-K^0{+}\pi^+$. These independent measurements are compared, to study systematic effects, and then combined to give our best measurement of the cross sections. The η' measurements serve as a calibration test of our methods and analysis cuts. The $x(1280)$ measurements represent the first substantial photoproduction differential cross sections for either candidate, $f_1(1285)/\eta(1295)$.

5.2.1 $\eta' \to \eta\pi^+\pi^-$ and $\eta' \to \rho^0\gamma$

As a systematic test of our analysis we measured differential cross sections for η' decaying to $\eta\pi^+\pi^-$ and $\rho^0\gamma$. We find our measurements in good agreement with recently published CLAS results[55] from fellow CMU researcher M. Williams using a partial-wave analysis method of $\eta' \to \eta\pi^+\pi^-$, also on the g11 dataset. Figure 5.1 shows our measured cross sections compared to the published values. Our measurements do not start at η' threshold, as we have not made the necessary tagger corrections for low energy photon rates. As discussed in §2.2, the trigger for g11 run period required a scattered electron from the radiator to strike one of the first 40 T-counters of the tagger spectrometer. This break-point corresponds to $W \approx 1.955$ GeV, which is well below threshold for the $x(1280)$ meson.

In considering the level of agreement between William's CLAS 2009 results and our work, it is important to point out the differences in binning between the analyses. William's results were extracted in a much finer binning appropriate for the η' statistics. Our binning was chosen based on the statistics of the $x(1280)$, and we kept the same bin width, 100 MeV, for the η' for purposes of systematics. Our lowest energy bin, from W of 2.0 to 2.1 GeV compares fairly well to the two William's bins of 2.040 to 2.050 GeV and 2.050 to 2.060 GeVfor such disparate bin sizes. From W of 2.10 to 2.36 GeV William's used 20 MeV wide bins and we are in better agreement in this region, except for being low in the forward angle for our second bin,W from 2.1 to 2.2 GeV. From 2.36 GeV onward, where we measure $d\sigma/d\Omega$ for the $x(1280)$, William's bins are 40 MeV wide and our results are in good agreement. The numerical results along with the deviation from published values are tabulated in Appendix C

We find the level of agreement between our $\eta\pi^+\pi^-$ and $\rho^0\gamma$ results to be good. While the $\rho^0\gamma$ values were found to be 5% higher on average than the $\eta\pi^+\pi^-$ values, this difference is only 0.209 times the standard deviation of the bin-by-bin ratio of the two. We apply the overall 5% correction to our branching ratio calculations later in this chapter.

5.2.2 $x(1280) \to K\bar{K}\pi$ and $x(1280) \to \eta\pi\pi$

Satisfied with the accuracy of our η' cross sections, we turn our attention toward the meson of interest for our analysis, the $x(1280)$. In calculating the differential cross sections for the $x(1280)$ meson from our measured yields we encounter a limitation of our dataset. Unlike the η' case, we do not *a priori* know the branching fractions for its decay modes as its identity is not determined yet. Also, the two-charged-track trigger configuration for g11 is blind to all-neutral particle decay modes of the $x(1280)$. Without the ability to measure the total yield for $\gamma p \to x(1280)p$, we can not empirically correct individual decay modes by experimentally determined branching fractions. Therefore, we must present our $x(1280)$ differential cross sections as the $x(1280) \to \eta\pi^+\pi^-$ final state differential cross sections rather than the full $\gamma p \to x(1280)p$ production cross sections.

The final distributions presented in this chapter are the combination of three measurements: $\eta\pi^+\pi^-$ data extracted via a Voigtian fit, $\eta\pi^+\pi^-$ data fit to a combination of Monte Carlo signal plus several simulated multi-pion backgrounds, and $K^\pm K^0\pi^\mp$ data fit with a Voigtian signal function. The differential cross sections extracted in $K^\pm K^0\pi^\mp$ are smaller than those measured in $\eta\pi^+\pi^-$ and have thus been scaled by the measured relative branching fraction

$$\frac{\Gamma(x(1280) \to K\bar{K}\pi)}{\Gamma(x(1280) \to \eta\pi\pi)} \tag{5.1}$$

before taking the weighted mean of the independently extracted measurements in the two decay modes. The calculation of this branching ratio will be presented in more detail later in §5.3. The final differential cross sections presented in Figures 5.2-5.6 are shown along with the total systematic error including both the values from Table 5.2 and comparison of the yield extraction methods in the $\eta\pi^+\pi^-$ channel, detailed in §4.5.

The differential cross section is fairly flat in production angle in the near threshold bin at W of 2.35 GeV, with large systematic error in the backward-most angle bins. The cross section also falls off in the forward-most angle bins. At W of 2.45 GeV, the cross section begins to rise with energy in the forward direction, before falling in the forward-most bin. From W of 2.55 upward, the forward peaking becomes more pronounced, even considering the large statistical and systematic error in the forward angle bins. This shape is generally associated with t-channel processes, even the dip back towards zero is seen in some Regge models as discussed in Chapter 1. This mechanism is also very evident in the η' results. Unlike the η', we do not see a strong enhancement at backward angles, the signature of a u-channel mechanism, except in the lowest energy bin. We observe no striking features at central angles in any energy bin.

Table 5.2 lists the systematic uncertainties for these measurements. Overall we estimate the systematic uncertainty to be between 10 to 13% for our differential cross sections.

Figure 5.7 shows a comparison of $d\sigma/d\Omega$ for η' and $x(1280) \to \eta\pi^+\pi^-$ for $W = 2.55$ GeV. The η' exhibits a much stronger $t-$ and $u-$channel signature in its $\cos\Theta_{CM}$ dependence than does the $x(1280)$. Lacking any prior experimental cross-section data, we compare our cross sections to recent Regge model predictions by Kochelev[60] discussed in §1.3.1 for both the $f_1(1285)$ and $\eta(1295)$. Figures 5.8-5.12 show our results compared to the Kochelev predictions for both mesons and their incoherent sum.

The model curves have been scaled by the PDG branching fraction $\Gamma(f_1(1285) \to \eta\pi^+\pi^-)$ for comparison. It is notable even though this is an ad-hoc scaling for the $\eta(1295)$, it is not a large enough effect to place the $\eta(1295)$ cross section above that of $f_1(1285)$ in $\gamma p \to \eta\pi\pi$. We also note the $\eta(1295)$ has been observed in $K\bar{K}\pi$ final states[31][61], so although of unknown branching fraction, $\eta\pi^+\pi^-$ is not its exclusive decay mode.

The Kochelev prediction utilizes the Regge model of t-channel meson exchange, with ρ and ω mesons as the exchanged particles. The model uses phenomenological input from related reactions for unknown parameters and obtains scale-appropriate predictions for nearby states η and η'. In comparison to our data it is clear that the t-channel alone does not reproduce our measurements

Source	Fractional Uncertainty		
	W GeV	$\eta\pi^+\pi^-$	$K^\pm K^0\pi^\mp$
Yields	2.35	0.041	0.032
	2.45	0.022	0.030
	2.55	0.026	0.022
	2.65	0.018	0.022
	2.75	0.040	0.057
Acceptance	2.35	0.11	
	2.45	0.08	
	2.55	0.08	
	2.65	0.11	
	2.75	0.085	
Event Selection	0.002		
Normalization	0.079		
	W GeV	$\eta\pi^+\pi^-$	$K^\pm K^0\pi^\mp$
Final	2.35	0.14	0.14
	2.45	0.11	0.12
	2.55	0.12	0.12
	2.65	0.14	0.14
	2.75	0.12	0.13

Table 5.2: Final systematic uncertainties on $x(1280)$ $d\sigma/d\Omega$ measurements, Combining results from Tables 4.2 and 4.3 with overall uncertainties.

especially near threshold. In our highest-energy bins we do find our data points converging towards the Kochelev $f_1(1285)$ prediction in the forward production angle bins, but the cross section in the middle to backward angles are not accounted for in the Regge model. Both Kochelev's model and comparison to η' suggest part of the strength of the $x(1280)$ comes from $s-$channel decay of baryon resonances.

The full numerical results for differential cross section measurements are tabulated in Appendix C.

5.3 Branching Fractions

Despite being unable to measure overall branching fractions for $x(1280)$, we do have several observable decay channels with which to compute relative branching fractions. The two relative branching fractions we calculate for this analysis are

$$\frac{\Gamma(x(1280) \to K\bar{K}\pi)}{\Gamma(x(1280) \to \eta\pi\pi)} \quad \text{and} \tag{5.2}$$

$$\frac{\Gamma(x(1280) \to \rho^0\gamma)}{\Gamma(x(1280) \to \eta\pi\pi)}. \tag{5.3}$$

In computing these ratios there were several possible ways to assemble the yields. In the $\eta\pi^+\pi^-$ and $K^\pm K^0\pi^\mp$ decay modes we have sufficient statistics to compute the yields for each kinematic bin used in our differential cross sections. We can sum the differential yields to determine the total yield for each decay channel. This method has the advantage of using bin-dependent σ values in the Voigtian function to parametrize the experimental resolution in missing mass off the proton, rather than using a single global value. We can also use results of our systematic studies of the yield extraction and acceptance discussed in the previous chapter. The alternative method is to fit

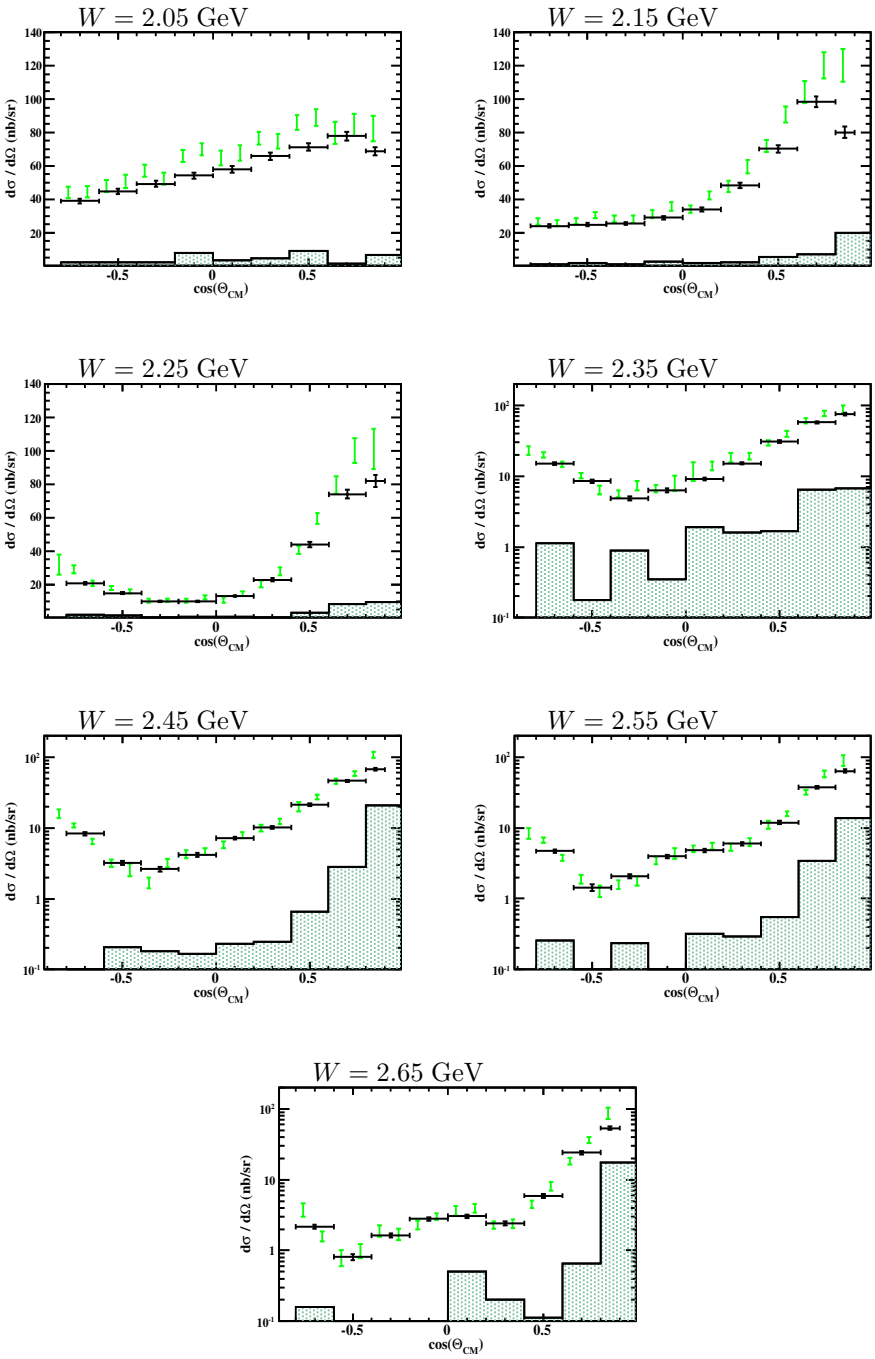

Figure 5.1: $d\sigma/d\Omega$ for η' compared to recent CLAS published results[55] for $\eta' \to \eta\pi^+\pi^-$ (green). The CLAS published results used smaller W binning, so the bin nearest to the center of our 100 MeV-wide bins were chosen for comparison. Our highest bin has been omitted due to insufficient overlap in binning. Shaded histogram is half the difference between the two measurements. Note bins from $W = 2.35$ GeV and up are on a logarithmic scale.

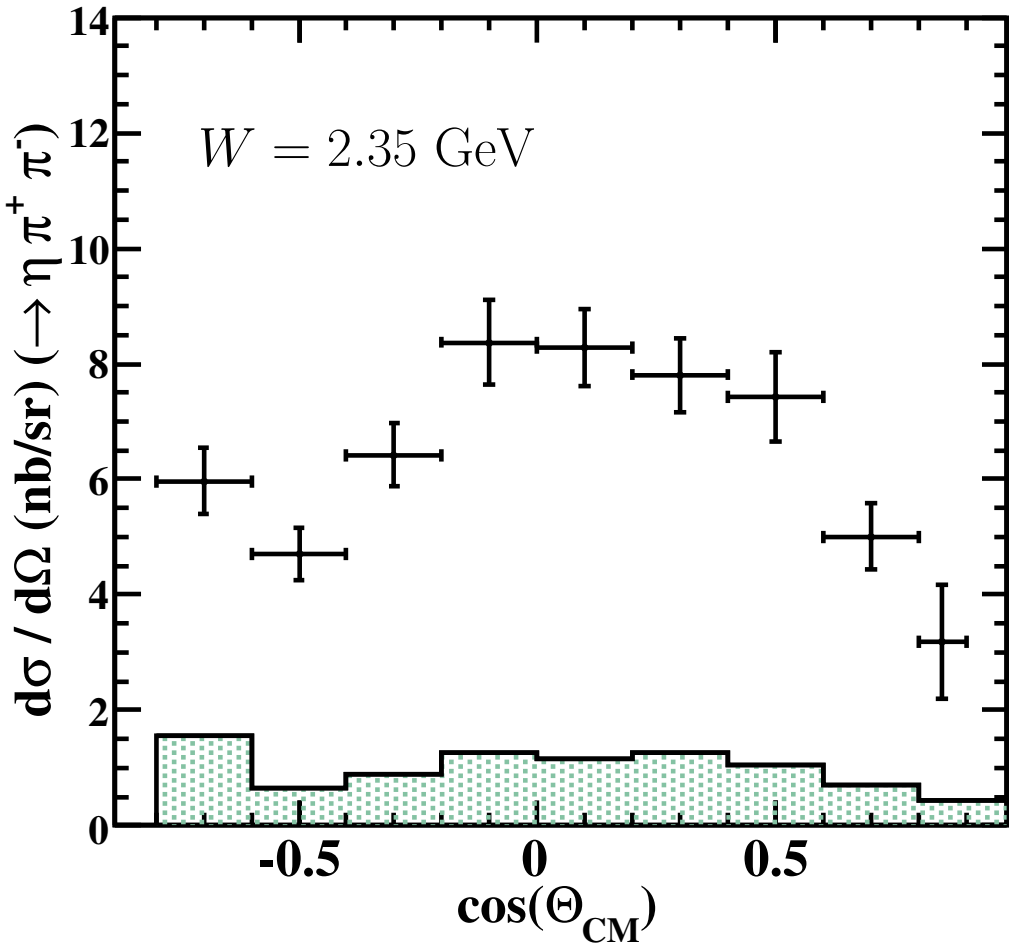

Figure 5.2: Weighted mean $d\sigma/d\Omega$ for $x(1280) \to K^{\pm}\pi^{\mp}K^{0}$, $\eta\pi^{+}\pi^{-}$ (Voigtian) and $\eta\pi^{+}\pi^{-}$ (MC Bkgd. method). The vertical error bars are the statistical uncertainties. The shaded histogram is the total systematic uncertainty.

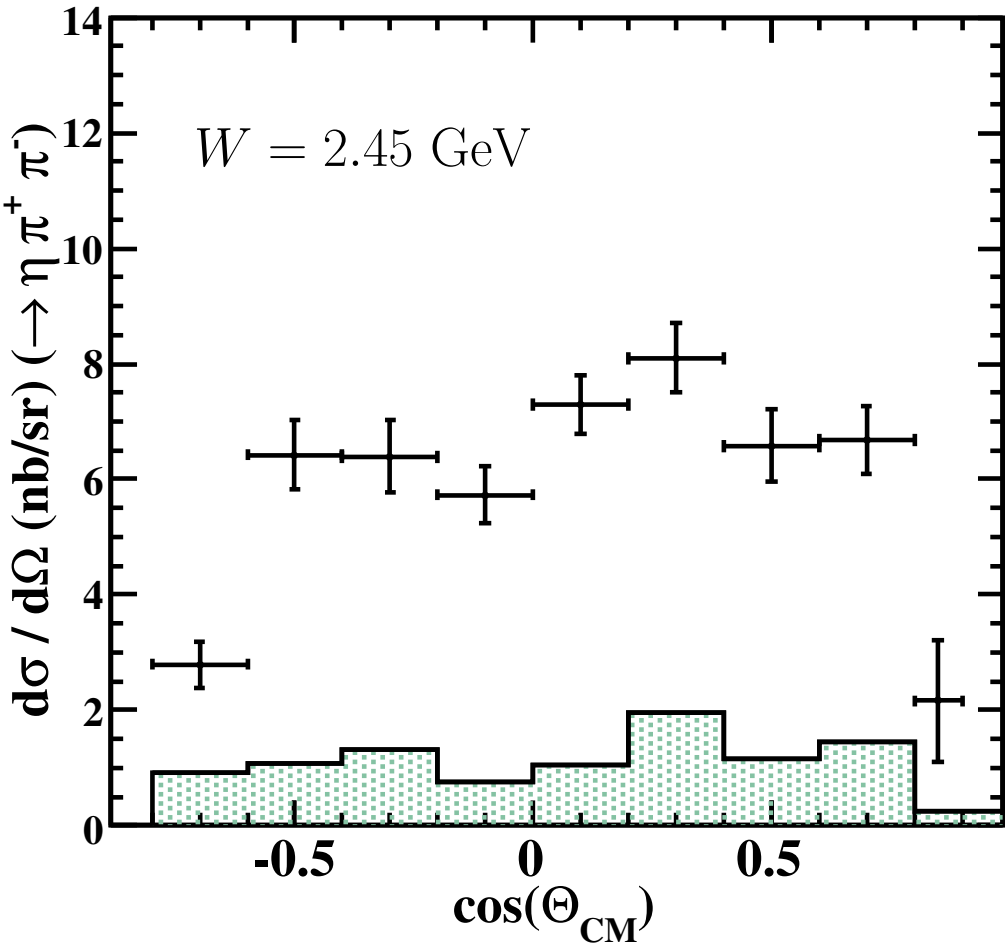

Figure 5.3: Weighted mean $d\sigma/d\Omega$ for $x(1280) \rightarrow K^{\pm}\pi^{\mp}K^0$, $\eta\pi^+\pi^-$ (Voigtian) and $\eta\pi^+\pi^-$ (MC Bkgd. method). The vertical error bars are the statistical uncertainties. The shaded histogram is the total systematic uncertainty.

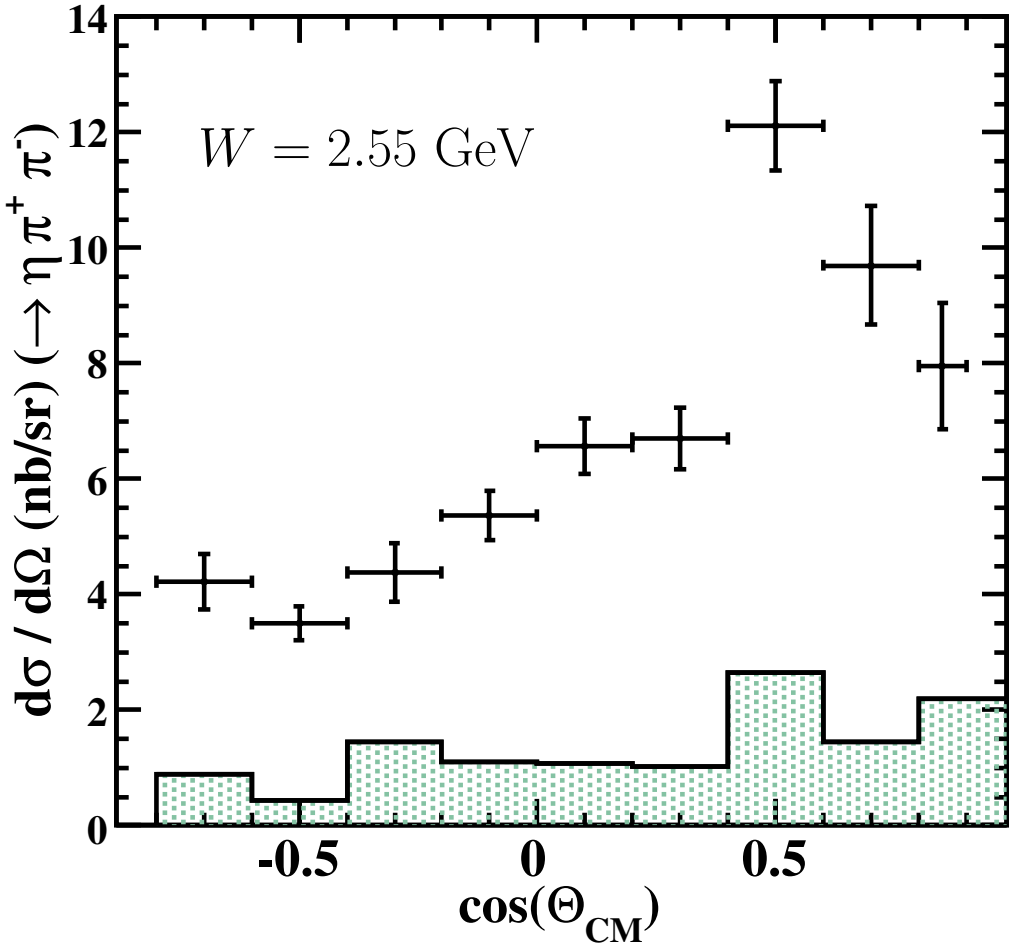

Figure 5.4: Weighted mean $d\sigma/d\Omega$ for $x(1280) \rightarrow K^{\pm}\pi^{\mp}K^0$, $\eta\pi^+\pi^-$ (Voigtian) and $\eta\pi^+\pi^-$ (MC Bkgd. method). The vertical error bars are the statistical uncertainties. The shaded histogram is the total systematic uncertainty.

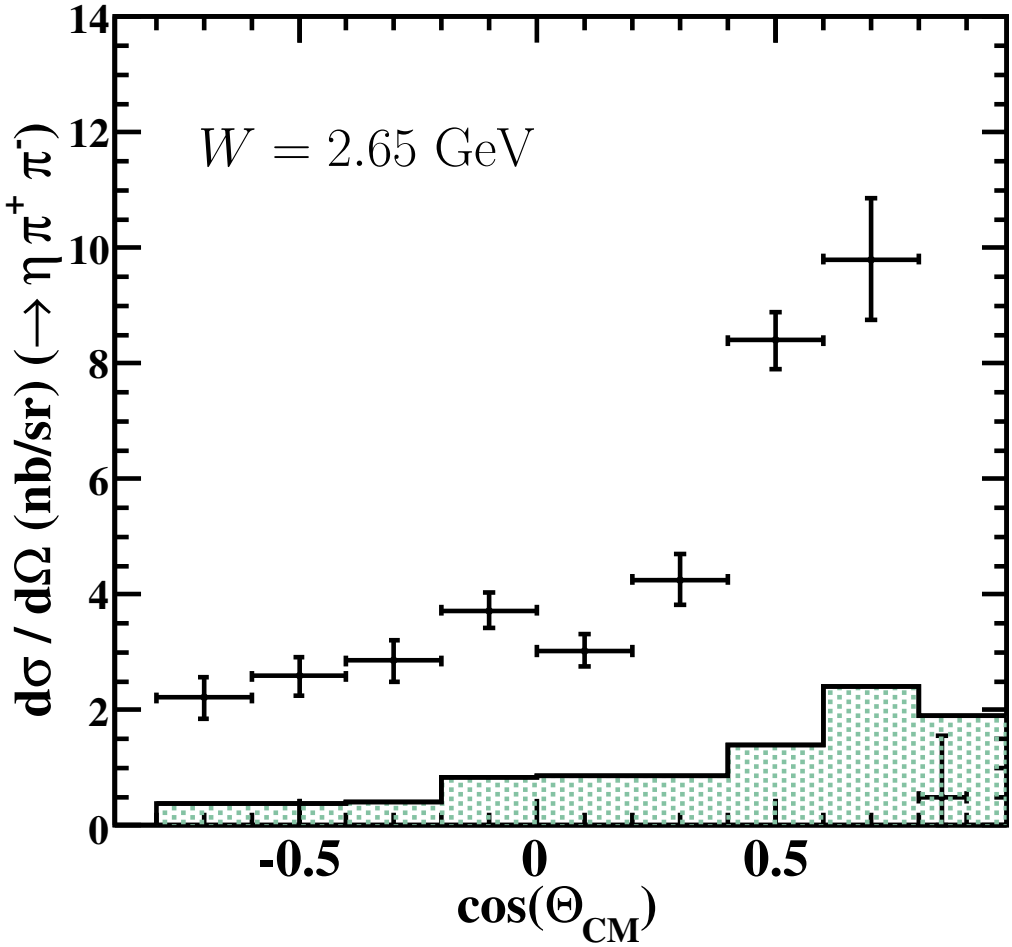

Figure 5.5: Weighted mean $d\sigma/d\Omega$ for $x(1280) \rightarrow K^{\pm}\pi^{\mp}K^0$, $\eta\pi^+\pi^-$ (Voigtian) and $\eta\pi^+\pi^-$ (MC Bkgd. method). The vertical error bars are the statistical uncertainties. The shaded histogram is the total systematic uncertainty.

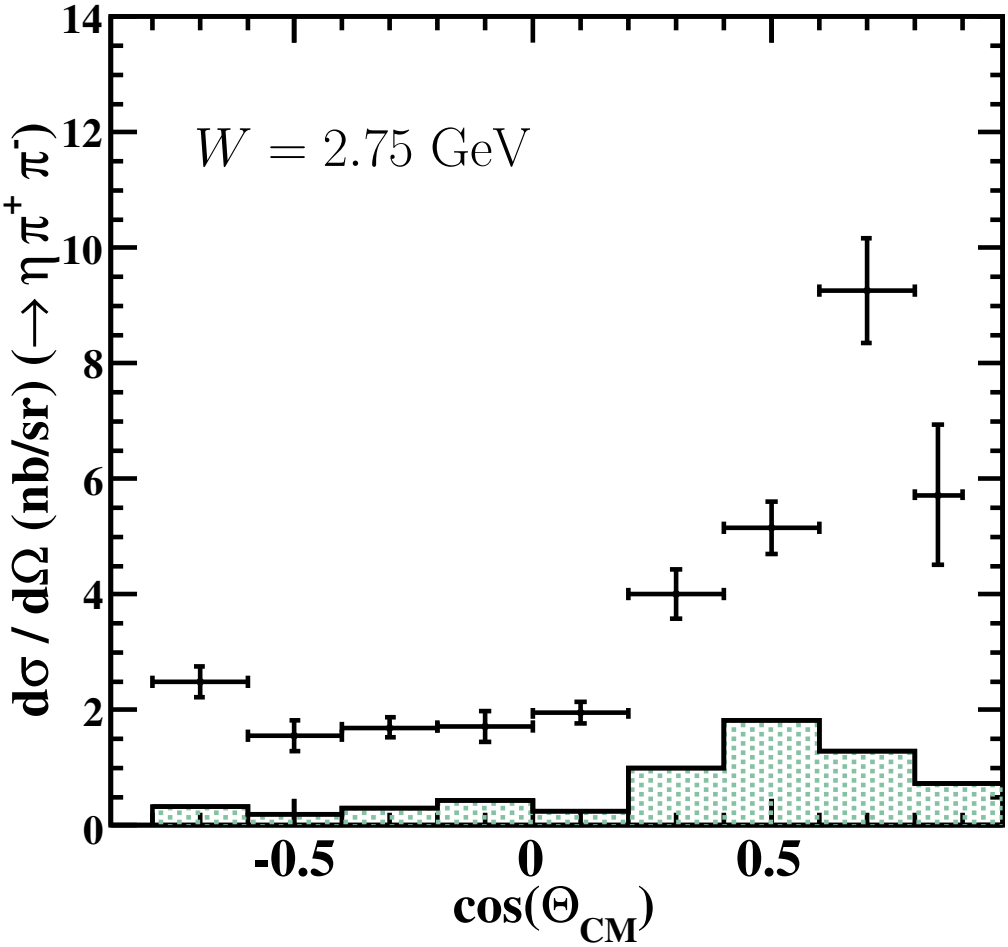

Figure 5.6: Weighted mean $d\sigma/d\Omega$ for $x(1280) \rightarrow K^{\pm}\pi^{\mp}K^0$, $\eta\pi^+\pi^-$ (Voigtian) and $\eta\pi^+\pi^-$ (MC Bkgd. method). The vertical error bars are the statistical uncertainties. The shaded histogram is the total systematic uncertainty.

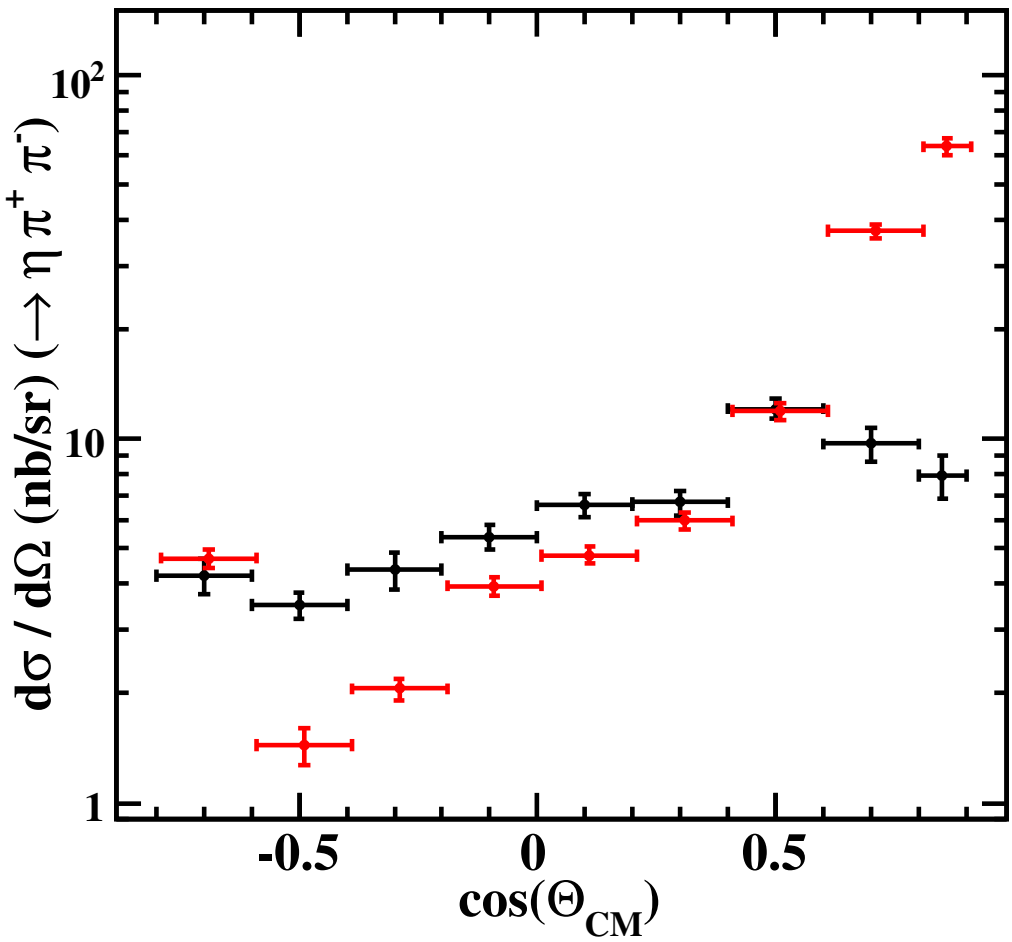

Figure 5.7: Final result $d\sigma/d\Omega$ for $\gamma p \to x(1280)p \to \eta\pi^+\pi^-p$ compared to $d\sigma/d\Omega$ for $\gamma p \to \eta' p \to \eta\pi^+\pi^-p$ (red) at $W = 2.55$ GeV. The $x(1280)$ differential cross section is clearly not as diffractive as the η'.

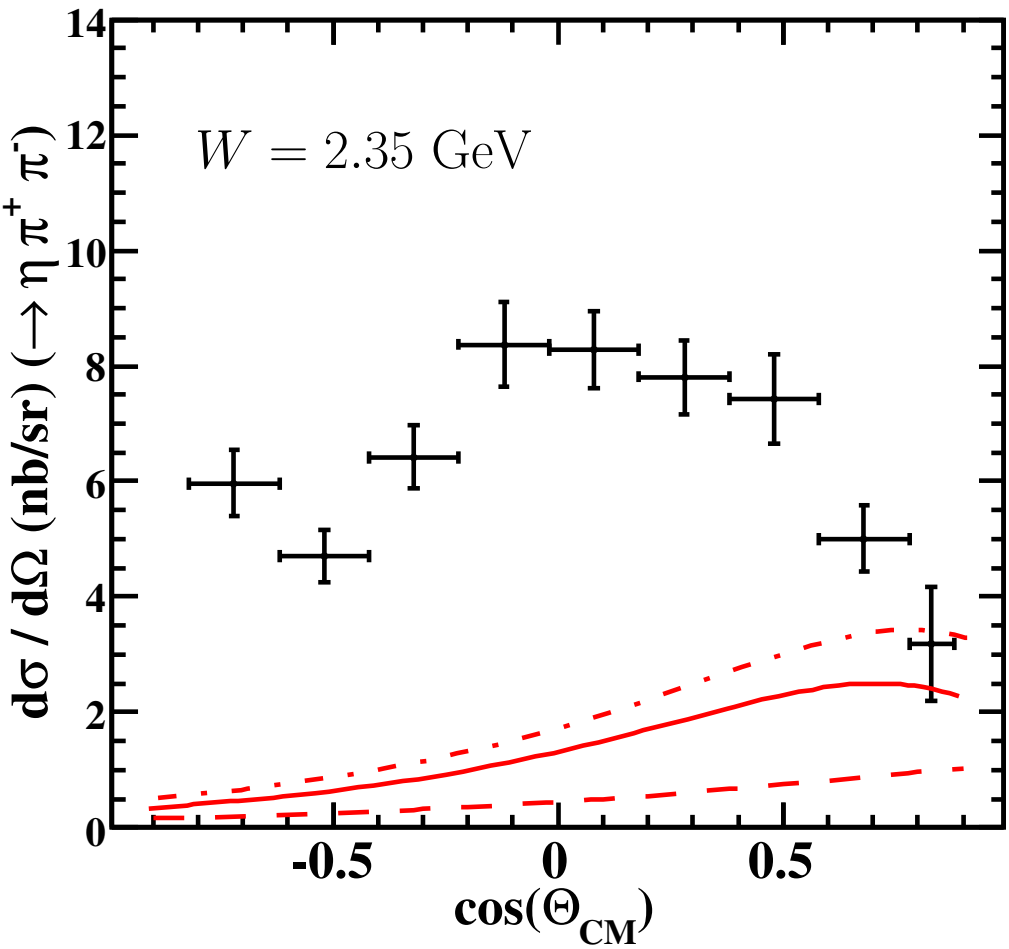

Figure 5.8: Weighted mean $d\sigma/d\Omega$ for $x(1280) \rightarrow K^{\pm}\pi^{\mp}K^0$, $\eta\pi^+\pi^-$ (Voigtian) and $\eta\pi^+\pi^-$ (MC Bkgd. method). The vertical error bars are the statistical uncertainties. The shaded histogram is standard deviation of the three measurements. Solid red line is Kochelev prediction[60] for $f_1(1285)$ and the dashed red line is the corresponding prediction for $\eta(1295)$. The curves are scaled by the PDG branching fraction for $f_1(1285) \rightarrow \eta\pi^+\pi^-$. Dash-Dot line is the incoherent sum of both mesons.

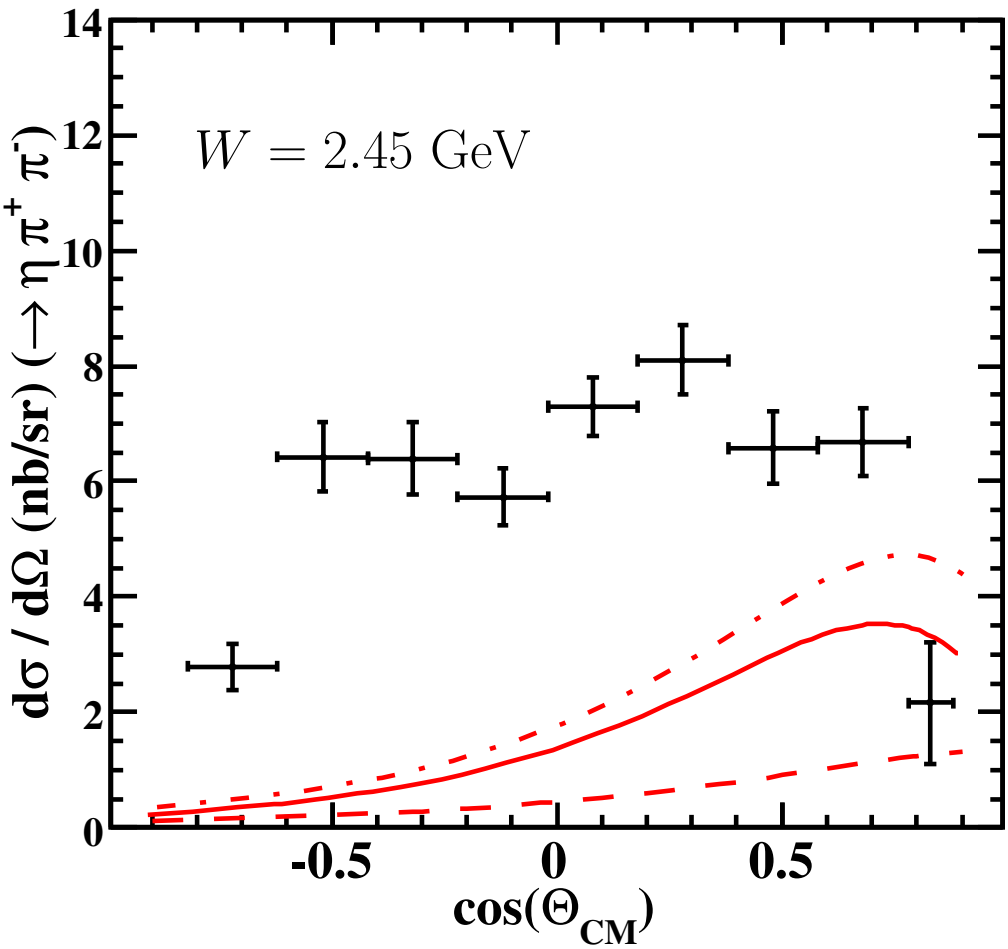

Figure 5.9: Weighted mean $d\sigma/d\Omega$ for $x(1280) \rightarrow K^{\pm}\pi^{\mp}K^0$, $\eta\pi^+\pi^-$ (Voigtian) and $\eta\pi^+\pi^-$ (MC Bkgd. method). The vertical error bars are the statistical uncertainties. The shaded histogram is the total systematic uncertainty. Solid red line is Kochelev prediction[60] for $f_1(1285)$ and the dashed red line is the corresponding prediction for $\eta(1295)$. The curves are scaled by the PDG branching fraction for $f_1(1285) \rightarrow \eta\pi^+\pi^-$. Dash-Dot line is the incoherent sum of both mesons.

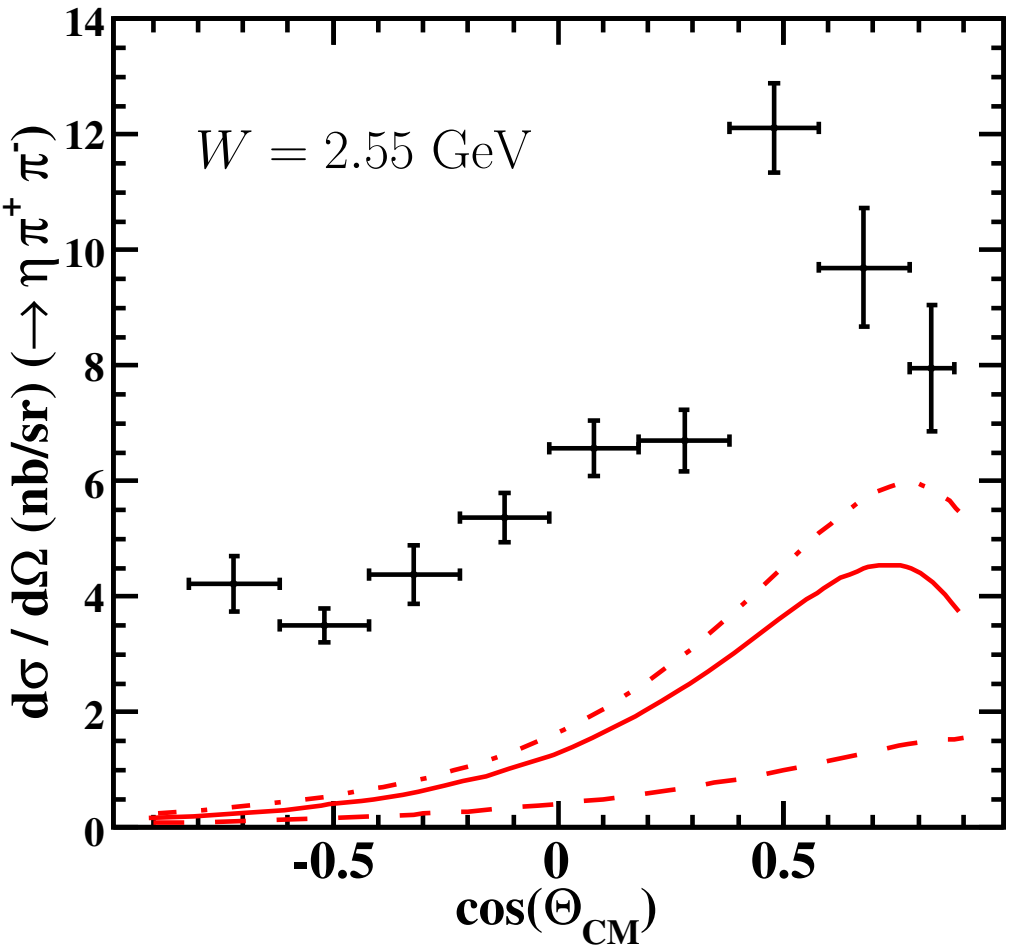

Figure 5.10: Weighted mean $d\sigma/d\Omega$ for $x(1280) \rightarrow K^{\pm}\pi^{\mp}K^0$, $\eta\pi^+\pi^-$ (Voigtian) and $\eta\pi^+\pi^-$ (MC Bkgd. method). The vertical error bars are the statistical uncertainties. The shaded histogram is the total systematic uncertainty. Solid red line is Kochelev prediction[60] for $f_1(1285)$ and the dashed red line is the corresponding prediction for $\eta(1295)$. The curves are scaled by the PDG branching fraction for $f_1(1285) \rightarrow \eta\pi^+\pi^-$. Dash-Dot line is the incoherent sum of both mesons.

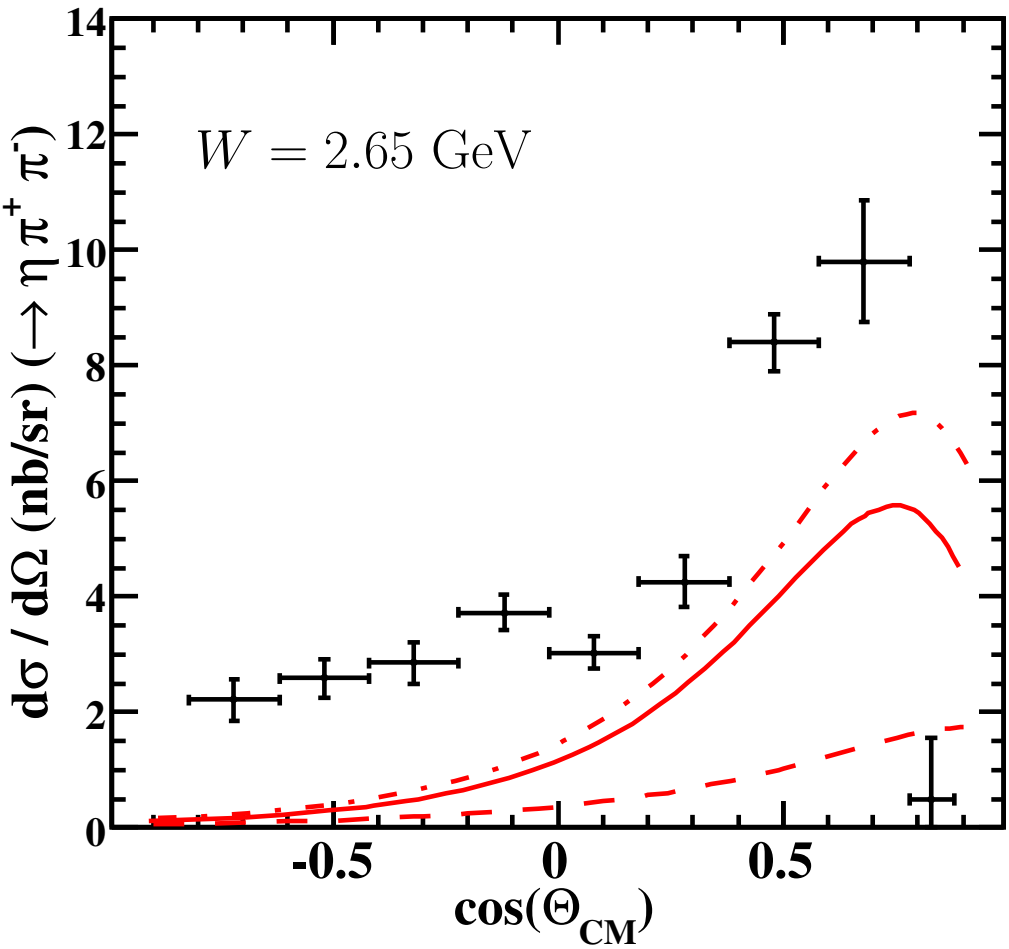

Figure 5.11: Weighted mean $d\sigma/d\Omega$ for $x(1280) \rightarrow K^{\pm}\pi^{\mp}K^0$, $\eta\pi^+\pi^-$ (Voigtian) and $\eta\pi^+\pi^-$ (MC Bkgd. method). The vertical error bars are the statistical uncertainties. The shaded histogram is the total systematic uncertainty. Solid red line is Kochelev prediction[60] for $f_1(1285)$ and the dashed red line is the corresponding prediction for $\eta(1295)$. The curves are scaled by the PDG branching fraction for $f_1(1285) \rightarrow \eta\pi^+\pi^-$. Dash-Dot line is the incoherent sum of both mesons.

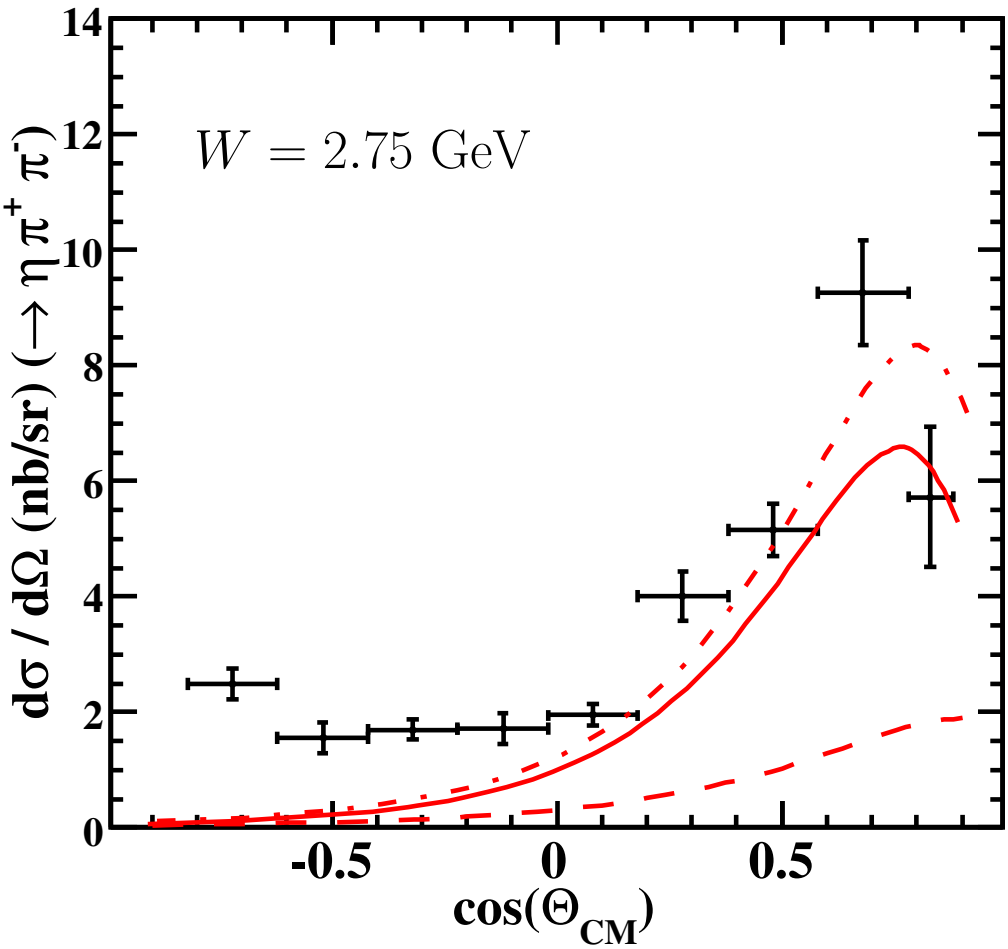

Figure 5.12: Weighted mean $d\sigma/d\Omega$ for $x(1280) \rightarrow K^{\pm}\pi^{\mp}K^0$, $\eta\pi^+\pi^-$ (Voigt) and $\eta\pi^+\pi^-$ (MC Bkgd. method). The vertical error bars are the statistical uncertainties. The shaded histogram is the total systematic uncertainty. Solid red line is Kochelev prediction[60] for $f_1(1285)$ and the dashed red line is the corresponding prediction for $\eta(1295)$. The curves are scaled by the PDG branching fraction for $f_1(1285) \rightarrow \eta\pi^+\pi^-$. Dash-Dot line is the incoherent sum of both mesons.

the missing-mass-of-the-proton spectrum integrated over W and $\cos(\Theta^x_{CM})$, excluding the bins with insufficient acceptance. This is the only possible method for computing the second ratio, as the $x(1280)$ signal in the $\rho^0\gamma$ decay mode is quite small. The details of estimating the systematic errors of these methods and the tests of the robustness of the faint $\rho^0\gamma$ signal are described in detail in §4.2. The systematic error on the acceptance of $x(1280) \to \rho^0\gamma$ events was estimated by iterating our Monte Carlo to match the differential cross sections. Table 5.3 presents the best values from considering these approaches along with supporting information and comparisons to world data where available for the $f_1(1285)$ and $\eta(1295)$.

step	value	stat. error	syst. error	PDG $f_1(1285)$
$\eta\pi^+\pi^-$ Yield	1.33×10^5	4.9×10^3	2.9×10^3	
$\eta\pi^+\pi^-$ Acceptance	0.0652	9.7×10^{-5}	0.0072	
$K^\pm K^0\pi^\mp$ Yield	6570	180	340	
$K^\pm K^0\pi^\mp$ Acceptance	0.0149	3.18×10^{-5}	0.0016	
$\rho^0\gamma$ Yield	3790	790	850	
$\rho^0\gamma$ Acceptance	0.0248	6.4×10^{-5}	0.0050	
Isospin $\Gamma(K^\pm K^0\pi^\mp)/\Gamma(KK\pi)$	2/3			
Isospin $\Gamma(\eta\pi^+\pi^-)/\Gamma(\eta\pi\pi)$	2/3			
$\rho^0\gamma$ systematic correction from η' $d\sigma/d\Omega$	0.95			
$\Gamma(KK\pi)/\Gamma(\eta\pi\pi)$	0.216	0.010	0.031	0.171 ± 0.013
$\Gamma(\rho^0\gamma)/\Gamma(\eta\pi\pi)$	0.047	0.010	0.015	0.105 ± 0.022

Table 5.3: Relative branching fractions of the $x(1280)$ meson.

We find our value for the first ratio, Eq. 5.2, to be higher than the PDG value for the $f_1(1285)$, but well within errors. The second ratio, Eq. 5.3, however, is lower than the world average by a considerable amount. Even with our large uncertainty in the $\rho^0\gamma$ yield extraction, we find a significant difference between our value the PDG average. Comparison of these values to the radiative decay models introduced in §1.3.2 will be discussed in the next chapter.

5.4 Dalitz Analysis

To further analyze the structure of the $x(1280)$ decay in the $\eta\pi\pi$ channel, we performed a Dalitz plot analysis. The methodology of the background subtraction, acceptance correction, and related cuts are discussed in §3.6. The resulting two dimensional scatter plot, Figure 3.35, clearly shows the $x(1280)$ decays through the intermediate resonance $a_0^\pm(980)$. The plot has been trimmed along the kinematic boundary of allowed $m^2_{\eta\pi^\pm}$ values for our measured mass of the $x(1280)$to suppress edge effects of the acceptance.

Figure 5.13 shows the half projections of the Dalitz plot along its axes, demonstrating the strength of the $a_0\pi$ signal over non-resonant $\eta\pi\pi$ events.

We can also project the intensity of the $a_0^\pm$ band along the $m^2_{\eta\pi^\mp}$ axis, as shown in Figure 5.14. The profile is relatively flat for low $m^2_{\eta\pi^\mp}$, then increasing to nearly double the height for $m^2_{\eta\pi^\mp}$ above 0.8 GeV^2.

5.4.1 Spin-Parity Determination

The strong $a_0^\pm(980)$ bands seen in Figure 3.33 show the decay of the $x(1280)$ occurs dominantly through the $a_0^\pm\pi^\mp$ intermediate. To first order the Dalitz plot contains no information about the spin and parity of the parent $x(1280)$. The invariant mass variables as given in Equations 3.49 and 3.50 depend on the angle between the pions and thus their distribution is dependent upon the

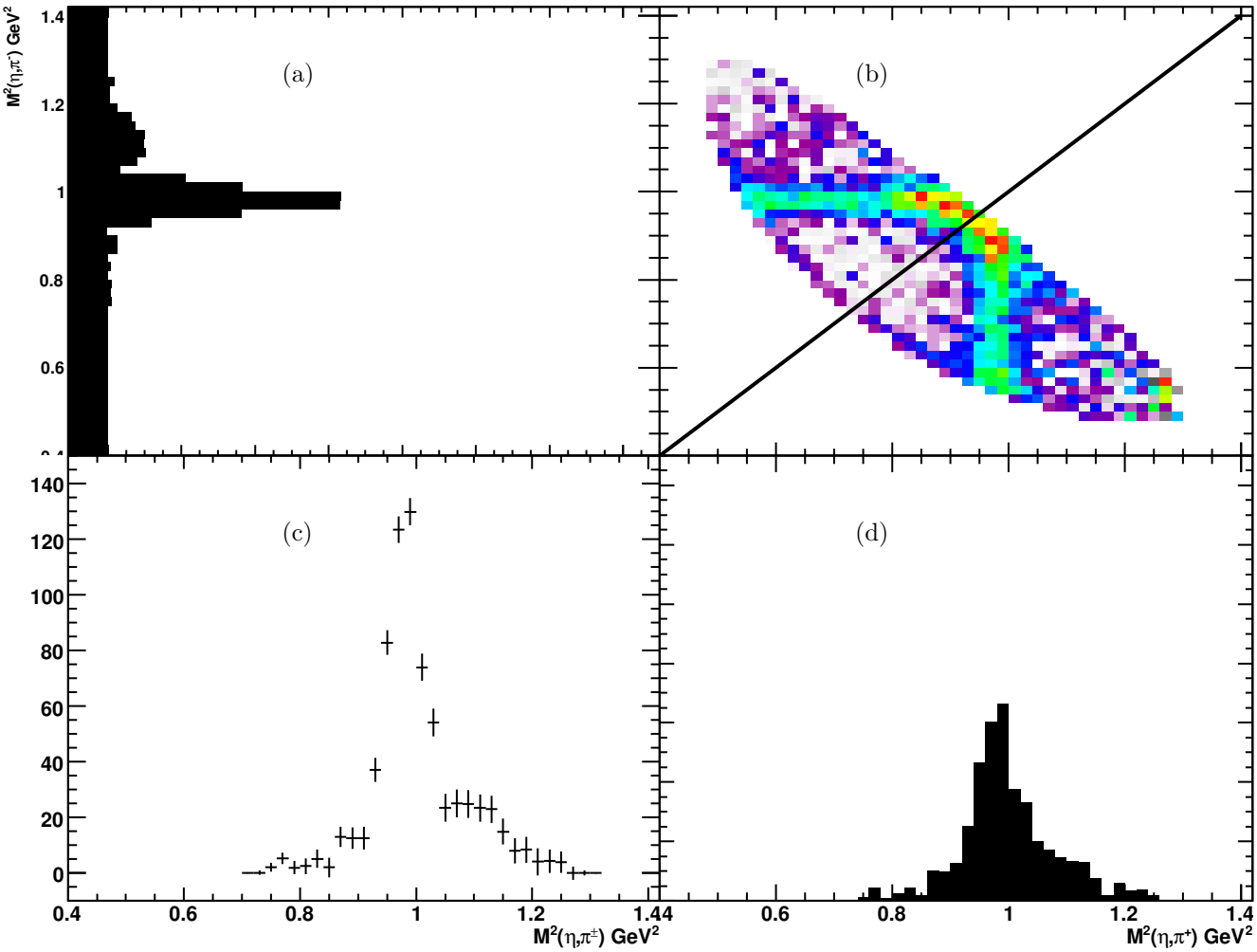

Figure 5.13: Histogram(a) is the projection of $a_0^-(980)$ half of Dalitz plot(b) for $x(1280) \to \eta\pi^+\pi^-$ cut along the diagonal boundary. Histogram(c) is the sum of $a_0^-(980)$ with the $a_0^+(980)$ half projection(d). The diagonal line in (b) shows division used for the projections.

spin of the intermediate resonance, the $a_0^\pm(980)$ in our case. Since the a_0 and π are spin zero states the spin of the parent $x(1280)$ would be revealed in the relative orbital angular momentum between them. If the $x(1280)$ is the $\eta(1295)$ the particles will be found in a S-wave configuration, and likewise if the $x(1280)$ is the $f_1(1285)$ they will be found in P-wave.

The angular dependence of the first decay does not directly map into the Dalitz mass variables. It is "washed out" by the S-Wave decay of the a_0, which yields the resultant angle between the pions that determines the Dalitz $m^2_{\eta\pi}$ variables. Thus, all angles between the pions are equally likely.

However, we have not included the interference between the two $a_0^\pm(980)$ resonances in this

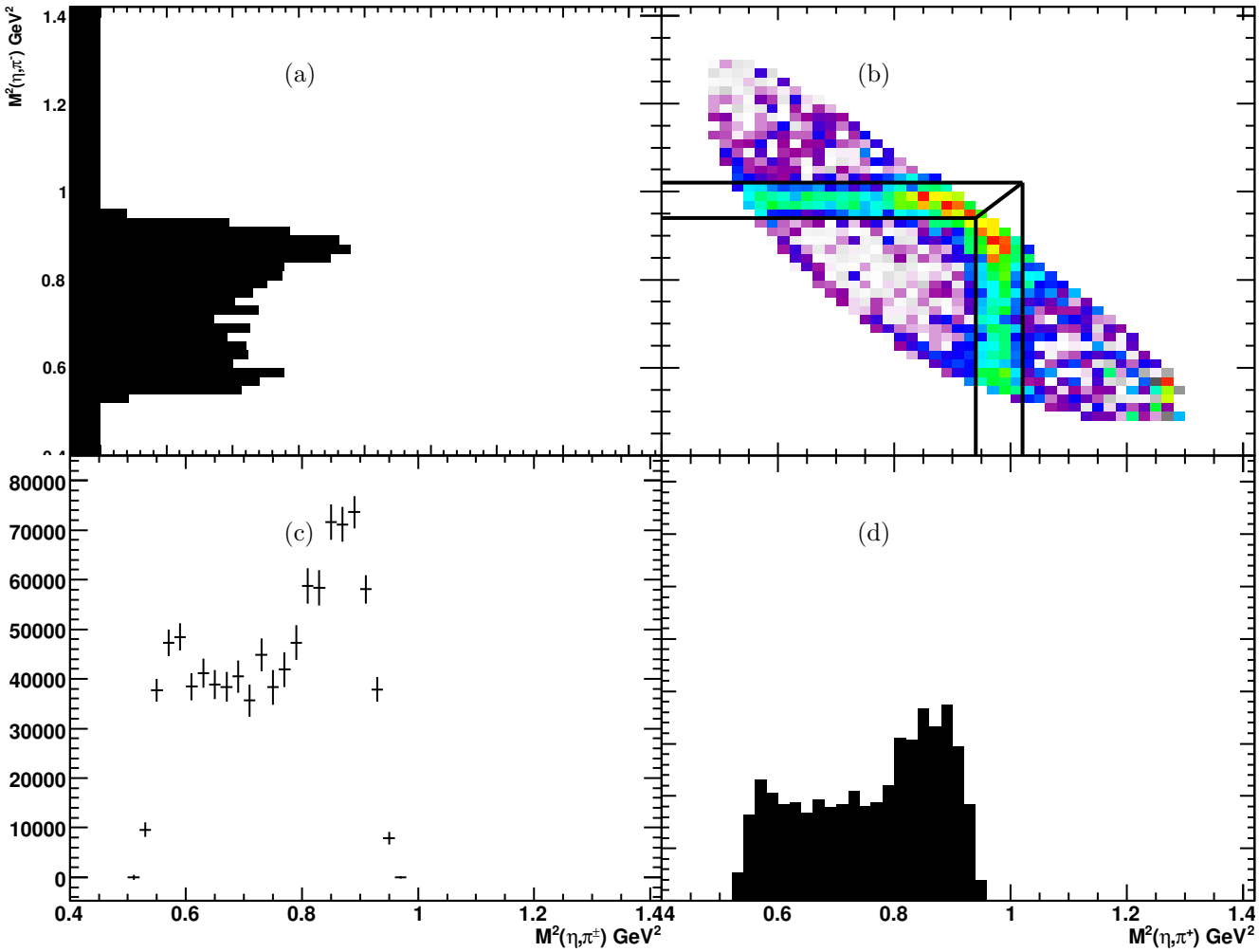

Figure 5.14: Histogram(a) is the profile of $a_0^+(980)$ of Dalitz plot(b) for $x(1280) \to \eta\pi^+\pi^-$ selection regions shown. Histogram(c) is the sum of $a_0^+(980)$ profile with the $a_0^-(980)$ profile(d).

picture. The decay amplitude for the $x(1280)$

$$A_{x\to\eta\pi\pi} = \langle \eta\pi\pi | x \rangle, \tag{5.4}$$

$$A_{x\to\eta\pi\pi} \propto \sum_{m,a_0^\pm} c_m BW(P_{a_0}, M_{a_0}, \Gamma_{a_0}) Y_l^m(\Theta_{a_0}, 0). \tag{5.5}$$

where

$$BW(P, M, \Gamma) = \frac{M\Gamma}{E^2 - M^2 + iM\Gamma}, \tag{5.6}$$

$$\tag{5.7}$$

is a coherent sum of the two charge state $a_0^\pm$ with the appropriate angular dependence expressed in the spherical harmonic Y_l^m where Θ_{a_0} is chosen to be the angle between the direction of the

$x(1280)$ and the a_0 in rest frame of the $x(1280)$. At this point we have chosen to represent the a_0 a relativistic Breit-Wigner of mass M_{a_0} and fixed-width Γ_{a_0}, though the a_0 is known to be a likely non-$q\bar{q}$ state [1][62].

Parity conservation requires $c_+ = c_-$ and the normalization condition requires $2c_\pm^2 + c_0^2 = 1$. Despite the individual angles being uncorrelated with the Dalitz mass variables, interference effects are possible as the cross term will depend on the both $\Theta_{a_0^+}$ and $\Theta_{a_0^-}$.

To test the size of this effect we weighted our $x(1280) \to \eta\pi^+\pi^-$ Monte Carlo events according to the extreme cases. First, no angular dependence which represents both the spin zero case and the special case of spin one with equal substates $c_\pm = c_0 = 1/\sqrt{3}$. Then taking $c_0 = 1$ yields $\cos\Theta_{a_0}$ weighting (all $m = 0$) while taking $c_0 = 0$ yields $\sin\Theta_{a_0}$ weighting (all $m = \pm 1$). The relativistic Breit-Wigner for the $a_0(980)$ was given a mass of 987 MeV and width $\Gamma = 50$ MeV. The mass and width of the a_0 are both highly dependent upon its physics model and decay channel as seen in the world data [62].

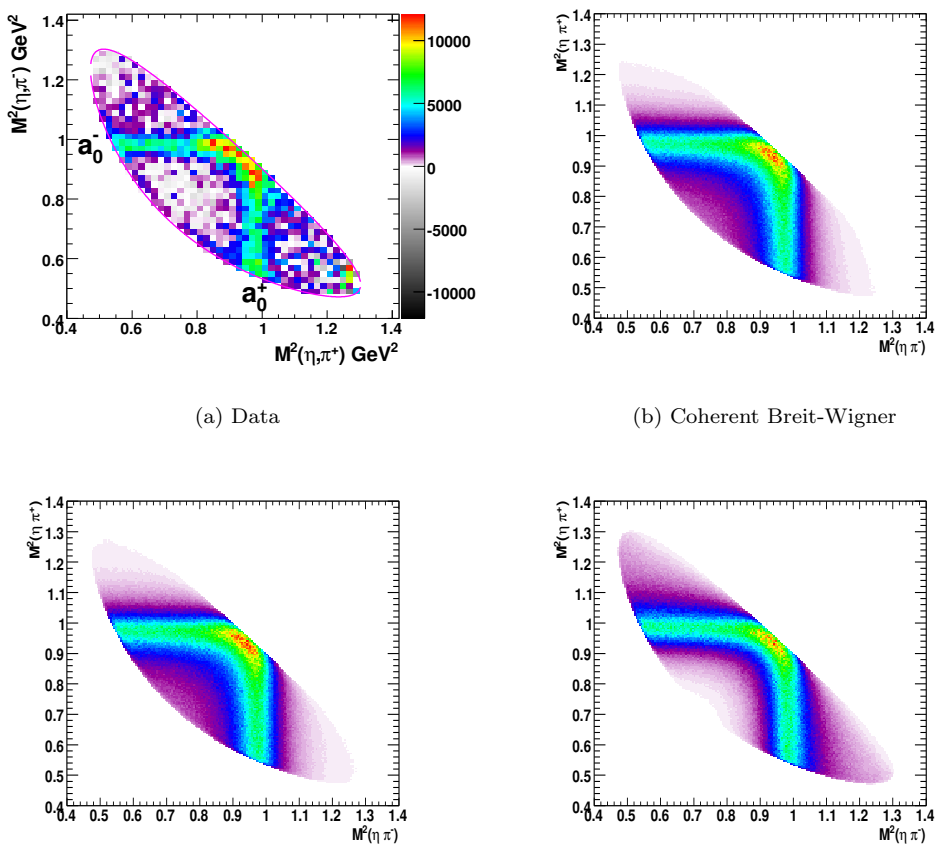

(a) Data

(b) Coherent Breit-Wigner

(c) $\sin\Theta$ weighted Breit-Wigner

(d) $\cos\Theta$ weighted Breit-Wigner

Figure 5.15: Interference of a_0 amplitudes compared to Data.

Figure 5.15 shows intensity of the coherent sum of Breit-Wigners for the three cases compared to the acceptance-corrected data. The straight sum and sine-weighted distributions are identical to the eye, while the cosine-weighted plot has more strength in the high invariant mass "wings" and less in the low mass central region between the a_0 bands. The cosine distribution more closely represents

the data. To better see the level of agreement we slice the Dalitz plot along the $m^2_{\eta\pi^+} = m^2_{\eta\pi^-}$ diagonal and project into four histograms, giving us the lineshape of the a_0's as well as the profiles along the bands.

Figure 5.16 shows the comparison between the data and Monte Carlo in these projections. Again it is seen that the cosine-weighted Monte Carlo better matches the data. The lineshape, however, is not well-reproduced on the high mass side.

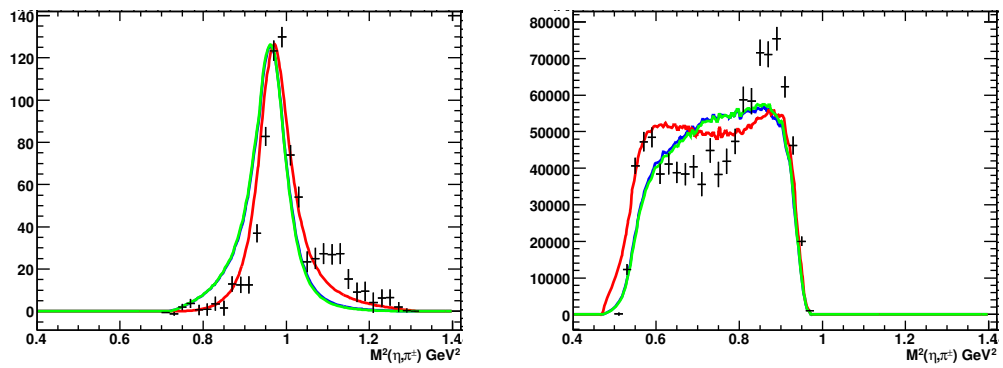

(a) $a_0^{\pm}(980)$ lineshape

(b) $a_0^{\pm}(980)$ profile

Figure 5.16: Comparison of acceptance-corrected data to Monte Carlo weighted by coherent sum of a_0 BW amplitudes with sine-weighting(blue), cosine-weighting(red) and flat(green). The cosine weighting better reproduces the lineshape (a) and profile (b) than the flat or sine curves, which are indistinguishable from one another.

The scalar $a_0(980)$ meson is thought to be a bound $K\bar{K}$ state or other non-$q\bar{q}$ candidate and as such is expected to have a channel dependent lineshape rather than the standard Breit-Wigner. The Flatté parametrization [63] uses a coupled-channel($\eta\pi$,$K\bar{K}$) approach with the mass dependent cross section given by

$$\frac{d\sigma}{dM} = C|A|^2 \tag{5.8}$$

where

$$A = \frac{\sqrt{\Gamma_0\Gamma_{\eta\pi}}M_r}{M_r^2 - M^2 - iM_r(\Gamma_{\eta\pi} + \Gamma_{K\bar{K}})}, \tag{5.9}$$

$$\Gamma_{\eta\pi} = g_{\eta\pi}q \tag{5.10}$$

and

$$\Gamma_{K\bar{K}} = \begin{cases} ig_{K\bar{K}}\sqrt{M_K^2 - (M/2)^2} & \text{below } K\bar{K} \text{ threshold} \\ g_{K\bar{K}}\sqrt{(M/2)^2 - M_K^2} & \text{above } K\bar{K} \text{ threshold} \end{cases} \tag{5.11}$$

where q is the momentum of the η in the rest frame of the $a_0(980)$, M_r is the mass of the a_0, M_K is the mass of the kaon (neglecting the small difference in mass between the charged and neutral kaons), and $g_{\eta\pi}$ and $g_{K\bar{K}}$ are the couplings to the two decay modes. Γ_0 is defined as the value of $g_{\eta\pi}q$ at $M = M_r$. Depending on the value of M_r with respect to the $K\bar{K}$ threshold and the relative coupling strengths the lineshape can be much sharper or broader than a Breit-Wigner of similar mass and width. In a Figure 5.17 a comparison of the Flatté peak to the best reproduce Breit-Wigner is shown. The couplings chosen were $g_{\eta\pi} = 0.190$ and $g_{K\bar{K}} = 0.285$ with the mass of the a_0 for both

Flatté and Breit-Wigner cases set to 990 MeV/c^2, and the width of the Breit-Wigner narrowed to 35 MeV/c^2 to better fit the data. The Flatté parameters were chosen by starting with values from the Brookhaven E852 analysis [62] and iterating the Monte Carlo weighting program. The effect of the Flatté parametrization is not sufficient to completely match the lineshape and profile seen in the data and the cosine weighting is still necessary, showing the $x(1280)$ to be spin-one decaying almost but not exclusively through $a_0\pi$.

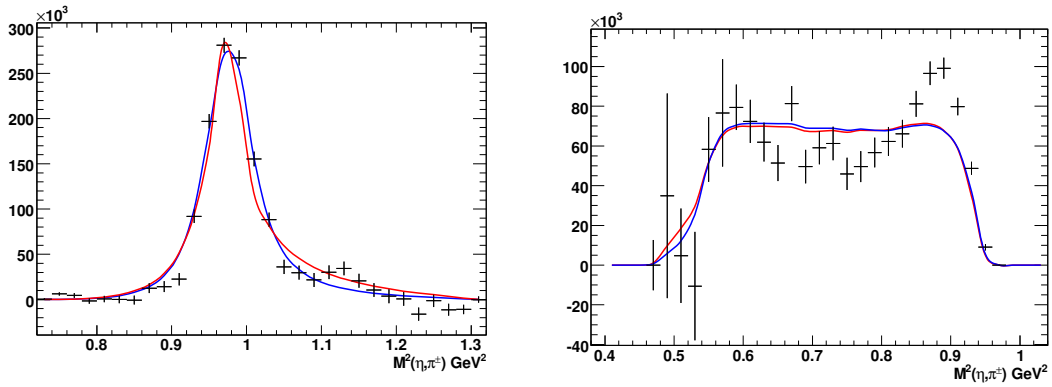

Figure 5.17: Comparison of the Flatté parametrization (red) to the Breit-Wigner (blue) case, both using a coherent sum of the $a_0^{\pm}$ amplitudes weighted by $\cos\Theta_{a_0}$. Left histogram shows combined $a_0^{\pm}$ lineshape projection while the right shows its profile projection.

5.5 Summary

In this chapter we have presented our results for a suite of measurements of the reaction $\gamma p \to xp$ in CLAS. From our yields in $\eta\pi^+\pi^-$, $K^+K^0\pi^-$, $K^-K^0\pi^+$ and $\rho^0\gamma$ decay modes we have calculated branching ratios and differential cross sections. We have performed a Dalitz analysis of the $\eta\pi^+\pi^-$ decay and found the Dalitz plot to be in good agreement with a model of spin-one $f_1(1285) \to a_0^{\pm}\pi^{\mp}$ decay and inconsistent with a spin-zero $\eta(1295)$ decay. We have also measured the mass and intrinsic width of the meson. We have made limited comparisons to world data, which will be expanded upon in our concluding chapter along with a comparison to the available theoretical predictions outlined in the Chapter 1.

Chapter 6

Conclusion

In the preceding chapter we have presented the results of our measurements of the reaction $\gamma p \to x(1280)p$ in the *g11* dataset, where the $x(1280)$ is one or both of the candidate meson states $f_1(1285)/\eta(1295)$. Neither of the candidate states had been studied in photoproduction before this work. We have obtained measurements of the mass, width, differential cross sections, relative branching fractions of several decay modes, and have presented a Dalitz plot analysis.

In this chapter we will discuss the agreement of our final results with the available theoretical predictions and world data for $f_1(1285)/\eta(1295)$.

6.1 Identity of the x

A primary goal of this analysis is to determine whether the $x(1280)$ signal observed in photoproduction by CLAS is the $f_1(1285)$, $\eta(1295)$, or some combination of the two. A direct measurement of the spin and parity of the $x(1280)$ through partial wave analysis is not feasible due to the large number of background events in the signal channels. However, a spin dependence in the interference of the the $a_0^+\pi^-$ and $a_0^-\pi^+$ intermediate states in $x(1280) \to \eta\pi^+\pi^-$ decay mode allows for J^{PC} determination through analysis of the Dalitz plot. Additionally, we compare our other measurements of the x to the world data and available theoretical models and for these states.

6.1.1 Mass and Width

We first examine our measurements of the mass and width of the $x(1280)$, summarized in Table 5.1 in the previous chapter. The mass of 1281.0 ± 0.8 MeV we measured in this analysis is in excellent agreement with the world average of 1281.8 ± 0.6 MeV computed by the Particle Data Group for the $f_1(1285)$[1]. The world average for the mass of the $\eta(1295)$, computed from just four experiments is 1294 ± 4 MeV. It should be noted that one of the included analyses, the E852 experiment, had results [21] in $\pi^-p \to \eta\pi^+\pi^-n$ yielding M_η of 1282 ± 5 MeV, compatible with our measurement.The measurements of the mass of the $\eta(1295)$ have all been extracted via PWA with different methodologies, implementations, and limitations upon the waves used. Thus, while our value for the mass supports the $f_1(1285)$ identity over the $\eta(1295)$ it cannot sufficiently rule out presence of $\eta(1295)$.

The intrinsic width, $\Gamma_x = 18.4 \pm 1.4$ obtained is about 3σ lower than the world average of $\Gamma_{f_1(1285)} = 24.3 \pm 1.1$ MeV[1] and much lower than $\Gamma_{\eta(1295)} = 55 \pm 5$ MeV (See Table 6.1). The width of the $x(1280)$ we obtained in this analysis is quite incompatible with the PDG $\eta(1295)$. However, the Brookhaven PWA analysis of $\pi^-p \to K^+K^-\pi^0n$ data [31] found the width obtained for the 1^{++} ($f_1(1285)$) wave was $\Gamma = 45 \pm 9 \pm 7$ MeV, but fitting only the intensity function for the $f_1(1285)$ 1^{++}-wave yielded a much smaller width, $\Gamma = 23 \pm 5$. They concluded that interference

between the $f_1(1285)$ and $\eta(1295)$ was important in determination of widths of these states. The background under the $x(1280)$ signal in our data precluded any reasonable PWA. Therefore we can only cannot rule out interference effects between the $f_1(1285)$ and $\eta(1295)$ influencing our observed width. We can state, however, that the width of the $x(1280)$ is more compatible with the world-average results of the $f_1(1285)$ than the $\eta(1295)$.

VALUE (MeV)	Source
55 ± 5	PDG AVERAGE
$57 \pm 23 \pm 21$	ADAMS E852
66 ± 13	MANAK E852
53 ± 6	FUKUI KEK
18.4 ± 1.4	CLAS

Table 6.1: World Data for width of the $\eta(1295)$compared to our measurement in red.

We see no clear evidence for any of the higher mass 0^{-+} or 1^{++} states: $\eta(1405)$,$\eta(1470)$,$f_1(1420)$ or $f_1(1510)$. Thus, we can not base our J^{PC} assignment upon a "set" of observed masses and widths matching the pseudoscalar or pseudovector spectra. Finally, the singlet and octet meson states of a nonet of the quark model can mix, along with possible inclusion of a gluonic component as well. Thus, there is insufficient theoretical constraint to predict the $f_1(1285)$ and $\eta(1295)$ masses and widths to the level of precision necessary to distinguish them.

6.1.2 Differential Cross Sections

There are no prior experimental differential cross sections for either candidate meson for comparison. However, there are two recent Regge-model predictions published that we will compare to our measurements. More in-depth summaries of the models were presented earlier in Section 1.3.1.

Kochelev

N. Kochelev's calculations[13] utilized exchange of ρ and ω mesons in the Regge framework for small momentum transfer ($|t| \leq 1\,\mathrm{GeV}^2$). The model uses phenomenological input from available experimental data to constrain the relevant couplings and vector meson dominance inspired form factors. The model predicts differential cross sections for both $f_1(1285)$ and $\eta(1295)$ mesons. Figures 5.8-5.12 show the theoretical curves in comparison to our final experimental results. The model curves have been scaled by the PDG value for the branching fraction $\Gamma(f_1(1285) \to \eta\pi^+\pi^-)$ for comparison with our experimental results. This is necessary as we have not corrected for the "unknown" branching fraction of the $x(1280)$ in CLAS. This results in an ad-hoc scaling for the $\eta(1295)$ but is not large enough of an effect to change the size hierarchy of the curves. That is, even if we assumed that the $\eta(1295)$ decayed exclusively to $\eta\pi^+\pi^-$, the $f_1(1285)$ curve would remain higher by a factor about two. We also note the $\eta(1295)$ has been observed in PWA analysis of $K\bar{K}\pi$ final states[31], so $\eta\pi^+\pi^-$ is not its exclusive decay mode.

The $t-$channel exchange of Kochelev's Regge model calculations is clearly not sufficient to describe the data. The experimental cross sections are about four times greater than predicted for the $f_1(1285)$ in the lowest energy bin of $W = 2.35$ GeV, and not forward peaked as predicted (see Figure 5.8). The agreement improves somewhat with increasing center-of-mass energy as the experimental distribution does become forward peaked in energy bins of $W = 2.55$ GeV(see Figure 5.10) and greater. Still even in our highest energy bin of $W = 2.75$ GeV the data points are around 60% higher than predicted at forward angles and do not fall off as dramatically at central and backward angles as predicted in the Regge model (see Figure 5.12). It is obvious some that additional s- and u-channel processes are needed to reproduce the data.

Domokos

Another Regge model discussed in §1.3.1, based upon a different theoretical starting point, was published by S. Domokos *et al.*[16] The paper included calculations using both single ρ exchange at low s and Reggeized ρ and ω exchange at large s and small $|t|$. The Domokos Regge model predicts a lower cross section than the Kochelev model, and does not go to to zero at $t = 0$ (forward $\cos\Theta_{CM}$) like the Kochelev prediction.

Calculating these cross sections for our energy range yielded predictions quite smaller in intensity than those of the Kochelev model. Appendix A details the calculation of differential cross sections for our kinematics from the formulae published in their paper. Figure 6.1 shows a comparison of the Domokos and Kochelev models for the $f_1(1285)$ in an example energy bins of $W = 2.45$ and 2.65 GeV. The predicted curve of Domokos is clearly incompatible with our data, even in the forward-most region where the $t-$channel process is dominant.

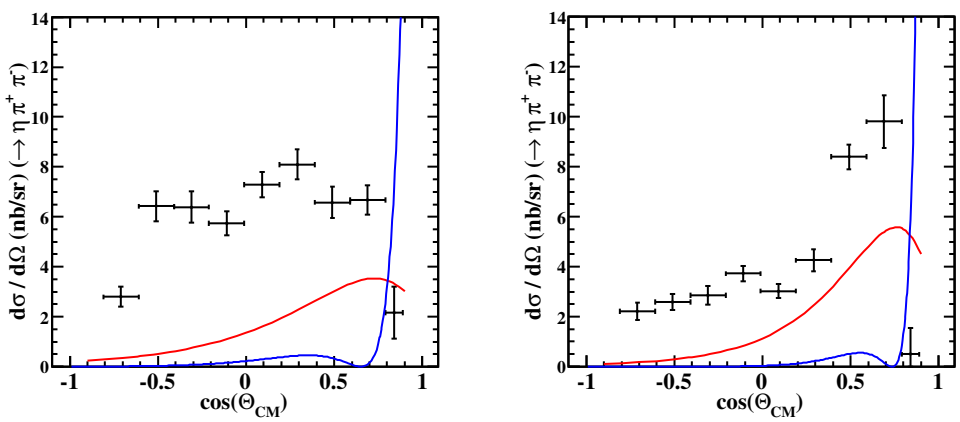

(a) W 2.45 (GeV) (b) W 2.65 (GeV)

Figure 6.1: Comparison of Regge models of $f_1(1285)$ photoproduction to our results. Kochelev *et al.*[13] $f_1(1285)$ (red) model predicts a stronger photoproduction cross section than by Domokos *et al.*[16](blue). Shaded histogram is the systematic error.

6.1.3 Branching Ratios

Our study of differential cross sections yields information regarding the production of the $x(1280)$; similarly, through studying the relative strength of the observed final states yields important information regarding its decay. The *g11*-trigger requirement of having at least two charged tracks per event prevents us from calculating absolute branching fractions for the $x(1280)$. Instead, we measure the ratios of acceptance corrected yields in the $\eta\pi^+\pi^-$, $K^\pm K^0\pi^\mp$, and $\rho^0\gamma$. Table 5.3 lists the yields and resulting branching ratios we observed for the $x(1280)$.

Charged Decay

The ratio $\Gamma(x \to K\bar{K}\pi)/\Gamma(x \to \eta\pi\pi) = 0.216\pm0.032$ is consistent with the PDG value of 0.171 ± 0.013 for the $f_1(1285)$. There is insufficient world data for this ratio for the $\eta(1295)$, but as mentioned above the $\eta(1295)$ has been observed in $K\bar{K}\pi$ final states with strength comparable to the $f_1(1285)$ [31].

Author	Prediction	$\Gamma(\rho^0\gamma)$
Lakhina and Swanson	rel. $f_1(1285)$	480 keV
	non-rel. $f_1(1285)$	1200 keV
	rel. $\eta(1295)$	240 keV
	non-rel. $\eta(1295)$	400 keV
Ishida	$f_1(1285)$ Θ_1	509 keV
	$f_1(1285)$ Θ_2	565 keV
Experiment	$\Gamma_x \times \mathcal{B}(f_1(1285) \to \eta\pi\pi)_{\mathrm{PDG}} \times \frac{\Gamma(\rho^0\gamma)}{\Gamma(\eta\pi\pi)}$	$\Gamma(\rho^0\gamma)$
CLAS	$(18.4 \pm 1.4$ MeV$) \times (0.52 \pm 0.05) \times (0.047 \pm 0.018)$	450 ± 180 keV
PDG $f_1(1285)$	$(24.3 \pm 1.1$ MeV$) \times (0.055 \pm 0.013)$	1330 ± 320 keV

Table 6.2: Radiative decay branching width predictions compared to value computed from our experimental results for the $x(1280)$ width Γ_x and branching ratio $\frac{\rho^0\gamma}{\eta\pi\pi}$ and using the world average for the branching fraction $\mathcal{B}(f_1(1285) \to \eta\pi\pi)_{\mathrm{PDG}}$. Our result is compatible with several models for the $f_1(1285)$, though it is not in agreement with the PDG world average [1].

Radiative Decay

The ratio $\Gamma(x \to \rho^0\gamma)/\Gamma \to \eta\pi\pi)$ is an interesting measurement because we have both experimental and theoretical values for comparison. We find a ratio of 0.047 ± 0.018 as detailed in Table 5.3, which is less than half the PDG average value of 0.105 ± 0.022, but is only inconsistent with world-average $f_1(1285)$ branching ratio by "2σ".

Table 6.2 lists the calculated widths for the radiative decays of the $f_1(1285)/\eta(1295)$ from several models compared to experimental values from the PDG and this work. As with our comparison of predicted cross sections to measured, we chose to use the PDG value for $\mathcal{B}(f_1(1285) \to \eta\pi^+\pi^-)$ in our calculation as no branching fraction is established for the $\eta(1295)$. The PDG value is in good agreement with the non-relativistic quark model radiative decay prediction by O. Lakhina and E. Swanson[18] if one assumes the PDG value for $\mathcal{B}(f_1(1285) \to \eta\pi\pi)$ is correct. Swanson's prediction uses a non-relativistic Coulomb-plus-linear potential and predicts a $\Gamma(f_1(1285) \to \rho^0\gamma)$ of 480 keV. Calculations were also made for $\eta(1295)$ and an older set of predictions for the $f_1(1285)$ were made by S. Ishida *et al.* using a covariant oscillator model [16].

The relativistic version of Lakhina and Swanson's model is substantial narrower, and is not in agreement with world data. The Ishida prediction is also narrower than world data. It predicted a width of between 509 to 565 keV depending on the mixing angle used. Lakhina and Swanson also calculated values for $\Gamma(\eta(1295) \to \rho^0\gamma)$ of 240 keV, though without having a corresponding value of $\Gamma_{\eta(1295)} \to \eta\pi^+\pi^-$ from either experiment or theory, this value can not be fairly compared to our experimental ratio. Like the Kochelev calculations, the $f_1(1285)$ is predicted to have a stronger coupling $g_{\gamma\rho x}$ than the $\eta(1295)$.

Both Swanson's and Kochelev's calculations suggest what one might suppose from the viewpoint of vector-meson dominance, that the coupling of a axial-vector $f_1(1285)$ to a should be stronger than for the pseudoscalar $\eta(1295)$. Our observation of $x(1280)$ in the $\rho^0\gamma$ final state suggests it is primarily the $f_1(1285)$. The disagreement of the $\Gamma(x \to \rho^0\gamma)/\Gamma \to \eta\pi\pi)$ branching ratio to prior experimental work does permit some $\eta(1295)$ contribution to our signal, though the absence of a known value for $\Gamma_{\eta(1295)} \to \eta\pi^+\pi^-$ prevents us using this result to quantitatively determine its contribution.

6.1.4 Dalitz Analysis

From our Dalitz analysis of $x(1280) \to \eta\pi^+\pi^-$ we determined that this decay occurs primarily through an $a_0^\pm\pi^\mp$ intermediate state, with the $a_0^\pm$ subsequently decaying to $\eta\pi^\pm$. From a comparison of data to physics-weighted Monte Carlo versions of the Dalitz plot shown in Figures 5.15, 5.16a and 5.16b, we were able to show the the data has a interference signature matching a cosine function of Θ_{a_0}, the angle between the direction of the $x(1280)$ and the a_0 in the rest frame of the x. This behavior is consistent with the decay of a spin one state, produced polarized in the $m = 0$ substate, with the polarization axis being the direction of the x.

6.1.5 Summary of Results

Taken together, the results from the suite of measurements in our analysis suggest the $x(1280)$ observed in CLAS photoproduction to be the 1^{++} $f_1(1285)$. The interference of the $a_0^\pm\pi^\mp$ bands in the Dalitz plot is consistent with the decay of a spin one meson produced in a polarized $m = 0$ state. The strength of its cross section in photoproduction, along with the presence of a signal in $M(\pi^+\pi^-\gamma)$, and a mass and intrinsic width consistent with world data also support this identity. Non-resonant $f_1(1285)$ and/or $\eta(1295)$ contribution is minimal.

6.2 Outlook and Future Work

This analysis remains, by necessity, a partial view of the $f_1(1285)$ in photoproduction. Further study of the Dalitz analysis is needed to determine quantitatively the J^{PC} states to better parametrize our spin and parity assignment toward setting an upper limit on the contribution from $\eta(1295)$ and/or non-resonant $f_1(1285) \to \eta\pi^+\pi^-$. The success of our background subtraction method is encouraging towards this goal. Exploratory investigation of four charge track data $(++--)$ shows that measuring the decay of the $x(1280)$ to a four charged pion final state is possible, which is another known decay branch for $f_1(1285)$. Additionally, future photo-production experiments with neutral particle detection and polarization measurements such as Glue-X and CLAS-12 offer a chance to study the production and decay of $f_1(1285)/\eta(1295)$ with direct spin-parity determining measurements and PWA analysis of the underlying physics.

We made investigative studies into determining the spin-parity of the $x(1280)$ through several fits as part of our Dalitz analysis. While we could not perform an event-based partial wave analysis our background subtraction in the Dalitz framework leaves us a fairly clean sample of events considering the large background in $\eta\pi^+\pi^-$. Monte Carlo study revealed the angles of the $x \to a_0^\pm\pi^\mp \to \eta\pi^+\pi^-$ reaction show up in the interference of the a_0 bands in the Dalitz mass variables, showing a clear signature of a spin-one state. This presence of a $P-$wave angular dependence in the decay products strongly suggests the $f_1(1285)$ identity. A quantitative determination of using a direct fitting of the data with amplitudes such as the Zemach method [64] remains to be done. Such a methods was used by the GAMS collaboration in study of $\eta\pi^0\pi^0$ decay mode [65].

The study of four pion decay modes of the $x(1280)$ was not pursued further due to the small acceptance and large background for that channel. Likewise analysis of data from other recent and future CLAS experiments would fall under a separate analysis project. Recent experimental runs utilized polarized beams and targets could use the polarization observables as well as improvements in detector hardware to improve selection of $x(1280)$ events in photoproduction. Finally, the construction of Hall D and the future operation of the Glue-X experimental search for glueballs and hybrid mesons looks to discover new states and clear up identity of puzzles such as the $f_1(1285)/\eta(1295)$ in hadron spectroscopy.

6.3 Summary

In conclusion, we have analyzed for the first time in photoproduction of the $f_1(1285)$ meson. We have measured its mass, width, differential cross section, branching ratios, and Dalitz distribution in several decay modes. We find the Dalitz analysis combined with the others measurements in comparison to world data and theoretical models support the identity of this meson being the $f_1(1285)$, with J^{PC} of 1^{++}. This meson is traditionally assigned to a mix of the f_1 and f_8 states of the axial-vector nonet. Its mixing angle and any gluonic component to its wave-function are an active area of study in the phenomenological sector. Contributing the first photoproduction differential cross section results for this state should provide important constraints for further theoretical investigation. A lower than expected signal in the $\rho^0\gamma$ final state admits the possibility of contribution from the $\eta(1295)$, a 0^{-+} state with some controversy surrounding its place in the spectrum of mesons. Future analysis of experiments with more favorable setups to handle spin-parity assignment through detection of neutral decay products and measurement of polarization observables should be able to more definitively quantify the photoproduction of the $f_1(1285)$ and $\eta(1295)$. The nature of both of these states and their position in meson spectroscopy have ramifications towards understanding the quark model and states outside of it. As the first photoproduction results for $f_1(1285)/\eta(1295)$ mesons, this analysis is an important initial step in mapping this area of meson spectroscopy.

Bibliography

[1] K. Nakamura *et al.* Review of particle physics. *J.Phys.G*, G37:075021, 2010.

[2] David J. Gross and Frank Wilczek. Ultraviolet Behavior of Non-Abelian Gauge Theories. *Phys. Rev. Lett.*, 30(26):1343–1346, Jun 1973.

[3] H. David Politzer. Reliable Perturbative Results for Strong Interactions? *Phys. Rev. Lett.*, 30(26):1346–1349, Jun 1973.

[4] Jozef J. Dudek *et al.* Isoscalar meson spectroscopy from lattice QCD. 2011, hep-lat/1102.4299.

[5] Simon Capstick and Winston Roberts. $N\pi$ decays of baryons in a relativized model. *Phys. Rev. D*, 47(5):1994–2010, Mar 1993.

[6] P. H. Baillon, D. Edwards, C. d'Andlau, and A. Astier. Further Study of the e-Meson in Antiproton Proton Annihilation at Rest. *Nuovo Cim.*, A50:393, 1967.

[7] Michael Birkel and Harald Fritzsch. Nucleon spin and the mixing of axial vector mesons. *Phys. Rev. D*, 53(11):6195–6202, Jun 1996.

[8] Isaac Cohen and Harry J. Lipkin. A phenomenological model for pseudoscalar meson mixing. *Nuclear Physics B*, 151:16 – 28, 1979.

[9] Ludvig Faddeev, Antti J. Niemi, and Ulrich Wiedner. Glueballs, closed fluxtubes, and $\eta(1440)$. *Phys. Rev. D*, 70(11):114033, Dec 2004.

[10] A. Masoni, C. Cicalo, and G.L. Usai. The case of the pseudoscalar glueball. *J.Phys.G*, G32:R293–R335, 2006.

[11] Eberhard Klempt and Alexander Zaitsev. Glueballs, hybrids, multiquarks: Experimental facts versus QCD inspired concepts. *Physics Reports*, 454(1-4):1 – 202, 2007.

[12] A. V. Anisovich, D. V. Bugg, N. Djaoshvili, C. Hodd, J. Kisiel, L. Montanet, A. V. Sarantsev, and B. S. Zou. Resonances in $p\bar{p} \to \eta\pi^+\pi^-\pi^+\pi^-$ at rest. *Nuclear Physics A*, 690(4):567 – 594, 2001.

[13] N. I. Kochelev, M. Battaglieri, and R. De Vita. Exclusive photoproduction of $f_1(1285)$ meson off the proton in kinematics available at the Jefferson Laboratory experimental facilities. *Phys. Rev. C*, 80(2):025201, Aug 2009.

[14] A. Sibirtsev, C. Elster, S. Krewald, and J. Speth. Photoproduction of η' mesons from the proton. *AIP Conf.Proc.*, 717:837–841, 2004, nucl-th/0303044.

[15] N. I. Kochelev. private communication.

[16] Sophia K. Domokos, Hovhannes R. Grigoryan, and Jeffrey A. Harvey. Photoproduction through Chern-Simons term induced interactions in holographic QCD. *Phys. Rev. D*, 80(11):115018, Dec 2009.

[17] O. Lahina. *Study of meson properties in quark models.* PhD thesis, University of Pittsburgh, 2006.

[18] Eric Swanson. private communication.

[19] Robert T. Deck. Kinematical Interpretation of the First $\pi - p$ Resonance. *Phys. Rev. Lett.*, 13(5):169–173, Aug 1964.

[20] N. R. Stanton *et al.* Evidence for Axial Vector and Pseudoscalar Resonances Near 1.275 GeV in $\eta\pi^+\pi^-$. *Phys. Rev. Lett.*, 42:346–349, 1979.

[21] J. J. Manak *et al.* Partial-wave analysis of the $\eta\pi^+\pi^-$ system produced in the reaction $\pi^- p \to \eta\pi^+\pi^- n$ at 18 GeV/c. *Phys. Rev.*, D62:012003, 2000, hep-ex/0001051.

[22] D. H. Miller *et al.* $K\bar{K}\pi$ Resonance at 1280 MeV. *Phys. Rev. Lett.*, 14:1074, 1965.

[23] C. d'Andlau, J. Barlow, and A. M. Adamson. Evidence for a Nonstrange Meson of Mass 1290 MeV. *Phys. Lett.*, 17:347, 1965.

[24] D. Barberis *et al.* A measurement of the branching fractions of the $f_1(1285)$ and $f_1(1420)$ produced in central pp interactions at 450 GeV/c. *Phys. Lett.*, B440:225–232, 1998, hep-ex/9810003.

[25] D. Barberis *et al.* A study of the centrally produced 4π channel in pp interactions at 450 GeV/c. *Phys. Lett.*, B413:217–224, 1997, hep-ex/9707021.

[26] D. Barberis *et al.* A spin analysis of the 4π channels produced in central pp interactions at 450 GeV/c. *Phys. Lett.*, B471:440–448, 2000, hep-ex/9912005.

[27] D. Barberis *et al.* A study of the $K\bar{K}\pi$ channel produced centrally in pp interactions at 450 GeV/c. *Phys. Lett.*, B413:225–231, 1997, hep-ex/9707022.

[28] C. N. Yang. Selection Rules for the Dematerialization of a Particle into Two Photons. *Phys. Rev.*, 77(2):242–245, Jan 1950.

[29] M. Acciarri *et al.* Light resonances in $K^0(S)K^\pm\pi^\mp$ and $\eta\pi^+\pi^-$ final states in gamma gamma collisions at LEP. *Phys.Lett.*, B501:1–11, 2001, hep-ex/0011035.

[30] P. Achard *et al.* $f_1(1285)$ formation in two photon collisions at LEP. *Phys.Lett.*, B526:269–277, 2002, hep-ex/0110073.

[31] G. S. Adams *et al.* Observation of pseudoscalar and axial vector resonances in $\pi^- p \to K^+K^-\pi^0 n$ at 18 GeV. *Phys. Lett.*, B516:264–272, 2001, hep-ex/0107042.

[32] M. Battaglieri *et al.* Spectroscopy of Exotic Baryons with CLAS: Search for ground and first excited states. *CLAS Analysis Proposal*, PR04-21, 2004.

[33] Jefferson Lab. The JLab Picture Exchange. http://www1.jlab.org/ul/jpix.

[34] B.M. Dumham. Jefferson Lab, a status report, 1997.

[35] D. I. Sober *et al.* The bremsstrahlung tagged photon beam in Hall B at JLab. *Nuclear Instruments and Methods in Physics Research Section A: Accelerators, Spectrometers, Detectors and Associated Equipment*, 440(2):263 – 284, 2000.

[36] B. A. Mecking *et al.* The CEBAF large acceptance spectrometer (CLAS). *Nuclear Instruments and Methods in Physics Research Section A: Accelerators, Spectrometers, Detectors and Associated Equipment*, 503(3):513 – 553, 2003.

[37] Steve Christo. The g11a Target Cell. http://www.jlab.org/~christo/g11a_target.html.

[38] Y.G. Sharabian *et al.* A new highly segmented start counter for the CLAS detector. *Nuclear Instruments and Methods in Physics Research Section A: Accelerators, Spectrometers, Detectors and Associated Equipment*, 556(1):246 – 258, 2006.

[39] M. D. Mestayer *et al.* The CLAS drift chamber system. *Nuclear Instruments and Methods in Physics Research Section A: Accelerators, Spectrometers, Detectors and Associated Equipment*, 449(1-2):81 – 111, 2000.

[40] M. Williams. *Measurement of Differential Cross Sections and Spin Density Matrix Elements along with a Partial Wave Analysis for $\gamma p \to p\omega$ using CLAS at Jefferson Lab.* PhD thesis, Carnegie Mellon University, 2007.

[41] E. Smith. PDL Report -g11. http://clasweb.jlab.org/group_meeting_minutes/Physics/2004/Minutes_2004_06_07.html Hall B Group Meeting Minutes June 7, 2004.

[42] M. Ungaro, R. De Vita, and L. Elouadrhiri. g11 Data Processing. *CLAS-Note*, 2005-004.

[43] M. McCracken. *A Study of $K^+\Lambda$ Photoproduction in the CLAS g11a Dataset: Differential Cross Section, Recoil Polarization, and a Partial-Wave Analysis.* PhD thesis, Carnegie Mellon University, 2008.

[44] K. Moriya. *Measurement of the Lineshape, Differential Photoproduction Cross Section, Spin and Parity of the $\Lambda(1405)$ Using CLAS at Jefferson Lab.* PhD thesis, Carnegie Mellon University, 2010.

[45] M. Williams and C.A. Meyer. Kinematic Fitting in CLAS. *CLAS-Note*, 2003-017.

[46] C.A. Meyer and M. Williams. Kinematic Fitting the Reaction $\gamma d \to K^+K^-p(n)missing$. *CLAS-Analysis-Note*, 2004-109.

[47] E. Pasyuk. Energy loss corrections for charged particles in CLAS. *CLAS-Note*, 2007-016.

[48] D. Sober, H. Crannell, and F.J. Klein. The Tagger Energy Scale: Interpreting the CMU Kinematic Fit Results. *CLAS-Note*, 2004-019.

[49] D. Applegate, M. Bellis, Z. Krahn, and M. Meyer, C. andWilliams. A detailed study of the sources of systematic errors in the clas g11 data. *CLAS-Note*, 2006-017.

[50] R. Bradford and R.A. Schumacher. Liquid Hydrogen Density in the G1C CLAS Target. *CLAS-Note*, 2002-003.

[51] J. Ball and E. Pasyuk. Photon Flux Determination Through Sampling of "out-of-time" Hits with the Hall B Photon Tagger. *CLAS-Note*, 2005-002.

[52] M. Holtrop. GSIM: CLAS GEANT Simulation. http://www.physics.unh.edu/maurik/gsim/gsim_info.html.

[53] R. H. Dalitz. On the analysis of τ-meson data and the nature of the τ-meson. *Phil. Mag.*, 44:1068–1080, 1953.

[54] M. Williams *et al.* Differential cross sections and spin density matrix elements for the reaction $\gamma p \to p\omega$. *Phys. Rev. C*, 80(6):065208, Dec 2009.

[55] M. Williams *et al.* Differential cross sections for the reactions $\gamma p \to p\eta$ and $\gamma p \to p\eta'$. *Phys. Rev. C*, 80(4):045213, Oct 2009.

[56] R.A. Schumacher. Photon Attenuation in the CLAS Beam Line. *CLAS-Note*, 2001-010.

[57] S. U. Chung *et al.* Spin and Parity Analysis of $K\bar{K}\pi$ System in the D and E/Iota Regions. *Phys. Rev. Lett.*, 55:779, 1985.

[58] A. Ando *et al.* Evidence for Two Pseudoscalar Resonances of $\eta\pi^+\pi^-$ System in the D(1285) and E/iota Regions. *Phys. Rev. Lett.*, 57:1296, 1986.

[59] J. Abdallah *et al.* Measurement of inclusive $f_1(1285)$ and $f_1(1420)$ production in Z decays with the DELPHI detector. *Phys. Lett.*, B569:129–139, 2003, hep-ex/0309057.

[60] N. I. Kochelev, M. Battaglieri, and R. De Vita. Exclusive photoproduction of $f1(1285)$ meson off the proton in kinematics available at the Jefferson Laboratory experimental facilities. *Phys. Rev. C*, 80(2):025201, Aug 2009.

[61] R. Ahohe *et al.* The search for $\eta(1440) \to K^0(S)K^\pm\pi^\mp$ in two-photon fusion at CLEO. *Phys. Rev.*, D71:072001, 2005, hep-ex/0501026.

[62] S. Teige *et al.* Properties of the $a(980)$ meson. *Phys. Rev. D*, 59(1):012001, Nov 1998.

[63] S. M. Flatté. Coupled-channel analysis of the $\pi\eta$ and KK systems near KK threshold. *Physics Letters B*, 63(2):224 – 227, 1976.

[64] Charles Zemach. Three-Pion Decays of Unstable Particles. *Phys. Rev.*, 133(5B):B1201–B1220, Mar 1964.

[65] D. Alde *et al.* Partial-wave analysis of the $\eta\pi^0\pi^0$ system produced in π^-p charge exchange collisions at 100-GeV/c. *Phys. Atom. Nucl.*, 60:386–390, 1997.

Appendix A

Domokos Regge Model

For comparison to our results and the predictions we obtained from Kochelev [15], we recomputed the formula from Domokos for $f_1(1285)$ photoproduction cross section calculations [16] in our kinematics and binned in $\cos\Theta_{CM}$ rather the the Mandelstam variable t used in the paper.

Starting with couplings and constants defined in the paper

$$r = 1 + \frac{g_{\omega NN} g_{\gamma\omega f_1}}{g_{\rho NN} g_{\gamma\rho f_1}} \simeq 2.25 \tag{A.1}$$

$$\alpha_{em} = \frac{e^2}{\hbar c} \tag{A.2}$$

$$g_{\rho NN} = 2.4 \tag{A.3}$$

$$g_{\gamma\rho f_1} = -0.99 \tag{A.4}$$

$$A'_v = 0.9 \tag{A.5}$$

$$s_0 = 1 \tag{A.6}$$

and the relevant masses and cutoffs

$$M_n = 0.938272 \quad \text{GeV} \tag{A.7}$$

$$M_{f_1} = 1.2817 \quad \text{GeV} \tag{A.8}$$

$$M_\rho = 0.7685 \quad \text{GeV} \tag{A.9}$$

$$M^2_{dipole} = 0.71 \quad \text{GeV}^2 \tag{A.10}$$

$$\Delta_{VNN} = 0.8 \quad \text{GeV} \tag{A.11}$$

$$\Lambda_{VNN} = 0.8\,\text{GeV} \tag{A.12}$$

and some helpful functions

$$\Gamma(z) = \int_0^\infty t^{z-1} e^{-t}\,\mathrm{d}t \tag{A.13}$$

$$A_V = r^2 \alpha_{em} g^2_{\rho NN} g^2_{\gamma\rho f_1} \tag{A.14}$$

we compute in the center-of-mass frame for each W bin

$$s = W^2 \tag{A.15}$$
$$E_{\gamma\,CM} = (w^2 - M_N^2)/(2w) \tag{A.16}$$
$$E_{pin\,CM} = (w^2 + M_N^2)/(2w) \tag{A.17}$$
$$E_{f\,CM} = (w^2 + M_{f_1}^2 - M_N^2)/(2w) \tag{A.18}$$
$$E_{pout\,CM} = (w^2 + M_N^2 - M_{f_1}^2)/(2w) \tag{A.19}$$
$$p_{\gamma\,CM} = e_{\gamma\,CM} \tag{A.20}$$
$$p_{pin\,CM} = \sqrt{e_{pin\,CM}^2 - M_N^2} \tag{A.21}$$
$$p_{f\,CM} = \sqrt{e_{f\,CM}^2 - M_{f_1}^2} \tag{A.22}$$
$$p_{pout\,CM} = \sqrt{e_{pout\,CM}^2 - M_N^2} \tag{A.23}$$

and the other Mandelstam variables

$$t = (e_{\gamma\,CM} - e_{f\,CM})^2 - (p_{\gamma\,CM} - p_{f\,CM}) - 2p_{\gamma\,CM}p_{f\,CM}(1 - \cos\Theta_f) \tag{A.24}$$
$$u = 2M_N^2 + M_{f_1}^2 - s - t \tag{A.25}$$
$$\tag{A.26}$$

used for the Regge trajectory, dipole Form Factor and finally differential cross section.

$$\alpha_v(t) = 0.5 + 0.9 \times t\mathrm{GeV}^2 \tag{A.27}$$
$$\alpha_v' = 0.9\mathrm{GeV}^2 \tag{A.28}$$
$$F(t) = \left(\frac{1}{(1 - t/M_{dipole}^2)}\right)^2 \tag{A.29}$$
$$\frac{d\sigma_R}{dt} \simeq \pi^2 A_V F^2(t) \frac{(1 - \frac{t}{2M_{f_1}})\alpha_V'^2}{16\Gamma^2(\alpha_V(t))\cos^2(\pi\alpha_V(t)/2)} \left(\frac{s}{s_0}\right)^{2(\alpha_V(t)-1)} \tag{A.30}$$

Using the relevent Jacobian transformation gives

$$\frac{d\sigma_R}{d\Omega} = \frac{p_\gamma p_f}{\pi} \times \frac{d\sigma}{dt} \tag{A.31}$$

then we multiply by

$$(\hbar c)^2 = 0.389379304(19)\,\mathrm{GeV}^2\,mbarn \tag{A.32}$$

to get from GeV^{-2} to units of cross section for comparison to our measured values.

Appendix B

Fit Results

Figures B.1 to B.5 show $x(1280)$ yield fits of the missing mass off the proton spectra using a Voigtian signal and polynomial background in the $\eta\pi^+\pi^-$ decay mode. Figures B.6 to B.10 show $x(1280)$ yield fits of the missing mass off the proton spectra using a set of Monte Carlo backgound spectra along with a Monte Carlo $x(1280)$ signal in the $\eta\pi^+\pi^-$ decay mode. Figures B.11 to B.15 show $x(1280)$ yield fits of the missing mass off the proton spectra using a Voigtian signal and polynomial background in the $K^\pm K^0\pi^\mp$ decay mode.

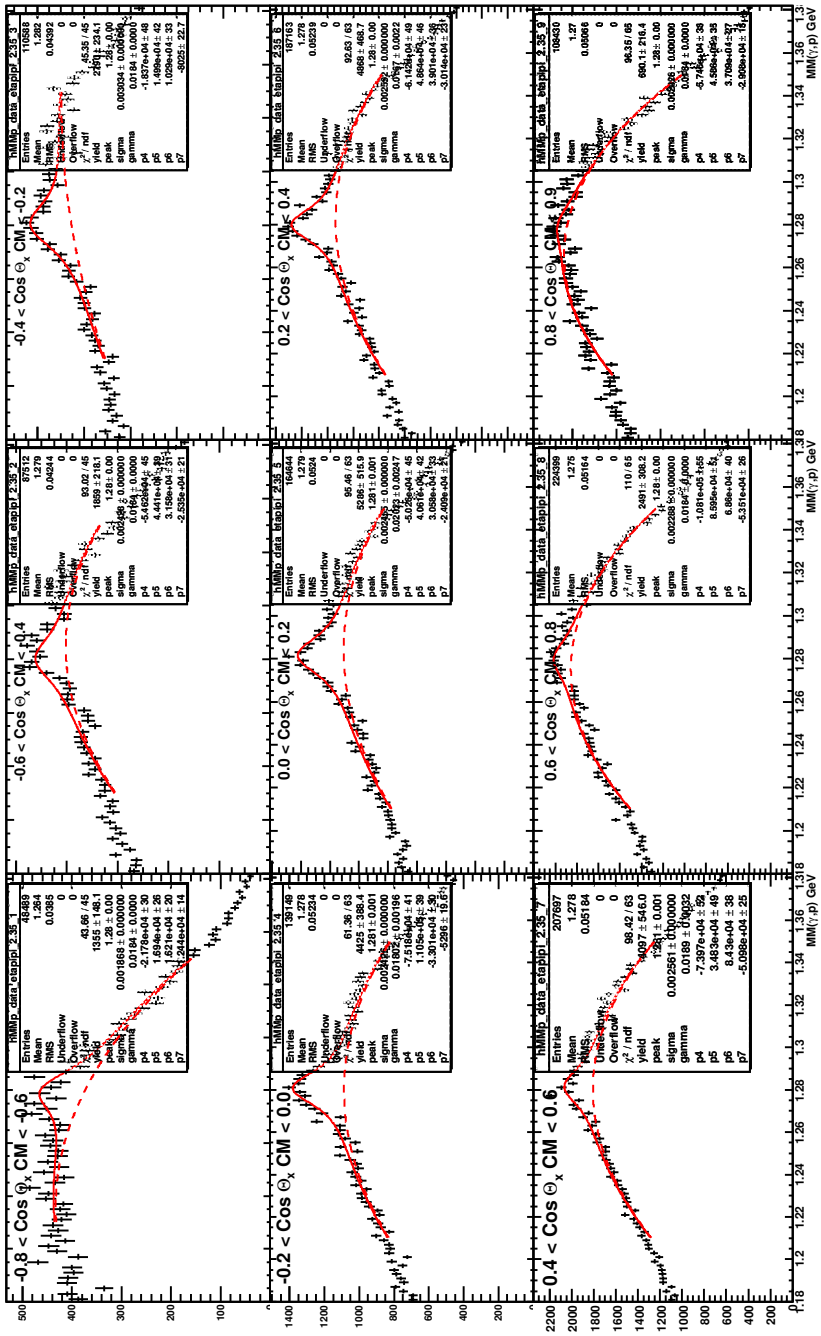

Figure B.1: $W = 2.35$ Yields for $x(1280) \rightarrow \eta\pi^+\pi^-$

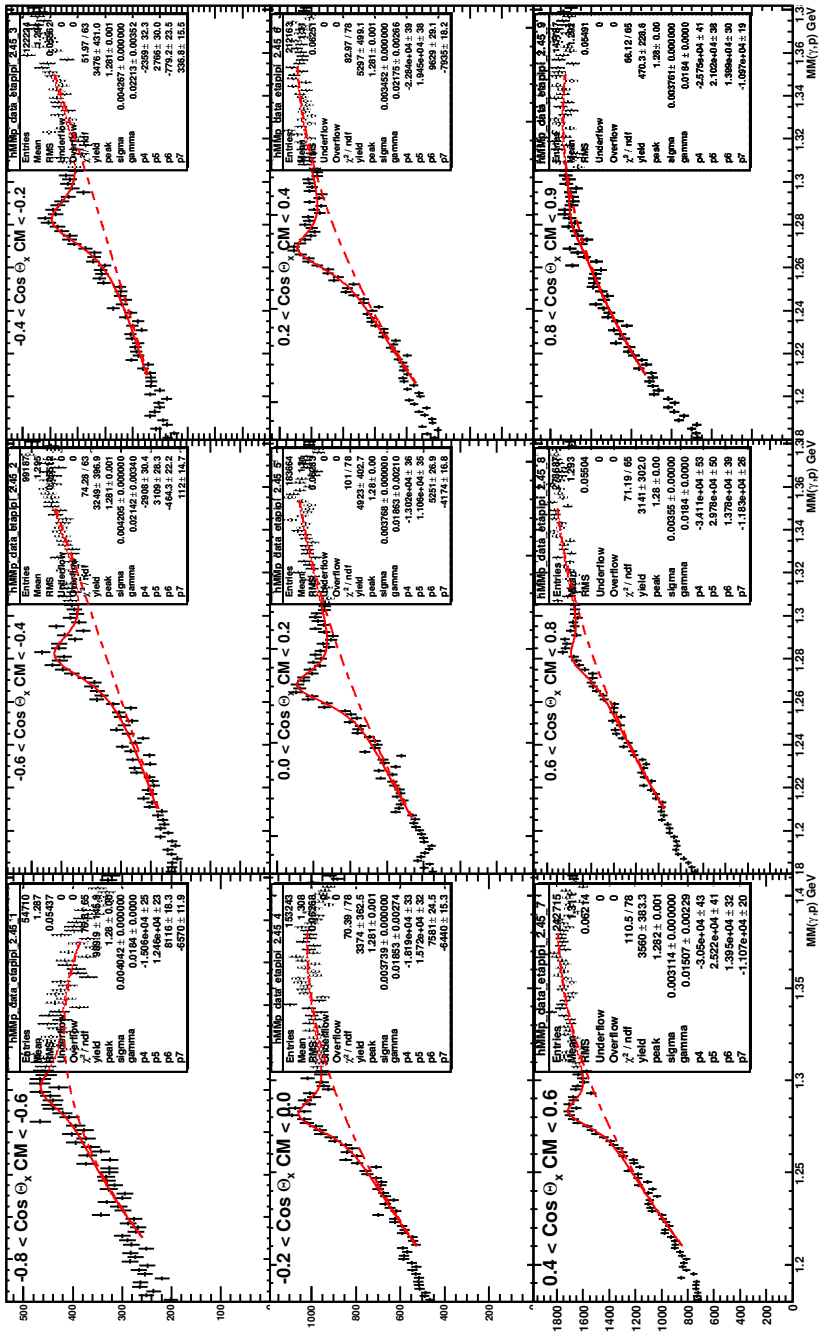

Figure B.2: $W = 2.45$ Yields for $x(1280) \rightarrow \eta\pi^+\pi^-$

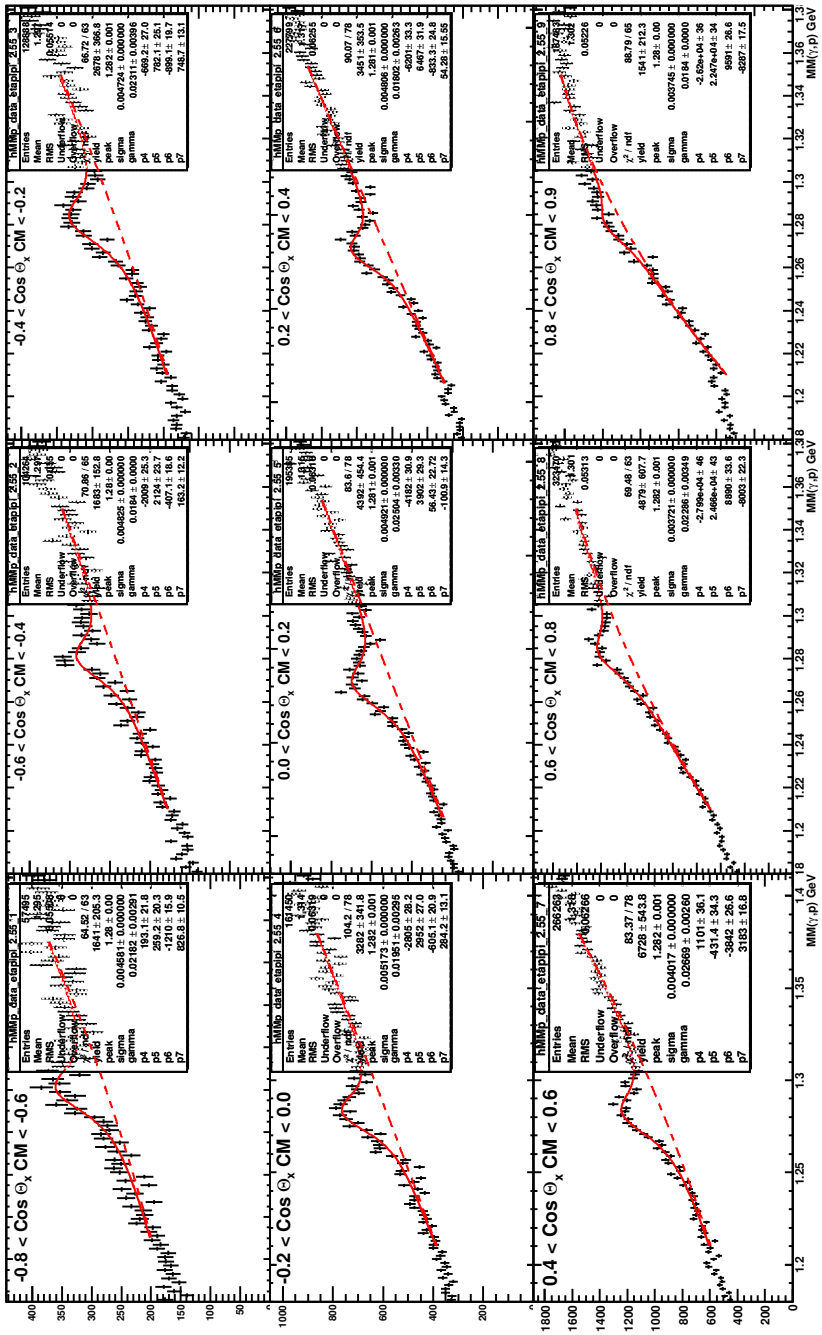

Figure B.3: $W = 2.55$ Yields for $x(1280) \rightarrow \eta\pi^+\pi^-$

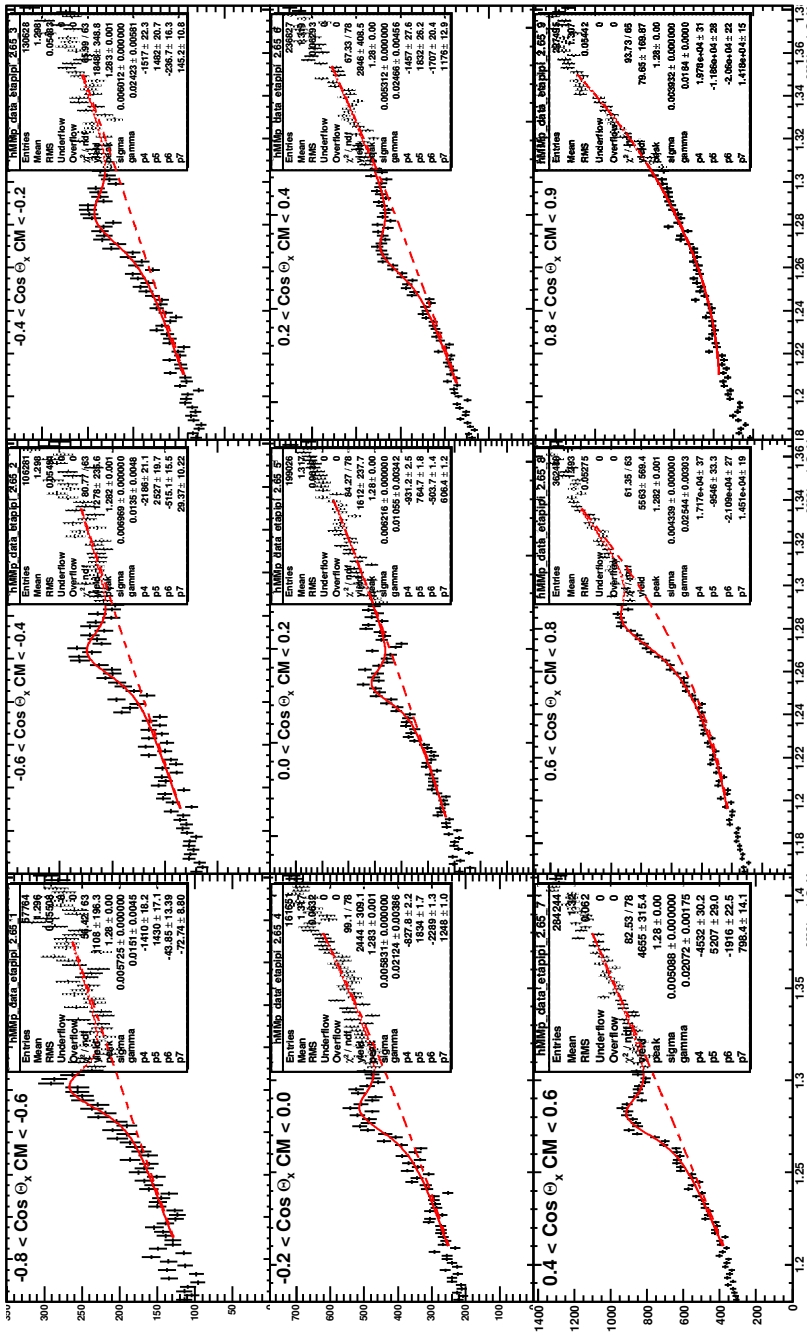

Figure B.4: $W = 2.65$ Yields for $x(1280) \rightarrow \eta\pi^+\pi^-$

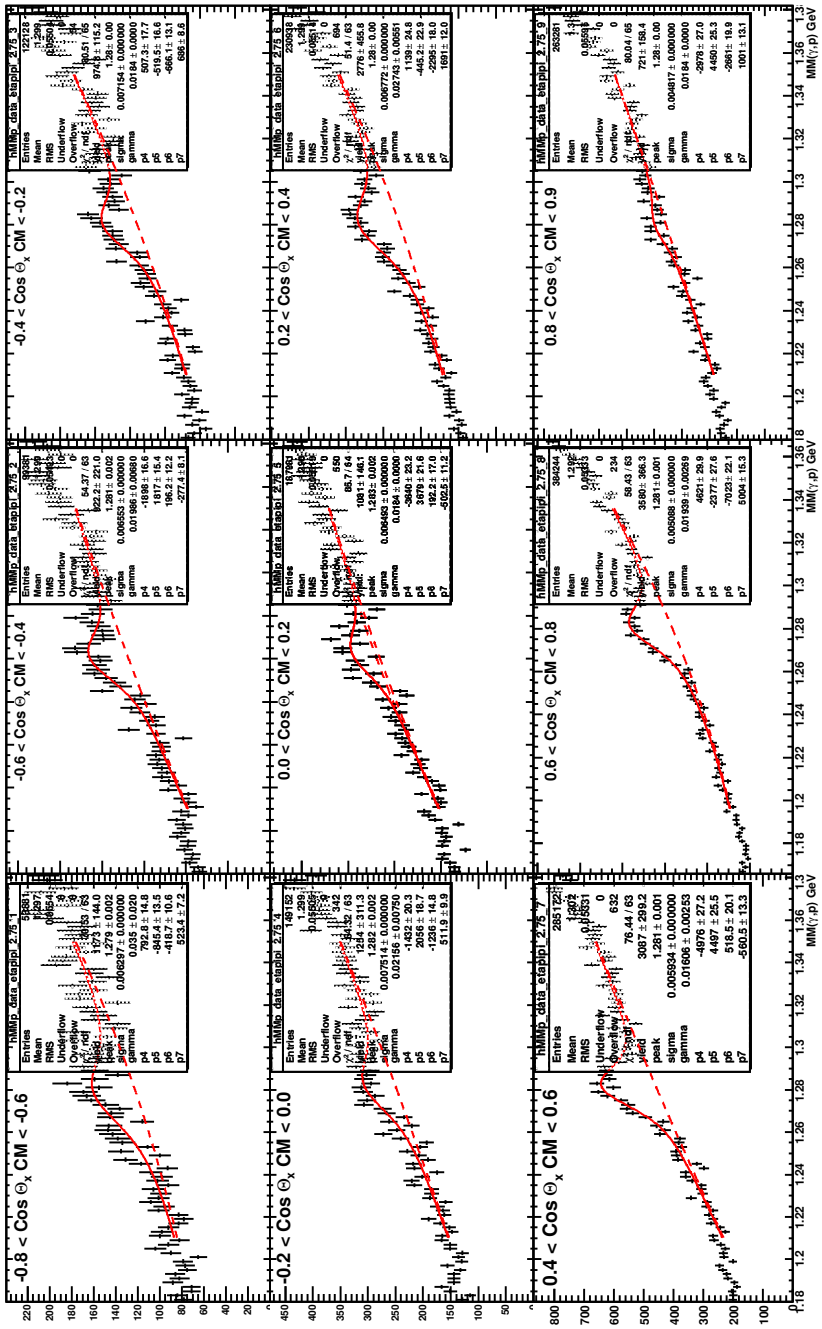

Figure B.5: $W = 2.75$ Yields for $x(1280) \rightarrow \eta\pi^+\pi^-$

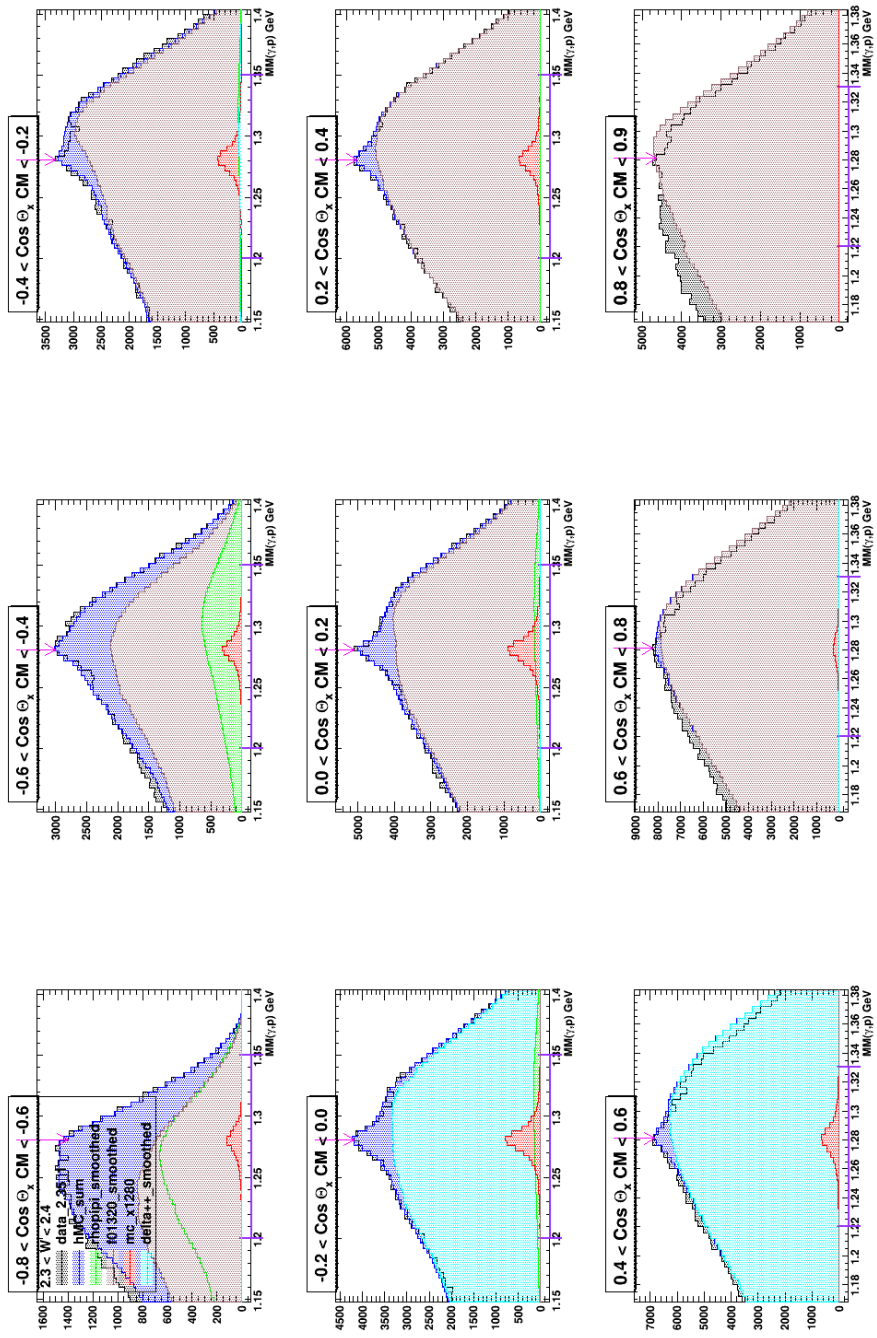

Figure B.6: $W = 2.35$ Yields for $x(1280) \rightarrow \eta\pi^+\pi^-$

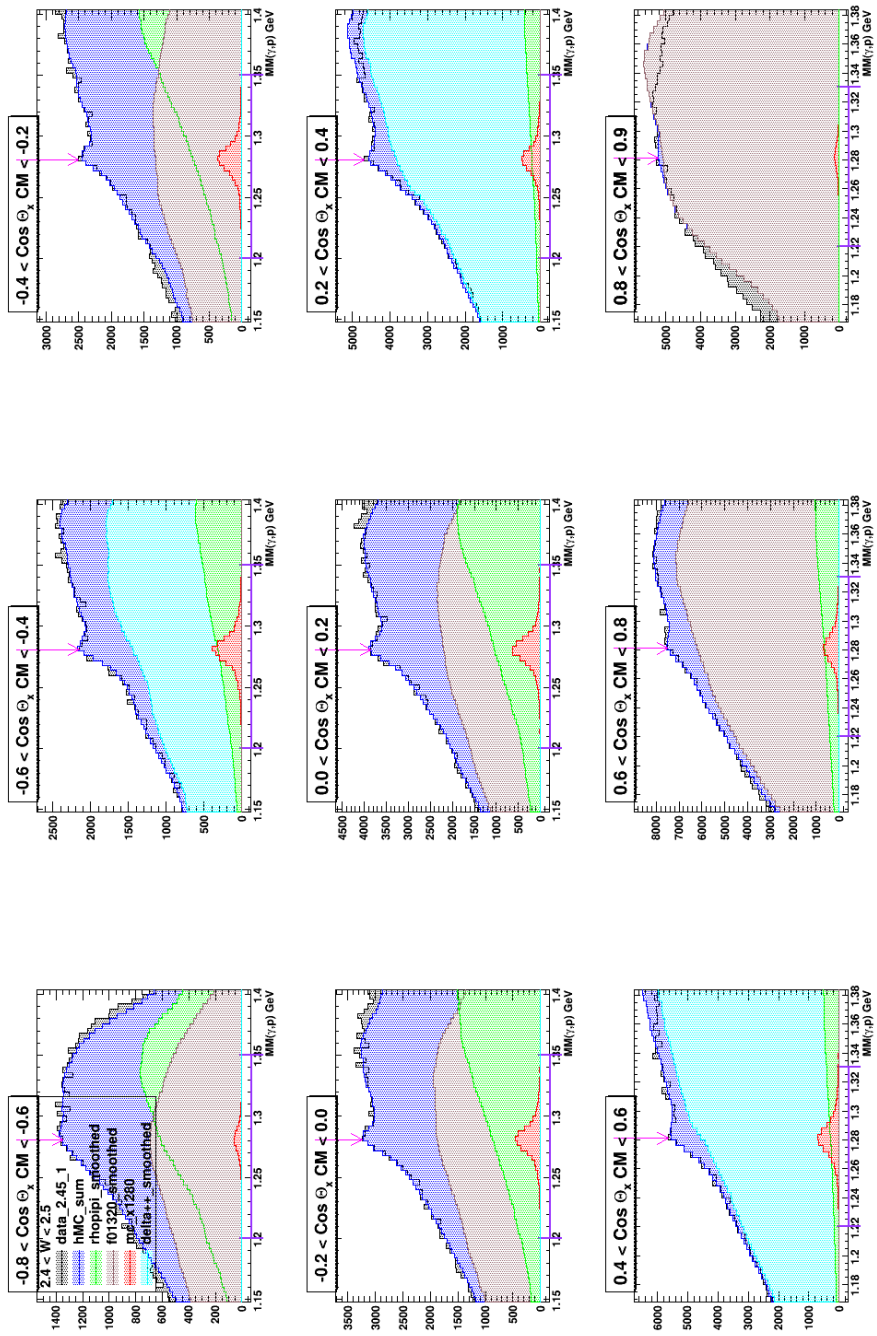

Figure B.7: $W = 2.45$ Yields for $x(1280) \rightarrow \eta\pi^+\pi^-$

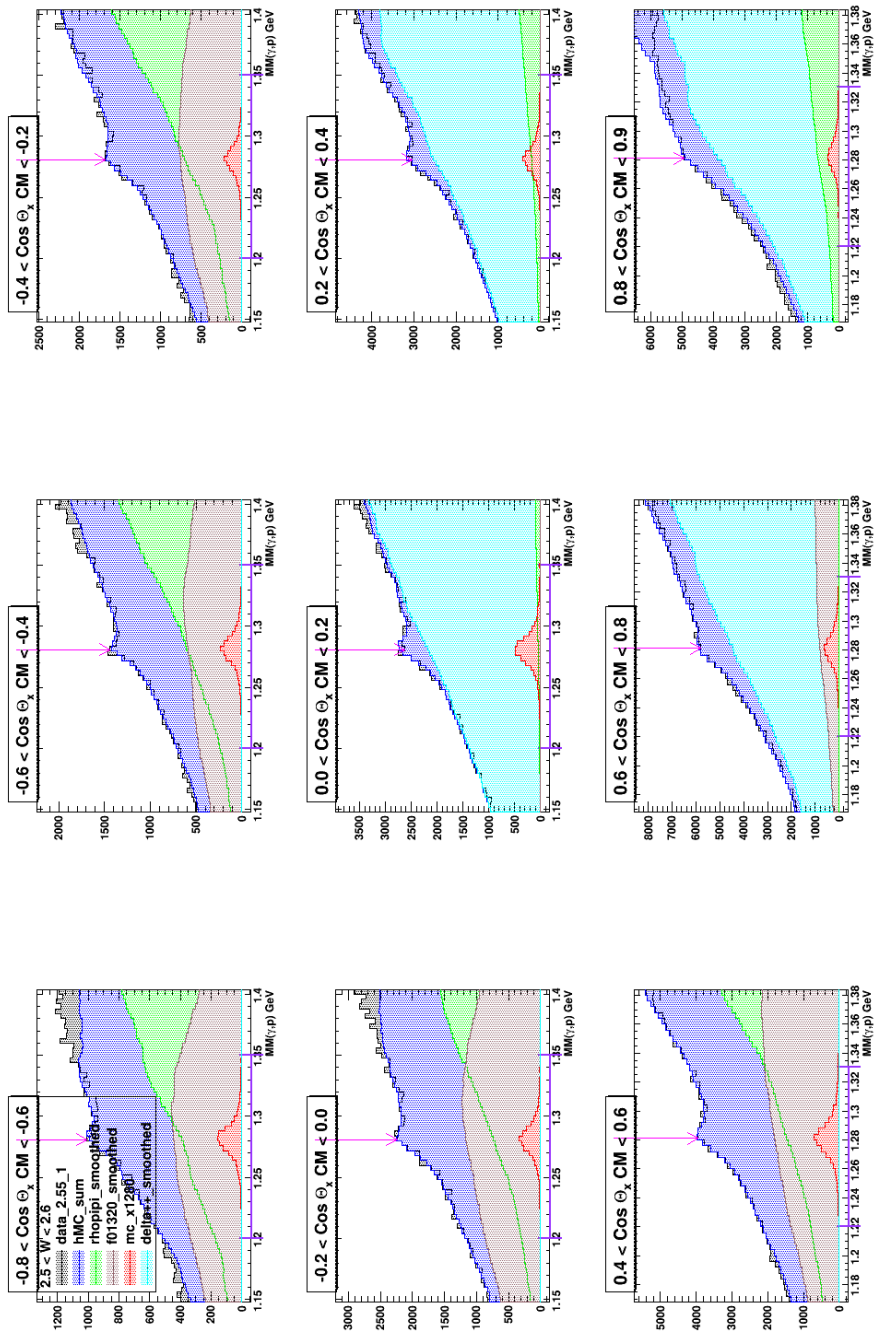

Figure B.8: $W = 2.55$ Yields for $x(1280) \to \eta\pi^+\pi^-$

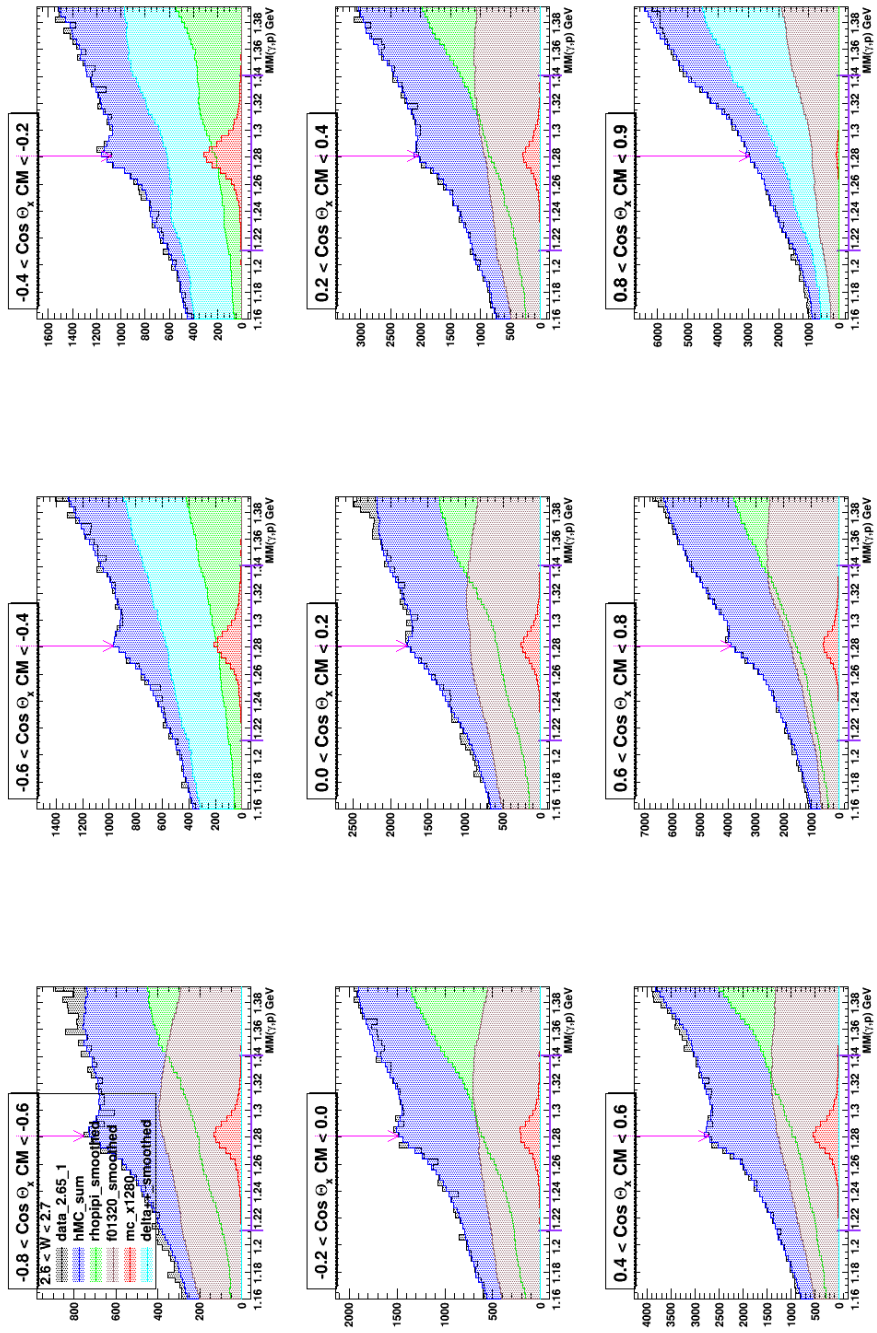

Figure B.9: $W = 2.65$ Yields for $x(1280) \rightarrow \eta\pi^+\pi^-$

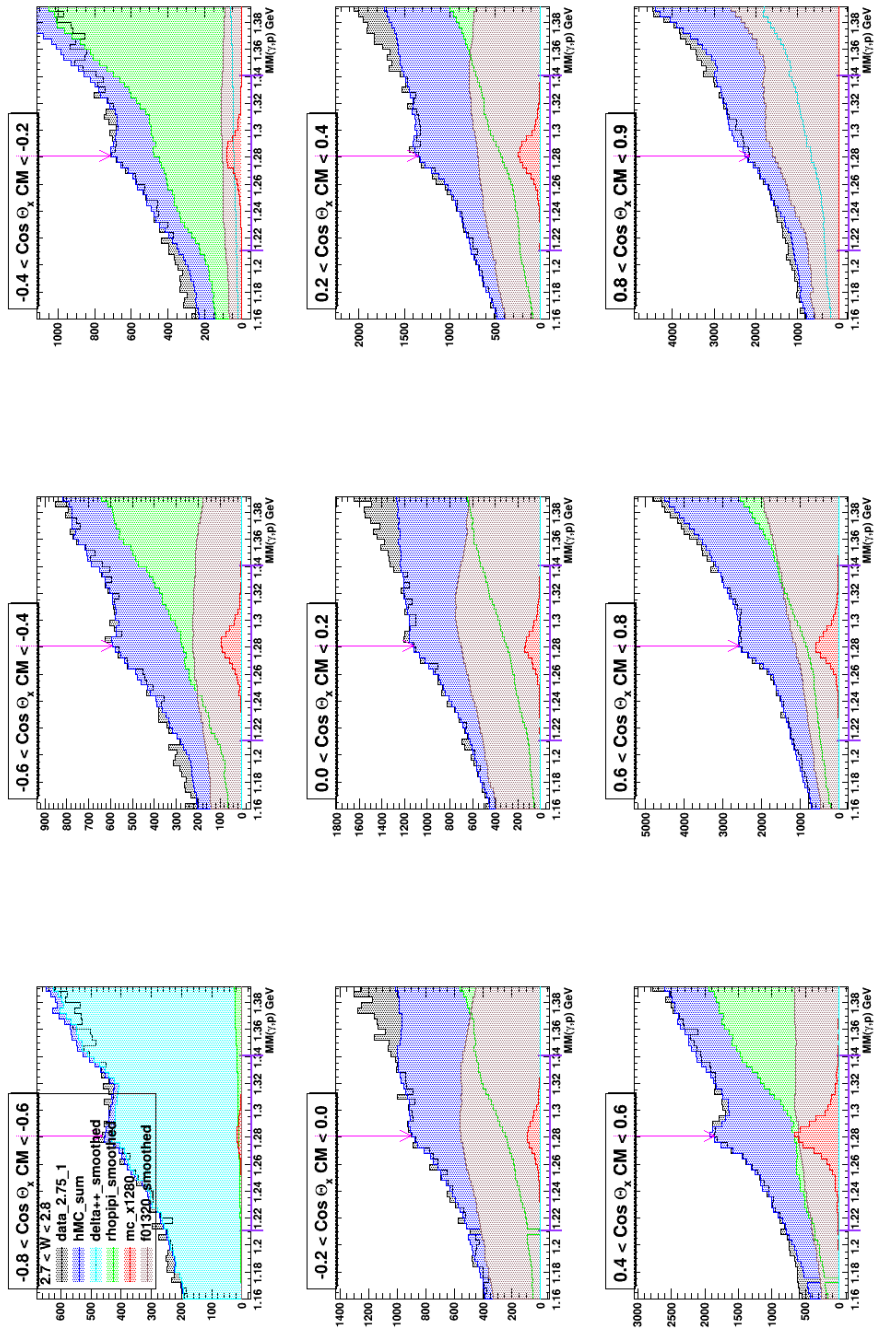

Figure B.10: $W = 2.75$ Yields for $x(1280) \rightarrow \eta\pi^+\pi^-$

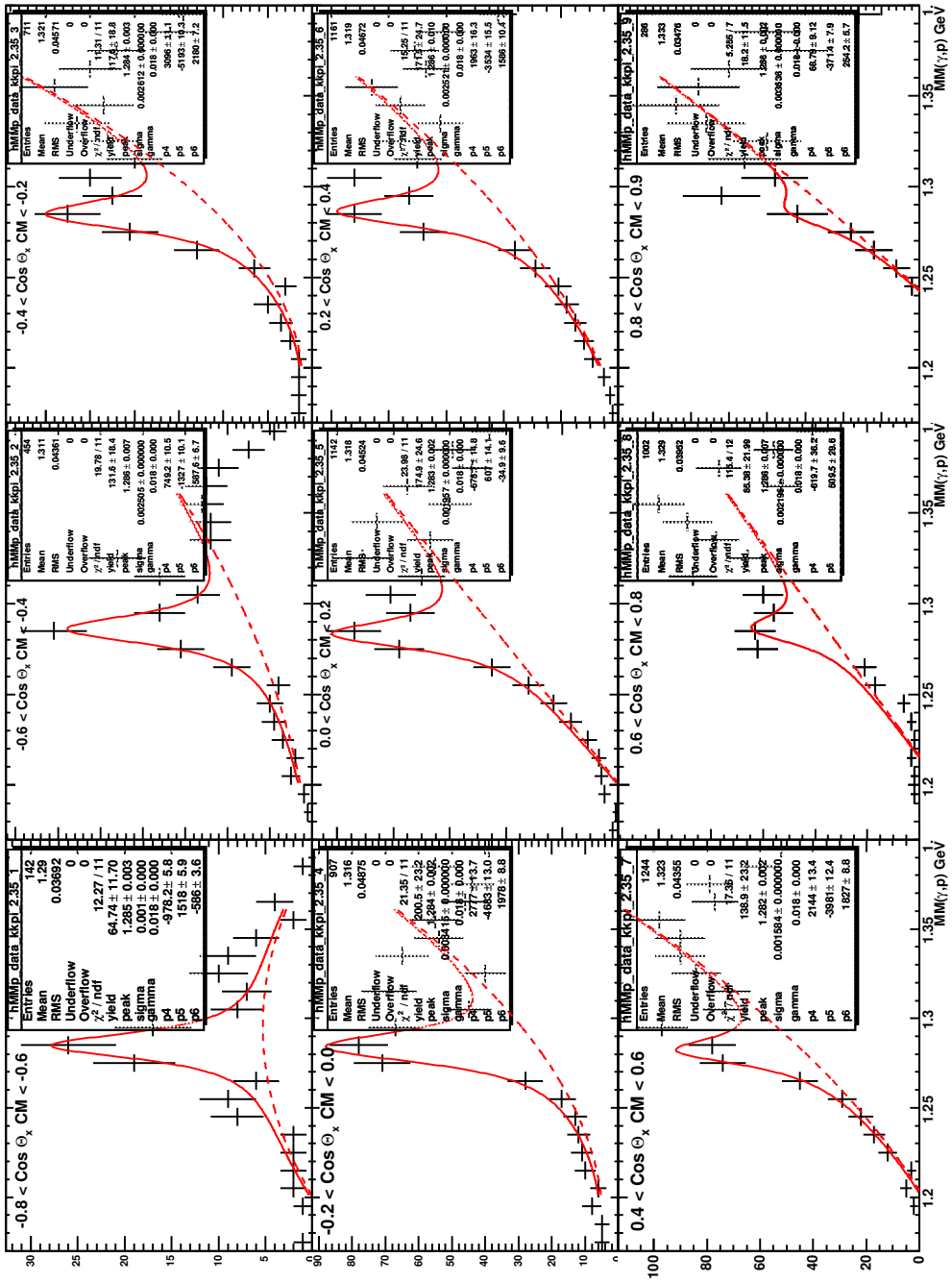

Figure B.11: $W = 2.35$ Yields for $x(1280) \rightarrow K^{\pm}K^{0}\pi^{\mp}$

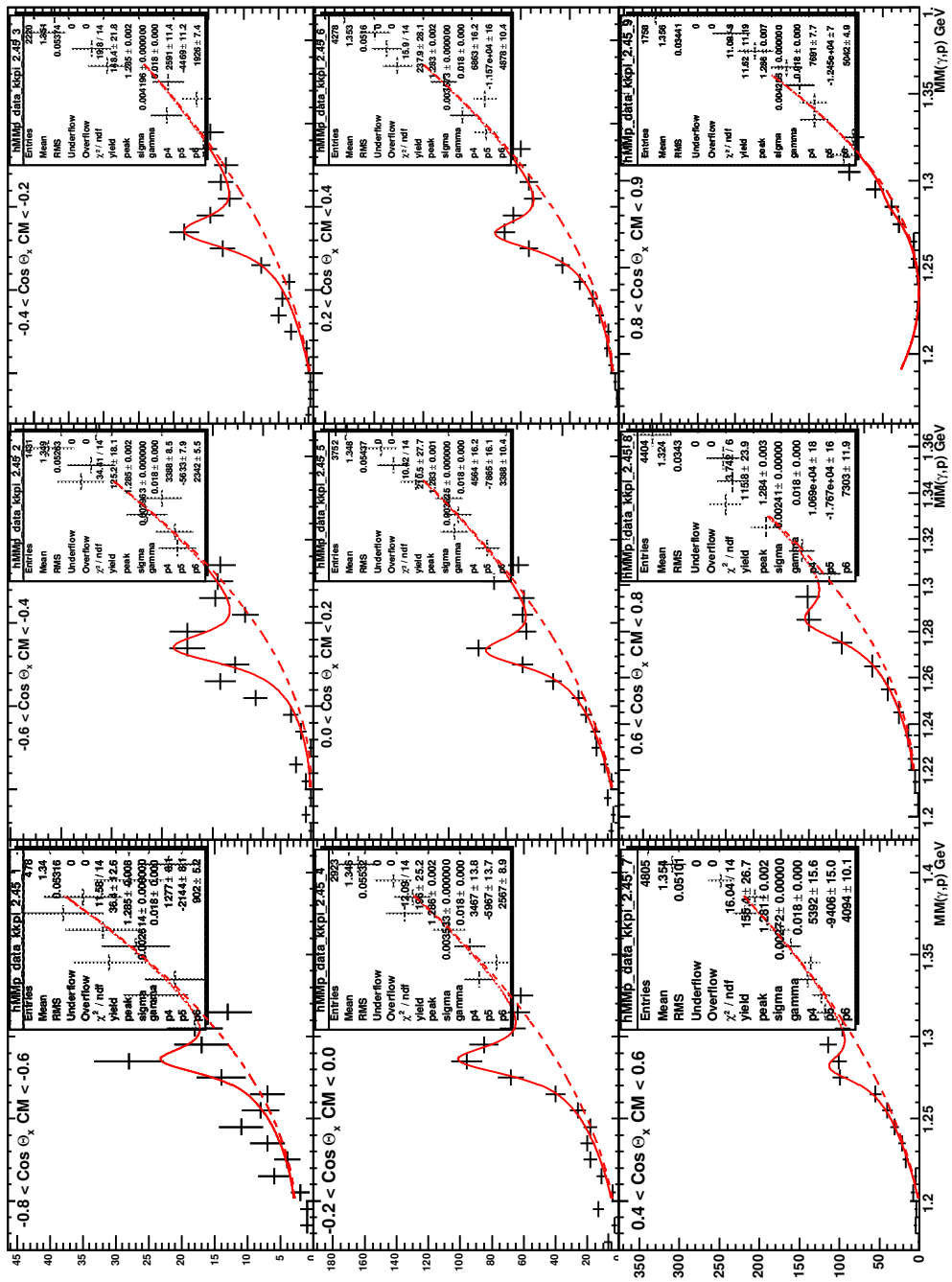

Figure B.12: $W = 2.45$ Yields for $x(1280) \rightarrow K^{\pm}K^{0}\pi^{\mp}$

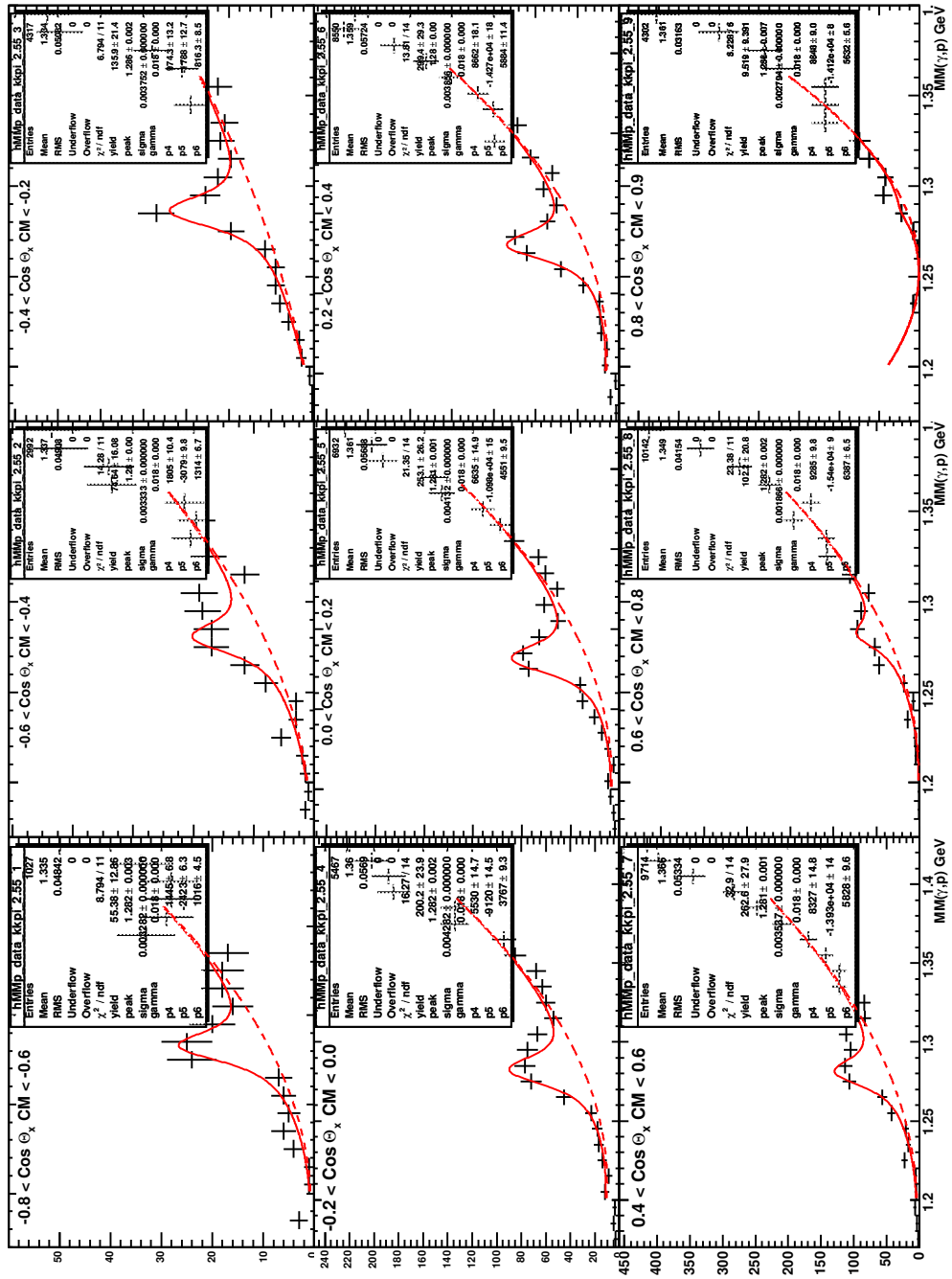

Figure B.13: $W = 2.55$ Yields for $x(1280) \rightarrow K^{\pm} K^{0} \pi^{\mp}$

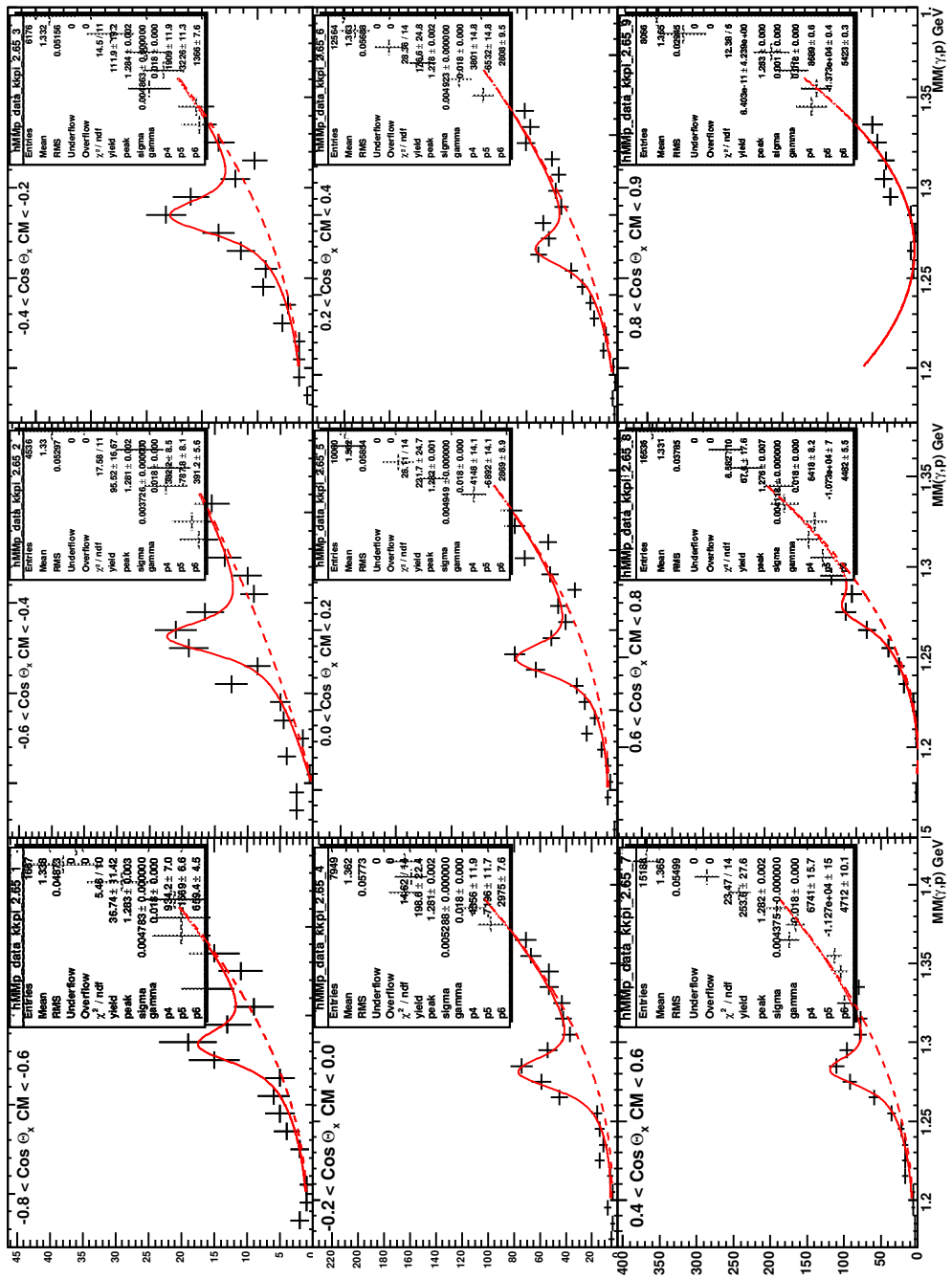

Figure B.14: $W = 2.65$ Yields for $x(1280) \rightarrow K^{\pm}K^{0}\pi^{\mp}$

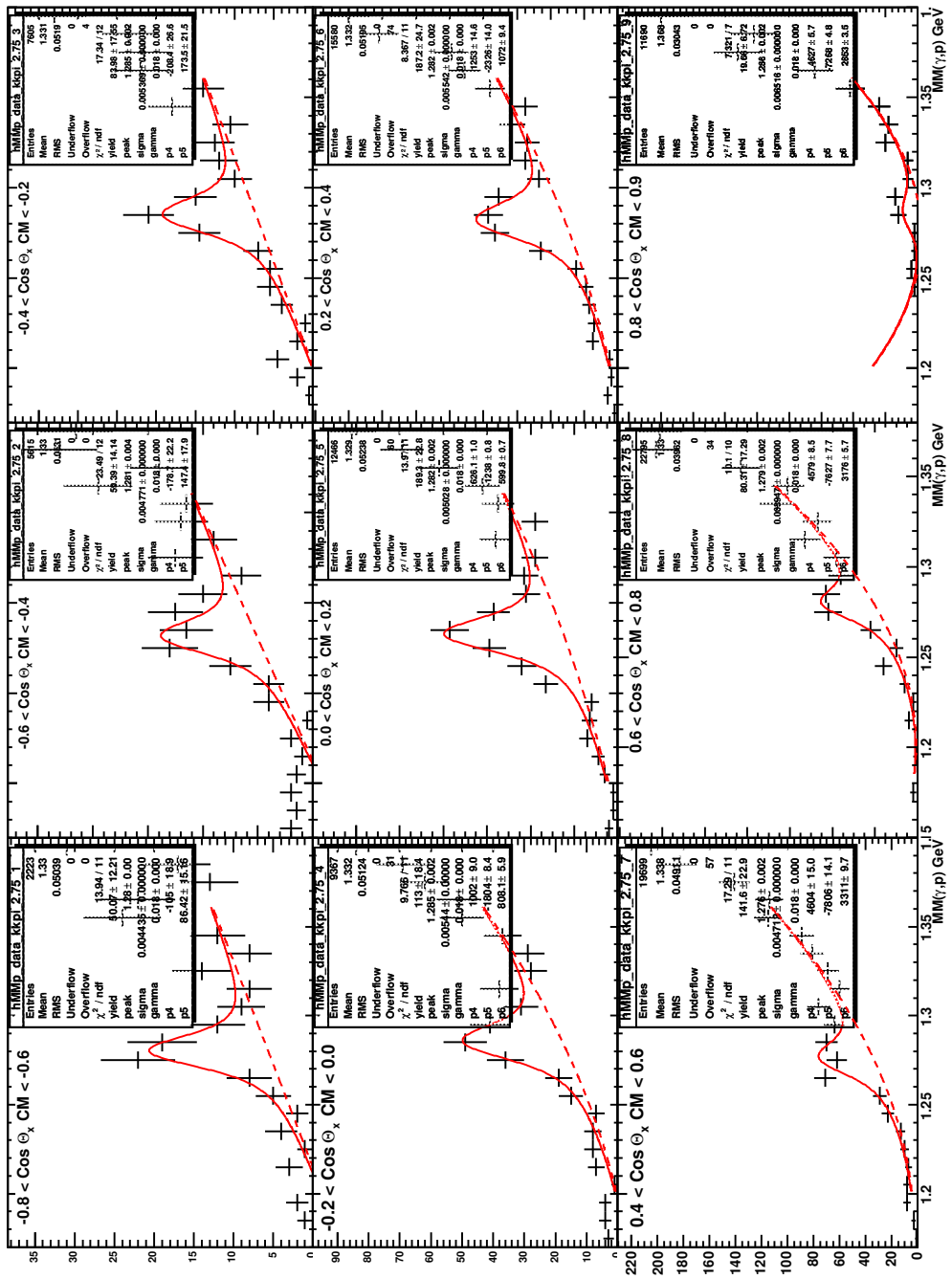

Figure B.15: $W = 2.75$ Yields for $x(1280) \rightarrow K^{\pm}K^{0}\pi^{\mp}$

Appendix C

$x(1280)$ Cross Section Results

C.1 $x(1280)$ results from $\eta\pi^+\pi^-$ and $K^\pm K^0\pi^\mp$

These results are the weighted mean of independent measurements in the $\eta\pi^+\pi^-$ and $K^\pm K^0\pi^\mp$ decay modes of the $x(1280)$. The $K^\pm K^0\pi^\mp$ results were first scaled using our measurement of the branching ratio $\Gamma(x(1280) \to K^\pm K^0\pi^\mp)/\Gamma(x(1280) \to \eta\pi^+\pi^-)$. These results have *not* been corrected for the unknown branching fraction $\Gamma(x(1280) \to \eta\pi^+\pi^-)/\Gamma_x$. The systematic uncertainty σ_{sys} given includes the sources listed in Table 5.2 and those discussed in §4.5.

$W(GeV)$	$\cos\Theta^x_{CM}$	$\frac{d\sigma}{d\Omega}$ (nb/sr)	σ_{stat} (nb/sr)	σ_{sys} (nb/sr)
2.35	-0.70	5.96	0.57	1.57
2.35	-0.50	4.70	0.45	0.66
2.35	-0.30	6.42	0.54	0.90
2.35	-0.10	8.37	0.74	1.26
2.35	0.10	8.29	0.67	1.17
2.35	0.30	7.81	0.64	1.26
2.35	0.50	7.42	0.76	1.05
2.35	0.70	5.01	0.58	0.70
2.35	0.85	3.18	1.00	0.45
2.45	-0.70	2.80	0.40	0.93
2.45	-0.50	6.42	0.60	1.07
2.45	-0.30	6.39	0.63	1.32
2.45	-0.10	5.73	0.48	0.75
2.45	0.10	7.29	0.52	1.04
2.45	0.30	8.10	0.60	1.96
2.45	0.50	6.58	0.62	1.16
2.45	0.70	6.68	0.59	1.45
2.45	0.85	2.16	1.05	0.26
2.55	-0.70	4.22	0.49	0.88
2.55	-0.50	3.50	0.30	0.44
2.55	-0.30	4.38	0.51	1.46
2.55	-0.10	5.37	0.42	1.10
2.55	0.10	6.57	0.48	1.08
2.55	0.30	6.70	0.52	1.01
2.55	0.50	12.12	0.78	2.66
2.55	0.70	9.70	1.04	1.46

Continued on next page

Table C.1 – continued from previous page

$W(GeV)$	$\cos\Theta^x_{CM}$	$\frac{d\sigma}{d\Omega}$ (nb/sr)	σ_{stat} (nb/sr)	σ_{sys} (nb/sr)
2.55	0.85	7.95	1.10	2.20
2.65	-0.70	2.21	0.35	0.37
2.65	-0.50	2.58	0.33	0.39
2.65	-0.30	2.85	0.37	0.40
2.65	-0.10	3.73	0.31	0.84
2.65	0.10	3.03	0.28	0.86
2.65	0.30	4.26	0.43	0.86
2.65	0.50	8.40	0.49	1.40
2.65	0.70	9.81	1.06	2.40
2.65	0.85	0.50	1.06	1.90
2.75	-0.70	2.49	0.28	0.32
2.75	-0.50	1.55	0.26	0.20
2.75	-0.30	1.70	0.18	0.30
2.75	-0.10	1.71	0.28	0.44
2.75	0.10	1.95	0.19	0.25
2.75	0.30	4.01	0.41	1.00
2.75	0.50	5.15	0.45	1.82
2.75	0.70	9.26	0.90	1.29
2.75	0.85	5.73	1.21	0.74

C.2 η' results from $\eta\pi^+\pi^-$ and $\rho^0\gamma$

The results for η' are presented for reference and systematic considerations. The listed deviation from M. Williams published results used a cubic spline interpolation between points in his $\cos\Theta_{CM}$ binning in order to compute the difference between our values and his results.

$W(GeV)$	$\cos\Theta^x_{CM}$	$\frac{d\sigma}{d\Omega}$ (nb/sr)	σ_{stat} (nb/sr)	Deviation from CLAS 2009 [55] (%)
2.05	-0.70	38.92	1.41	-5.8
2.05	-0.50	44.73	1.56	-4.6
2.05	-0.30	49.33	1.69	-4.7
2.05	-0.10	54.21	1.79	-14.7
2.05	0.10	58.02	1.91	-5.7
2.05	0.30	65.76	2.12	-7.4
2.05	0.50	71.30	2.32	-12.9
2.05	0.70	77.96	2.60	-1.9
2.05	0.85	68.89	2.42	-9.8
2.15	-0.70	24.08	0.94	-4.1
2.15	-0.50	24.82	0.93	-8.3
2.15	-0.30	25.45	0.92	-4.6
2.15	-0.10	29.00	1.03	-8.8
2.15	0.10	33.80	1.19	-5.6
2.15	0.30	48.23	1.66	-5.0
2.15	0.50	70.21	2.30	-7.9
2.15	0.70	98.44	3.21	-7.1
2.15	0.85	80.09	3.36	-25.0
2.25	-0.70	20.72	0.87	-9.3
2.25	-0.50	14.78	0.64	-8.9

Continued on next page

Table C.2 – continued from previous page

$W(GeV)$	$\cos\Theta^x_{CM}$	$\frac{d\sigma}{d\Omega}$ (nb/sr)	σ_{stat} (nb/sr)	Deviation from CLAS 2009 [55] (%)
2.25	-0.30	9.68	0.41	-1.5
2.25	-0.10	9.91	0.45	-7.9
2.25	0.10	13.07	0.56	4.2
2.25	0.30	22.84	0.86	-1.4
2.25	0.50	44.01	1.55	-6.5
2.25	0.70	74.04	2.56	-11.3
2.25	0.85	81.93	3.48	-11.8
2.35	-0.70	15.14	0.63	-7.4
2.35	-0.50	8.51	0.48	2.1
2.35	-0.30	4.85	0.29	-18.4
2.35	-0.10	6.27	0.38	-5.5
2.35	0.10	9.14	0.44	-20.8
2.35	0.30	15.17	0.61	-10.4
2.35	0.50	30.77	1.23	-5.4
2.35	0.70	57.36	2.16	-11.3
2.35	0.85	75.88	3.34	-8.9
2.45	-0.70	8.31	0.40	-0.8
2.45	-0.50	3.20	0.22	6.4
2.45	-0.30	2.62	0.18	7.0
2.45	-0.10	4.17	0.26	-3.9
2.45	0.10	7.21	0.34	3.2
2.45	0.30	10.11	0.45	-2.4
2.45	0.50	21.41	0.89	-3.1
2.45	0.70	46.14	1.86	-6.1
2.45	0.85	67.09	3.07	-31.2
2.55	-0.70	4.70	0.26	-5.5
2.55	-0.50	1.44	0.17	0.1
2.55	-0.30	2.06	0.14	11.5
2.55	-0.10	3.95	0.23	-1.4
2.55	0.10	4.79	0.25	-6.6
2.55	0.30	5.96	0.32	4.9
2.55	0.50	11.93	0.63	-4.6
2.55	0.70	37.34	1.68	-9.1
2.55	0.85	63.72	3.16	-21.8
2.65	-0.70	2.17	0.15	-7.4
2.65	-0.50	0.81	0.08	3.3
2.65	-0.30	1.64	0.11	-6.0
2.65	-0.10	2.78	0.14	2.0
2.65	0.10	3.05	0.18	-16.7
2.65	0.30	2.41	0.17	8.4
2.65	0.50	5.94	0.39	1.9
2.65	0.70	24.10	1.24	-2.7
2.65	0.85	53.44	2.82	-32.5
2.75	-0.70	1.14	0.10	-43.5
2.75	-0.50	0.56	0.07	-7.9
2.75	-0.30	1.13	0.08	-17.0
2.75	-0.10	1.47	0.09	-17.0
2.75	0.10	1.62	0.13	-25.5

Continued on next page

Table C.2 – continued from previous page

$W(GeV)$	$\cos\Theta^x_{CM}$	$\frac{d\sigma}{d\Omega}$ (nb/sr)	σ_{stat} (nb/sr)	Deviation from CLAS 2009 [55] (%)
2.75	0.30	1.43	0.17	-24.4
2.75	0.50	3.35	0.32	-6.8
2.75	0.70	16.89	1.09	-17.3
2.75	0.85	40.43	2.96	-2.4